7-12-2010

Comprehensive Process Maps for Synthesizing High Density Aluminum Oxide-Carbon Nanotube Coatings by Plasma Spraying for Improved Mechanical and Wear Properties

Anup K. Keshri
Florida International University, akesh001@fiu.edu

DOI: 10.25148/etd.FI10080903

FLORIDA INTERNATIONAL UNIVERSITY

Miami, Florida

COMPREHENSIVE PROCESS MAPS FOR SYNTHESIZING HIGH DENSITY ALUMINUM OXIDE-CARBON NANOTUBE COATINGS BY PLASMA SPRAYING FOR IMPROVED MECHANICAL AND WEAR PROPERTIES

A dissertation submitted in partial fulfillment of the

requirements for the degree of

DOCTOR OF PHILOSOPHY

in

MATERIALS SCIENCE AND ENGINEERING

by

Anup Kumar Keshri

2010

To: Dean Amir Mirmiran
College of Engineering and Computing

This dissertation, written by Anup Kumar Keshri, and entitled Comprehensive Process Maps for Synthesizing High Density Aluminum Oxide-Carbon Nanotube Coatings by Plasma Spraying for Improved Mechanical and Wear Properties, having been approved in respect to style and intellectual content, is referred to you for judgment.

We have read this dissertation and recommend that it be approved.

_____
Norman D. H. Munroe

_____
Wonbong Choi

_____
Wenzhi Li

_____
Arvind Agarwal, Major Professor

Date of Defense: July 12, 2010

The dissertation of Anup Kumar Keshri is approved.

_____
Dean Amir Mirmiran
College of Engineering and Computing

_____
Interim Dean Kevin O'Shea
University Graduate School

Florida International University, 2010

DEDICATION

This dissertation is dedicated to the loving memory of my father. He would have been extremely proud of this moment. I dedicate this dissertation to my parents and my brother and sister.

ACKNOWLEDGMENTS

I would like to express my deepest gratitude to Dr. Arvind Agarwal, my major advisor for his support, patience and encouragement throughout my graduate career. I sincerely thank him serving as chair of my dissertation committee. I have been really fortunate to have an advisor like him who has widened my knowledge and taught me how to challenge myself. He always encouraged me to grow as an independent thinker. His promptness and dedication towards the work have always been motivation for me to work harder. I learned a lot from him especially as how to approach for research problem and the need to be persistent to achieve the goal. His enthusiastic spirit and energetic approach have been major driving forces thought out my research, even during tough time of my PhD. I sincerely thank him for giving me an opportunity to work in various projects simultaneously, which has stretched my scope of research work. I greatly appreciate for his concern towards my research, innovative ideas and funding to make my research experience more productive and stimulating. This dissertation would not have been possible without his efficient planning, and supervision.

I would also like to thank my committee members Dr. Wonbong Choi, Dr. Norman D. H. Munroe and Dr. Wenzhi Li for serving on my dissertation committee. Their insightful comments and suggestions on the several aspects of my dissertation have been very helpful and valuable to my research. I received encouragement from them which has motivated me a lot for working hard towards my research. I would like to sincerely thank Dr. Wonbong Choi for extending use of his lab facility. Without his help, this dissertation would not have completed in time.

I would like to acknowledge financial support from Florida International University in terms of Dissertation Year Fellowship. I also acknowledge the financial support received from Office of Naval Research (grant number: N00014-08-1-0494). I would also like to acknowledge the funding from Army Research Office (ARO) (grant number: W911NF-05-1-0391).

I would like to thank Prof. Sudipta Seal, Director, Advanced Materials Processing and Analysis Center (AMPAC), Mr. Virendra Singh at University of Central Florida (UCF), for helping with HR-TEM and XPS of samples.

I gratefully acknowledge Advanced Materials Engineering Research Institute (AMERI) for providing the various facilities used in this research work. I thank Dr. Yanqing Liu for his assistance with Scanning Electron Microscopy (SEM) and Transmission Electron Microscopy (TEM). I would also like to acknowledge Florida Center for Analytical Electron Microscopy (FCAEM) for providing the SEM/EDS facility. I thank Mr. Tom Beasley for his assistance with SEM/EDS. I also thank Mr. Neal Ricks for helping me whenever I was in need. I would like to thank Center for Study of Matter at Extreme Conditions (CeSMEC) for Raman spectroscopy. I would like to thank Dr. Surendra Saxena and Dr. Vadym Drozd for their support and encouragement with the experiments. I thank Mr. Rick Zicarelli, Engineering Manufacturing Center, FIU who has assisted me for designing the several mechanical fixtures for my research work.

I would like to thank Dr. Kantesh Balani, Dr. Tapas Laha, Dr. Srinivas Rao Bakshi and Dr. Yao Chen for their help and suggestions. I would like to sincerely thank Bakshi for his innovative ideas and valuable suggestions towards my research. His way of approaching towards any research problem was always inspiring for me. I would like

to sincerely thank Dr. Yao Chen who has been very friendly to me and always boosted me up in my initial days of PhD. I would like to thank Mrs. Debrupa Lahiri who has always helped me professionally as well as personally. I have been always motivated by seeing her dedication towards the work. I also thank her for the informative discussion, valuable suggestions towards my research. I would like to acknowledge Indranil Lahiri for his moral support and for his encouragement. I am really impressed with his cool and calm nature. I would like to sincerely thank Mr. Riken Patel for helping me in experiments.

I want to extend my thanks to my friends and colleagues Juan Huang, Ved Prakash, Harindra Vedala, Jorge Tercero, Venkata Pasumarthi, Sunil Anand Musali, Di Wang, Yamini Parikh, Puneet Gill, Santanu Das and many more who have always helped me during my tough time. My special thanks goes to Juan Huang who has helped me in my experiment during his tough time of dissertation writing.

I would like to acknowledge Miss Puja Keshri for her care, emotional and moral support during the hardest day of my life. She was my source of inspiration and strength during my research.

Finally I would like to thank my family for being supportive throughout my four years of research. Without their support, I would not have been in a position to finish my PhD.

ABSTRACT OF THE DISSERTATION

COMPREHENSIVE PROCESS MAPS FOR SYNTHESIZING HIGH DENSITY ALUMINUM OXIDE-CARBON NANOTUBE COATINGS BY PLASMA SPRAYING FOR IMPROVED MECHANICAL AND WEAR PROPERTIES

by

Anup Kumar Keshri

Florida International University, 2010

Miami, Florida

Professor Arvind Agarwal, Major Professor

Plasma sprayed aluminum oxide ceramic coating is widely used due to its outstanding wear, corrosion, and thermal shock resistance. But porosity is the integral feature in the plasma sprayed coating which exponentially degrades its properties. In this study, process maps were developed to obtain Al_2O_3-CNT composite coatings with the highest density (i.e. lowest porosity) and improved mechanical and wear properties. Process map is defined as a set of relationships that correlates large number of plasma processing parameters to the coating properties.

Carbon nanotubes (CNTs) were added as reinforcement to Al_2O_3 coating to improve the fracture toughness and wear resistance. Two novel powder processing approaches *viz* spray drying and chemical vapor growth were adopted to disperse CNTs in Al_2O_3 powder. The degree of CNT dispersion via chemical vapor deposition (CVD) was superior to spray drying but CVD could not synthesize powder in large amount. Hence optimization of plasma processing parameters and process map development was limited to spray dried Al_2O_3 powder containing 0, 4 and 8 wt. % CNTs.

An empirical model using Pareto diagram was developed to link plasma processing parameters with the porosity of coating. Splat morphology as a function of plasma processing parameter was also studied to understand its effect on mechanical properties.

Addition of a mere 1.5 wt. % CNTs via CVD technique showed ~27% and ~24% increase in the elastic modulus and fracture toughness respectively. Improved toughness was attributed to combined effect of lower porosity and uniform dispersion of CNTs which promoted the toughening by CNT bridging, crack deflection and strong CNT/Al_2O_3 interface. Al_2O_3-8 wt. % CNT coating synthesized using spray dried powder showed 73% improvement in the fracture toughness when porosity reduced from 4.7% to 3.0%. Wear resistance of all coatings at room and elevated temperatures (573 K, 873 K) showed improvement with CNT addition and decreased porosity. Such behavior was due to improved mechanical properties, protective film formation due to tribochemical reaction, and CNT bridging between the splats. Finally, process maps correlating porosity content, CNT content, mechanical properties, and wear properties were developed.

TABLE OF CONTENTS

LIST OF TABLES

LIST OF FIGURES

LIST OF SYMBOLS

SYMBOL	: QUANTITY
E	: Elastic modulus
E’	: Storage modulus
E’’	: Loss modulus
m	: Mass of Sensor
t	: Time
x	: Displacement
$\dot{x}$	: Rate of Change of Displacement
$\ddot{x}$	: Acceleration
A	: Area
A_c	: Contact Area of Nanoindenter Tip
C	: Damping of System
C_2	: constant (1.4388 cm.K)
D	: Distance
ϕ	: Phase Shift
ω	: Frequency
H	: Hardness
P	: Applied Load
c	: Radial crack length
χ	: Empirical constant
K_c	: Fracture toughness
V	: Wear volume
S	: Sliding distance
F_f	: Frictional force
μ	: Coefficient of friction
ζ_{max}	: Maximum spread
T_s	: Surface Tension
V	: Volume
ρ	: Density

T	: Temperature of particle in plasma spraying
V	: Velocity of particle in plasma spraying
μ	: Viscosity of molten liquid
γ	: Liquid-gas surface tension
θ_a	: Liquid-solid contact angle
D_0	: Initial droplet diameter
α	: Thermal diffusivity
P_e	: Prandtl number
C	: Specific heat
λ	: Wavelength
ε	: Spectral emissivity
T	: Surface Temperature of Radiating Body
k	: Stiffness
F_0	: Sinusoidal force
σ	: Standard deviation
N	: Number of Walls in CNT
ΔG	: Free energy change
σ_c	: Fracture strength of composite
ν_{fm}	: Volume fraction of matrix
ν_{fr}	: Volume fraction of reinforcement
w_m	: Weight fraction of matrix
w_r	: Weight fraction of reinforcement
R_a	: Average surface roughness

1. INTRODUCTION

The objective of the present research work is to develop process maps for achieving "*high density"* carbon nanotube (CNT) reinforced aluminum oxide (Al_2O_3) coatings with improved fracture and wear properties. Figure 1.1 shows the overall research work that has been carried out to meet this objective.

Plasma sprayed Al_2O_3 coating are effective for wear resistance, corrosion resistance, heat and thermal shock resistance and have been widely used in US navy systems and by other industries [4, 13-17]. However, plasma sprayed coatings often suffer from the presence of porosity which subsequently leads to degradation of mechanical properties [4, 18]. Also, "*reproducibility*" of the coating's micostructure is another major concern due to large number of variable and complexities involved with plasma spraying technique [4, 19-21]. Porosity in the coating can be by tailored by controlling the powder feedstock and plasma processing variables. In spite of decades of research on this topic, there is still a lack of understanding between process-structure-property relationships for synthesizing dense coatings by plasma spray technique.

Inherent brittleness of Al_2O_3 ceramic is another major factor that limits its performance in practical applications [22-25]. Hence, there is a need to toughen Al_2O_3 coatings for their use in structural applications. Due to their excellent mechanical and thermal properties, carbon nanotubes (CNT) has attracted much attention as an ideal reinforcement to toughen the ceramics, including Al_2O_3 [2, 4, 5, 7, 9, 18, 22, 24-39].

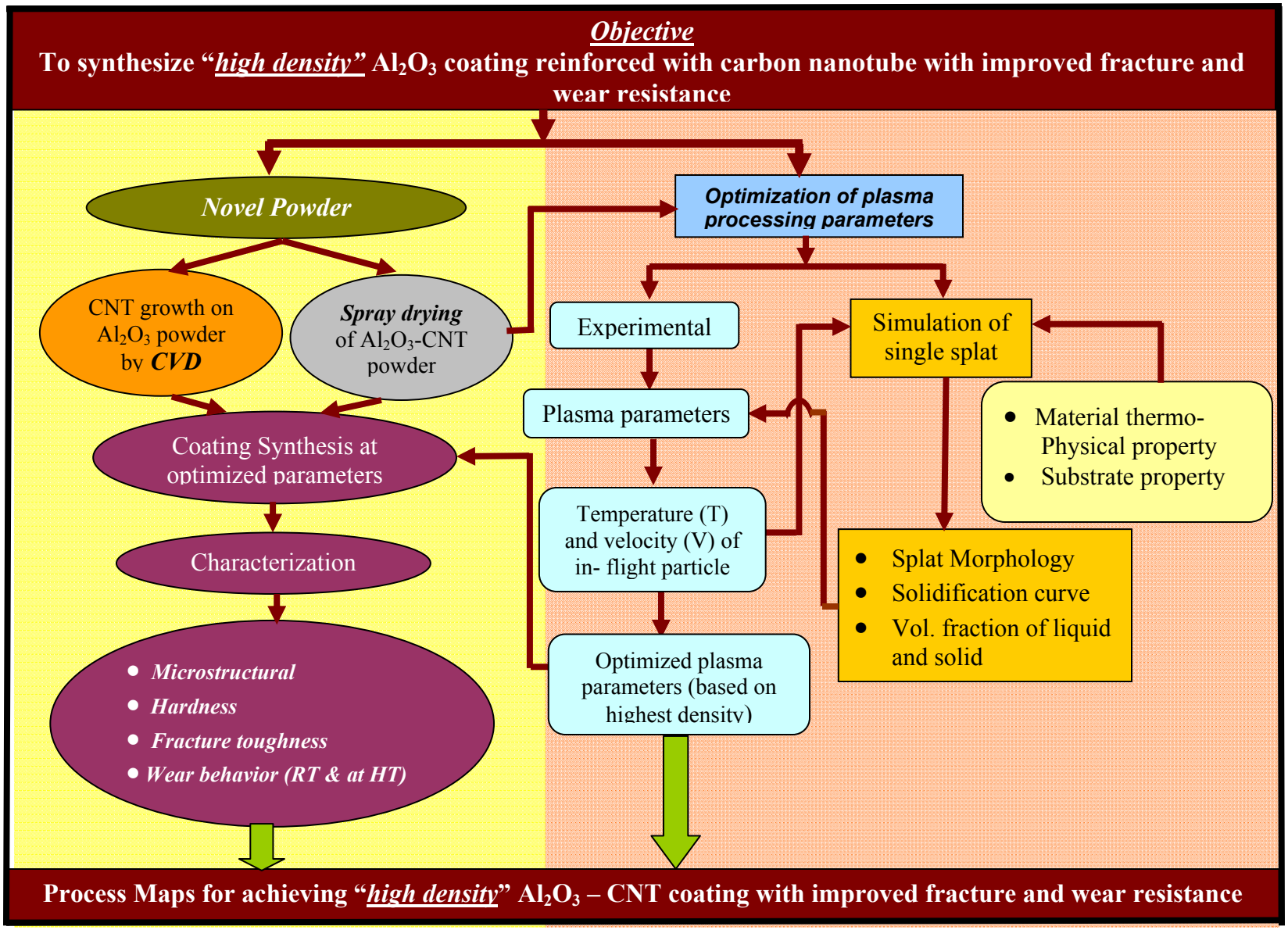

Figure 1.1: Flow diagram showing summary of research work

Novel powder processing approaches *viz* in situ growth of CNTs via chemical vapor deposition (CVD) technique and spray drying of Al_2O_3-CNT powder have been adopted in this study to reinforce and uniformly disperse CNT in the Al_2O_3 matrix. In order to achieve reproducible dense coatings, optimization of plasma processing parameters has been carried out and process map relating plasma parameters to coating's properties have been developed. Role of splat morphology in porosity and effect on coating properties has been addressed. The challenges associated with this research are summarized in the next section.

1.1 Challenges in Fabrication of Al_2O_3-CNT Coatings

1.1.1. Dispersion of CNTs in Al_2O_3 Matrix via. CVD Technique

Dispersion of CNTs in ceramic matrix including Al_2O_3 has challenged several researchers in the fabrication of CNT composites [2, 40, 41]. Due to larger surface area of CNTs, they tends to agglomerate and form clusters as a result of strong Van der Wall force [5, 42]. In situ growth of CNTs on each powder particle via CVD technique has been adopted in this study for improved CNT dispersion. Dense Al_2O_3 powder served as a substrate during CVD growth of CNTs. However controlling the CNT length during CVD process is a major challenge which has been addressed by optimizing the CNT growth time.

1.1.2. Process Maps for Achieving Dense Reproducible Coating

Plasma spraying involves more than hundreds of variables in terms of process, equipment and starting powder feedstock which affect the coating's density and

ultimately the mechanical properties [4, 19-21]. Also, reproducibility of the dense coating is major concern. To deal with this problem, optimization of plasma process parameters has been carried out. Process maps haver been developed in order to understand the influence of "key processing parameters" on the thermal and kinetic energy of the particle that affect "porosity" and, hence "mechanical properties" of the coating.

1.1.3. Role of Splat Morphology in Coating's Porosity

Porosity is the inherent feature in plasma sprayed coatings which mainly depends on the splats morphology and their stacking. The porosity can be controlled by tailoring the splat morphology and size. The splat morphology mainly depends on the powder material properties, in-flight particle's thermal and kinetic state and the substrate conditions. Detailed study has been carried out in order to understand the splat morphology and its effect on porosity.

1.2 Past Work and Limitations on Al_2O_3-CNT Nanocomposites

Our research group at Plasma Forming Laboratory at Florida International University has pioneered the synthesis of CNT reinforced Al_2O_3 nanocomposite coatings by plasma spray techniques [4, 5, 9, 18, 28, 43]. Balani et al. from our group did the composite spray drying of nano Al_2O_3 powder with 4 wt. % and 8 wt. % CNT and successfully synthesized plasma sprayed Al_2O_3-4 wt. % CNT and Al_2O_3-8 wt. % CNT composite coatings [4, 18]. Following were the outcomes of their research work.

- Successful dispersion of CNTs in the Al_2O_3 matrix [4, 18].

- Fracture toughness enhancement up to 57% by reinforcement of 8 wt. % of CNT in Al_2O_3 matrix [4].
- Modulus increase up to 200% from 210 GPa in Al_2O_3 coating to 425 GPa in Al_2O_3-8 wt. % CNT coating because of CNT addition and dispersion [44].
- Improvement in the dry sliding wear resistance up to 49 times by reinforcement of 8 wt. % of CNT in Al_2O_3 matrix [9].

However, relative density of these coatings was reported 88-94% [4]. There is further scope of increasing the density of coatings. It is known that elastic modulus and porosity can be correlated by the semi empirical equation [45].

$$E = E_0 \exp[-(bp + cp^2)] \tag{1.1}$$

where p is the porosity, E_0 is the elastic modulus of fully dense material and E is the overall elastic modulus of porous material and b and c are constants. Equation 1.1 indicates that elastic modulus of coating degrades exponentially with the porosity (and so does fracture toughness and wear resistance). Hence, there is a need to enhance the density of the plasma sprayed Al_2O_3-CNT coatings which will significantly affect the microstructures and properties.

High density coating can be achieved by novel powder processing approach and by optimizing plasma processing parameter. In another work, Balani et al. [5] did preliminary study of growing CNTs on dense Al_2O_3 powder via CVD technique. CVD powder was blended with 50 vol. % Al_2O_3 without CNTs and mixture was plasma sprayed to form a coating [5]. The relative density of the Al_2O_3-CNT composite coating

was found ~90% and the relative fracture toughness of the coating enhanced by 11.6% [5]. However, the length of CNTs grown on Al_2O_3 powder were ~4-7 μm long which might lead to entanglement of CNTs and can result in poor densification of coating. There is a further scope of achieving the critical CNT length by optimizing the CVD processing times. Fan et al. [46] has reported that critical CNT length of 100 nm is sufficient for load transfer. Apart from CNT length, it will be also of interest to use 100% CVD powder for synthesizing the coating instead of blended mixture of CVD powder and 50 vol. % of Al_2O_3 powder. Balani et al. [4] also attempted to develop preliminary process map for plasma sprayed CNT reinforced Al_2O_3 coating. However, this study did not provide the effect of various plasma parameters on mechanical properties of coatings.

1.3 Focus of the Present Research Work

The overall aim of the current research work is to develop the process map for synthesizing high density Al_2O_3-CNT coating with improved fracture and wear resistance. Following are the specific aims of this work.

- In situ growth of CNTs on dense Al_2O_3 powder via CVD technique.
- Optimization of plasma processing parameters and development of process map.
- Understanding role of porosity and CNT reinforcement in fracture toughness of coating under indentation loading.
- Evaluation of wear resistance as a function of porosity, CNT content and operating temperature.
- Understanding the role of single splat in coating's microstructure via experimentation and simulation.

- Establishing the correlation between coating's porosity, fracture toughness, wear resistance and CNT content.

The research work carried out is systematically presented in this dissertation in various chapters. Chapter 2 is the literature review which describes the successive progression of work done by various researchers. Development of process map has been summarized in this chapter. Chapter 3 describes the methodology of the experiment carried out in this work. Chapter 4-10 is the heart of this dissertation i.e. results and discussion where process maps, toughening mechanism of Al_2O_3 by CNT, tribological behavior at room and elevated temperatures and single splat formation has been analyzed and discussed. Correlations between the process and coating's property have also been presented in Chapter 10. Conclusions have been stated in the chapter 11 where key findings are listed. Chapter 12 lists down several recommendations for future work which seems to be necessary in continued improvement of this research area. Appendix includes technical papers related to this work which are published in peer-reviewed journal.

2. LITERATURE REVIEW

2.1 Carbon Nanotubes as Reinforcement

Since their discovery by Ijima in 1991, carbon nanotubes with high aspect ratio, larger surface area, low density as well as excellent mechanical, electrical, and thermal property have been identified as a potential reinforcement in ceramics matrix [2, 4, 5, 7-9, 24-26, 30-39, 44]. According to the geometric configuration, carbon nanotube can be divided into two following categories: i.e. (a) single-wall CNT (SWCNT), (b) and multi-wall CNT (MWCNT) with an interlayer spacing of 0.34-0.36 nm [47]. The SWCNT is a single graphite sheet which has been rolled into a hollow cylinder (as shown in Figure 2.1a). On the other hand, the MWCNT consist of many concentric graphite layers (as shown in Figure 2.1b). The interaction between the layers is dominated by the Van der Waal forces. Unless mentioned otherwise, CNT in this dissertation refers to multi walled carbon nanotube.

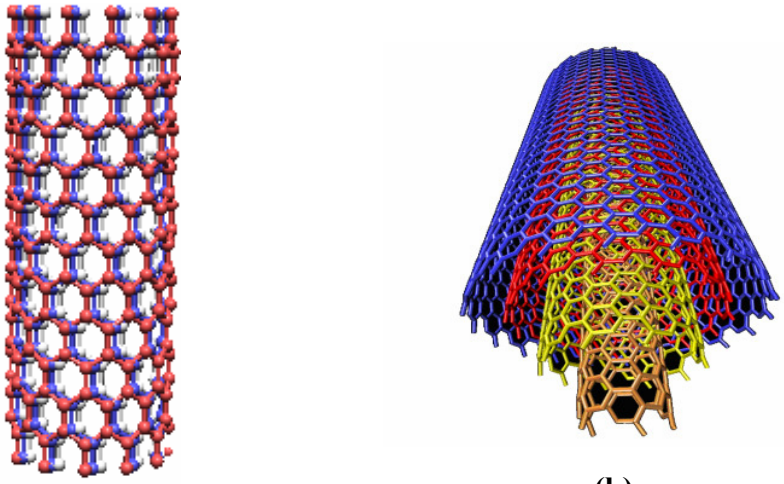

(a) **(b)**

Figure 2.1: (a) Single walled carbon nanotube (b) Multi-walled carbon nanotube

The outstanding mechanical property of CNT aroused particular interest to develop ceramic nanocomposite with improved fracture toughness and wear resistance. Researchers have measured the mechanical properties of CNT by several methods [37, 39, 48]. Yu et al. has measured the mechanical property of CNT by in situ tensile testing using atomic force microscope (AFM) tip inside scanning electron microscope (SEM)[39] . Tensile strength of CNT ranges between 11-63 GPa and Young's modulus varied between 270-950 GPa [39]. Treacy et al. measured the Young's modulus of CNT by measuring the amplitude of thermal vibrations at different temperature in transmission electron microscope (TEM) [37] . Young's modulus was measured in range of 0.4-4.15 TPa with an average value of 1.8 TPa [37]. These properties of CNT make it as an ideal reinforcement for the fabrication of nanocomposite with improved mechanical properties.

Huang et al. [49] reported that, SWCNT can undergo superplastic deformation at high temperature and can be 280% longer and 15 times narrower before breaking. This superplasticity behavior of SWCNT can be attributed to nucleation and motion of kinks in the structure [49]. Hence, SWCNT could serve as a potential reinforcement to improve the ductility of the nanocomposite. However, the major challenge in reinforcement of CNTs in the ceramic matrix is its uniform dispersion [1, 41, 50]. Researchers have adopted different techniques to uniformly disperse CNTs in the ceramic matrix which is discussed in details in next section.

2.2 Dispersion of CNT in Ceramic Matrix

Uniform dispersion of CNTs has been the major challenge in CNT reinforced ceramic composites. This is due to the large surface area of CNT which leads to formation of clusters as results of Van der Wall force [1, 5, 41, 42, 50]. CNT clusters degrade the mechanical properties of coatings [51, 52]. Hence, in order to achieve homogeneous properties, uniform dispersion of CNTs in matrix is critical. CNT dispersion techniques can broadly be divided into two major category viz. (a) mechanical methods and (b) Physical (non-covalent treatment) methods or chemical methods (covalent treatment) [53].

Mechanical dispersion method such as ultrasonication, ball milling, stirring can uniformly disperse CNTs, but these processes reduce the aspect ratio of CNTs [53, 54]. Table 2.1 summarizes the different CNT dispersion technique in the ceramic matrix and the property achieved by the other researchers. Advantages and limitations of different CNT dispersion techniques are also summarized in Table 2.1

Chemical dispersion method involves the functionalization of CNT under which they are treated with acid at high temperature. Poyato and co-workers [1] have effectively dispersed SWCNTs (10 vol. %) on Al_2O_3 nanoparticles by using acid treatment in conjunction with aqueous colloidal processing. Figures 2.2a and b shows the fracture surface of blended Al_2O_3-10 vol. % SWCNT and colloidal Al_2O_3-10 vol. % SWCNT composite respectively showing the difference between the dispersion of SWCNT. Clusters of SWCNT (arrow marked in Figure 2.2a) were observed in Al_2O_3-10

Table 2.1: Overview of CNT dispersion techniques in the ceramic matrix and property achieved				
Author	**Matrix**	**CNT Content**	**Dispersion technique**	**Remarks (%) indicates property improved compared to monolithic**
Poyoto et al. [1]	Al_2O_3	SWCNT-10 vol. %	Colloidal Processing	• Density of colloidal Al_2O_3-10 vol. % SWCNT composite : 98% • Density of blended Al_2O_3-10 vol. % SWCNT : 94% Better dispersion in colloidal process
Lei et al. [3]	Al_2O_3	CNT-2 wt. %	Hetrocoagulation	• Fracture toughness: 6.35 $MPam^{1/2}$ (25%). • Flexural strength: 331 MPa (10%)
Mo et al. [40]	Al_2O_3	CNT-0-3.3 vol. %	Sol-gel	• Fracture toughness increased by 10% by 1.5 vol. % CNT and decreases with 3.3 vol. %.
Duszova et al. [55]	ZrO_2	1.07 wt. % CNT	Ultrasonication	• Density of ZrO_2-CNT was lower than ZrO_2 due to presence of CNT clusters • Hardness and fracture toughness of ZrO_2-CNT decreased by 30% and 10%. • Electrical resistivity decreased by 13 times.
Yamamoto et al. [56]	Al_2O_3	0.9 vol. % CNT	Precursor method (CNT were modified by acid treated)	• Bending strength and fracture toughness improved by 27% and 25% respectively.
Balani et al. [4]	Al_2O_3	0- 8 wt. % CNT	Spray drying	• Fracture toughness enhancement : 42% (4wt. % CNT), 57% (8wt. % CNT) • Wear resistance improvement : 5.1 times (4wt. % CNT), 49 times (8wt. % CNT)
Balani et al. [5]	Al_2O_3	0.5 wt. % CNT	In situ CVD	• Fracture toughness improvement : 11.6 %

vol. % SWCNT and most of the Al_2O_3 boundaries appeared clean. But for colloidal Al_2O_3-10 vol. % SWCNT, nanotubes were well dispersed and present at most of the Al_2O_3 grain boundaries (Figure 2.2b). The composite synthesized by spark plasma sintering was ~97.6% dense but 40% weight loss of SWCNT was observed due to acid treatment [1]. Also, use of acid at high temperature for surface functionalization might introduce structural defects in CNTs [57, 58]. Elastic modulus of CNTs decreases gradually with increasing functionalization due to introduction of sp^3 hybridized sites [18]. Also, it has been reported that the maximum compressive force for ethyne functionalized nanotubes reduced by 15% due to the repulsive force from functionalization [59].

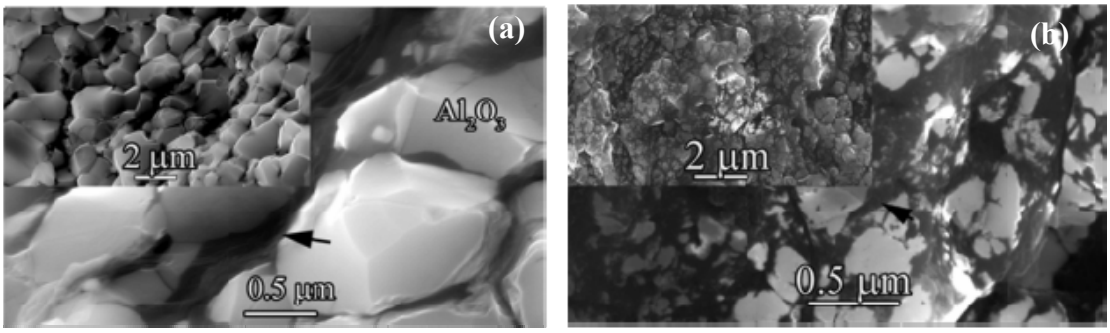

Figure 2.2.: SEM micrograph of (a) conventional Al_2O_3-10 vol. % SWCNT composite (b) Colloidal Al_2O_3-10 vol. % SWCNT composite. The arrow marked dark regions are SWCNTs while the bright regions are Al_2O_3. Inset is the corresponding lower magnification SEM image. [1]

Molecular level mixing (covalent treatment) has shown outstanding results to achieve uniform dispersion of CNTs in the Al_2O_3 matrix (as shown in Figure 2.3a) [2]. In this process, functionalized CNTs and metal ions are mixed uniformly in an aqueous

solution at a molecular level and hence, the major challenge of strong agglomeration of CNTs in ceramic matrix can be avoided. However, molecular level mixing restricted dispersion to low CNT content as it caused agglomeration for a composition over 1.8 vol. % CNTs (as shown in Figure 2.3b) [2].

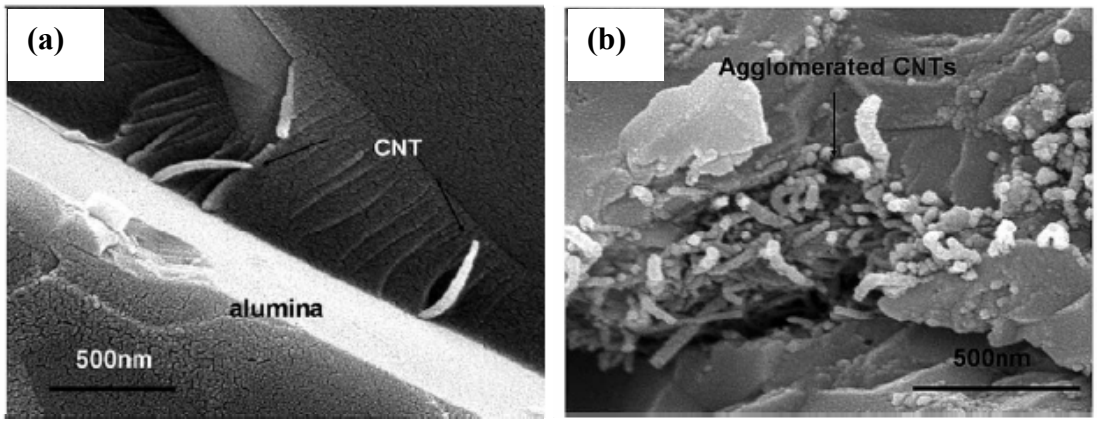

Figure 2.3: SEM micrograph of fracture surface of (a) Al_2O_3-1vol. % CNT showing uniformly dispersed CNT and pull out of CNT (b) Al_2O_3-1.8 vol. % CNT showing agglomeration of CNT [2]

In last few years, non covalent treatment such as hetrocoagulation technique has been widely used to obtain uniformly dispersed carbon nanotubes [3, 41]. In hetrocoagulation technique, surfactants change the surface property of CNTs from hydrophobicity to hydrophilicity, resulting in an improved dispersion of CNTs in aqueous solution. Lei et al. [3] observed effective dispersion of CNTs in Al_2O_3 matrix by hetrocoagulation technique and found ~25% increase in the fracture toughness of Al_2O_3-2 wt. % CNT composite. Improvement in the fracture toughness of Al_2O_3-2 wt. % CNT

composite was attributed to uniform dispersion of CNT, pull out of CNT at fracture surface and bridging by CNTs (as shown in Figures 2.4a and b). However, surfactants may introduce undesirable impurities which can affect composites properties [1, 2].

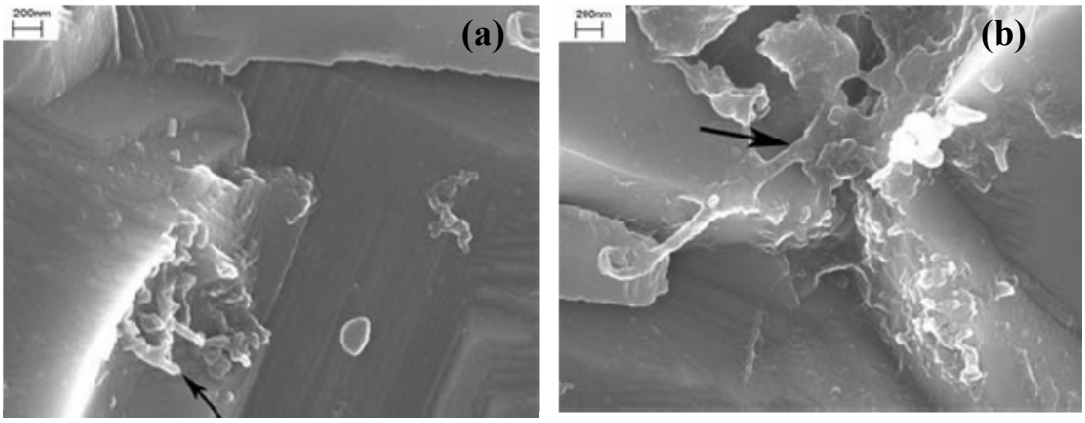

Figure 2.4: SEM micrograph of fracture surface of Al_2O_3-2wt. % CNT composite (a) showing CNT pull out (b) bridging by CNTs [3].

Sol-gel process is another CNT dispersion technique that has shown promising results to achieve homogeneous dispersion in the ceramic matrix. Mo et al. [40] dispersed CNTs in Al_2O_3 matrix using sol-gel process as shown in Figure 2.5a. Relative fracture toughness of Al_2O_3 nanocomposite was enhanced by ~10% by adding 1.5 vol. % of CNTs to Al_2O_3 [40]. However, sol-gel method also resulted in CNT agglomeration (as shown in Figure 2.5b) for higher concentration (> 3.3 vol. %) which reduced the fracture toughness. Cha et al. [2] concluded that sol-gel process leads to weak interface between the CNT and Al_2O_3.

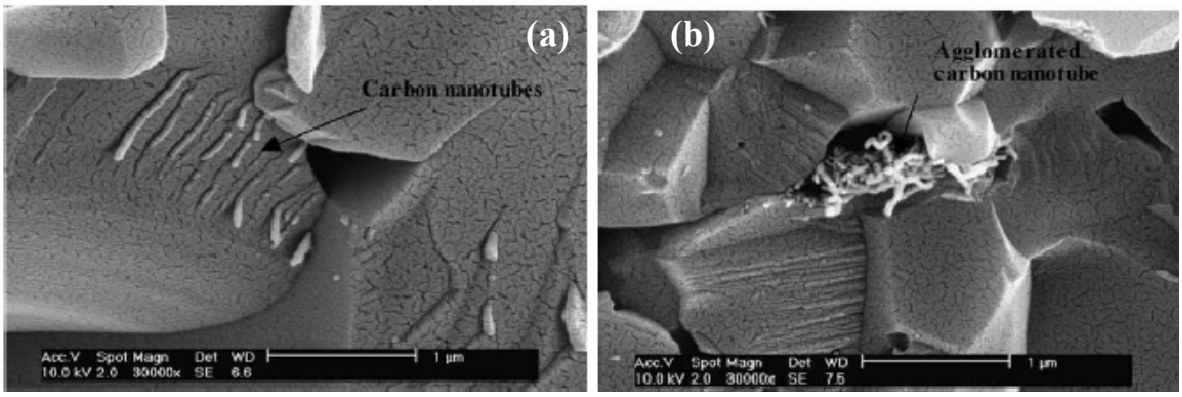

Figure 2.5: SEM micrograph of fracture surface of (a) Al_2O_3-1.5 vol. % CNT composite showing uniformly dispersed CNT (b) Al_2O_3-3.3 vol. % CNT composite resulting agglomeration of CNTs [40].

Balani et al. [4, 18] from our research group utilized spray drying technique to disperse CNTs with nano-Al_2O_3 powder to form a composite spherical agglomerate powder. Spray drying involves mixing ceramic powder and CNTs in poly-vinyl alcohol (PVA) binder to form aqueous slurry. The slurry was subsequently spray dried by hot gas atomization in a chamber to form composite spherical agglomerates. CNTs were uniformly distributed on the surface (as shown in Figure 2.6) and the core of the spray dried agglomerate. However, spray dried agglomerate contains 30-45% porosity [18]. Balani et al. successfully synthesized Al_2O_3-8 wt. % CNT composite coating by plasma spraying of spray dried Al_2O_3-8 wt. % CNT powder to obtain 57% improvement in the fracture toughness [4]. However, relative density of the coating was 88-94% due to porosity in spray dried powder that causes splashing during plasma spraying.

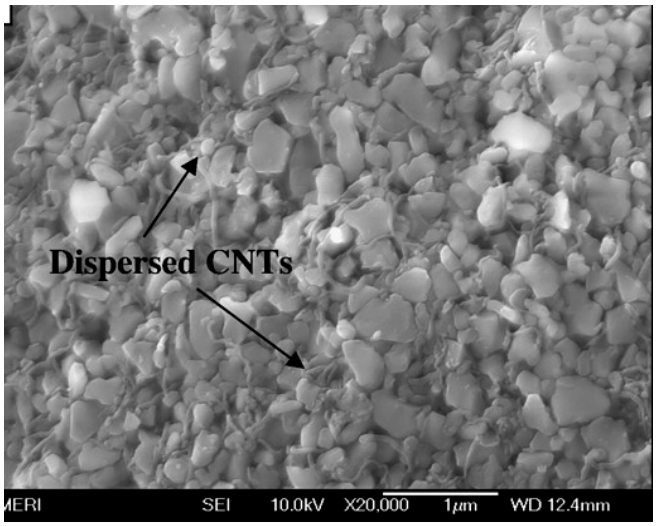

Figure 2.6: SEM image showing dispersion of CNT over Al_2O_3-8 wt. % CNT powder surface [4].

A dense powder would result in improving the density of the CNT reinforced composite. To alleviate the problem of low density of spray dried powder, Balani et al. [5], conducted a preliminary study on growing CNTs on dense Al_2O_3 powder via chemical vapor deposition (CVD) technique. Though CVD technique has limitations of "slow kinetics" and "low yield of pure CNTs", it has potential to uniformly disperse CNTs in the matrix. In the study carried out by Balani et al., CVD powder was blended with 50 vol. % Al_2O_3 (without CNTs) and mixture was plasma sprayed to form a coating. The relative density of the Al_2O_3-CNT composite coating was found ~90% and the relative fracture toughness of the coating enhanced by 11.6% [5]. Improvement in the fracture toughness of coating was attributed to the presence of CNT tentacles (Figure 2.7a) and the uniform occurrence of CNT bridging (shown in Figure 2.7b) between the splats. However, the length of CNTs grown on Al_2O_3 powder were ~4-7 μm long which lead to entanglement of CNTs in the powder and resulted in poor flowability through

plasma gun and resulting in low density. There is a need to obtain the critical CNT length by optimizing the CVD processing times. Fan et al. [46] has reported that critical CNT length of 100 nm is sufficient for load transfer. It will be also of interest to use 100% CVD powder for synthesizing the coating instead of blended mixture of CVD powder and 50 vol. % of Al_2O_3 powder, as used by Balani et al [5].

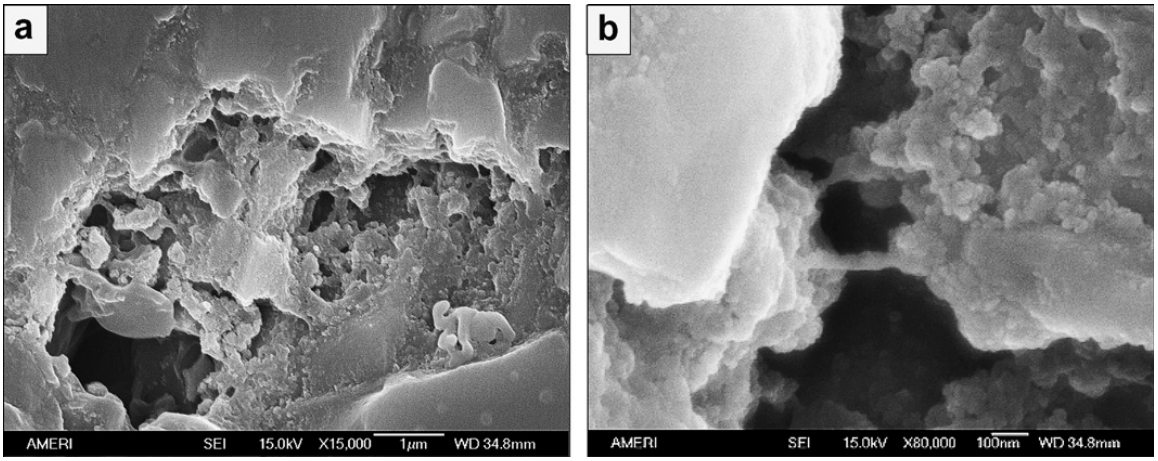

Figure 2.7: Fracture surface of plasma sprayed Al2O3-0.5wt. % CNT coating showing (a) presence of CNT tentacles arising out of Al_2O_3 splats (b) CNT bridging between Al_2O_3 splats [5].

The dispersion method discussed above resulted in varying degree of CNT dispersion in powder. But it is equally important to maintain the dispersed CNT in the composites after consolidation. Since plasma spraying is a layer by layer deposition technique, it is expected that uniformly distributed CNTs within powder/agglomerate will also lead to uniform dispersion of nanotubes in the composite coating. Our group has pioneered the synthesis of CNT reinforced metal and ceramic composite coating via plasma spraying which is discussed in the next section [4, 5, 9, 18, 27, 44, 60-64].

2.3 Plasma Spraying Technique

A schematic of the plasma spraying technique is shown in Figure 2.8. An arc is stuck between tungsten cathode and copper anode to generate the plasma. The temperature at the core of the plasma reaches in excess of 10,000K [65, 66]. During plasma spraying process, powder is injected into the high temperature plasma jet, where powder get melted/heated and accelerated towards the substrate. Molten/semi-molten particles exiting from the plasma jet impacts on the substrate, flattens and rapidly solidifies at a cooling rate of approximately 10^6-10^8 K/s [65, 66] . Successive deposition of molten particles ***(splats)*** builds up the coating thickness.

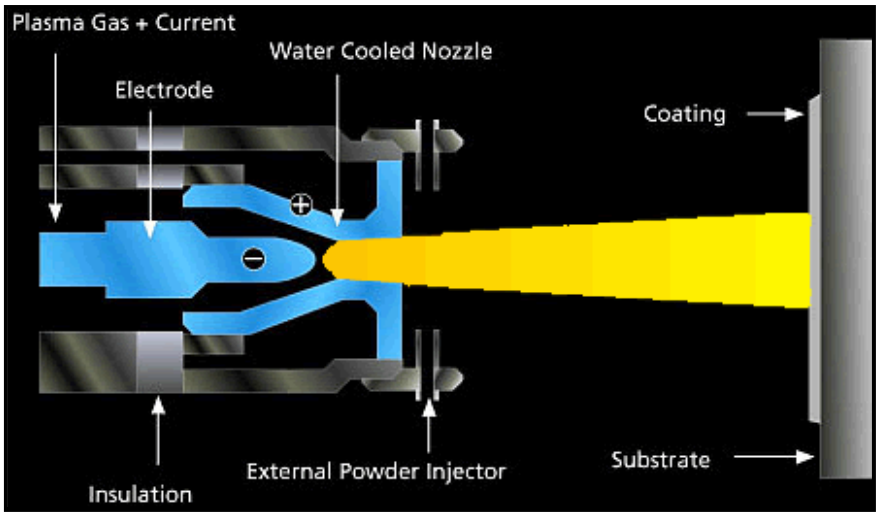

Figure 2.8: Schematic of plasma spraying

2.3.1 Complexities Involved in Plasma Spraying

Plasma spraying is widely used technique to synthesize metallic, ceramic, intermetallics, and composites coating to protect the substrate against wear, corrosion, and high temperature environment [4, 61, 67, 68]. However, plasma spraying involves

hundreds of variables (as shown in Figure 2.9) such as process, equipment and powder parameters which have a direct effect on the coating properties [19, 20, 69-73]. Despite scientific and technical progress at many aspects, there is lack of understanding between process-structure-property relationships due to large number of variables and complexities involved with plasma spraying. Also, reproducibility of the dense coating is still a major challenge [21, 65, 74]. Hence, there is need of optimization of plasma processing parameters and to understand the effect of process parameters on the coating property.

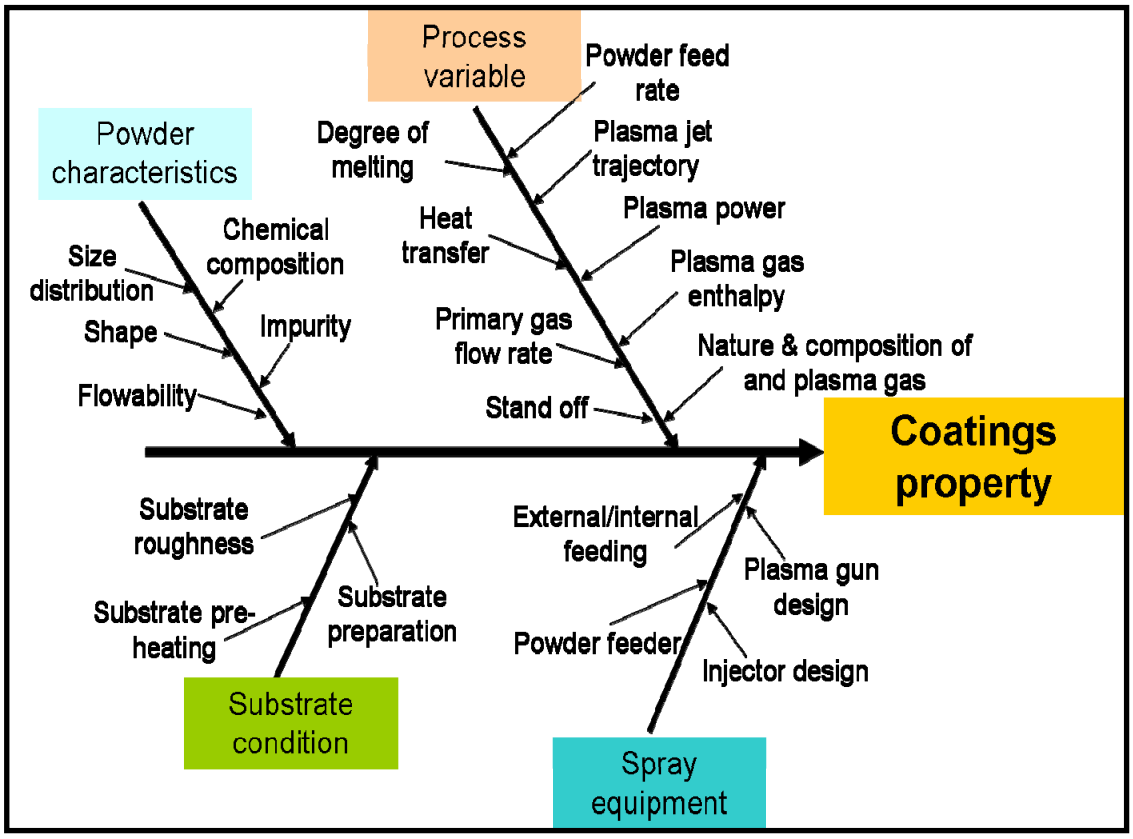

Figure 2.9: Variables in plasma spray process which affects the coatings property

Figure 2.10 shows the number of research publications in the last decade on the optimization of plasma process parameters for ceramic coatings. This indicates that optimization of process parameters with respect to coatings property has not been much explored and is in nascent stage.

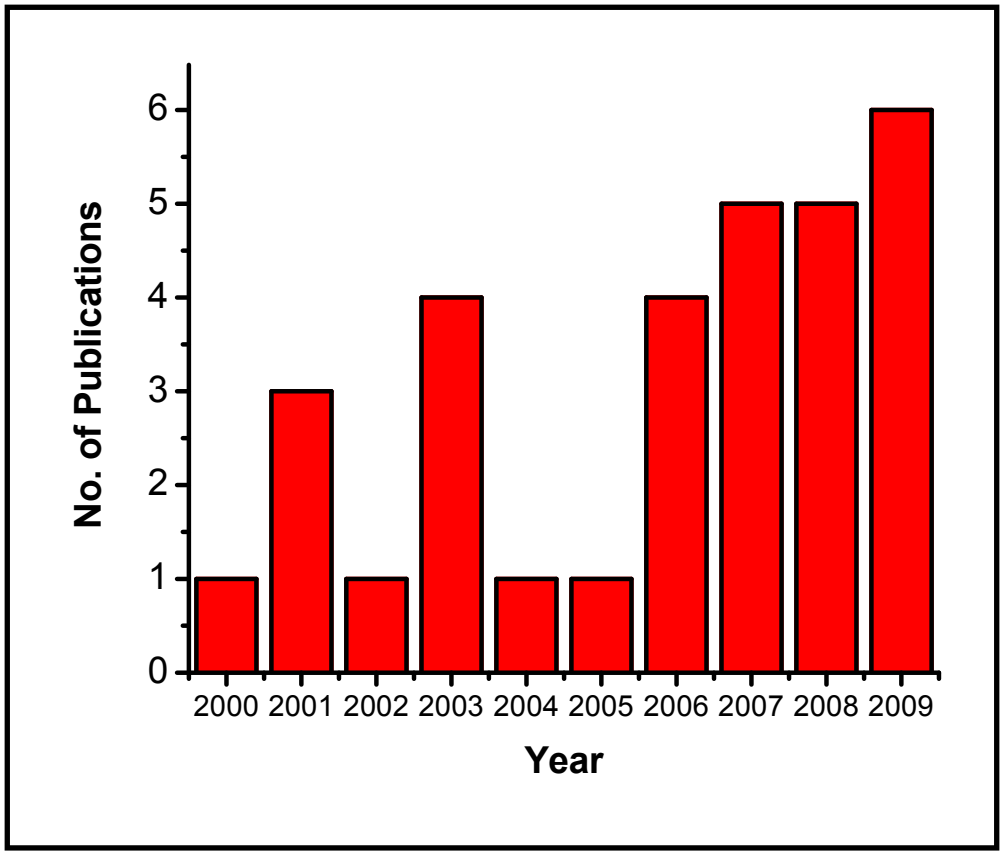

Figure 2.10: Year wise work carried out on optimization of plasma process parameters for plasma sprayed ceramic based coatings

The influence of plasma process parameters on the coating property has largely been studied by empirical approach. Empirical approach involves changing only one process parameter at a time to observe its effect on coating property [20]. However, this approach requires prohibitively large number of experimental trials to systematically

identify the most significant parameters affecting the coating characteristics [20]. Researchers [20, 75, 76] have adopted the statistically design of experiment approach to optimize the plasma process parameters. Table 2.2 summarizes the list of studies which shows that most of the optimization of plasma process parameters was carried out using design of experiment (DOE) approach. The detail of design of experiment approach has been reviewed in the following section.

2.4 Design of Experiment Approach for Optimization of Plasma Process Parameters

Design of experiment (DOE) method is widely used in thermal spraying and it involves the methodology for constructively changing process parameters to determine their effect on the coating property [20, 75, 76]. The initial step in performing the design of experiment is the choice of variables i.e. which plasma process parameter is significant from the tens of variables. . The parameters can be fixed at low (-1) and high (+1) level and the experimental domain lie inside these parameters. The properties of sprayed coating in different experiments can be represented as a form of polynomial equation (Equation 2.1) [76];

$$Y = b_0 + \sum b_j X_j + \sum b_{ij} X_i X_j + \sum b_{ijk} X_i X_j X_k \quad (2.1)$$

where i, j, k vary from 1 to number of chosen plasma process variables and b0 is the mean of response (coating property) of all the experiments, coefficient bi represents the effect of variables Xi and bij, bijk are the coefficients of regression which represent the effect of interaction of variables XiXj, XiXjXk respectively.

Table 2.2: Optimization of plasma process parameters by various methods				
Year	**Materials and processing technique**	**Optimization Method**	**Parameters chosen for optimization**	**Remarks**
2001 Baik et al. [77]	SiC fiber reinforced $MoSi_2$ (Low pressure plasma spray)	Design of experiment approach	• Gun current, • primary and secondary gas • Flow rate • Chamber pressure Flow rate	Porosity & surface roughness almost constant with different LPPS parameter Deposit thickness varied
2001 Mawdsley et al. [78]	Al_2O_3 coating (Atmosphere plasma spraying)	Design of experiment approach and regression analysis	• Power • Spray distance • Total plasma gas flow • % of H_2 in plasma gas • Injector offset and angle • Carrier gas flow	H(GPa) = 9.0 0.9(SD) 0.5(TGF) 0.4(P) 0.3(A) %Corrosion = 54 16(SD) 8(TGF) 11(%H) Thickness(mm) = 229 27(TGF) 23(IO) 23(P) 19(%H) 12(A),
2003 Friss et al. [19]	YSZ Thermal barrier coating (Atmosphere plasma spraying)	Process map by In-flight diagnostic	• Gun current Primary gas flow rate	Increasing spray gun current and primary gas flow rate decreases porosity in the coating
2003 Sampath et al. [79]	Molybdenum coating (Atmosphere plasma spraying)	Process map by In-flight diagnostic	• Torch current • Auxiliary gas flow rate Carrier gas flow rate	Plasma current has dominant influence on T &V, Increasing powder carrier gas flow decreasing T &V Helium gas flow has small effect on T &V
2004 Gussasma et al. [80]	Al_2O_3-13% TiO_2 coating (Plasma spraying)	Statistical method (Artifical neural network)	• Spray distance, • Spray angle Arc current intensity	ANN method was successfully applied to atmosphere plasma spray and predective results showed good agreement with experimental

2005 Li et al. [20]	YSZ Thermal barrier coating (Atmosphere plasma spraying)	Uniform design of experiment	• Current • Primary and secondary gas flow rate • Spray distance • Powder feed rate	Argon flow rate and the hydrogen flow rate were most intensive two parameters affecting deposition efficiency, porosity and microhardness
2006 Dyshloven ko et al. [81]	Hydroxyapatite, (Atmosphere plasma spraying)	Design of experiment approach and regression analysis	• Electric power • Plasma forming gas mixture • Carrier gas flow rate	24 full factorial design has been used. Electric power used is most sensitive for resonse function i.e. fraction of HA crystal phase & two phase of its decomoposition
2007 Lin et al. [82]	Partially stabilized zrconia, (Atmosphere plasma spraying)	Response surface methodology & fractional factorial experiment	• Arc current • Powder feed rate • Primary gas flow rate	The most significant variables affecting the plasma spraying processes were identified as arc current, powder feeder rate and primary gas. These three variables account for about 60% of the experimental variance.
2008 Vaidya et al. [6]	YSZ coating (Atmosphere plasma spraying)	Design of experiment approach and in-flight diagnostic	• Total mass flow rate of plasma gas, • Gun current • Volume ratio of H_2 w.r.t primary gas	For given mass flow rate, increase in gun current and secondary flow rate result in increase in temperature and velocity. Increase of mass flow rate of plasma gas increases particles velocity while temperature decreases
2008 Balani et al. [4]	Al_2O_3-CNT coatings Plasma spraying	Process map by In-flight diagnostic	• Plasma power • Feed rate	CNT reinforced Al_2O_3 powder showed reduced thermal exposure compared to 0 wt% of CNT in Al_2O_3 powder.
2010 Dwivedi et al. [83]	YSZ Thermal barrier coating (Atmosphere plasma spraying)	Process map by In-flight diagnostic	• Arc current, • Argon flow rate • Hydrogen flow rate	First order process map allowed examination of parameters specific variability and hence enhanced reliability of coating

Coefficients in equation 1 can be determined by different design of experiment approaches which are as following:

- Hadamard or Plackett-Burman matrices [76, 84]
- Two-level full factorial design (2^k) [85-87]
- Two level fractional factorial design (2^{k-m}) [88]
- Response of surface methodology (RSM) designs [82]

The Hadamard matrix is used to optimize large number of factors (i.e. plasma process parameters) X_i (i>4) which can affect the response function (i.e. coating property). Each factor can have two level (-1 or +1) (e.g. powder feed rate f_1 = 3 g/min correspond to X_i= -1 and powder feed rate f_2 = 6 g/min correspond to X_i = +1). To determine whether factors are critical, first order polynomial equation is developed (Equation 2.2) and first factors are checked whether they are statistically significant.

$$Y = b_0 + \sum b_i X_i \tag{2.2}$$

The effect b_i having the greatest absolute value corresponds to the most critical factor.

Two-level full factorial design (2^k) is used when interaction between X_i and X_j factors are suspected while two level fractional factorial design (2^{k-m}) is used to extract the part of experiment from full factorial design, when number of factors (k) are high. Response of surface methodology (RSM) design is used when the response and factors does not have a linear relationship. In this case, factors at multiple levels have to be used to determine quadratic ($b_{ii}X_i^2$) or cubic term ($b_{iii}X_i^3$) using RSM methodology.

Taguchi and orthogonal design methods are other techniques to optimize the plasma process parameters [89]. Both of these methodologies statistically outline the impact of each process variable on the measured coatings property across all combinations of other factors. However, the drawback of these method is that, it involves larger number of experimental trials [20]. Recently Fang et al.[90, 91] have developed a new statistical experiment method i.e. the uniform design of experiments technique to optimize the plasma process parameters which involves fewer experiments for large number of factors. Uniform design of experiment approach has been discussed in detail in the following section.

2.4.1 Uniform Design of Experiment Approach

Uniform design of experiment technique needs its design points to be uniformly scattered on the experimental domain. Wang et al. [92] proposed a method for constructing the uniform distribution on the experimental domain which is based on the stochastic representation and the inverse transformation method in Monte-Carlo method. There are several other methods to construct the uniform design such as good lattice method [91], Latin square method [90], expending orthogonal design method [93] and optimization searching method [94] which uses the algorithm to obtain the uniform design of experiments. Compared with the conventional statistical experimental methods, uniform design method reduces the number of experimental trials for experiments involving quite a number of factors [75].

Li et al. [20] optimized the plasma processing parameter for YSZ coating using uniform design experiment method with respect to deposition efficiency, porosity and microhardness. Using a uniform design of experiments approach, the influence of the five process parameters (arc current, primary gas flow rate, secondary gas flow rate, spray distance and powder feed rate) on the coatings characteristics (deposition efficiency, porosity and microhardness) was identified and expressed in form of polynomial equations [20]. These polynomial equations were regressed from first to third order. Third-order equations were most appropriate to identify the influence of the process parameters on the deposition efficiency, porosity and microhardness [20].

The drawbacks of above statistical design are the low reproducibility and low quality standards of the synthesized coatings [19]. Also, long lead-time between synthesis of the coating and the destructive coating evaluation, makes these approaches very time-consuming and expensive [19]. Hence, there is need of establishing the process-structure-property relationship in an efficient manner in order to achieve the reliability and reproducibility of coating.

It is well known to thermal spray community that temperature and velocity of the in-flight particle are two main parameters which largely affect the coatings microstructure. Temperature controls the degree of melting whereas velocity affects the degree of flattening of the splats and subsequent coating formation. The advent of in-flight diagnostic sensors has made it possible to control the plasma spray technique in a

more precise manner by developing "process maps". Following section discusses development of process map in detail.

2.5 Development of Process Maps

Process map can be defined as a set of relationships that correlates processing parameters to the coating properties. Figure 2.11a shows the concept of process map for plasma sprayed coatings. The entire process has been sub-divided into two regions: (i)first order process map and (ii) second order process map. Spray stream largely depends on process parameters, process hardware, and feedstock characteristics and can be adjusted by changing any of these parameters. The ability to characterize the spray stream as function of input variables refers to *first order process map*. However, first order process maps do not reflect the effect of process variable on the final microstructure of the coating. Linkage between spray streams and coating property is referred as *second order process map*. Hence, process-structure-property relationship can be established by combination of first and second order process map. Figure 2.11b shows how process map relates to optimization and tailoring of coating microstructure.

.

Researchers have developed process maps for different material-substrate systems in order to obtain the effective design and optimization of the coatings. Sampath et al. [79] developed the process map for plasma sprayed molybdenum and investigated the importance of spray parameter such as gun current, primary gas flow, auxiliary gas flow, and powder carrier gas flow on modulus, hardness, thermal conductivity and porosity of

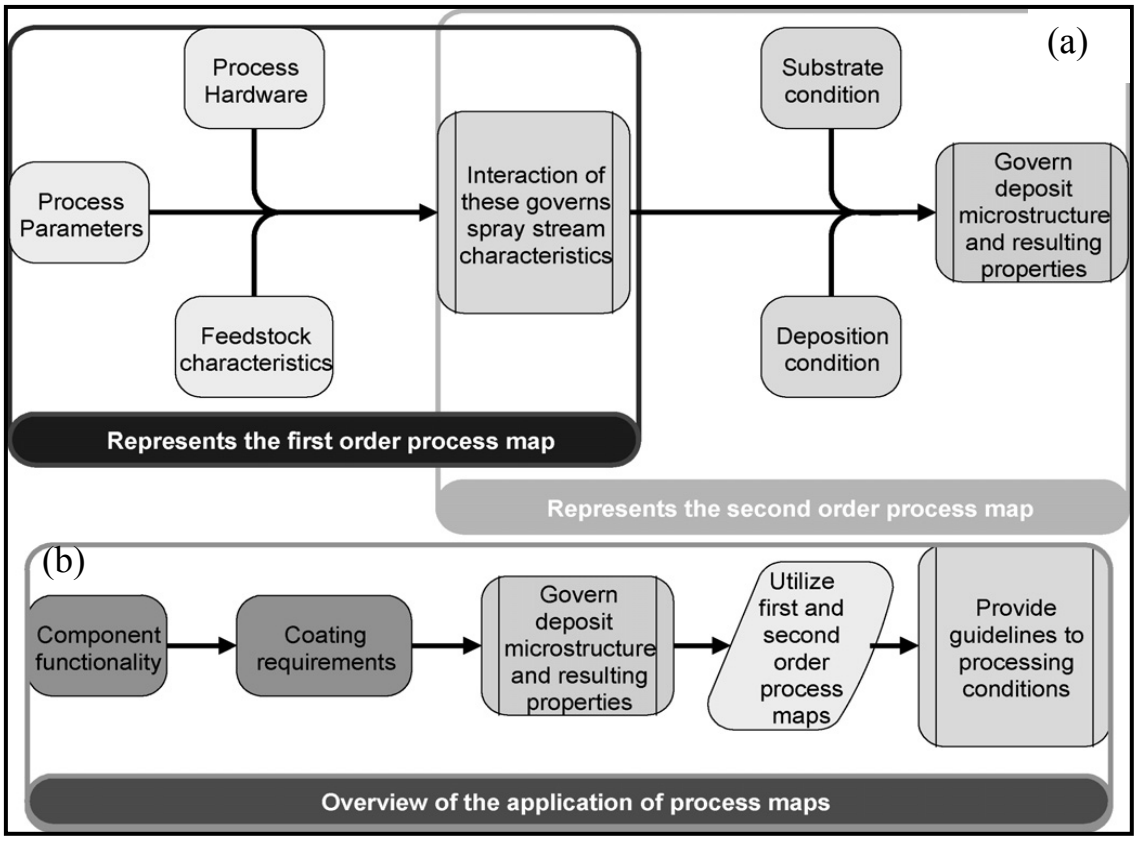

Figure 2.11: (a) Schematic of process map for plasma sprayed coatings (b) Overview of how process map relate to optimization and tailoring of microstructure [6]

coating. Their complete methodology of developing the process map involved two major steps *viz.* development of empirical model relating in-flight particle characteristics with input variable (i.e. first order process map) and finally correlating in-flight particle characteristics with coating property (i.e. second order process map) [79]. The mean velocity and temperature of in-flight particle was found strongly dependent on the gun current. Hardness and thermal conductivity of the coating increased with the particle velocity while porosity of the coating decreased with increasing particle velocity. Significant improvement in the thermal conductivity and elastic modulus of the coating

was obtained with the increase in substrate deposition temperature [79]. Vaidya et al. [6] developed the process map for plasma sprayed YSZ and they linked the plasma torch parameters with the particle state through design of experiment approach and in-flight diagnostics. Process window was identified by correlating first order process map to coating property. Improvement in the elastic modulus was found with the increase in particle kinetic energy [6]. Above all listed studies on process map relates plasma input parameter to coating property. However the reproducibility of coatings still remains a concern due to dynamic variables such as erosion/wear of plasma gun hardware and variation in different batches of the powder feedstock.

Balani et al. [4] from our research group, attempted to develop *preliminary processing map* for plasma sprayed CNT reinforced Al_2O_3 coatings, where the prime objective was to determine the effect of type of CNT dispersion *(blending vs. spray drying*) in the powder feedstock on the microstructural evolution such as fully melted zone and partially melted zone. This preliminary analysis was based on a smaller number of processing variables and experiments and *did not* rank the key plasma processing parameters in terms of the effect on the coating density and hardness.

Motivated by this scenario, the ***objective*** of this study is to develop the process maps to understand the influence of "key processing parameters" on the thermal and kinetic energy of the particle that effect "density" and "hardness" of the coating. Effect of CNT content on the thermal and kinetic history of the particle in the plume is also investigated to obtain the coating with the highest density and hardness. Based on the

literature and our past experience, the key process variables selected to develop process maps for Al_2O_3-CNT coating with the ***"highest density"*** are as following.

- *Plasma power:* directly influences the particle temperature which determines the extent of melting of the particles in the plasma plume.
- *Primary gas*: is the main source of generating thermal energy to the plasma system.
- *Stand-off distance*: Distance between plasma gun and the substrate influences the velocity and degree of flattening of the molten/heated powder particle.
- *Powder feed rate*: The amount of powder in the plasma plume impacts its thermal and kinetic properties. A high feed rate could lead to reduced particle temperature and presence of un-melted particles in the coating resulting in low density.

Since the ultimate aim of developing the process map is to enhance the mechanical properties, it is important to review the current state of the art of mechanical properties of CNT-ceramic composites which is presented in the following section.

2.6 Mechanical Properties of CNT-Ceramic Composites

Though ceramics have high stiffness, outstanding thermal stability, and low density, it has some inherent drawback which includes relatively lower fracture toughness and degradation of mechanical properties at high temperature [14, 62, 64, 95, 96]. Reinforcement of second phase in the ceramic matrix may lead to improvement in fracture toughness and mechanical property of ceramics. Because of their exceptional resilience [49], carbon nanotube (CNT) has emerged as a potential reinforcement for ceramics. One other outstanding characteristic of CNTs are its very high aspect ratio

which can be useful for load transfer with matrix and can provide effective reinforcement to ceramic. Since the focus of the current work is on Al_2O_3-CNT nanocomposite, detailed review is restricted to Al_2O_3 matrix.

2.6.1 Fracture Toughness of Al_2O_3-CNT Composites

Table 2.3 summarizes fracture toughness of Al_2O_3–CNT composite reported in the literature. Siegel et al. [36] reported that addition of 10 vol. % CNT to monolithic Al_2O_3 could lead to 24% increase in fracture toughness. Zhang et al. [25] reported 21.1% increase in fracture toughness by reinforcing 7.39 wt% CNT to Al_2O_3. Balani et al. [4] reported 57% increase in fracture toughness value by reinforcing 8 wt. % CNT to Al_2O_3. Xia et al. [7] did the indentation test using nanoindenter on CNT/alumina composites produced by in-situ CVD technique followed by hot-press sintering. Figure 2.12a shows the crack generated in the composite after the indentation. Three major toughening mechanisms in CNT reinforced ceramic composite are reported which are as Following: (i) crack deflection at CNT/matrix interface (as shown in Figure 2.12b) (ii) crack bridging by CNTs (as shown in Figure 2.12c) (iii) CNT pullout on the fracture surface (as shown in Figure 2.12d) [7]. Zhan et al. [8] synthesized the Al_2O_3/10 vol. % SWCNT composite using spark plasma sintering and measured the toughness using Vicker indentation technique. Fracture toughness of Al_2O_3/10 vol. % SWCNT composite was achieved 9.7 $MPam^{1/2}$ [8], which was three times to that of pure nanocrystalline alumina ($3.3MPam^{1/2}$).

Table 2.3: Overview of mechanical property of Al_2O_3 – CNT composite reported in literature				
Year	**Matrix material**	**CNT content**	**Processing route**	**Investigated property (%) indicates property improvement compared to monolithic**
2002 Sun et al. [84]	Al_2O_3	SWCNT 0.1 wt. %	Colloidal Processing	Fracture toughness (VI): 4.9 MPa $m^{1/2}$ (31%)
2002 Zhan et al. [19]	Al_2O_3	SWCNT 10 vol. %	Powder Processing	Fracture toughness (VI): 9.7 MPa $m^{1/2}$ (200%)
2002 Wang et al. [15]	Al_2O_3	SWCNT 10 vol. %	Powder Processing	Fracture toughness (SENB): 3.33 MPa $m^{1/2}$ (3%)
2003 An et al. [85]	Al_2O_3	MWCNT 4 vol. %	Powder Processing	Friction coefficient: 0.45 (-10%), Wear loss: 2 MPa $m^{1/2}$ (-45%)
2005 Mo et al.[33]	Al_2O_3	MWCNT 1.5-3.3 vol. %	Sol Gel	Fracture toughness (VI): 1.1 MPa $m^{1/2}$ (10%) with 1.5 wt. %
2005 Sun et al.[83]	Al_2O_3	MWCNT 1 wt. %	Colloidal Processing	Bending strength: (10%)
2006 Fan et al. [86]	Al_2O_3	MWCNT 12 vol. %	Colloidal Processing	Fracture toughness (SENB): 5.55 MPa $m^{1/2}$ (80%)
2007 Zhu et al. [87]	Al_2O_3	MWCNT 2 wt. %	Colloidal Processing	Fracture toughness (SENB): = dir. 4.66 MPa $m^{1/2}$ (23.2%), \ dir. 3.65 MPa $m^{1/2}$ (-3.4%)
2007 Jiang et al. [88]	Al_2O_3	SWCNT 10 vol. %	Powder Processing	Fracture toughness (VI): 9.71 MPa $m^{1/2}$ (200%), Hardness: 1610 kg/mm^2
2008 Yamamoto et al.[35]	Al_2O_3	MWCNT 0.9 vol. %	Colloidal Processing	Fracture toughness (SENB): 5.9 MPa $m^{1/2}$ (25%), 6.64 MPa (41%), Bending strength: 689.6 MPa (27%)
2008 Ahmad et al. [41]	Al_2O_3	MWCNT 7 vol. %	Powder Processing	Fracture toughness (SENB): 6.8 MPa $m^{1/2}$ (117%), Bending strength: 490 MPa (44%)

2008 Yamamoto et al. [89]	Al_2O_3	MWCNT 0.5 wt. %	Colloidal Processing	Fracture toughness (SENB): 4.8 MPa $m^{1/2}$ (20%), Flexural strength: 572 MPa (17%)
2008 Wei et al.[90]	Al_2O_3	MWCNT 3 vol. %	Colloidal Processing	Fracture toughness (SENB): 5.01 MPa $m^{1/2}$ (79%), Bending strength: 410 (13%)
2008 Balani et al.[5]	Al_2O_3	MWCNT 0.5 wt. %	In Situ CVD	Fracture toughness (VI): 4.62 MPa $m^{1/2}$ (12%), Hardness: 905.9 VHN (12%)
2008 Estili et al.[91]	Al_2O_3	MWCNT 3.5 vol. %	Colloidal Processing	Fracture toughness (VI): 5.2 MPa $m^{1/2}$ (99.5%)
2008 Xia. Et al. [16]	Al_2O_3	MWCNT 10 vol. %	In Situ CVD	Frictional coefficient: 0.073 (-50%)
2008 Balani et al. [2]	Al_2O_3	MWCNT 8 wt. %	Spray drying	Fracture toughness : 5.12 MPa $m^{1/2}$ (57%), Wear resistance : 49 times
2009 Kim et al.[92]	Al_2O_3	MWCNT 1.5-3 vol. %	In Situ CVD	Flexural strength : (40%) with 1.5 vol. % CNT Flexural strength lower than momolithic Al_2O_3 with 3 vol. % CNT Fracture toughness : 4.7 MPa $m^{1/2}$ (40%) with 3 vol. % CNT
2009 Zhang et al.[20]	Al_2O_3	MWCNT 3-19 wt. %	In Situ CVD	Fracture toughness :3.50 +0.07 MPa $m^{1/2}$ (0 wt. % CNT) Fracture toughness :3.83 +0.48 MPa $m^{1/2}$ (3.19 wt. % CNT) Fracture toughness :4.70 +0.74 MPa $m^{1/2}$ (7.39 wt. % CNT) Fracture toughness :2.47 +0.65 MPa $m^{1/2}$ (8.25 wt. % CNT) Fracture toughness :1.32 +0.32 MPa $m^{1/2}$ (19.1 wt. % CNT)
2010 Zhang et al. [93]	Al_2O_3	MWCNT 1-5 vol. %	Colloidal Processing	Flexural strength (540 MPa) higher than monolithic Al_2O_3 (400 MPa) with 1 vol. % CNT Flexural strength (230-240 MPa) with higher content of CNT Fracture toughness : 3.3 + 0.5 MPa $m^{1/2}$ (0 vol. % CNT) Fracture toughness : 4.1 + 0.6 MPa $m^{1/2}$ (1 vol. % CNT) Fracture toughness : 3.5 + 0.4 MPa $m^{1/2}$ (3 vol. % CNT)

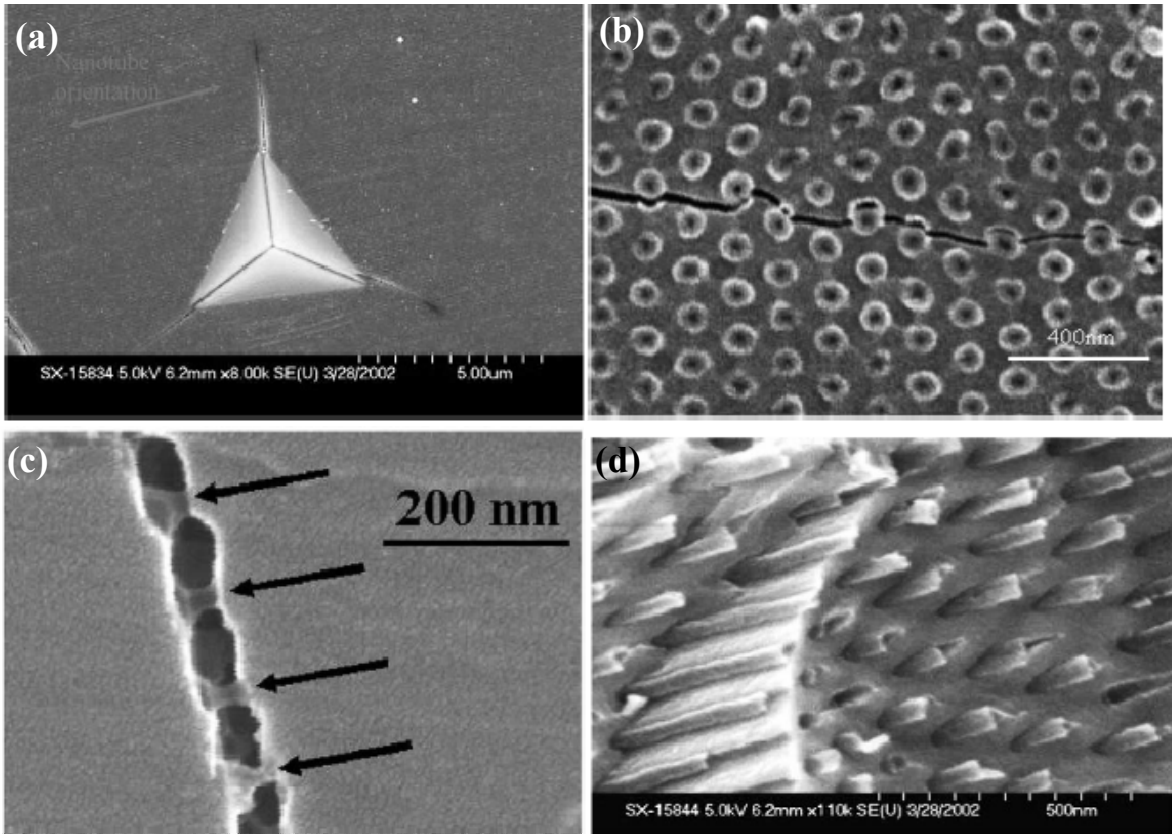

Figure 2.12: SEM images showing (a) crack generated by nanoindenter and different failure mechanisms including (b) crack deflection, (c) CNT bridging, (d) CNT pull-out in CNT/alumina composites produced by in situ CVD technique followed by hot-press sintering [7].

Figure 2.13 shows the comparative fracture toughness results as a function of CNT content of Zhan et al. work with other studies in the literature. The substantial increase in fracture toughness of SWCNT reinforced Al_2O_3 composite was attributed to stronger interfacial bonding between SWCNT and Al_2O_3 and the crack deflection by SWCNT in the composite [8, 24].

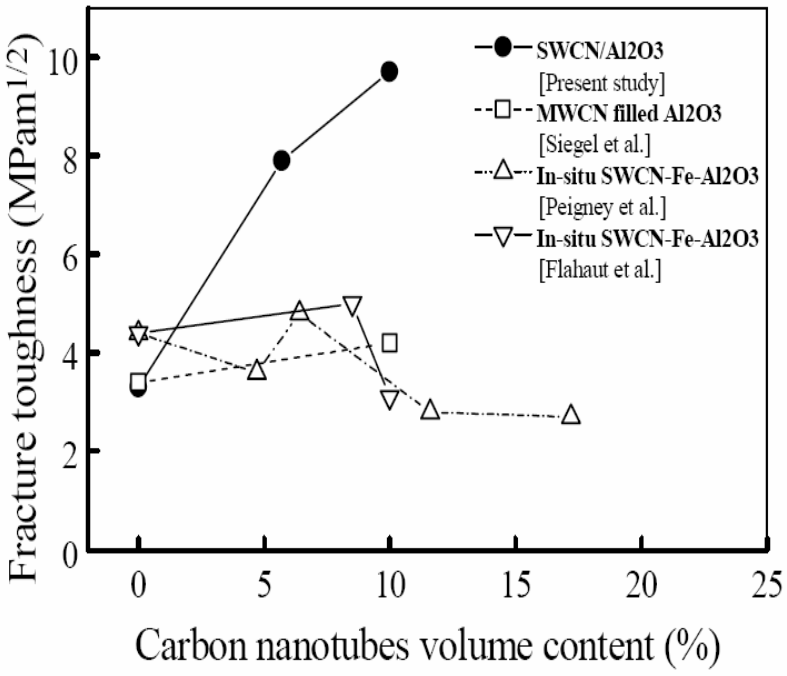

Figure 2.13: Fracture toughness versus carbon nanotube volume content in aluminum oxide based composites as reported in literature [8].

Most of the studies shown in Table-2.3 have used Anstis equation (Equation-2.3) to measure the , fracture toughness of the composite [92].

$$K_c = \chi\left(\frac{E}{H}\right)^{1/2}\frac{P}{c^{3/2}} \tag{2.3}$$

P is the applied load, E is the elastic modulus, H is the Vickers hardness, c is the radial crack length (measured from center of indent), and χ is an empirical constant which depends on the geometry of the indenter. For a cube corner indenter, $\chi = 0.04$ while for Vickers and berkovich indenter is 0.016 and 0.032 respectively [107, 108]. Wang et al. [38] contradicted that Vickers indentation for measuring the fracture toughness is an indirect technique and fracture toughness depends mainly on the elastic/anelastic

contact-mechanical response of the materials. Addition of carbon may allow shear deformation under the indenter which can limit the cracking around indentation resulting in high fracture toughness value [38]. They synthesized similar composite of Al_2O_3/10 vol. % SWCNT using spark plasma sintering and measured the toughness of the composite using Vickers indentation technique as well as by direct toughness measurement (single edge V-notched beam, or SEVNB) [38]. Vickers indentation test on composite showed very small crack in the composite which indicates that composites are crack resistant i.e. higher toughness of the composite while the toughness value measured by SEVNB technique (3.22 $MPam^{1/2}$ for Al_2O_3 and 3.32 $MPam^{1/2}$ for Al_2O_3/10 vol. % SWCNT) indicates that composites are not tough which is in contrast to Zhan et al results. The discrepancy observed between both the tests is explained by following facts. In indentation test, highly concentrated load acts on a very small area which leads to intense confined-shear, while in bend test the crack tip is subjected to mode I tension only. Secondly, homogeneous and heterogeneous ceramic both respond differently in case of contact loading. It is difficult to rule out the shear deformabilities of homogeneous and heterogeneous ceramics because both deform anelastically under the intense confined-shear [38].

Recently, Quinn et al. [109] did a comprehensive review on the Vickers indentation test for fracture toughness measurement and discussed the limitations of this technique. They supported the finding of Wang et al. and recommended that Vickers indentation technique should not be used to determine the absolute value of fracture toughness in ceramics [109]. However, in response to Wang et al. work, Jinag et al.

reported that SEVNB is not a standard and reliable testing method for measuring the fracture toughness. The bluntness of the notch tip remains an issue. In addition, residual stress generated during the notch making process influences the toughness which can develop the complexities. Further, it has been mentioned that, both of these two techniques does not give absolute reliable K_{IC} for really brittle material, but still they can be used to measure the crack propagation resistance under comparative frame.

It is well accepted that fracture toughness also have a significant impact on the tribological behavior of coatings [9, 98, 110-112]. Tribological behavior of CNT-ceramic composites is reviewed in the following section

2.6.2 Tribological Behavior of Al_2O_3-CNT Composites

Evans and Marshall [110] has proposed the wear of ceramic material based on the fracture toughness value which is represented in equation 2.4.

$$V = P_n^{1.125} K_c^{-0.5} H^{-0.625} \left(\frac{E}{H}\right)^{0.8} S \tag{2.4}$$

where, V is the wear volume (m^3), P_n is applied load (MPa), K_c is fracture toughness, H is the hardness, E is the elastic modulus (GPa) and S is the sliding distance (m). Equation 4 clearly indicates that high fracture toughness of the material will result in improved wear resistance of the ceramic.

An et al. [98] studied the effect of 4 wt. % CNT additions on the tribological behavior of hot pressed Al_2O_3 and observed that relative wear weight loss decreased by

45% with CNT addition. The decrease in weight loss was attributed to the combined effect of increased hardness and decreased coefficient of friction [98]. Decrease in coefficient of friction might be due to lubricating effect of CNTs which may arise both from the graphitic nature of CNT and the rolling of CNTs between the specimen and the ball. However, the wear resistance of the composite significantly decreased with the addition of 10 wt. % CNT which was attributed to inhomogeneous dispersion of CNT and poor cohesion between CNT and Al_2O_3 matrix [98]. Another study on the tribological performance of Al_2O_3-CNT by Lim et al. [113] showed that wear weight loss continuously decreased with an increase in CNT content up to 12 wt.%. This was attributed to the enhanced dispersion of CNT in Al_2O_3 composite which was achieved by tape casting followed by lamination and hot pressing. Balani et al. [9] reported an improvement of 49 times in the pin-on-disk sliding wear resistance by addition of 8 wt. % CNT to Al_2O_3. Such improvement was attributed to a uniform dispersion of nanotubes, CNT bridging between the splats and enhanced densification by CNTs. Figure 2.14 shows wear densification by CNTs on the wear surface of Al_2O_3-8 wt. % CNT coating [9]. Xia et al. concluded that that coefficient of friction in aligned MWCNT/Al_2O_3 composite also depends on the contact and buckling behavior of the CNTs in addition to their lubrication characteristic [7].

These all studies investigated tribological behavior of the Al_2O_3-CNT coating at room temperature. *However, no attempt has been made to study the tribological behavior of CNT-reinforced ceramic composites at elevated temperature.* Though there are some

studies that provide an insight into tribological characteristics of Al_2O_3 without CNT reinforcement at the elevated temperature [112, 114].

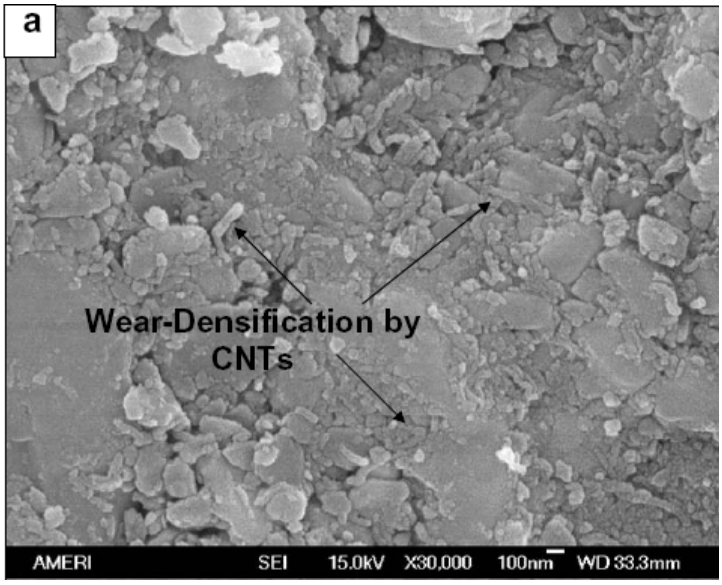

Figure 2.14: SEM image of wear surface of Al_2O_3-8 wt. % CNT coating showing wear densification by CNTs [9]

Ouyang et al. [114] studied the tribological characteristics of low-pressure plasma-sprayed Al_2O_3 coating from room temperature to 800°C and found a transition from mild to severe wear with the increasing temperature. At room temperature, Al_2O_3 coating exhibited low friction (0.17) and wear rate (1.07×10^{-5} mm^3/Nm) when sliding against Al_2O_3 ball. However, when temperature is increased above 400°C, coefficient of friction (COF) and wear of the Al_2O_3 coating increased rapidly and reached a maximum (COF: 1.52, wear rate: 2.97×10^{-4} mm^3/Nm) at 800°C [114]. Similar result was found by Lin et al. [112] who studied the tribological behavior of titanium oxide (TiO_2) reinforced Al_2O_3 (Al_2O_3-3 wt.% TiO_2) coating against silicon nitride (Si_3N_4) ball from room

temperature to 873 K. They found that the wear rate of coating was too small to be measured accurately at the room temperature and increased (~5.5×10^{-5} mm^3/Nm) with the increase in the temperature. Improved wear resistance at room temperature was attributed to the formation of protective silicon oxide (SiO_2) layer on the wear track. This protective SiO_2 layer was the result of the oxidation of Si_3N_4 (counter body) ball in the presence of the moisture [112]. It was observed that, with the increasing temperature, the absorption tendency of moisture on the worn surface decreased and there was no more protective SiO_2 layer resulting in higher wear of the coating [112]. Formation of the protective layer between the ball and the coating occurs due to tribochemical reaction which is caused by the moisture/oxygen absorption from the atmosphere [112].

In this dissertation, study, the tribological behavior of plasma sprayed Al_2O_3-CNT coatings is investigated at *room* and *elevated temperature (up to 873 K)* using ball-on-disk tribometer. This is the *first study* which presents the high temperature tribological behavior of CNT reinforced Al_2O_3 coating. Wear and friction behavior of the Al_2O_3-CNT composite coating against tungsten carbide (WC) and silicon nitride (Si_3N_4) ball at temperature ranging from room temperature to 873 K is investigated.

It has been emphasized that mechanical properties of plasma sprayed coating depend on the microstructure is build up of layers of splats. Hence, it is critical to study individual splat formation and its characteristics. In this dissertation, an attempt has been made to understand the effect of CNT and plasma process parameters on the splat

formation and its role in the coating microstructure. Following section presents a short review on the single splat formation and its impact on coating properties.

2.7 Splat Formation and its Effect on Coating Properties

Properties of plasma sprayed coating such as porosity, hardness, elastic modulus mainly depends on the microstructure [115-118]. Splat is the fundamental unit of plasma sprayed coating's microstructure, which forms when a molten/semi-molten droplet impacts on the substrate. It is the shape of the individual splat and their interaction and distribution in three dimensional space, which affects the coating microstructure and properties [115-118]. Figure 2.15 shows the effect of plasma process parameters on coating's microstructure and ultimately on the coating's properties. Coating microstructure can be tailored by controlling the splat shape and size which depends on the plasma process parameters (as shown in Figure 2.15). The impact of the individual

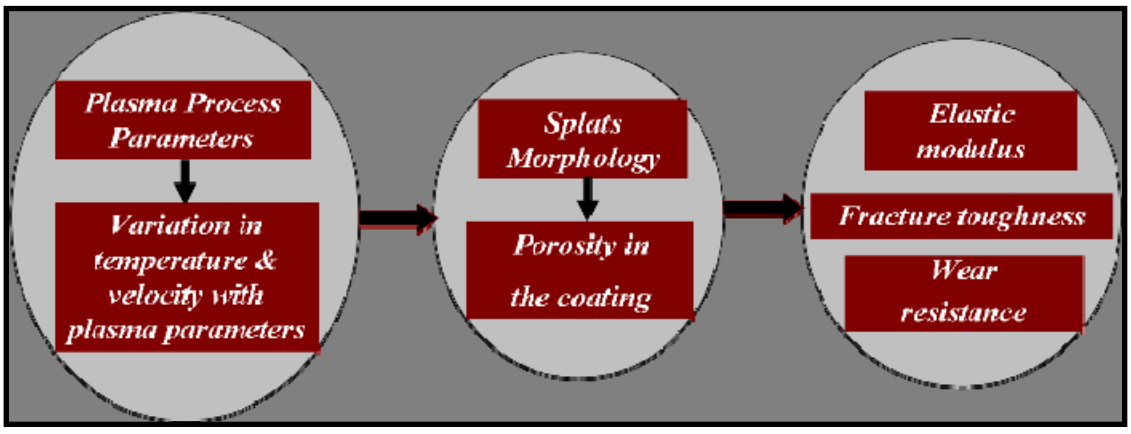

Figure 2.15: Schematic showing the effect of plasma parameters on coating's microstructure and ultimately on the coating's property.

molten droplet may lead to formation of splat of different geometries such as disk shape, disk with fingers, or fragmented splats. The shape of splat determines the porosity and adhesion at inter-splat boundaries which play a critical role in determining the mechanical, thermal [119] and electrical [120, 121] properties of coatings [12, 115-118, 122]. Splat shape depends on many factors such as thermo-physical properties of powder and substrate, in-flight particle characteristics, substrate topography and temperature [12, 115-118, 122].

Several studies have been reported on morphological aspects of splats formation. Bianchi et al. [11] sprayed single splat of zirconia on cold 304L stainless steel substrate (~100°C) and observed a highly fragmented splat. Perfect disc shaped splats were obtained for the hot substrate (~300°C). Fukumoto et al. [123] sprayed several metallic splats at various substrate temperature and observed distinct changes in splat morphology as a function of substrate temperature. Sampath et al. [10] did a detailed study on the effect of substrate temperature on the splat formation for partially stabilized zirconia (PSZ). It was concluded that a threshold transition temperature exists for the substrate surface beyond which the splat morphology changes from fragmented to disk shaped splat morphology. Figures 2.16a and b show the PSZ splat deposited on cold and hot substrate respectively. and Figure 2.16c and d are the corresponding 3D surface profile of the splats [10]. Fragmented splat was observed on the cold substrate while perfectly round splat was seen on the hot substrate. In case of PSZ, the transition temperature was found in range of 250-300°C. This change in splats morphology in cold and hot substrates has been explained by following facts. In the case of cold substrate, initiation

or localized solidification is responsible for the spreading instability which leads to splashing [10]. However in hot substrate, better contact and uniform heat conduction minimizes the localized solidification and even delays its initiation until after spreading is

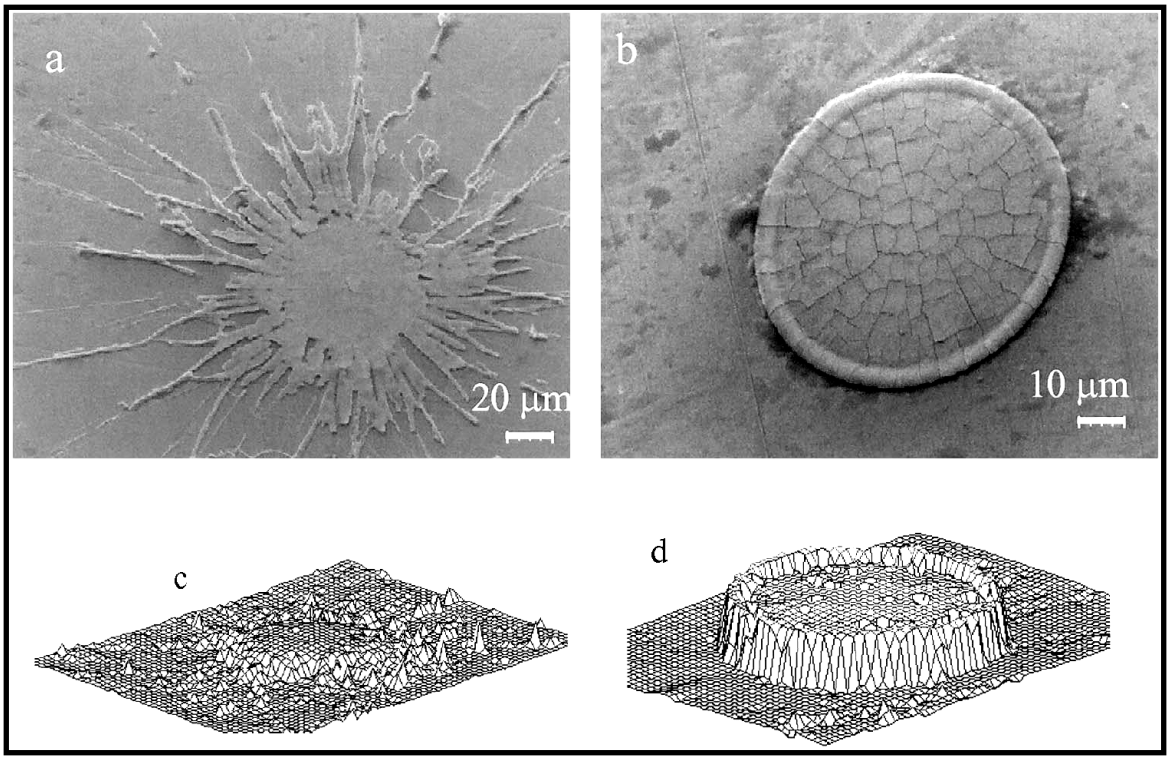

Figure 2.16: PSZ splats deposited on (a) cold and (b) hot substrate. (c) and (d) are the 3D surface file of the corresponding splats [10].

completed. This indicates that substrate temperature is the powerful tool for tailoring the microstructure of the coating and ultimately is the tool for manipulating the properties of coating. Sampath et al. also observed significant improvement in the splat-substrate and intersplat contact resulting in reduced porosity, increased thermal conductivity and strength [10].

Apart from the substrate temperature, very few researchers have studied the effect of surface roughness on the splat formation. Bianchi et al. [11] studied the effect of surface roughness on the splat formation and observed perfectly disc splat on smooth substarte (shown in Figure 2.17a) while splat was fragmented on the rough substrate (shown in Figure 2.17b). Also, the degree of flattening was lower in rough substrate (~4.2) as compared to the smooth substrate (~5.0). Fragmented and lower flattening ratio of the splat on the rough substrate was attributed to an increased friction as a result of increased roughness which ultimately promotes the splash formation [11].

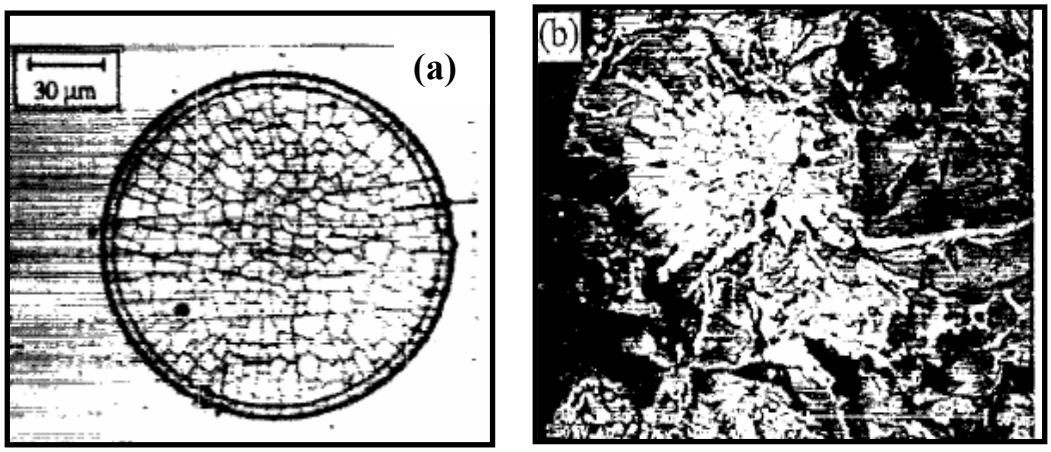

Figure 2.17: YSZ splats collected on (a) smooth and on (b) rough substrate preheated at 300°C [11]

Despite all the development in the field of splat formation, mechanism behind the transition temperature i.e. at which splat morphology changes from fragmented to disk shape is not clear. Also, it is not clear which all process parameters are critical in splat shape formation. Pasandideh-Fard et al. [124] showed the analytical expression (Equation 2.5) for the maximum spread (ζ_{max}) of the droplet which is as follow.

$$\xi_{\max} = \frac{D_{\max}}{D_0} = \sqrt{\frac{W_e + 12}{3(1-\cos\theta_a) + 4(\frac{We}{\sqrt{R_e}})}} \quad (2.5)$$

where, $W_e = \frac{\rho V_0^2 D_0}{\gamma}$ is the measure of droplet inertia to surface tension and,

$R_e = \frac{\rho V_0 D_0}{\mu}$ is the measure of droplet inertia to viscous force

ρ = Liquid density,

μ = Liquid viscosity,

D_0 = Initial droplet diameter

V_o = Impact velocity

γ= Liquid-gas surface tension

θ_a = Liquid-solid contact angle

For thermal spray conditions, the first term in the denominator in Equation 2.5 is negligible as compared to the second term (typically We >>12) [124], hence Equation 2.5 can be represented as following (Equation 2.6).

$$\zeta_{\max} = 0.5 R_e^{0.25} \quad (2.6)$$

For plasma spray process, typically the maximum spread factor lies between 3 and 6. Taking solidification into account, Pasandideh-Fard et al. [124] also obtained an analytical expression for the maximum spread (Equation 2.7) which is as follow.

$$\xi_{\max} = \sqrt{\frac{W_e + 12}{3(1-\cos\theta_a) + 4\left(\frac{We}{\sqrt{R_e}}\right) + W_e\sqrt{\frac{3\,Ste}{4\,Pe}}}} \tag{2.7}$$

where, $Ste = \frac{C(T_m - T_{w,i})}{H_f}$ is the Stefan number, C is the droplet heat capacity, T_m is the droplet melting temperature, and $T_{w,i}$ is the initial substrate temperature.

$P_e = \frac{\nu}{\alpha}$ is the droplet Prandtl number, ν and α are droplet kinematic viscosity and thermal diffusivity respectively.

Equation 2.7 partially provides the relation between maximum spreading of the droplet to the impact variable [124]. However, above expression has not attracted much consideration due to several simplification associated with this expression.

Splat formation experiments are time consuming and very challenging. To better understand the dynamics of splats, impact, spreading and its solidification, simulation of single splats based on several numerical models has been carried out [125, 126]. Simulation of single splat based on the different models has been discussed in the following section.

2.8 Simulation of Single Splat

Simulation can play an effective role in understanding of the splat formation, and its solidification behavior. Several models have been developed to simulate splat formation [125, 126]. However, these models have focused on the axisymmetric or two dimensional

impact of droplet on the substrate and cannot be used for a splashing droplet which has fingers [12]. Bussmann et al. [127, 128] designed 3D numerical model and mentioned that it could be used for splashing droplet. However, this model did not take heat transfer in consideration and all the cases were used only for isothermal condition. Pasandideh-Fard et al. [129-131] extended the Bussmanna et al's work and included the heat transfer and solidification issue for simulating the impact and splashing of molten droplet in 3D domain. Splat formation model developed by Pasandideh-Fard et al. has potential to solve following facts [129-131].

i. Relationship between final splat shape and impact parameters, powder and substrate properties.
ii. Mechanism behind splashing and break-up of the splats.
iii. Interaction between splats.

Model developed by Pasandideh-Fard et al. [129-131] was based on three-dimensional finite-difference algorithm which solves the full Navier-Stokes equation including heat transfer and phase change. Volume of fluid (VoF) tracking algorithm is used in this model to track the droplet-free surface. Also, thermal contact resistance (usually 10^{-7} m^2K/W for thermal spray process) at the droplet-substrate interface is included in this model. Based on this model, Mostaghimi et al. [12] simulated the nickel droplet (60 μm diameter) impacting on a stainless steel substrate at 290°C with a velocity of 73 m/s . Initial droplet temperature of nickel was 1600°C. Figure 2.18 shows the simulated view of nickel droplet on stainless steel substrate [12] for different time frame. Immediately after the impact, droplet starts spreading in the radial direction.

Solidification of the droplet starts and all the liquid, which is in contact with the substrate freezes in 0.5 µs after the impact. Once the bottom layer of splat solidified, remaining

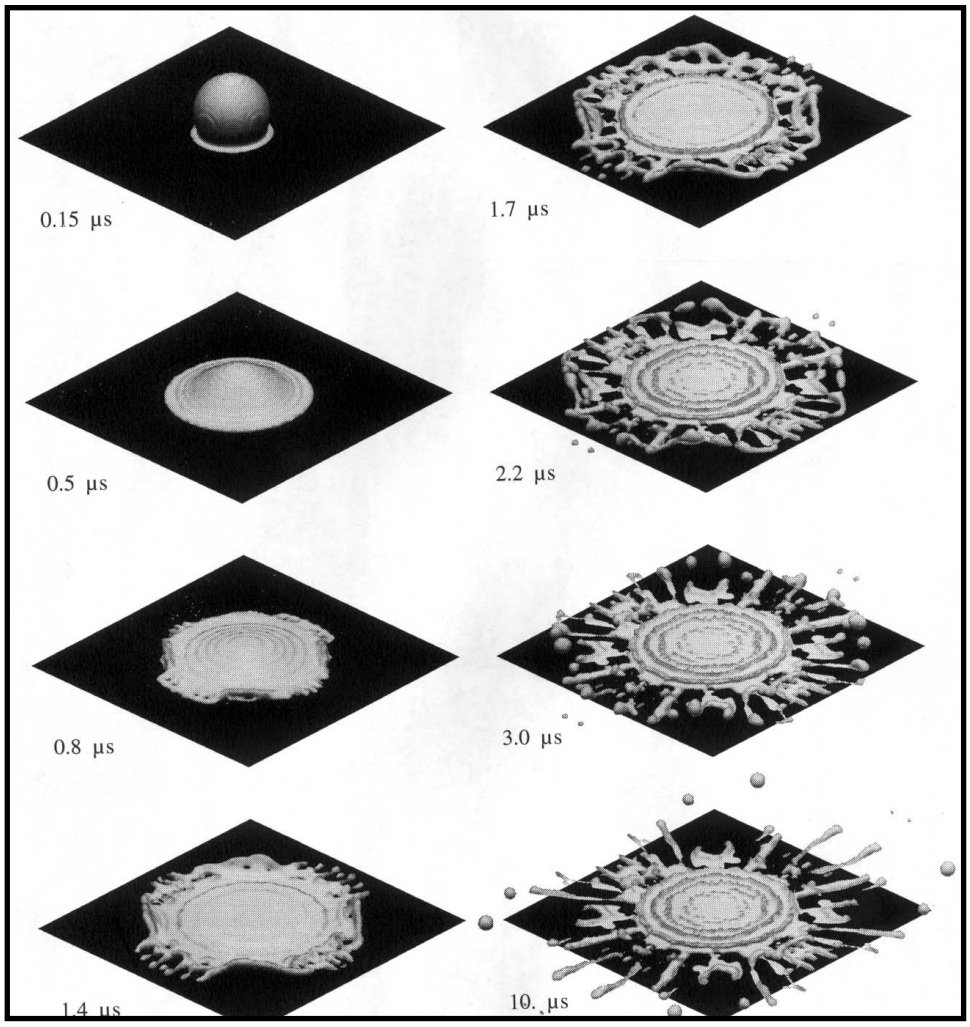

Figure 2.18 : shows the simulation of nickel droplet at 1600°C landing with a velocity of 73m/s on stainless steel substrate initially at temperature of 290°C [12].

liquid jets out over the rim of the splat. Detachment of the liquid ligaments from the bulk of the splat is due to instability of the contact line between the solidified splat (bottom layer) and molten splat (top layer of splats). The shape of these detached liquid ligaments

changes due to surface tension effect. During this shape change, liquid ligament is dragged on the substrate forming finger around the bulk splats (Figure 2.18 at 10 μs). Simulation of the splats proved a potential tool in order to understand the splats formation and solidification behavior at various conditions which directly affects the coating microstructure. However, there are certain limitations associated with the simulation of molten droplet which are as follows.

- For surface roughness, it is assumed that all three parameters *viz.* peak to valley height (R_z) , peak to peak distance (R_{pp}), and width of the tooth (RSm) are uniform throughout the substrate surface.
- Throughout the calculation, a single density is used for both liquid and solid phase of the drop. This density is the liquid phase.
- Thermal resistance between the droplet and the substrate: This property could vary with time and/ or position on the interface. A constant value is used through out the simulation.

2.9 Justification for Further Studies on Al_2O_3-CNT Coatings

A review of Al_2O_3-CNT research has shown tremendous potential in achieving enhanced fracture toughness and wear resistance of the composites. But there are several aspects which needs further attention.

- Researchers have attempted different techniques to effectively disperse the CNTs in the ceramic matrix. These dispersion techniques have evinced varying degree of

success with some limitations. Homogeneous dispersion of CNTs in the Al_2O_3 matrix still remains a challenge.

- Process map for ceramic coatings are still in embryonic stage and needs attention in order to establish the "reproducibility" of coatings by plasma spray technique.
- Tribological behavior of Al_2O_3-CNT coatings showed significant improvement at room temperature, however, their behavior at elevated temperature is unknown.
- The parameters affecting the splat morphology and coating properties have been discussed in the literature for ceramics and metals but the role of CNT in splat formation/morphology and its subsequent effect on coating's microstructure and properties need to be investigated.

Based on above observations and limitations on Al_2O_3-CNT nanocomposite, present work addresses these specific challenges by developing comprehensive process maps for Al_2O_3-CNT system. Process maps will establish the correlations between coating density, fracture toughness, wear resistance at RT and at high temperature, and CNT content. The details of the experimental methods will be discussed in the next section.

3. EXPERIMENTAL PROCEDURE

This chapter focuses on the processing details for synthesizing the "high density" plasma sprayed Al_2O_3-CNT nanocomposite coatings. The various characterization techniques and tools used for the microstructural and mechanical evaluation of coatings are also discussed.

3.1 Powder Feedstock

The powder feedstock characteristics such as particle shape, size distribution and composition play a crucial role in determining the flowability of powder in the plasma gun. In-flight thermal and kinetic history of the powder and its degree of melting are also dependent on the powder characteristics, which ultimately affect the coating properties. Spray drying and chemical vapor deposition (CVD) techniques have been adopted in this study for the powder pre-treatment. Both techniques are very effective in dispersing CNTs in Al_2O_3 powder. Also, the spray dried spherical aggmolerates provide excellent flowablitity in the plasma gun to ensure uniform melting and high quality coating. Following section discuss about the powder feedstock.

3.1.1 Spray Drying (SD) of Al_2O_3 and CNT

Nano Al_2O_3 (~150 nm) powder and multiwall carbon nanotubes (95% +purity, OD 40–70 nm, 0.5–2.0 μm in length) were obtained from Inframat Corporation, Farmington, CT and were used as the starting material. Since nanoparticles cannot be plasma sprayed because of their high interparticle friction and inconsistent flow in the

plasma gun nozzle, spray drying was carried out to enhance the flowability of powder. Inconsistent flow of powder results in poor melting and hence severe porosity in the coating. Commercial spray drying facility at Inframat Corporation was used in order to get spherical agglomerates of Al_2O_3 and Al_2O_3-CNT particle. In spray drying process, nanosized powder particles are dispersed in an aqueous organic binder (poly-vinyl alcohol) to form slurry. Resulting slurry is subsequently spray dried by hot gas atomization in a chamber to form composite spherical agglomerates. In addition to enhanced flowability, spray drying also assists in homogeneous dispersion of CNTs in Al_2O_3 matrix. Spray drying of nano-Al_2O_3 (referred as A-SD) results in spherical agglomerates of 30±10 μm in diameter. Nano-Al_2O_3 powder was also spray dried with 4 wt. % CNTs (referred as A4C-SD) and 8 wt. % CNTs (referred as A8C-SD) to produce spherical agglomerates of 26±7 μm and 24±5 μm respectively. A-SD powder feedstock served as the control sample to evaluate the effect of CNT addition.

3.1.2 CVD Growth of CNTs on Dense Al_2O_3 Powder

Chemical vapor deposition (CVD) technique was employed for uniform growth and dispersion of CNTs on dense, sintered and crushed Al_2O_3 powder (ALO 101, Praxair Inc., Danbury, CT). It is expected that, dense nature of the powder will contribute towards high density of coating. Iron (III) Nitrate Nonahydrate ($Fe(NO_3)_3.9H_2O$) was used as a catalyst for growing CNTs. In order to complete mixing of iron catalyst with Al_2O_3 powder, iron catalyst (1 wt. %) was mixed with methanol and sonicated for 5 min. Catalyst suspension was mixed with Al_2O_3 powder and then mixture was dried on the hot

plate. Dried mixture of catalyst and Al_2O_3 powder was loaded in the quartz tube wherein argon was purged (500 sccm) for 5 minutes to deoxidize the environment. Easy tube furnace 1000 (Firstnano, NY) was used to heat the quartz tube to 973 K. Once the set temperature was achieved, H_2 (400 sccm) and C_2H_4 (100 sccm) gas supply was turned on. In order to achieve the critical length of CNT required for reinforcement, CVD experiment was carried out for several growth time (i.e. 10, 12, 17, 22, 27 minutes) and the growing time was selected at 27 min. After the reaction time of 27 min, C_2H_4 and H_2 gas supply was turned off but Ar gas flow was continued till furnace cools to room temperature. The resulting CNT grown Al_2O_3 powder was named as *ICP-1*. Carbon analysis was done by high temperature carbon analyzer (Eltra CS 500, Germany) by combustion of ICP-1 powder at 1573 K. CNT yield of 1.5 wt. % in the ICP-1 powder was determined.

3.2 Optimization of Plasma Processing Parameters

In order to synthesize *"high density"* (i.e. low porosity) plasma sprayed coatings, optimization of process parameters was done by continuous monitoring of temperature and velocity of in-flight particles. Details of the in-flight particle diagnostic have been discussed in the following section. Since there is a limitation on large scale synthesis of CVD CNT- Al_2O_3 powder (ICP-1), all the optimization studies were carried out on spray dried powder.

3.2.1 In-flight Particle Diagnostic

Temperature and velocity of the in-flight powder particle was measured using AccuraSpray™ in-flight diagnostic sensor (Tecnar Automation Ltée, QC, Canada) as shown in Figure 3.1. Accuraspray diagnostic system provides ensemble average data which represents the particle characteristics in a measurement volume of approximate 75 mm^3. Velocity of the particle is determined by time of flight technique, where two optical fibers sense and gather light, which is transmitted to photomultiplier. Photomultiplier generates the electronic pulse, which identify the particle and trigger a pulse to calculate its traveling time for a certain distance. A cross-correlation factor (CCF) value of 0.9 or higher confirms the 99.5% precision for the measured velocity. Temperature of the particle is measured by two color pyrometry. Two color pyrometry measures spectral energy in two different wavelength bands (785±20 and 995±20 nm) and the surface temperature of the radiating body can be obtained using Planck's law and Wein's approximation (Equation 3.1) [132],

$$\frac{1}{T} = \frac{\ln\left[\frac{\varepsilon_{(\lambda_1,T)}}{\varepsilon_{(\lambda_2,T)}}\left(\frac{\lambda_2}{\lambda_1}\right)^5 \frac{I_{(\lambda_2)}}{I_{(\lambda_1)}}\right]}{c_2\left(\frac{1}{\lambda_1} - \frac{1}{\lambda_2}\right)} \tag{3.1}$$

where λ_1 and λ_2 are the two wavelengths, and C_2 is constant (= 1.4388 cm.K), and $\varepsilon_{(\lambda,T)}$ is the spectral emissivity. The minimum temperature that can be measured is 900°C with 0.5% precision while the minimum velocity that can be measured is 5 m/s with 0.5% precision. Error in the velocity and temperature measurement is <1.5 m/s, and <15°C respectively at a cross-correlation factor > 0.9.

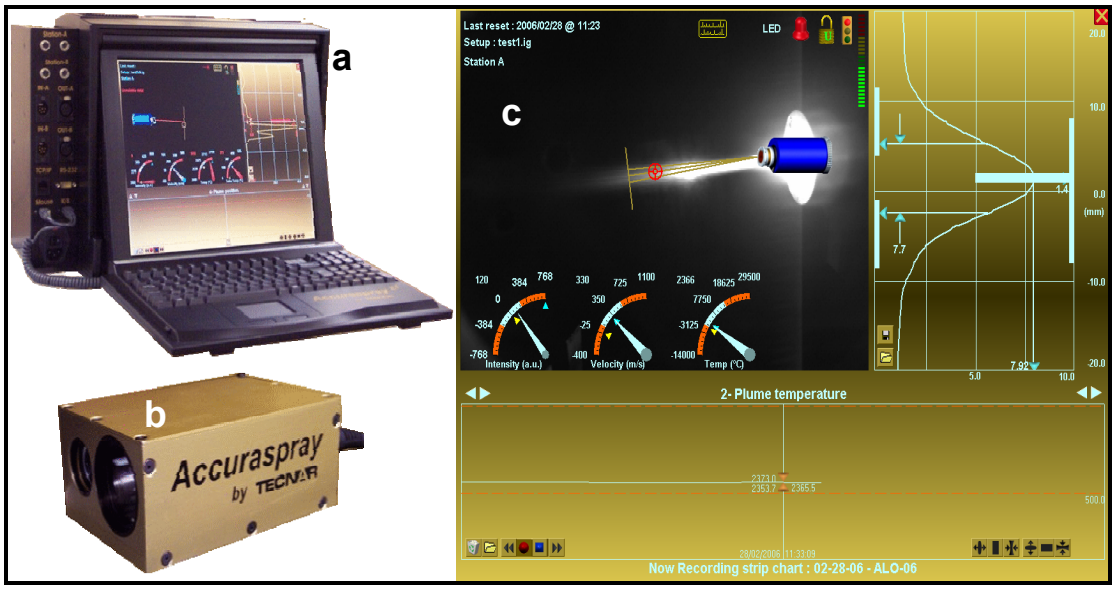

Fig. 3.1: AccuraSpray^{TM} in-flight diagnostic sensor: (a) Display monitor, (b) the sensor head, and (c) a screenshot showing temperature and velocity of in-flight particle and plume profile.

The other component of this system consists of a CCD camera which enables the analysis of the plume appearance (position, width, distribution, intensity). Figure 3.2 shows the schematic of plasma gun and in-flight sensor. Accuraspray detector was placed at 75 or 100 mm stand-off from the plasma gun to obtain temperature and velocity of the in-flight particle.

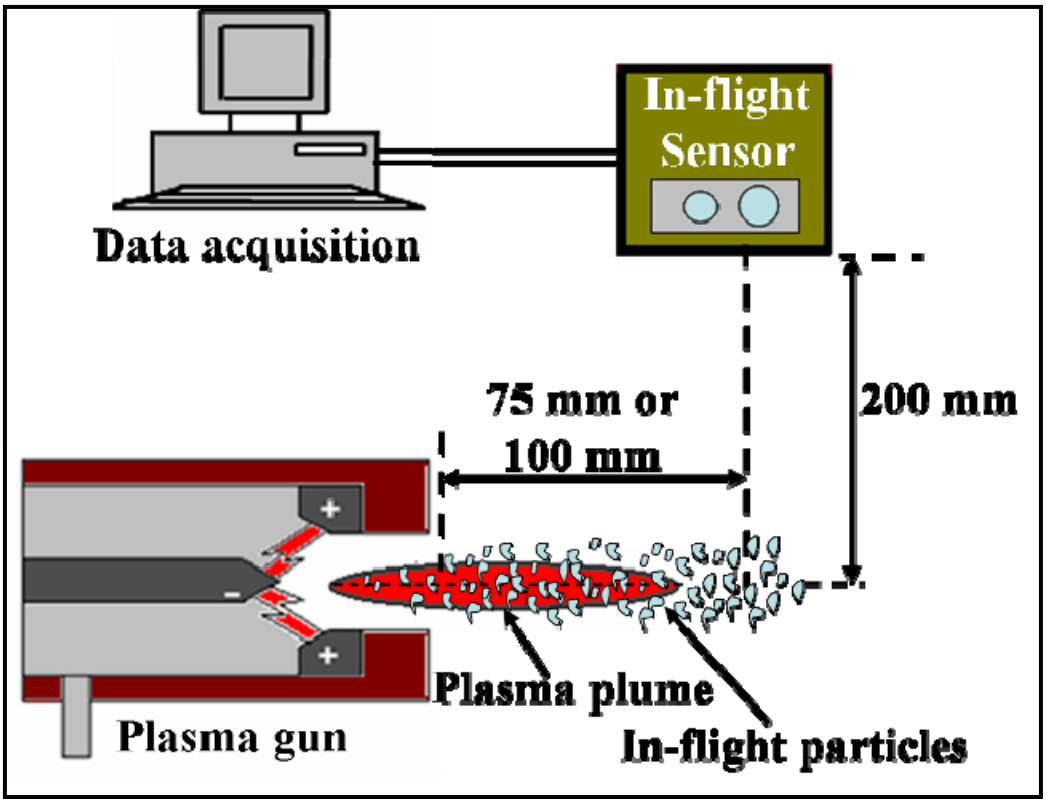

Figure 3.2: Schematic layout for in-flight-particle sensing and data acquisition

3.2.2 Synthesis of Free-Standing Coatings for Porosity Measurement

Plasma spraying of three powders (A-SD, A4C-SD and A8C-SD) was carried out using Praxair SG 100 plasma gun (Praxair, Danbury, CT, USA) on an AISI 1020 steel substrate. Powders were carried by argon gas through Praxair model #1264 powder feeder and internally injected in the plasma gun. The methodology for optimization of plasma process parameters to obtain high density coatings (i.e. low porosity) is outlined in flow chart in Figure 3.3. In-flight experiments were carried out for all powders, starting with A-SD and followed by A4C-SD and A8C-SD powders. The number of in-flight experiments for A4C-SD and A8C-SD powders were successively reduced based

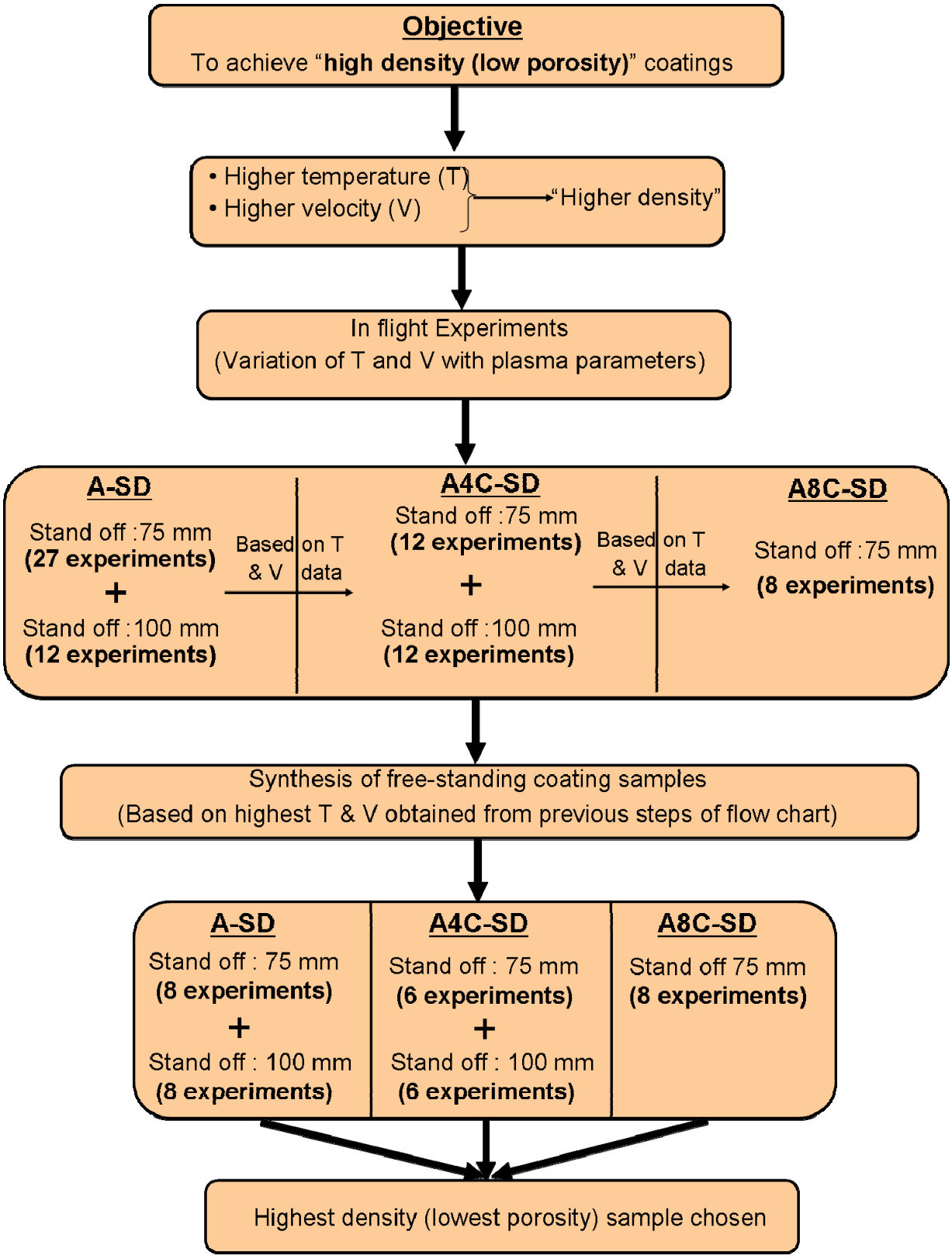

Figure 3.3: Process map evolution for obtaining highest density coatings.

on the T (temperature) and V (velocity) results from the preceding powder feedstock. Based on the higher temperature and velocity data for a set of plasma parameters, free-standing coatings were synthesized and porosity of the coatings was measured using Archimedes (water immersion) technique which has been discussed in detail in next section (section 3.2.3). The deposit with the lowest porosity (i.e. high density) was selected to establish correlation with the processing parameters and microhardness.

Based upon our previous studies [4, 5, 9, 18, 27, 64] and other literature [133, 134] on plasma sprayed Al_2O_3 coatings, the initial envelope of processing variables was chosen which is optimized in this work. Figure 3.4 shows the optimization of plasma processing parameter for A-SD powders. Stage 1 (Figure 3.4) and Table 3.1 shows that a total of 54 experiments were required to obtain thermal and kinetic history of A-SD powder for the selected plasma parameters. First 27 experiments were carried out at a stand-off distance of 75 mm. Based on the temperature and velocity results obtained from the first 27 experiments, the lowest plasma power (26 kW) and highest feed rate (9.7 g/min) were dropped for in-flight experiments of A-SD powder at stand-off 100 mm. Hence, out of initially possible 54 experiments, total 39 (27 experiments at stand-off 75 mm and 12 experiments at a stand-off 100 mm) in-flight experiments were carried out for A-SD powder. Based on the temperature and velocity data for A-SD in-flight experiments, lowest plasma power (26 kW) and highest feed rate (9.4 g/min) were not considered for A4C-SD powder. Hence, only 24 in-flight data experiments were carried out for A4C-SD powder i.e. 12 experiments at each stand-off as shown in Figure 3.5, stage 1.

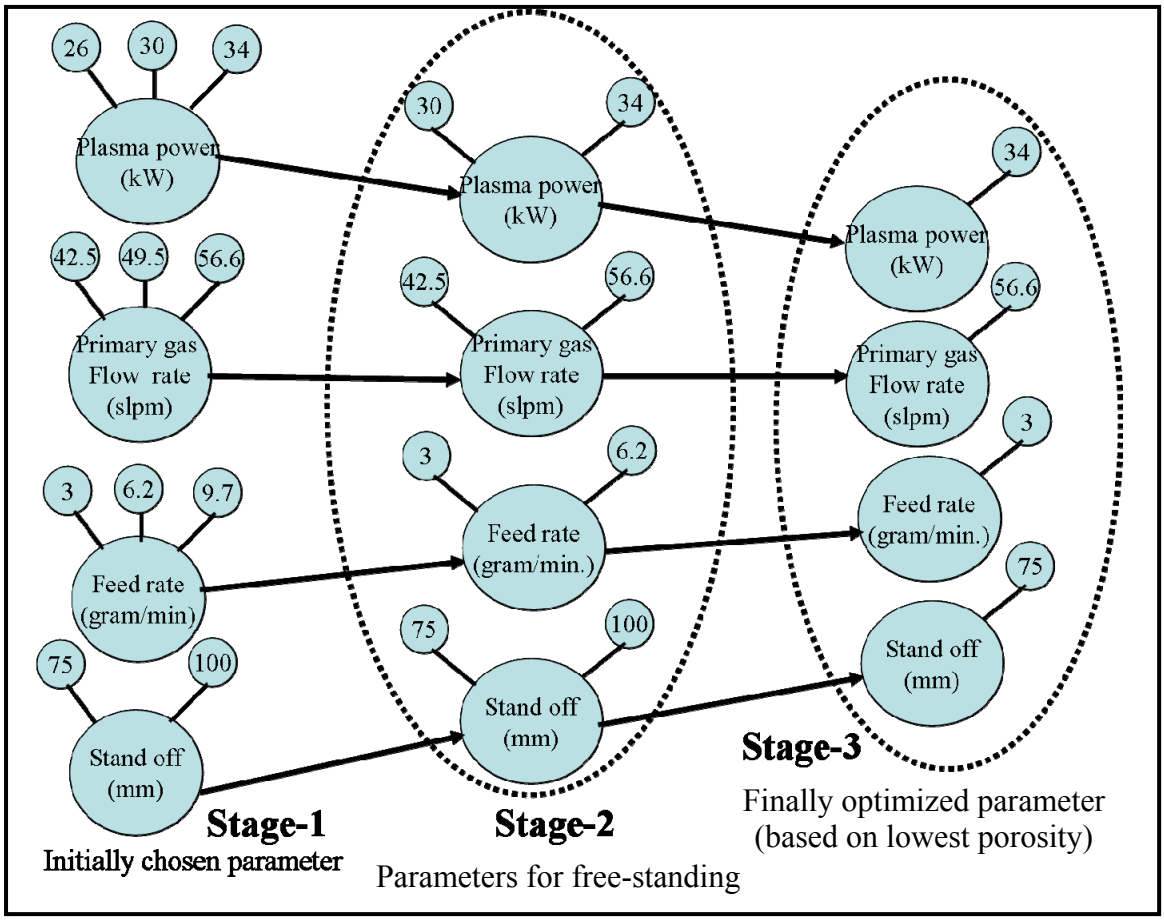

Figure 3.4: Optimization of plasma processing parameters for A-SD powder

Table 3.1: List of plasma processing parameters for obtaining temperature and velocity data using in-flight particle diagnostic sensor. Free standing coatings for the porosity measurement were made for the parameters shown in italics and bold font.

Plasma parameters	**A-SD Powder**	**A4C-SD Powder**	**A8C-SD Powder**
Plasma power (kW)	26, ***30, 34***	***30, 34***	***30, 34***
Primary gas flow (slpm)	***42.5***, 49.5, ***56.6***	***42.5, 49.5, 56.6***	***42.5, 56.6***
Powder feed rate (gram/minute)	***3, 6.2***, 9.7	***3***, 6.2	***3.1, 6.3***
Stand off distance (mm)	***75, 100***	**75, 100**	***75***

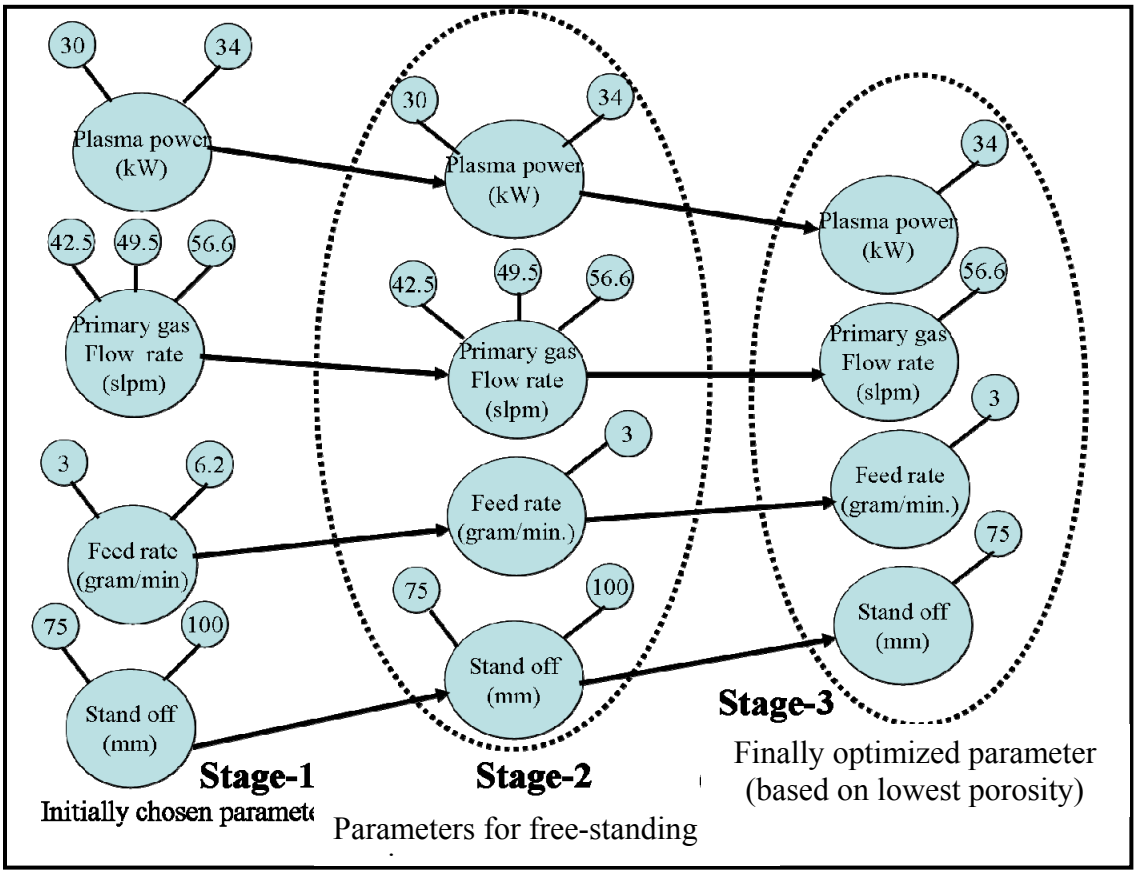

Figure 3.5: Optimization of plasma processing parameters for A4C-SD powder

By observing the temperature and velocity data for A-SD (39 experiments) and A4C-SD (24 experiments) powders, the number of in-flight data experiments for A8C-SD powder was reduced to 8 as shown in stage 1 of Figure 3.6. No experiment was conducted for A8C-SD powder for the lowest plasma power (26 kW), highest feed rate (9.5 g/min), intermediate primary gas flow rate (49.5 slpm) and high stand-off (100 mm). This approach of successively reducing the number of experiments for each Al_2O_3 based composition was effectively utilized by dropping the experiments for those parameters

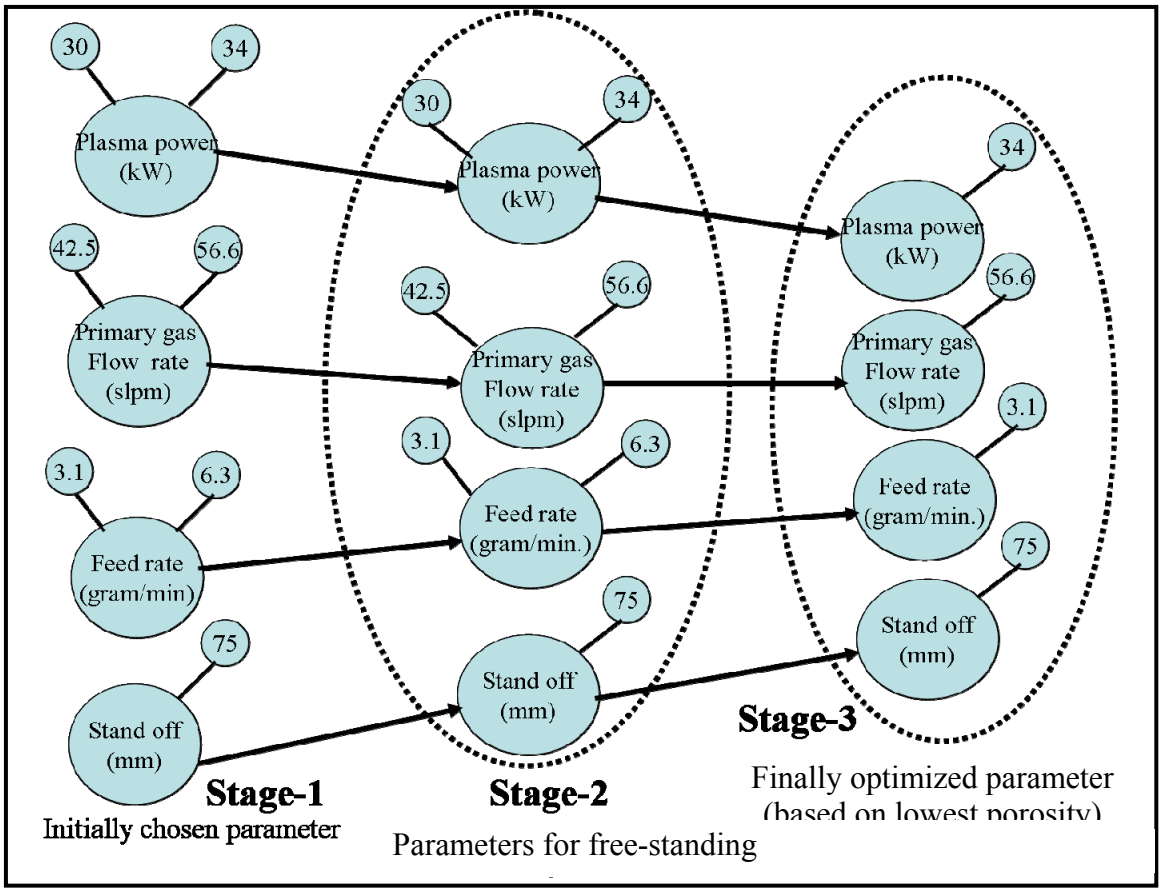

Figure 3.6: Optimization of plasma processing parameters for A8C-SD

which provided lowest temperature and velocity from the in-flight particle diagnostic experiments. This approach was also very effective in studying the role of carbon nanotube in altering the thermal and kinetic history of the in-flight particle, and hence the final microstructure. Stage 2 in Figures 3.4, 3.5 and 3.6 shows those plasma processing parameters for which free-standing coatings were synthesized for the porosity measurement. Free-standing coatings were synthesized at only those process parameters which indicated higher temperature and higher velocity from in-flight experimental results during stage 1. Italics and bold fonts in Table 3.1 show the plasma processing parameters for synthesizing the free-standing coatings. A total of 16 free-standing coating

samples (8 at each stand-off 75 and 100 mm) were made for A-SD powder particle as shown in stage 2 of Figure 3.4. In case of A4C-SD powder, a total of 12 free-standing coating samples were synthesized, i.e. 6 free-standing coating samples at each stand-off distance (Figure 3.5, stage 2) while, only 8 free-standing coating samples were synthesized for A8C-SD powder (Figure 3.6, stage 2) at the 75 mm stand-off distance. Stage 3 in Figures 3.4, 3.5 and 3.6 show the optimized plasma processing parameters to achieve the lowest porosity in A-SD, A4C-SD and A8C-SD coatings.

3.2.3 Porosity Measurement

Porosity of the free-standing coatings was calculated using below Equation 3.2. This equation involves the term apparent density (AD) which was measured using Archimedes (water immersion) technique.

$$Porosity(\%) = \left(\frac{TD - AD}{TD}\right) * 100 \tag{3.2}$$

here TD =Theoretical density
AD = Apparent density

$$\text{Apparent density (grams/cc)} = \frac{\text{Weight in air (in grams)}}{\text{(Weight in air - weight in water) (in grams)}} \tag{3.3}$$

The apparent density (AD) of the coating was calculated by measuring weight of the free-standing coating in air and in water (Equation 3.3). Ohaus digital balance with an accuracy of 10^{-5} gram has been used for measuring the weight of the free-standing coating. For calculating the theoretical density of CNT-reinforced coating, volume fraction of CNT and Al_2O_3 has been calculated as shown in Equation 3.4 and 3.5. Finally,

theoretical density (TD) of the CNT reinforced Al_2O_3 coatings were calculated using rule of mixture (Equation 3.6), which is as shown below.

Theoretical density of Al_2O_3 (ρ_{Al2O3}) : 3.99 g/cm^3

Density of CNT (ρ_{CNT}) : 2.1 g/cm^3 [37]

For A4C-SD coating (Al_2O_3-4wt% CNT):

Weight fraction of Al_2O_3 (w_{Al2O3}) : 0.96

Weight fraction of CNT (w_{CNT}) : 0.04

From the known weight fraction, volume fraction of CNT and Al_2O_3 were obtained from equation 4 and 5 respectively.

$$v_{f_{CNT}} = \frac{\rho_{Al_2O_3} * w_{CNT}}{\rho_{CNT} * w_{Al_2O_3} + \rho_{Al_2O_3} * w_{CNT}} \tag{3.4}$$

$$v_{f_{Al_2O_3}} = \frac{\rho_{CNT} * w_{Al_2O_3}}{\rho_{Al_2O_3} * w_{CNT} + \rho_{CNT} * w_{Al_2O_3}} \tag{3.5}$$

Volume fraction of Al_2O_3 : 0.926

Volume fraction of CNT : 0.073

From rule of mixture:

$$\rho_{A4C-SD} = v_{f_{Al_2O_3}} \times \rho_{Al_2O_3} + v_{f_{CNT}} \times \rho_{CNT} \tag{3.6}$$

TD of Al_2O_3-4wt.% CNT coating $\rho_{A4C\text{-}SD}$ = 3.85 g/cm^3

Similarly, theoretical density of A8C-SD was calculated.

TD of Al_2O_3-8 wt. % CNT coating $\rho_{A8C\text{-}SD}$ = 3.72 g/cm^3

Porosity was measured for 4 samples for each coating condition. The error in porosity data was found to be ± 0.3%.

3.2.4 Statistical Analysis for Porosity of Free-Standing Coatings

Porosity of the free-standing coating is a response function of the plasma processing parameters. The influence of various plasma processing parameter (plasma power, powder feed rate, primary gas flow rate, stand-off distance) on the porosity of free-standing coating was analyzed by means of regression analysis using *Statistical Package for the Social Sciences* (SPSS) 14.0 software, (SPSS Inc. Chicago, Illinois, USA). An empirical equation for the porosity was developed and only statistically significant processing parameters were included in the regression equation. The coefficients of determination (R^2) of the equations were also calculated.

3.3 Synthesis of Al_2O_3-CNT Coatings on Steel Substrate

Al_2O_3-CNT coatings were deposited on steel substrate using spray dried and CVD powders. The details of coating synthesis are discussed in the following sections.

3.3.1 Coatings Synthesized from Spray Dried Powder

Three different spray dried powder *viz.* A-SD, A4C-SD, A8C-SD were plasma sprayed using SG 100 gun (Praxair Surface Technology, Danbury, CT) on AISI 1020 steel substrate (100 mm×19 mm×3.2 mm) to synthesize Al_2O_3-CNT composite coating. These coatings were synthesized at *optimized plasma process parameters* which showed

lowest porosity in the coatings. It should be noted that optimized plasma process parameters were similar for all three powders (i.e. A-SD, A4C-SD, and A8C-SD). In order to see the effect of porosity on coating's mechanical property, another set of coatings were synthesized at those plasma process parameters which showed *highest porosity* in the coating at the same feed rate (i.e. 3 g/min.) for all three coatings (i.e. A-SD, A4C-SD, A8C-SD). The reason to select the parameters resulting in highest porosity at the same feed rate was to compare the porosity content among all coatings. The plasma processing parameters utilized for both (i.e. lowest and highest porosity) coatings are tabulated in Table 3.2. Substrate preheat temperature was maintained at 453 K for synthesizing both sets of coatings.

Table 3.2: Plasma spray parameters for synthesis of Al_2O_3-CNT coatings with lowest and highest porosity.

Plasma process parameters for synthesizing **"lowest porosity"** coating					
Current (A)	**Voltage (V)**	**Primary Gas, Argon (slm)**	**Secondary Gas, Helium (slm)**	**Stand-off (mm) from the substrate**	**Powder feed rate (gram/min.)**
850	40	56.6	59.5	75	3
Plasma process parameters for synthesizing **"highest porosity"** coating					
Current (A)	**Voltage (V)**	**Primary Gas, Argon (slm)**	**Secondary Gas, Helium (slm)**	**Stand-off (mm) from the substrate**	**Powder feed rate (gram/min.)**
750	40	42.5	59.5	75	3

3.3.2 Coatings Synthesized from CVD Al_2O_3-CNT Powder

Similar to spray dried powder, ICP-1 powder was plasma sprayed using SG 100 gun (Praxair Surface Technology, Danbury, CT) on AISI 1020 steel substrate (100 mm×19 mm×3.2 mm) to synthesize Al_2O_3-CNT composite coating. Since there was only limited amount of CVD powder available, optimization of plasma process parameters was not done for ICP-1 powder. Optimized plasma process parameters for the lowest porosity using spray dried powder were used for synthesizing ICP-1 coating. The plasma processing parameters are tabulated in Table-3.3. Dense Al_2O_3 powder (ALO 101 powder without CNTs) was also plasma sprayed as coating using the same processing parameters as listed in Table 3.3. Al_2O_3 coating served as the control sample to evaluate the effect of CNT reinforcement.

Table 3.3: Plasma spray parameters for synthesis of Al_2O_3 and ICP-1 coatings.

Current (A)	Voltage (V)	Primary Gas, Argon (slm)	Secondary Gas, Helium (slm)	Stand-off (mm) from the substrate	Powder feed rate (gram/min.)
850	40	56.6	59.5	75	3

3.3.3 Single Splat Experiment

In order to understand the role of splat in coating microstructure and properties, , single splat experiments were performed. Spray dried powder *viz* A-SD, A4C-SD, A8C-SD were plasma sprayed using SG 100 gun (Praxair Surface Technology, Danbury, CT) on an grit blasted (R_a= 2.405 μm) and polished (R_a= 0.03 μm) AISI 1020 steel substrate

(22 mm ×19 mm ×3.2 mm) to obtain the single splat. Splats were obtained at optimized plasma process parameters which showed lowest and highest porosity in the coating. Substrate roughness (R_a = 0.03 μm, 2.405 μm) and substrate preheat temperature (453 K, 553 K) were varied in order to understand the role of these variables in splat formation. It is recalled that all coatings were synthesized at a substrate preheat temperature of 453 K. Hence similar substrate temperature was kept for synthesizing the single splat. Table 3.4 summarizes the plasma process parameters for both sets of splat experiments. Figure 3.7 shows the set up for plasma spraying of single splats.

Table 3.4: Plasma spray parameters for obtaining splats at lowest and highest porosity

Plasma process parameters for synthesizing ***"lowest porosity"*** single splat					
Current (A)	**Voltage (V)**	**Primary Gas, Argon (slm)**	**Secondary Gas, Helium (slm)**	**Stand-off (mm) from the substrate**	**Powder feed rate (gram/min.)**
850	40	56.6	59.5	75	3
Plasma process parameters for synthesizing ***"highest porosity"*** single splat					
Current (A)	**Voltage (V)**	**Primary Gas, Argon (slm)**	**Secondary Gas, Helium (slm)**	**Stand-off (mm) from the substrate**	**Powder feed rate (gram/min.)**
750	40	42.5	59.5	75	3

A shield plate with series of 2 mm dia. hole was used to obtain relatively uniform splats on the steel substrate. The steel substrate was positioned behind the shield plate for a total spraying distance of 75 mm. Substrate was preheated using the heat gun (STEINEL, HG 2510 ESD, MN, USA). The substrate temperature was measured using thermocouple (KMQSS-020U, Omega Engineering Inc.) inserted through the substrate thickness as shown in Figure 3.8a. Other end of the thermocouple was connected to temperature datalogger (TDL) to store the measured data. Figure 3.8b is the schematic of steel substrate showing dimensions of all the faces and holes.

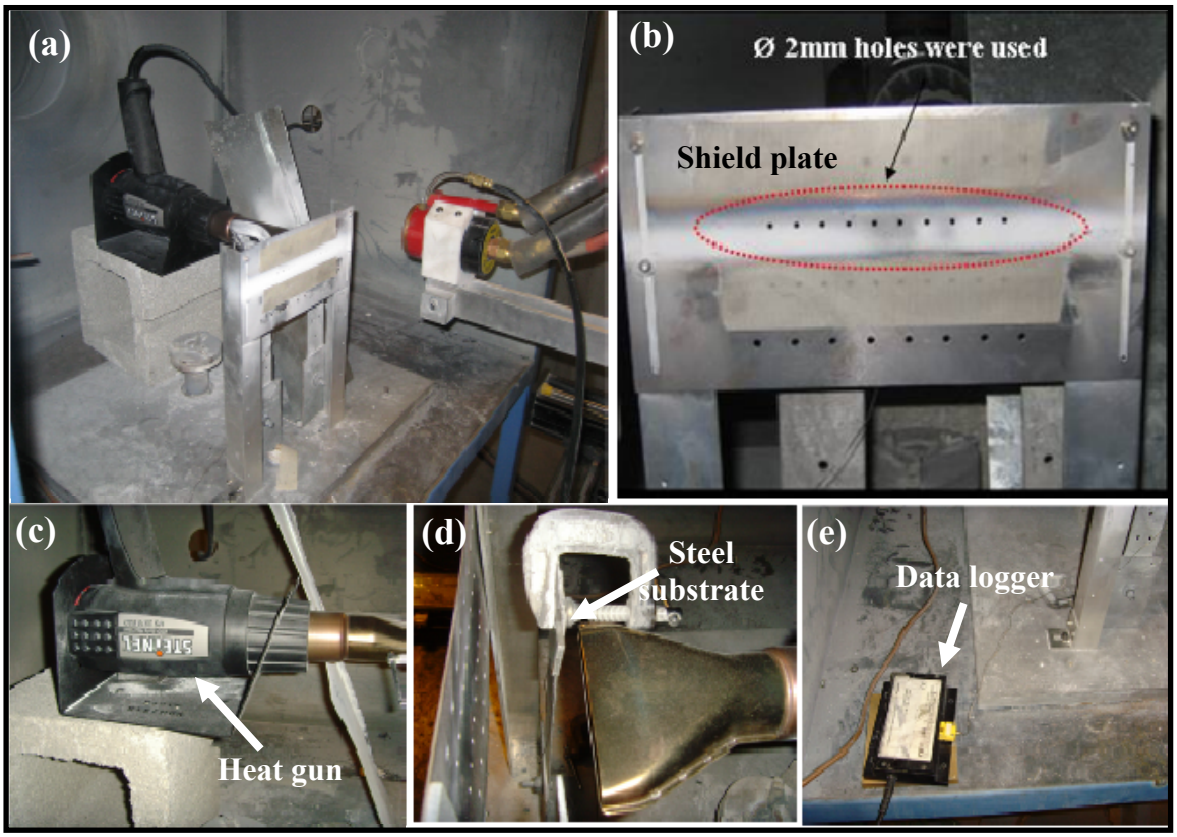

Figure 3.7: (a) Plasma spray set-up for obtaining single splat (b) Shield plate in front of plasma gun having series of holes of 2 mm diameter (c) Heat gun used to preheat the

substrate (d) Steel substrate (22 mm×19 mm×3.2 mm) positioned on the back of the shield plate (e) Data logger for storing the substrate temperature.

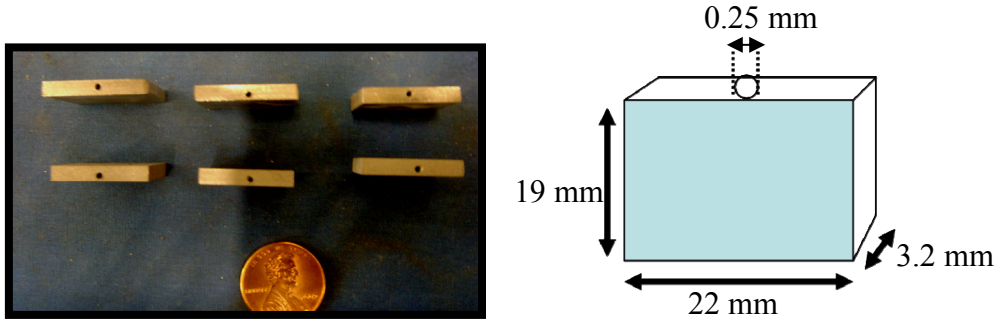

Figure 3.8: (a) Steel substrate showing through thickness hole (Ø=0.25 mm) for inserting thermocouple (b) schematic of steel substrate showing dimensions of all faces and hole.

3.4 Characterization

3.4.1 Microstructure and Phase Evaluation

A JEOL JSM 6330 F field emission scanning electron microscope was used to investigate the microstructural features of starting powder and plasma sprayed Al_2O_3-CNT coatings. Philips/FEI Tecnai F30 high resolution transmission electron microscope (HRTEM) operating at an accelerating voltage of 300 kV was used to study the CNT microstructure and CNT/Al_2O_3 interface. X-ray mapping was performed using a JEOL JSM 5910LV scanning electron microscope (SEM) operating at 15 kV and 16 frames in a matrix of 1024 x 800 pixels taking 50 µs per square pixel, each pixel of dimensions 0.336 µm in x and y equally.

Physical Electronics (PHI 5400) ESCA X-ray Photoelectron Spectroscopy (XPS) was used for characterizing the worn surface of plasma sprayed Al_2O_3-CNT coatings. Non-monochromatic X-ray radiation from MgKα source of 300 W was used for the analysis. The survey spectra, and multiplex spectra were recorded with pass energies of 35.7 and 17.9 eV, respectively to achieve better resolution. The spectrometer was calibrated using a metallic gold standard (Au $4f_{7/2}$ = 84.07±0.1 eV). The peaks shift due to charging produced by the specimen was removed by using a binding energy scale referred to that of C(1s) of the hydrocarbon part of the adventitious carbon line at 284.6 eV. The nonlinear least-squares curve fitting was carried out using a Gaussian–Lorentzian distribution. Curve fitting was accomplished by first smoothing the data using a Savitsky–Golay routine and then fitting this smoothed data by assuming a 100% Gaussian peak shape. All data smoothing and curve fitting is performed using Peak Fit software (version 4.05, SPSS Inc., Chicago, Illinois, USA) with modified fit routine.

3.4.2 Micro-Raman Spectroscopy

Micro-Raman spectroscopy was used to study the CNT structure. A Ti-sapphire crystal target with a laser wavelength of 785 nm was used and the laser was produced using source from Spectra Physics (Model 3900S, CA, USA) with the detector from Kaiser optical system, Inc. (MI, USA). The spot size is typically 5μm.

3.5 Mechanical Properties Characterization

3.5.1 Vickers Microhardness and Fracture Toughness

Zhongguo HXD-100 TMC Shanghai Taiming Optical Instruments microhardness tester (1000 g load and 30 s dwell time) was used for estimating microhardness of the plasma sprayed coatings. In order to generate long cracks in the coating for fracture toughness evaluation, microhardness tester (MHT Micro Photonics Inc., CA) with a Vickers indenter was used at a load of 4 kg and dwell time of 30 s. Fracture toughness of the coatings were evaluated using Anstis equation (Equation 3.7) [135],

$$K_c = \chi\left(\frac{E}{H}\right)^{1/2} \frac{P}{c^{3/2}} \tag{3.7}$$

P is the applied load, E is the elastic modulus, H is the Vickers hardness, c is the radial crack length (measured from the center of indent), and χ (=0.016) is the calibration constant.

3.5.2 Modulus Mapping of Coatings via Nanoindentation

Elastic modulus of the Al_2O_3-CNT coatings in modulus mapping mode were evaluated by nanoindentation technique. The 2D Modulus Mapping has been carried out on the coatings using Hysitron TriboIndenter® (Hystrion Inc., Minneapolis, MN) with the nano-DMA (Dynamic Mechanical Analyzer) transducer. Berkovich diamond indenter (100 nm) was used for the indentation. During modulus mapping in nano-DMA mode, a static load of 3 μN was applied on the coating with a dynamic load of 0.5 μN with a fixed frequency (200 Hz). At the same time, the tip rasters over the defined area (5 μm x 5 μm)

of the sample in order to measure the loss and storage modulus at each point to produce a 2D map.. The sensitivity (2 mV) and time constant (10 ms) were optimized to obtain the best resolution. The transducer is capable of capturing a matrix of 256 X 256 data points in the given area. The results can be obtained as a 2D map with properties represented in colored gradient of the elastic modulus of 256 X 256 points. At least 3 such scans were made for each coating.

3.5.3 Tribological Behavior of Coatings

Surface of the plasma sprayed coatings was polished prior to wear tests. Surface roughness of the polished coating was measured using TR 200 surface roughness analyzer (Micro Photonics Inc., CA). Ball-on disk tribometer (Nanovea Inc., CA) was used to evaluate the wear resistance of the composite coatings at room (298 K) and intermediate temperatures (573 K, 873 K). Room temperature wear tests were carried out at 250 rpm (wear track diameter: 12 mm) and at normal loads of 10 N, 30 N, and 50 N while intermediate temperature wear test was performed only at 30 N load. A 3 mm diameter tungsten carbide (WC) ball (Hardness: ~24-27 GPa) was used to slide against ICP-1 coating whereas silicon nitride (Si_3N_4) ball (Hardness: ~15-20 GPa) was used to slide against the spray dried Al_2O_3-CNT coating surface. Different counter part was used to evaluate its effect on tribochemical reaction which ultimately affects the wear mechanism of the coating. Table 3.5 summarizes the wear test parameters at room and intermediate temperatures for spray dried and ICP-1 coatings.

The average roughness value (R_a) of the coated surface was ~1-3 μm. Wear test was conducted for 60 minutes resulting in 15000 revolutions, which corresponds to 565 meter linear traverse distance. The weight change in the sample was measured after every 12 minutes of wear for the room temperature experiments. For intermediate temperature wear tests, weight change in the coating was measured after the end 60 minutes. Up to three wear tests were conducted for each condition to evaluate the consistency. The wear weight loss was measured using Ohaus digital balance with an accuracy of 10^{-5} gram. The frictional force between the ball and the coating surface was measured by the linear variable differential transformer (LVDT) sensor. The data was acquired at a rate of 1000 data points per minute.

Table 3.5: Wear test parameters at room and intermediate temperatures for spray dried coatings and ICP-1 coatings.

	Room Temperature		**Intermediate Temperature**	
	Spray dried coating	**ICP-1 coating**	**Spray dried coating**	**ICP-1 coating**
Load used (N)	10, 30, 50	10, 30, 50	30	30
Sliding speed (rpm)	250	250	250	250
Ball used	Si_3N_4	WC	Si_3N_4	WC
Wear Track diameter (mm)	12	12	12	12

4. CHARACTERIZATION OF POWDER FEEDSTOCK

Powder feedstock morphology and its characteristics have a very significant impact on the coating's final microstructure. Dispersion of CNTs in the initial powder feedstock plays an important role in obtaining improved mechanical properties of coating. Two approaches *viz.* (i) spray dried Al_2O_3-CNT powder and (ii) in situ CVD growth of CNTs on dense Al_2O_3 powder have been adopted in this study to achieve uniform dispersion of CNTs in the Al_2O_3 matrix. Details of these two approaches are explained below.

4.1 Spray Dried Composite Al_2O_3-CNT Powder

Figures 4.1a and 4.1b show the SEM images of nano-Al_2O_3 powder (~150 nm particle size) and as-received CNTs (95% + purity, OD 40–70 nm, 0.5–2.0 μm in length) respectively. Spray drying (explained in section 3.1.1) of nano-Al_2O_3 without and with CNTs (4 and8 wt.%) was carried out. Since nano-Al_2O_3 particles have high surface area,

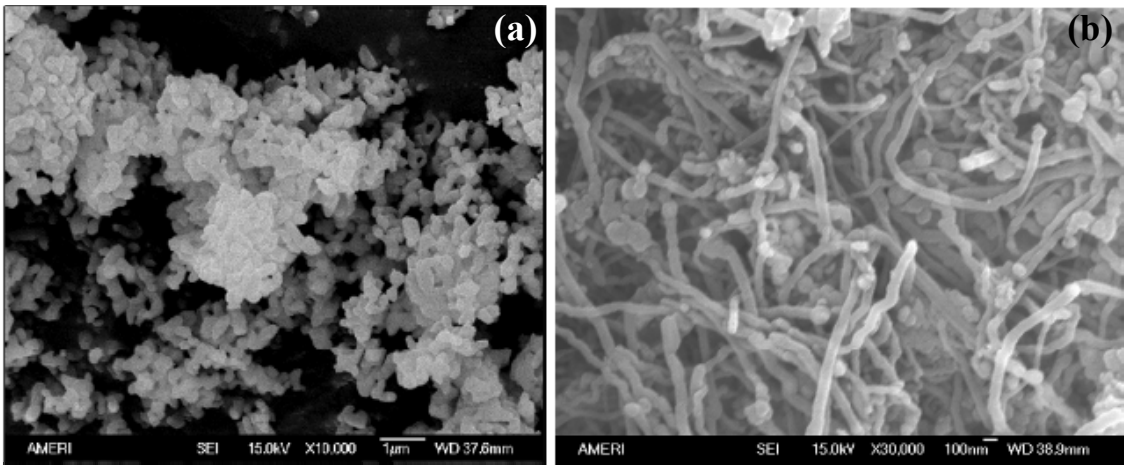

Figure 4.1: SEM image of (a) nano-Al_2O_3 particle and (b) as received CNTs

CNT associates easily with nano-Al_2O_3 particles. As a result of spray drying,, spherical agglomerates of Al_2O_3 (referred as A-SD), Al_2O_3-4 wt. % CNT (referred as A4C-SD), Al_2O_3-8wt. % CNT (referred as A8C-SD) were obtained. Figures 4.2a-c show the high magnification SEM micrographs of the surface of A-SD, A4C-SD and A8C-SD agglomerates respectively. The inset shows low magnification image of spherical agglomerates of each composition. The particle size distributions of three powders are shown in Figure 4.3. The particle size distribution of A-SD, A4C-SD and A8C-SD was found to be 30 ± 10 μm, 26 ± 7 μm, and 24 ± 5 μm respectively. The spray dried agglomerates contains high amount of porosity (~30-40%) and have improved flowability due to their spherical shape and reduced interparticle friction. From Figure 4.2b and c, it can be seen that the CNTs are dispersed uniformly on the surface of agglomerate. Uniform dispersion of CNTs is critical for an improvement in the mechanical and tribological properties of coating.

An initial signature of Raman spectrum was obtained from the powder feedstock in order to compare the retention of CNT structure in the plasma sprayed coatings. Figure 4.4 shows the Raman spectra of as-received CNTs and A4C-SD and A8C-SD powders in which D and G peaks correspond to defect and graphitic structure of CNT. Though CNTs are uniformly dispersed by spray drying, it contains 30-40% of porosity which can largely affect the coating's microstructure. To alleviate the problem of high porosity of spray dried powder, another powder processing approach has been used in which CVD growth of CNTs was done on "dense" Al_2O_3 powder. Also, CVD growth of CNTs will contribute towards obtaining the homogeneous dispersion of CNTs over each Al_2O_3

powder particle. Details of the in situ growth of CNT on Al_2O_3 particles are discussed in the next section.

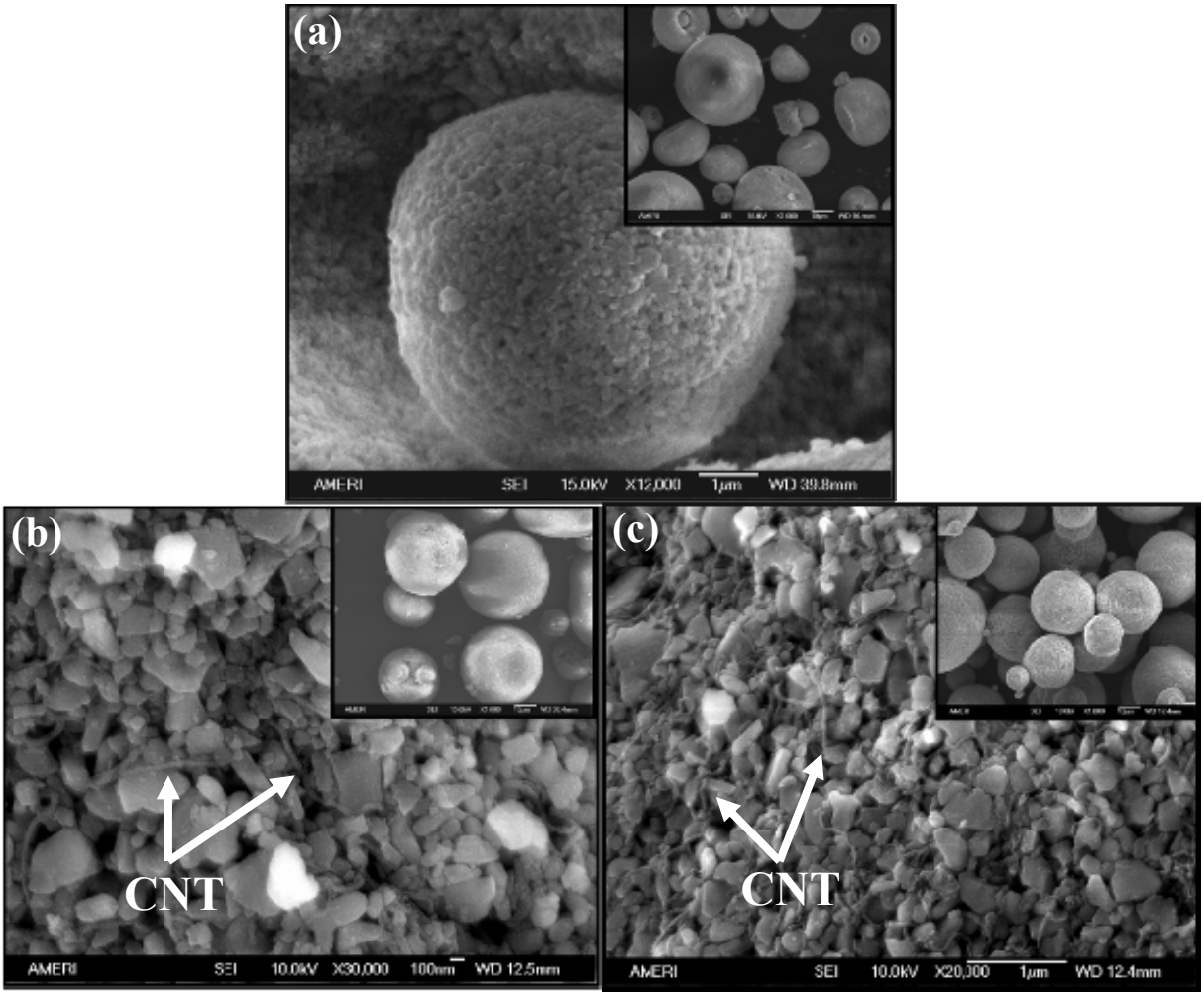

Figure 4.2 High magnification SEM images of spray dried (a) Al_2O_3 (A-SD) powder particle (b) Al_2O_3-4 wt. % CNT (A4C-SD) particle showing homogeneous dispersion of CNTs on the surface (c) Al_2O_3-8 wt. % CNT (A8C-SD) particle showing homogeneous dispersion of CNTs on surface. Inset shows low magnification image of spray dried agglomerate of each composition.

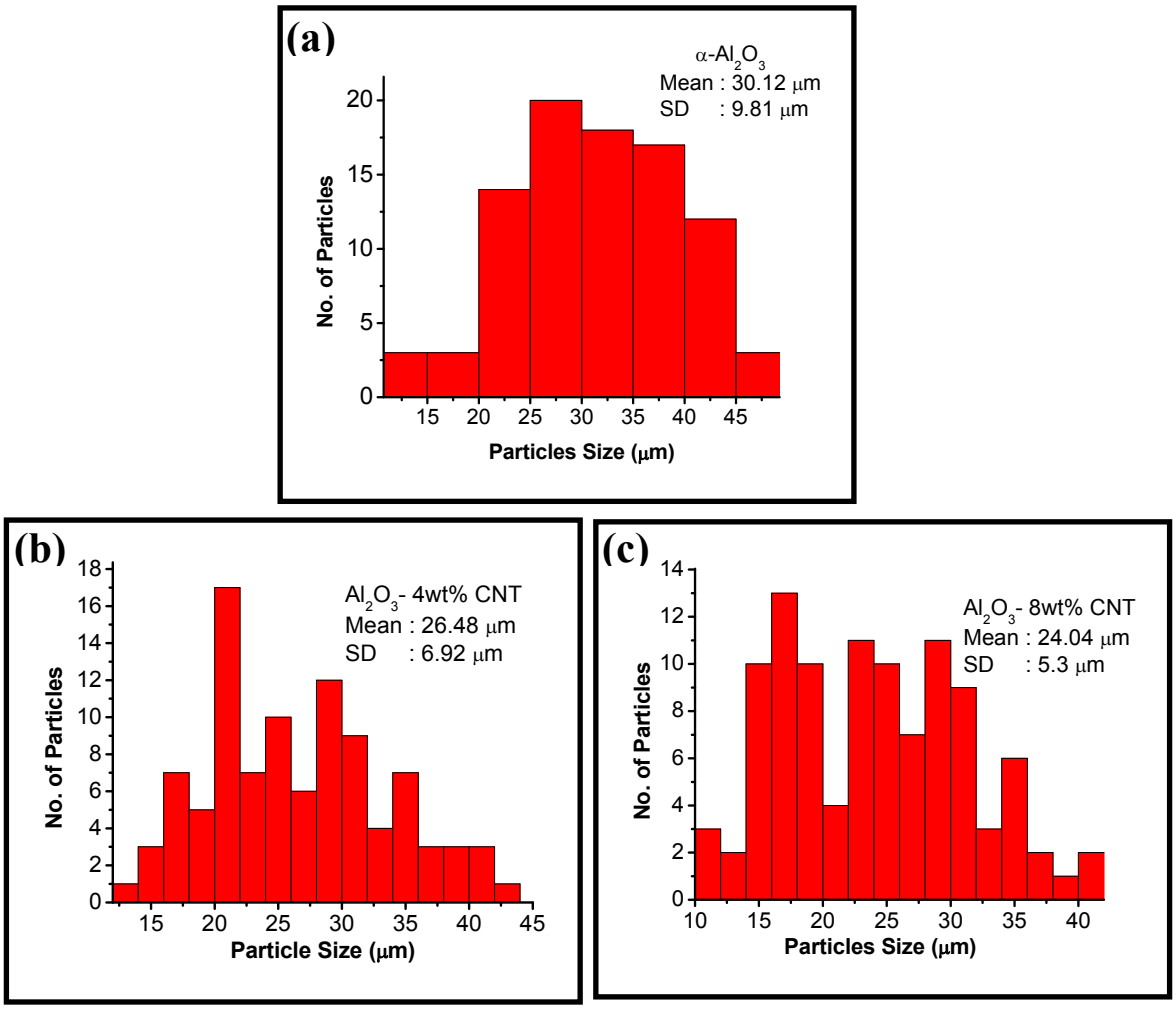

Figure 4.3: Particle size distribution of (a) Al_2O_3 (A-SD) spherical agglomerates (b) Al_2O_3-4 wt. % CNT (A4C-SD) spherical agglomerates (c) Al_2O_3-8 wt. % CNT (A8C-SD) spherical agglomerates.

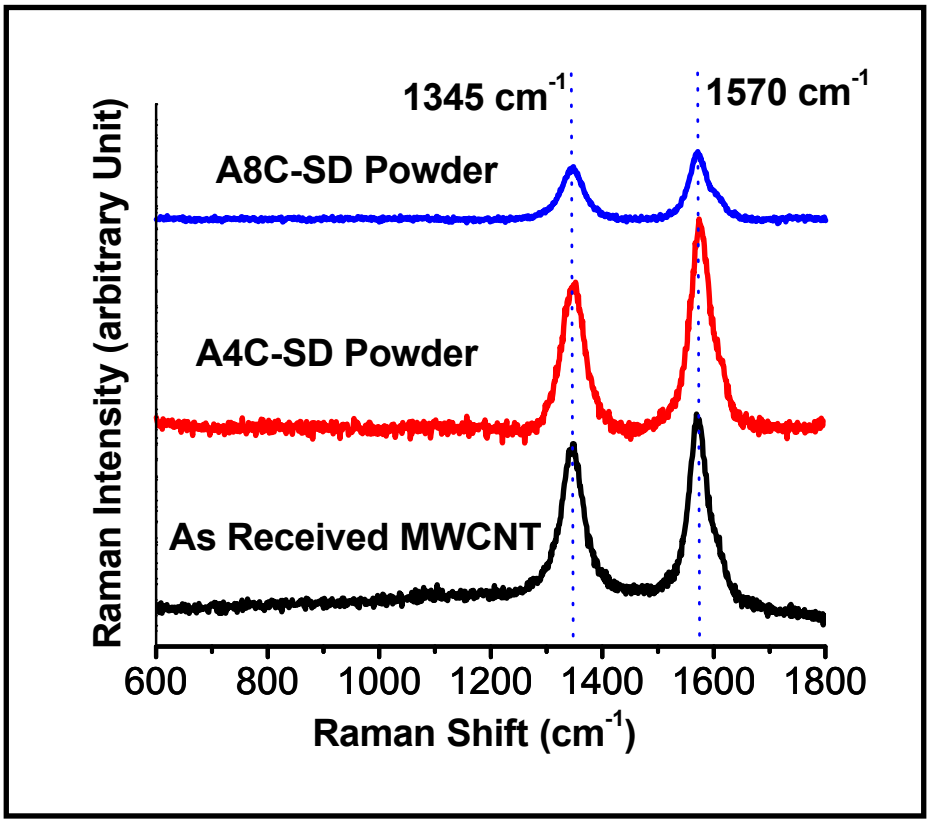

Figure 4.4: Raman spectra of as-received CNTs and initial powder feedstock showing D and G peaks which corresponds to defect and graphitic structure of CNT.

4.2 CVD Grown Nanotubes on Al_2O_3 Powder

In this study CNT has been grown on "dense" Al_2O_3 powder and not on the "spray dried" Al_2O_3 powder (A-SD). This is attributed to following facts: (i) spray dried powder contains high amount of porosity (~30-40%) which might lead to inhomogeneous dispersion of CNT and (ii) porosity of spray dried powder can also affect the coating's microstructure and properties. Ortega-Cervantez et al. [136] attempted to grow the CNT on porous Al_2O_3 via CVD technique and found that nanotubes did not grown inside the

pore. This was attributed to entrapped air inside the pores which prevents the catalyst particle to go inside the pore resulting in inhomogeneous dispersion of CNTs [136].

Figure 4.5a shows the dense, sintered and crushed Al_2O_3 powder (size range: 15-45 µm, 99.5% purity) which was used as the substrate to grow CNTs. Figure 4.5b is the high magnification SEM image of Al_2O_3 powder showing the shape of the powder which is angular and faceted with ridges on its surface. Figure 4.6 shows the in situ grown CNTs on dense Al_2O_3 powder for growth time of 22 mins. This reveals that initial CNTs growth starts between the ridges present within each powder particle and subsequent growth continues on the entire powder surface. The preferred nucleation of CNTs between the ridges is attributed to possible higher retention of catalyst particles at the inter-ridge spacing which serve as localized crevices. Since, CNT length is critical for achieving the best splat- reinforcement and coating densification,

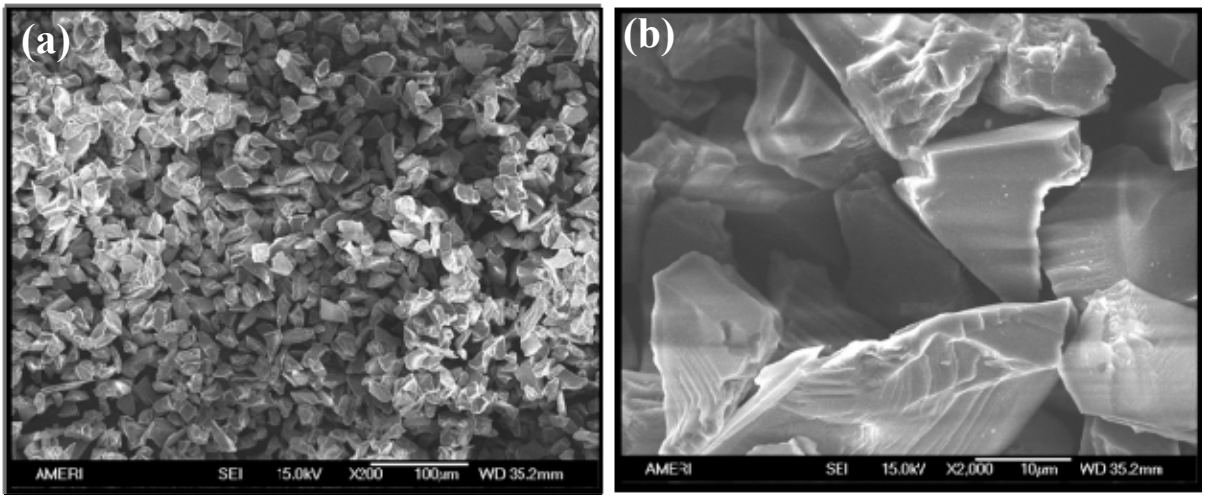

Figure 4.5: (a) SEM images showing as-received dense, sintered and crushed Al_2O_3 powder (b) High magnification SEM image showing shape of the powder.

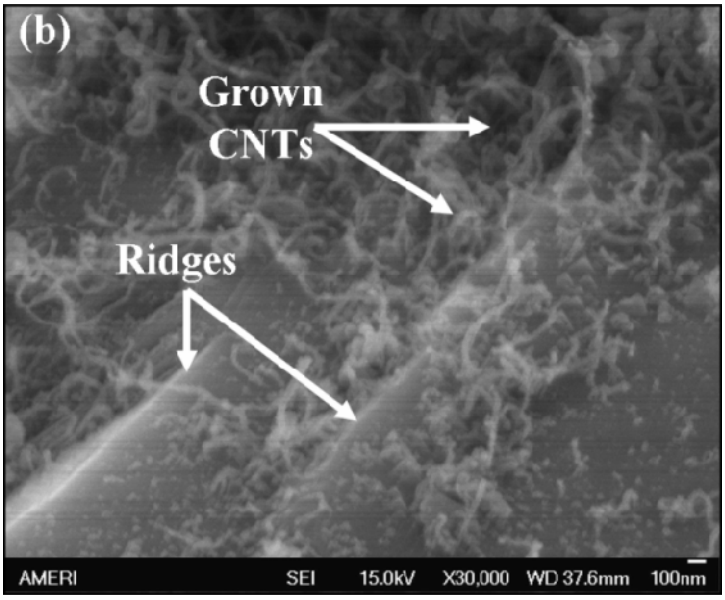

Figure 4.6: CVD grown CNTs concentrated between the ridges of the Al_2O_3 powder particle.

it has been optimized by adjusting the CNT growth time. Figure 4.7 shows the SEM image of grown CNTs on Al_2O_3 particle at different growth time of 12 17 22 and 27 minutes. As seen from Figure 4.7, higher CVD processing time leads to increased CNTs content and relatively long CNTs. Due to slow kinetics of CNT growth in CVD process, it is not feasible to individually control the "length" and "content" of CNTs in the Al_2O_3. CNT length has been plotted as a function of growing time (Figure 4.8) which shows that length of the CNTs successively increases with the growing time. Figure 4.8 also indicates that some of the CNTs are longer than as expected for shorter growth time. This might happen due to large volume of reaction chamber in which ethylene gas can remain be with a considerable partial pressure in the chamber even after the gas flow has been turned off.

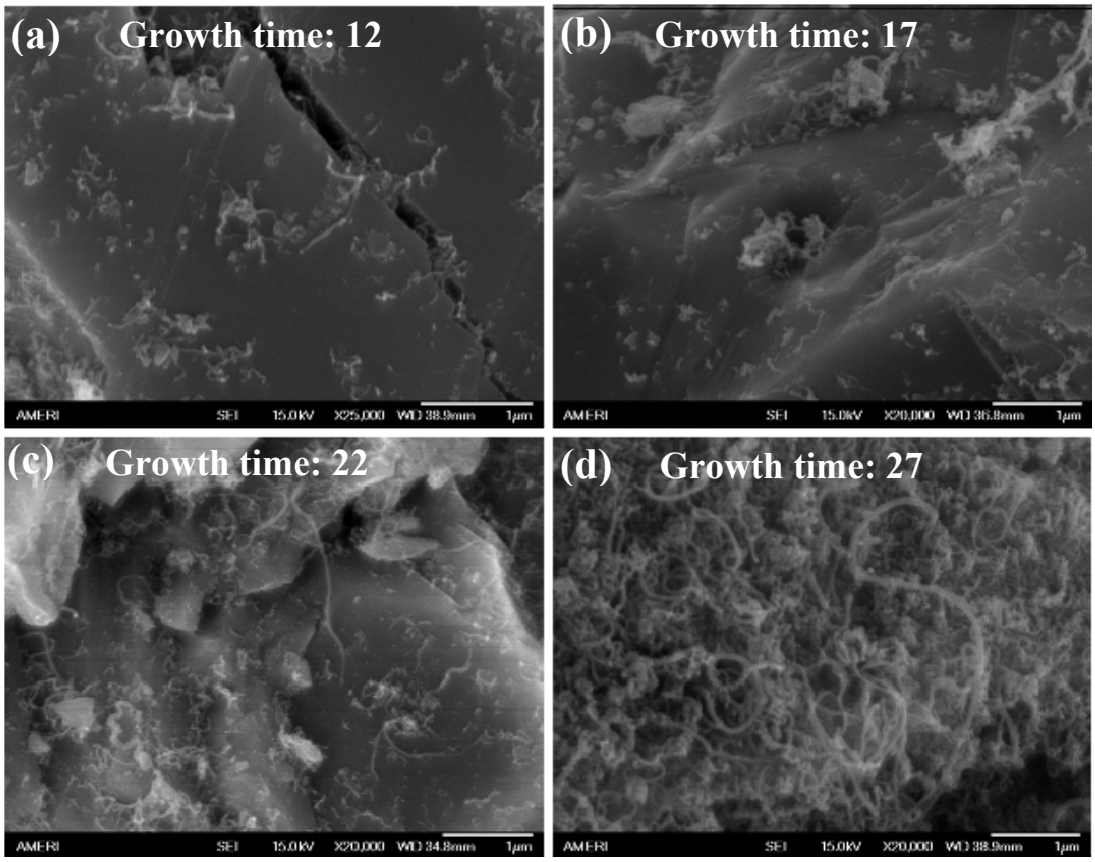

Figure 4.7: High magnification SEM image showing grown CNTs on Al_2O_3 powder particle for growth time of (a) 12, (b) 17, (c) 22, and (d) 27 minutes.

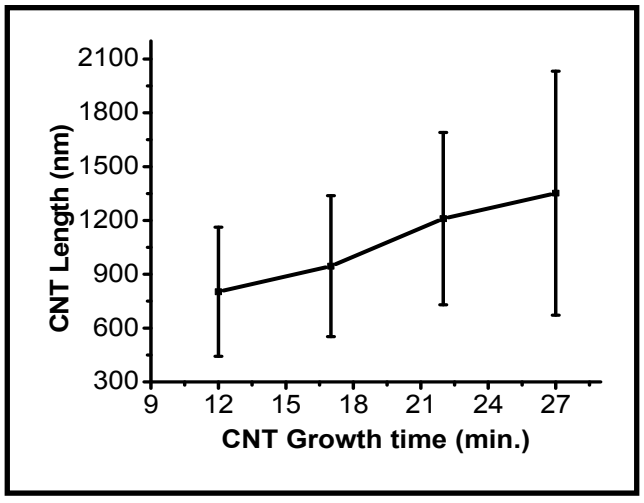

Figure 4.8: Length of in situ grown CNT as a function of CNT growth time.

CNT growth time was optimized at 27 minutes. The length of CNTs achieved varied between 0.6-2 μm. The resulting Al_2O_3-CNT composite powder with a growth time of 27 minutes will be referred as *ICP-1*. CNT yield of 1.5 wt. % in the ICP-1 powder was determined by combustion of ICP-1 powder at 1573 K.

Figure 4.9a shows the HRTEM image of ICP-1 powder which shows the presence of CNTs and catalyst particles. Presence of metal catalyst embedded in the nanotube may create defects along the graphene walls which could ultimately affect the graphitization of CNT. Figure 4.9b is the HRTEM image of CVD grown CNTs which shows the fringe in each side of the tube indicating the individual cylindrical graphitic layer. Inset

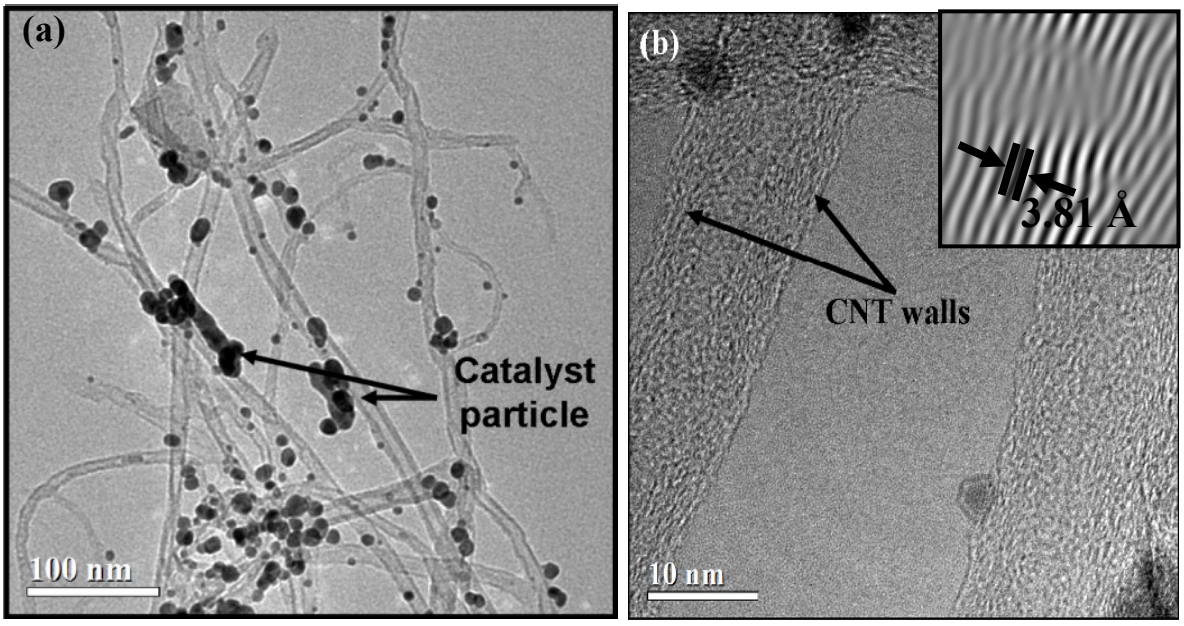

Figure 4.9: (a) TEM image of CVD grown CNTs and catalyst particles in ICP-1 powder (b) HRTEM image of CVD grown CNTs showing 19±4 walls of graphitized carbon. Inset shows IFFT image of CNT with an interlayer spacing of 3.81Å for in situ grown CNT

image in Figure 4.9b is the Inverse Fast Fourier transformed (IFFT) image of CNT showing an interlayer spacing of 3.81 Å for CVD grown CNT. Average of six CNT samples showed that, CNT has approximately 19±4 walls of graphitized carbon. Figure 4.10 shows the distribution of CNT diameter, which is in the range of 15-50 nm. Average diameter of CNT was found to be 30.4 ±7.6 nm.

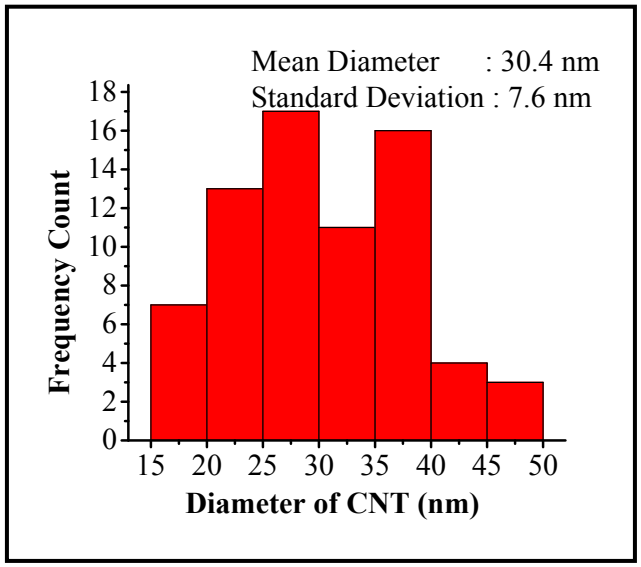

Figure 4.10: Histogram showing the distribution in diameter of in situ grown CNTs.

Figure 4.11 shows the Raman spectra for the ICP-1 powder in which D and G peaks corresponds to defect and graphitic structure of CNT. From this Raman spectrum, ratio of intensity of D and G peak was determined which was 1.56. Higher I_D/I_G ratio corresponds to lower degree of graphitization of CNT which might be due to presence of impurity (catalyst particle) or defect in CNT walls in the in situ grown CNTs.

Though CNTs can be uniformly dispersed via CVD technique, it has limitations of large scale synthesis of ICP-1 powder. In order to synthesize "high density" coating plasma process parameters should be optimized. Optimization of plasma process parameters requires large amount (e.g. 1-2 kg) of powder. Since CVD process cannot has a limitation of producing large amount of powder, ***Optimization of plasma process parameters were done only spray dried powder and not on the ICP-1 powder.*** Optimization of processing parameters is discussed in chapter 5.

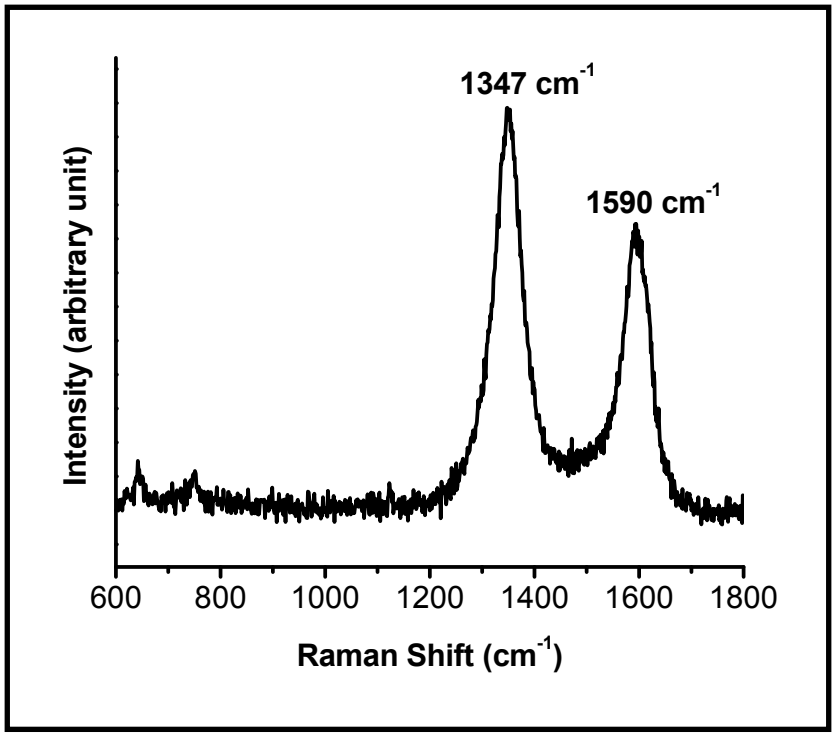

Figure 4.11: Raman spectra of ICP-1 powder showing the D and G peaks which corresponds to defect and graphitic structure of CNTs.

5. OPTIMIZATION OF PLASMA PROCESS PARAMETERS

Plasma spraying involves myriad of process, equipment and powder parameters which has a direct effect on the coating properties [19, 20, 69-73]. Hence, there is a need of optimizing the plasma process parameters in order to achieve "dense" coating. The objective of the optimization of plasma process parameters is to develop the process maps to understand the influence of "key processing parameters" on the thermal and kinetic energy of the particle that affect "porosity" and hence "mechanical properties" of the coating. Effect of CNT content on the thermal and kinetic history of the particle in the plume is also investigated to obtain the coating with the lowest porosity. Development of process map for all three powders (A-SD, A4C-SD, and A8C-SD) has been discussed below.

5.1 Process Map for A-SD Powder

Figure 5.1 is the integrated process map for A-SD powder at 75 mm stand-off which correlates the plasma processing parameters (plasma power, feed rate and primary gas flow) with the particle state and effect of particle state on the coating's porosity and microhardness. Figures 5.1a and b show the temperature and velocity of the A-SD particles at the 75 mm stand-off. The relative size of the legends in Figures 5.1-5.4 is proportional to the plotted characteristic i.e. temperature, velocity, porosity and microhardness. It is observed that both particle temperature and velocity increased with the increasing plasma power. An increase in the primary (argon) gas flow rate showed marginal improvement in the temperature but has significant improvement on the

velocity. As powder feed rate was increased, temperature and velocity of the powder particle dropped down. The highest temperature (2745 K) and velocity (338 ms^{-1}) of the A-SD powder was achieved at the highest plasma power (34 kW), highest primary gas

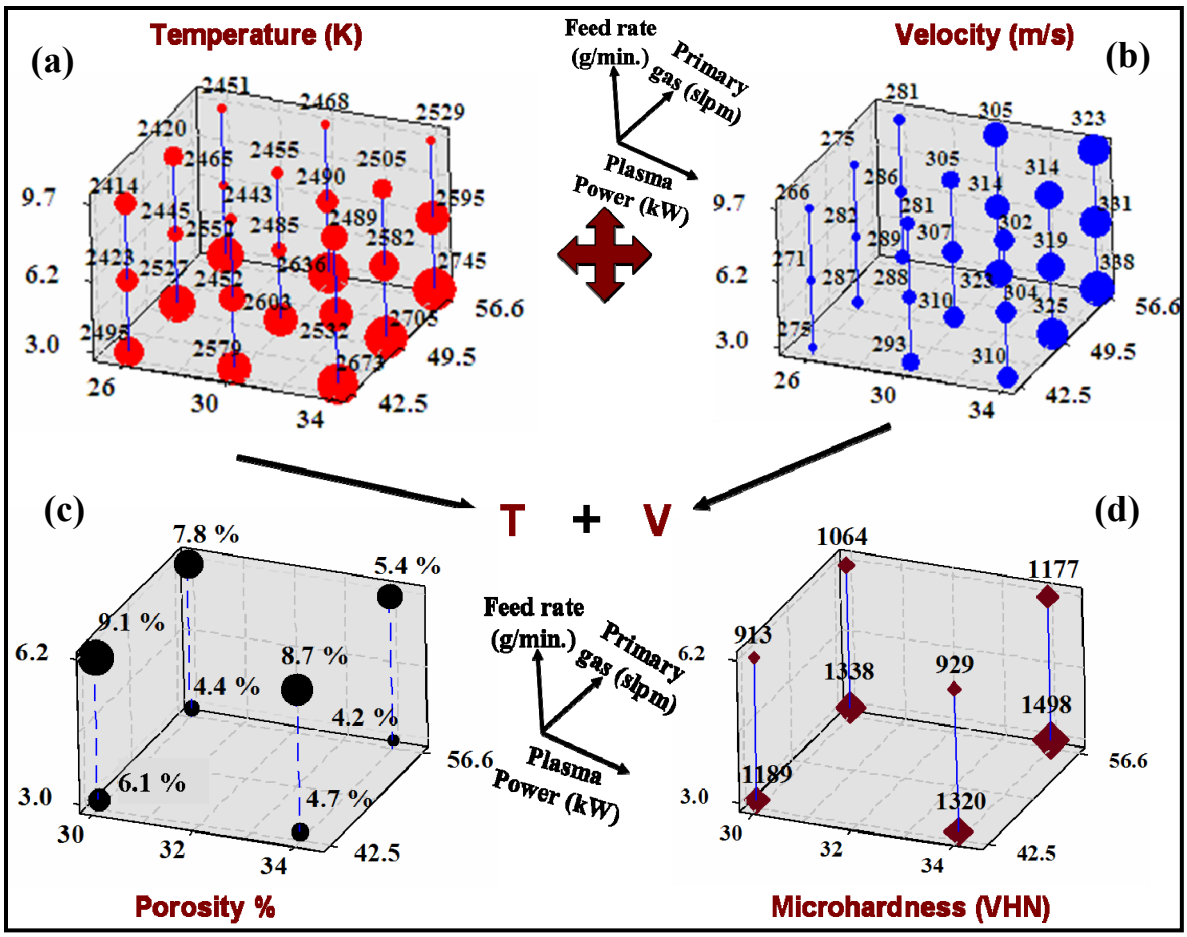

Figure 5.1: Process map showing (a) temperature and (b) velocity distribution of in flight A-SD powder particle at 75 mm stand-off distance for various plasma processing parameters (c) Porosity and (d) Microhardness distribution of A-SD coating at 75 mm stand-off at optimized plasma processing parameters. The size of the circle and diamond legend is proportional to the numerical value

flow rate (56.6 slpm) and at the lowest feed rate (3 g/min). Porosity of the A-SD coating measured is shown in Figure 5.1(c). The lowest porosity of 4.2% was achieved at highest plasma power (34 kW), highest primary gas flow rate (56.6 slpm) and lowest feed rate (3 g/min.). The reverse is true for the highest porosity (9.1%) at the lowest plasma power (30 kW), lowest primary gas flow rate (42.5 slpm) and the highest feed rate (6.2 g/min). Microhardness of all the free-standing coatings samples were measured and shown in Figure 5.1(d). It should be noted that marginal difference in porosity of A-SD coating at 30 kW (~4.2%) and 34 kW (~4.4%) at 75 mm stand-off distance (as shown in Figure 5.1c) leads to ~12% improvement in hardness at higher plasma power. An increase in the hardness at higher power is attributed to (i) its exponential dependence on the porosity as shown in equation 5.1 [137] and (ii) improved intersplat bonding as a result of enhanced degree of melting of powder particle at higher plasma power.

$$H = H_0 \exp(-aP) \tag{5.1}$$

In equation 5,1,p is porosity, H_0 is the hardness of fully dense material, H is the overall hardness of the porous material and a is the arbitrary constant. Further, a direct correlation between the highest hardness (1498 VHN) and the lowest porosity (4.2%) was found. A similar correlation exists for the lowest hardness (913 VHN) obtained at the highest porosity (9.1%) suggesting one-to-one mapping.

A similar trend in the temperature and velocity of the in-flight particle was observed for A-SD powder at 100 mm stand-off, as seen in Figures 5.2a and b. It shows that stand-off distance has a significant effect on the particle state. Table 5.1 shows the comparative particles temperature and velocity, porosity and microhardness at the

optimized processing parameter (plasma power: 34 kW, primary gas: 56.6 slpm, feed rate: 3 g/min) for stand-off distance of 75 and 100 mm. Temperature and velocity of the powder particle achieved at the 100 mm stand-off is ~3% and ~8% lower respectively, than temperature and velocity of the powder particle at 75 mm stand-off. With increasing stand-off distance, porosity of the coating increased resulting in low hardness.

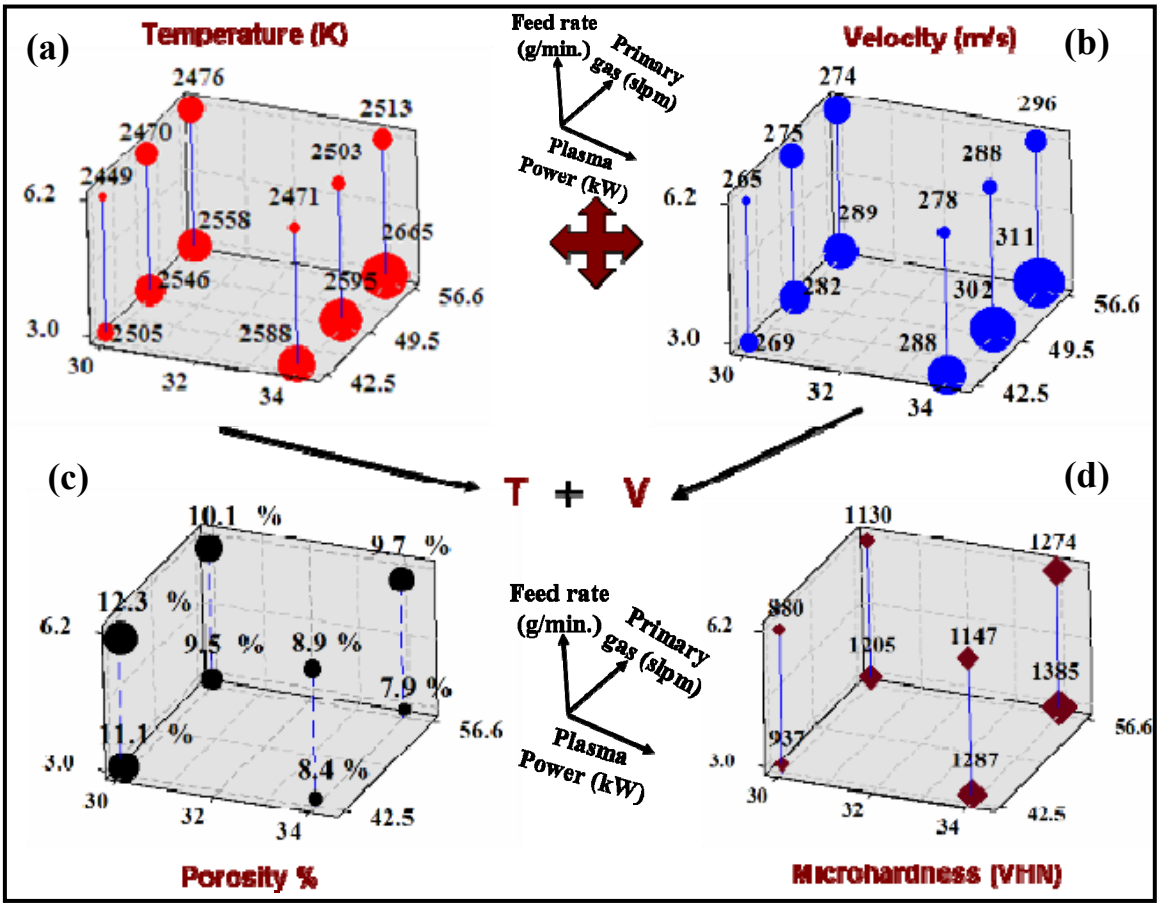

Figure 5.2: Process map showing (a) temperature and (b) velocity distribution of in flight A-SD powder particle at 100 mm stand-off for various plasma processing parameters (c)) Porosity and (d) Microhardness distribution of A-SD coatings at 100 mm stand-off at optimized plasma processing parameters. The size of the circle and diamond legend is proportional to the numerical value.

Table 5.1: Particle characteristics and coating porosity for A-SD powder at optimized plasma process parameters for different stand-off distances.

	Temperature (K)	**Velocity (m/s)**	***Porosity %**	**Hardness (VHN)**
Stand off: 75 mm	2745±9	338±0.6	4.2	1498±49
Stand off : 100 mm	2665±11	311±0.8	7.9	1385±69

* Error in porosity data was found to be ±0.3

5.2 Process Map for A4C-SD Powder

As earlier explained for A-SD powder, same methodology has been adopted for developing the process map for A4C-SD powder. Figures 5.3a and b illustrate the temperature and velocity of the particle respectively, at 75 mm stand-off whereas Figures 5.3c and d show the temperature and velocity of the particle at 100 mm stand-off. As the plasma power increased from 30 kW to 34 kW, both temperature and velocity of the particle increased. An increasing primary gas flow rate also increased the temperature and velocity of the in-flight particle. The higher feed rate of 6.2 g/min leads to lowering of the temperature and velocity due to larger mass in the plasma plume. The highest temperature and velocity of the particle achieved at 75 mm stand-off and 3 g/min feed rate is 2423 K and 319 m/s respectively. The temperature and velocity of the in-flight A4C-SD particle reduced to 2378 K and 281 m/s respectively for the higher stand-off (100 mm) at the same feed rate of 3 g/min. Figure 5.3 (e) and (f) represents the porosity

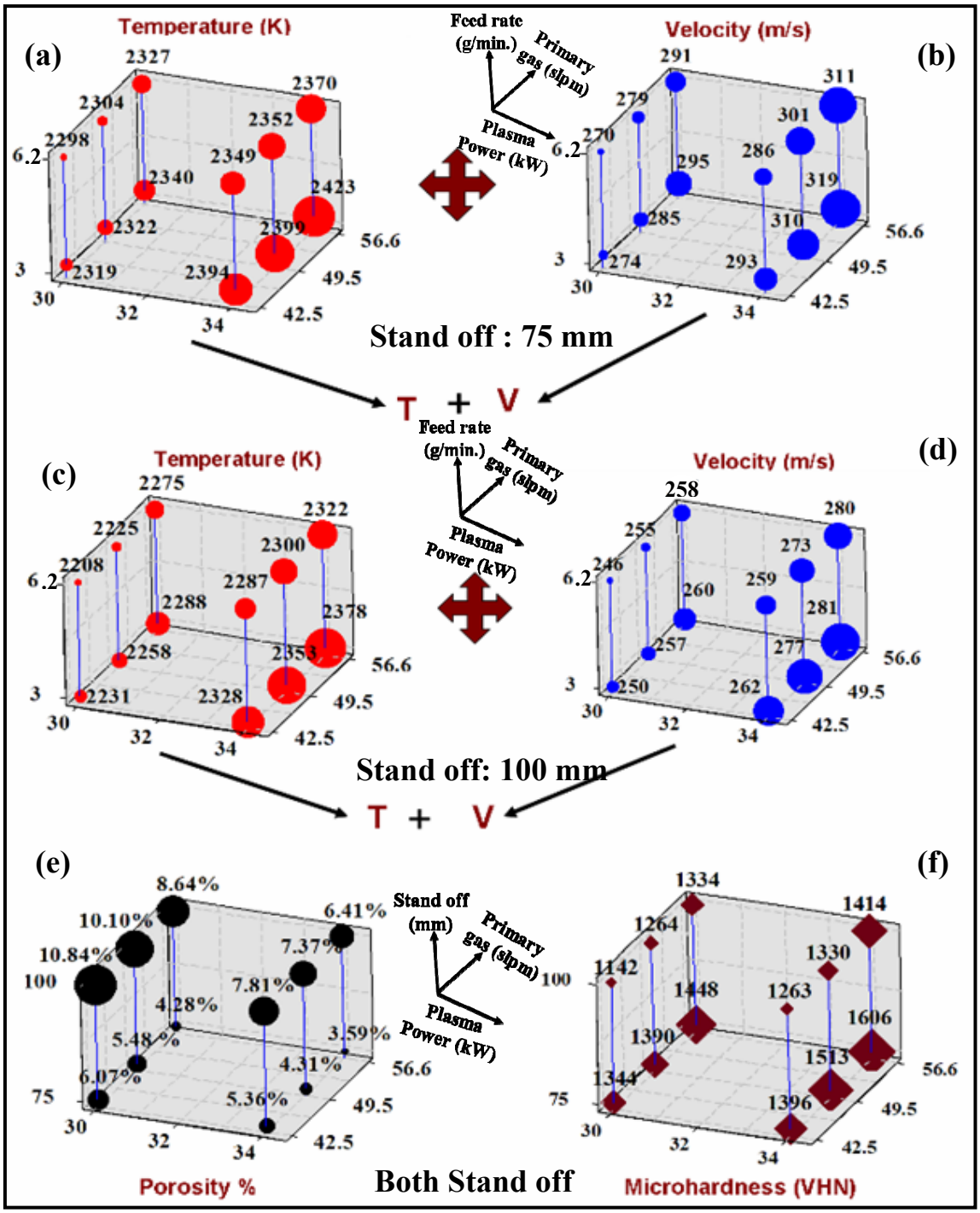

Figure 5.3: Process map showing (a) temperature and (b) velocity distribution of in flight A4C-SD powder particle at 75 mm stand-off for various plasma processing parameter (c) temperature and (d) velocity distribution of in flight A4C-SD powder particle at 100 mm stand-off for various plasma processing parameter (e) Porosity and (f) Microhardness distribution of A4C-SD coatings at both stand-off (75 mm & 100 mm) distances.

and microhardness of A4C-SD coatings at both stand-off distances. Porosity increased from 3.59 % to 6.41 % on changing the stand-off from 75 to 100 mm for 34 kW plasma power and 56.6 slpm of primary gas flow rate. It should be recalled that feed rate was kept constant as 3 g/min. for synthesizing A4C-SD coatings for porosity measurement. A direct correlation of one-to-one mapping between porosity and microhardness was also observed for A4C-SD coating.

5.3 Process map for A8C-SD Powder

Based on the results from A-SD and A4C-SD powders, it was observed that stand-off is the critical factor affecting the particle state in the plasma plume. Increasing stand-off distance leads to lower particle temperature and velocity. Hence, for the case of A8C-SD powder, lower stand-off distance (75 mm) was maintained. Figures 5.4 (a) and (b) show the temperature and velocity of in-flight particle at 75 mm stand-off. As the plasma power increased from 30 kW to 34 kW, both temperature and velocity of the particle increased. The same behavior is observed for increasing primary gas flow rate. Also, increasing the feed rate to 6.3 g/min leads to lowering of the temperature and velocity. The highest temperature and velocity of the particle achieved at 75 mm stand-off for 3.1 g/min feed rate is 2397 K and 314 m/s. Figures 5.4 (c) and (d) represent the porosity and microhardness of A8C-SD coatings at stand-off distance of 75 mm. Lowest porosity (3 %) was achieved at the highest plasma power (34 kW), highest primary gas flow rate (56.6 slpm) and lowest feed rate (3 g/min). Reverse is true for the highest porosity (6.4 %) i.e. lowest plasma power (30 kW), lowest primary gas flow rate (42.5 slpm) and. highest feed rate (6.2 g/min). Higher hardness (1670 VHN) was achieved at

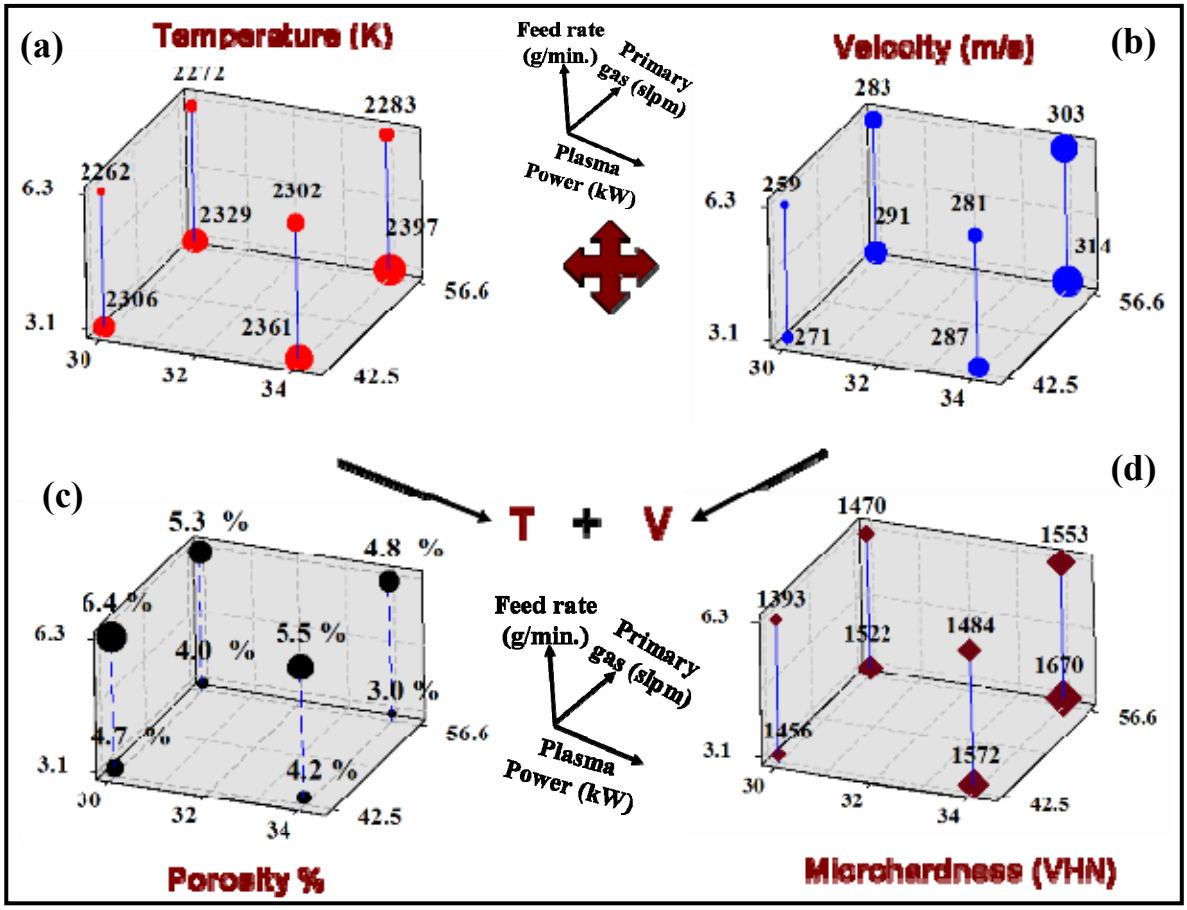

Figure 5.4: Process map showing (a) temperature and (b) velocity distribution of in flight A8C-SD powder particle at 75 mm stand-off for various plasma processing parameter (c) Porosity and (d) Microhardness distribution of A8C-SD coating samples at 75 mm stand-off.

lowest porosity (3%) while lower hardness (1393 VHN) of the sample was obtained at highest porosity (6.4%) for A8C-SD coating Table 5.2 summarizes the porosity and hardness of all three coatings (A-SD, A4C-SD, A8C-SD coatings) at finally optimized plasma process parameters. Table-5.2 clearly indicates that, with increasing CNT content,

Table 5.2: Porosity% and hardness of all three optimized coatings

Coating Nomenclature	*Porosity%	Hardness (VHN)
A-SD	4.2	1498±49
A4C-SD	3.5	1606±54
A8C-SD	3.0	1670±59

*Error in porosity data was found to be ±0.3

porosity in the coatings decreased while an improvement in the hardness of the coatings was observed. This suggests that CNTs has significant effect on thermal and kinetic history of in-flight particle which causes lower porosity with increasing CNT content. Effect of CNTs on the particle state has been discussed in next section.

5.4 Effect of CNTs on the Particle State

The microstructure of the plasma sprayed coatings is largely dependent on the temperature (degree of melting) and velocity (degree of flattening) of the in-flight particles. In addition to plasma process parameters, CNT content and degree of CNT dispersion in the feedstock powder also affects the thermal and kinetic history of the particle in the plume. Since agglomerate size distribution for three powders (A-SD is 30 ± 10 μm, A4C-SD is 26 ± 7 and A8C-SD is 24 ± 5 μm) is more or less similar, strong influence of CNTs in impacting the thermal exposure to the in-flight particle is observed in Table 5.3 and Figure 5.5. The reduction in the particle temperature and velocity with an increasing CNT content is plotted in Figure 5.5. Reduced thermal exposure of A4C-SD and A8C-SD particle in the plasma plume can be understood with the help of schematic shown in Figure 5.6. Plasma plume has been divided in two zones. Particles

Table 5.3: Effect of CNTs on particle temperature and velocity at optimized processing parameters for the lowest porosity.

	Temperature (K)	Velocity (m/s)
A-SD	2745±9	338±0.66
A4C-SD	2423±14	319±0.79
A8C-SD	2397±12	314±0.84

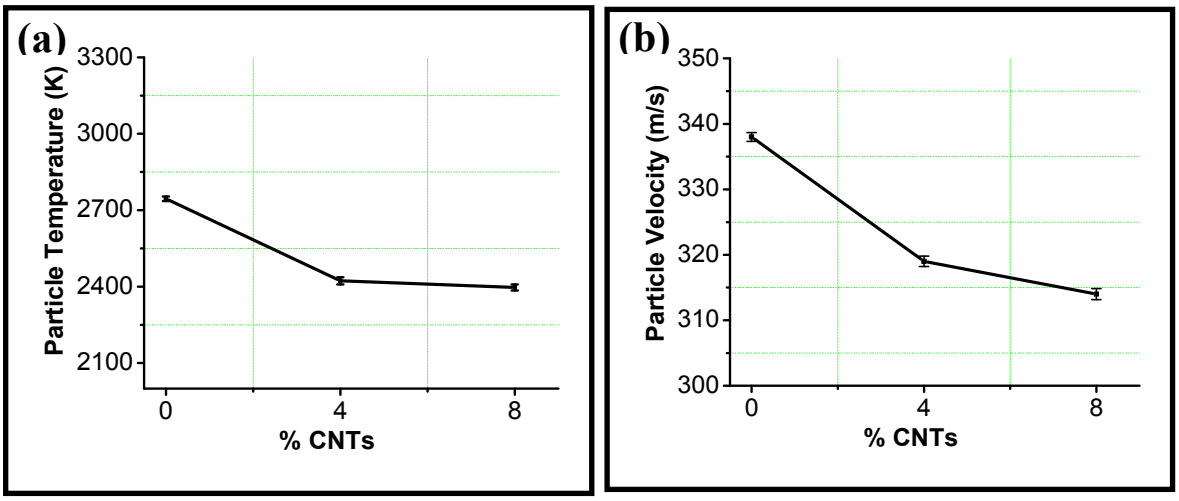

Figure 5.5: Effect of CNTs content on in-flight particle (a) temperature and (b) velocity at finally optimized plasma processing parameter for the coatings with the lowest porosity.

were internally injected and first experiences zone 1 in the plasma plume. Zone 2 is identified as the location where in-flight sensor measures the temperature and velocity of the particle exiting the plasma plume. In zone 1, when both the powders (Al_2O_3 and Al_2O_3-CNT) were injected into the plasma plume separately, heat transfer from the plasma plume to powder agglomerate takes place. In the case of Al_2O_3-CNT agglomerates, due to excellent thermal conductivity of CNTs (~3000 W/m-K) as compared to Al_2O_3 (~36 W/m-K) [4], heat transfer occurs from the reinforcement to the

ceramic matrix which improves the melting of the powder particle in the plume. However, in case of zone 2, there is heat loss associated with the molten powder particle due to thermal heat radiation (Equation 5.2). In the case of Al_2O_3-CNT particles, radiation heat loss arising from the dispersed CNTs dissipates heat rapidly.

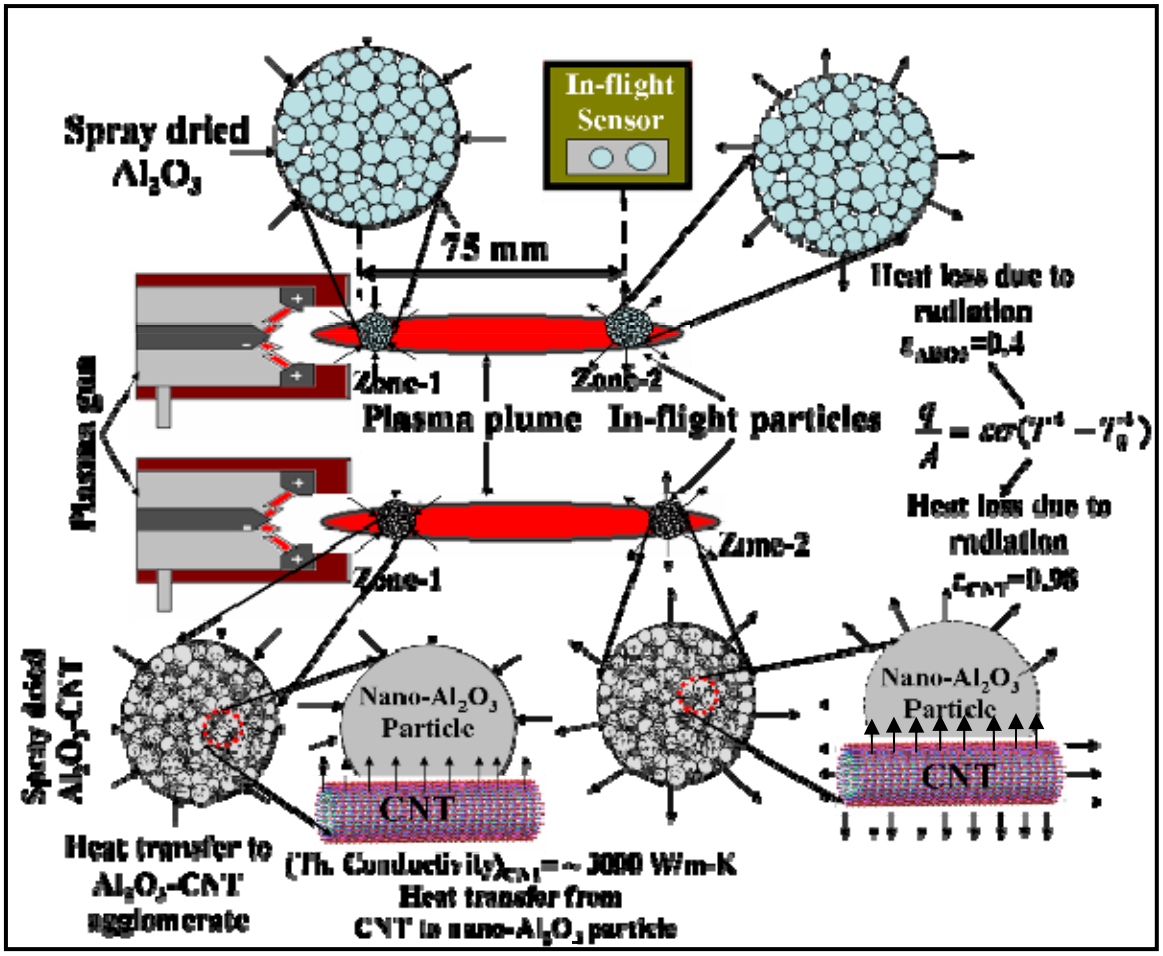

Figure 5.6: Schematic of in-flight particle and corresponding heat transfer phenomena in two different zone of plasma plumes for Al_2O_3 and Al_2O_3-CNT powder agglomerates.

Heavy radiation loss of CNT arises because of its high emissivity (0.98) compare to radiation loss of Al_2O_3 particle (emissivity 0.4) [4, 29].

$$\frac{q}{A} = \varepsilon\sigma(T^4 - T_0^4) \tag{5.2}$$

here, T = hot body's temperature (K)
T_0 = surroundings temperature (K)
A = area of hot body (m^2)
σ = 5.6703 10-8 (W/m2K4)
ε = 0.98 (graphite)
ε = 0.4 (Al_2O_3)

Further, CNTs located inside the hollow A4C-SD agglomerate 'soaks' the heat acquired by the CNTs on surface of the agglomerate and hence, lowers the thermal exposure (2423 K, ΔT = -322 K) of the particles compared to the A-SD in-flight particle. Though higher CNT content in A8C-SD powder can slightly increase the surface temperature, but uniform CNT distribution inside the particle also increases and hence, heat extraction rate also increases, resulting in slight lowering of the temperature (2397 K, ΔT = -348 K) of the A8C-SD particle compared to A-SD particles.

Velocity of the in-flight particles was also reduced with increasing the CNTs content which is relatively complex phenomena. Since the mass of the Al_2O_3-CNT agglomerate is lower (density of CNT is 2.1 g/cm^3) than Al_2O_3 agglomerate, it is expected that particle velocity will be more for Al_2O_3-CNT agglomerate. On the contrary, due to their hollow tubular structure, CNTs will provide a larger drag resistance as compared to solid particle resulting in lower velocity of Al_2O_3-CNT particle. It may be possible that drag resistance of CNTs dominate, resulting in lower velocity of Al_2O_3-CNT particles. Overall, velocity effect is complex and not completely understood. Similar results were observed by Balani et al. [4], who developed the preliminary process

map for Al_2O_3-CNT nanocomposite coating and found that CNTs has significant effect in lowering the temperature and velocity of the particle in plasma plume. Reduced thermal exposure of the particle as a result of CNT content and its uniform dispersion indicates that higher plasma power is required to melt the Al_2O_3 particle and to obtain thick coatings from A4C-SD and A8C-SD powder. However, as shown in Figure 5.6 (Zone-2), some part of lost heat by CNTs will also be transferred to Al_2O_3 particle resulting enhanced degree of melting of the powder. This might be the one of the reasons why dense and thick CNT reinforced-Al_2O_3 coatings were achieved at the same optimized plasma power i.e. at 34kW. Though lower temperature and velocity of in-flight A4C-SD (ΔT = -322 K, Δv = −19 m/s) and A8C-SD (ΔT = -348 K, Δv = −24 m/s) particle was observed as compare to A-SD particle, slightly lower porosity were achieved for A4C-SD (-0.7%) and A8C-SD (-1.2 %) coatings. Other reason is attributed to the uniform dispersion of CNT in the agglomerates (as shown in Chapter-4, Figure 4.2) which causes uniform melting and intersplat void filling (as shown in Figure 5.7).

Thus, it becomes clear how plasma process parameters and degree of CNT content and its dispersion in Al_2O_3 affect the thermal and kinetic state of in-flight particles. However, still it is not clear that which plasma parameters have most significant effect on the porosity of coating. In order to rank the significance of different plasma processing parameters, empirical model for porosity has been developed. It is envisaged that such approach would improve the reproducibility of dense Al_2O_3-CNT composite coatings. Details of empirical model for porosity are discussed in the next section.

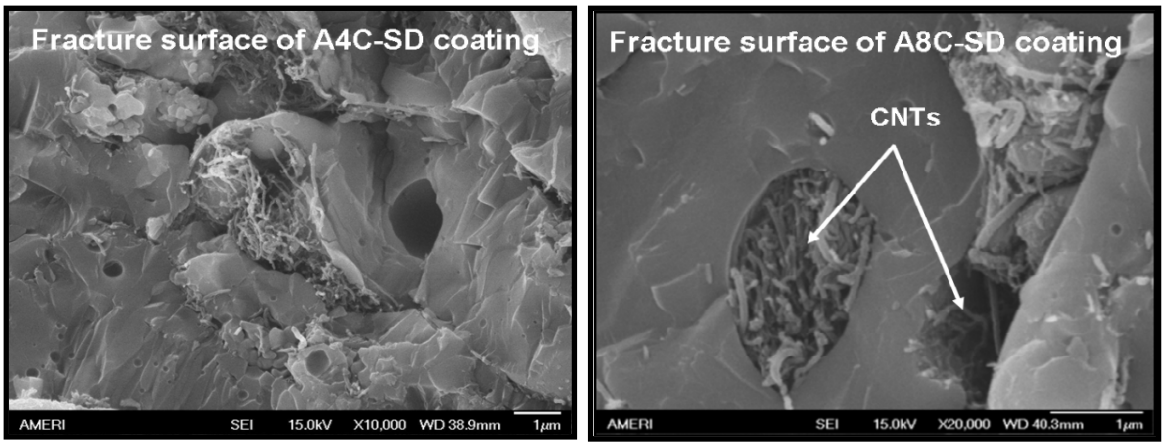

Figure 5.7: High magnification SEM image of fracture surface of (a) A4C-SD coating and (b) A8C-SD coating showing CNT residing in intersplat voids.

5.5 Empirical Models for Porosity

The porosity data of plasma sprayed A-SD, A4C-SD and A8C-SD coatings was utilized to create an empirical model. Based on 16 porosity data points of A-SD coating, a linear regression equation was fitted which provided the relationship between response parameters (porosity) and the control factors (plasma processing parameters). The data was first normalized i.e. each of the processing parameters (Plasma power, Feed rate, primary gas flow rate, stand-off distance) was divided by its own highest value. This allows data on different *scales* to be compared, by bringing them to a common scale. As an example, Table 5.4 is the porosity data with respect to plasma process parameters for A-SD coating at 75 mm and 100 mm stand-off distance which is normalized and shown in Table-5.5.

Table 5.4: Porosity data with respect to plasma process parameters for A-SD coating at 75 mm and 100 mm stand-off

Power (kW)	Primary gas (Slpm)	Feed rate (g/min.)	Stand off (mm)	Porosity %
30	42.5	3	100	11.13
30	42.5	6	100	12.30
30	56.6	3	100	9.52
30	56.6	6	100	10.05
34	42.5	3	100	8.45
34	42.5	6	100	8.86
34	56.6	3	100	7.94
34	56.6	6	100	9.69
30	42.5	3	75	6.12
30	42.5	6.2	75	9.15
30	56.6	3	75	4.45
30	56.6	6.2	75	7.85
34	42.5	3	75	4.77
34	42.5	6.2	75	8.77
34	56.6	3	75	4.20
34	56.6	6.2	75	5.43

Table 5.5: Normalized" porosity data with respect to plasma process parameters for A-SD coating at 75 mm and 100 mm (for regression analysis)

Power(kW)/34 kW	Primary gas (slpm)/56.6 slpm	Feed rate (g/min)/6.2 g/min	Stand off (mm)/ 100 mm	Porosity %
0.882	0.751	0.484	1.000	11.13
0.882	0.751	1.000	1.000	12.30
0.882	1.000	0.484	1.000	9.52
0.882	1.000	1.000	1.000	10.05
1.000	0.751	0.484	1.000	8.45
1.000	0.751	1.000	1.000	8.86
1.000	1.000	0.484	1.000	7.94
1.000	1.000	1.000	1.000	9.69
0.882	0.751	0.484	0.75	6.12
0.882	0.751	1.000	0.75	9.15
0.882	1.000	0.484	0.75	4.45
0.882	1.000	1.000	0.75	7.85
1.000	0.751	0.484	0.75	4.77
1.000	0.751	1.000	0.75	8.77
1.000	1.000	0.484	0.75	4.20
1.000	1.000	1.000	0.75	5.43

Regression analysis using SPSS software was done on the normalized data and empirical equation for porosity % was developed. Normalization of the each of the processing parameters was done so that relative importance of each term in the empirical model can be accurately judged.

For the A-SD coating, equation is given by:

$$\begin{aligned} \text{Porosity (\%)} = 10.217 &- 13.141 * \text{Power} \\ &- 5.185 * \text{Primary gas} \\ &+ 3.852 * \text{Feed rate} \\ &+ 13.544 * \text{Stand off} \end{aligned} \quad (5.3)$$

The resulting equation has a coefficient of determination (R^2) of 0.88. Similarly, based on 12 porosity data points of A4C-SD coating, an empirical equation is given by,

$$\begin{aligned} \text{Porosity \%} = 15.259 &- 14.139 * \text{Power} \\ &- 8.066 * \text{Primary gas} \\ &+ 14.827 * \text{Stand-off} \end{aligned} \quad (5.4)$$

Equation 5.4 has a coefficient of determination (R^2) of 0.93.

Further, based upon 8 porosity data points of A8C-SD coating, empirical relation is given by equation 5.5, which has a coefficient of determination (R^2) of 0.98.

$$\begin{aligned} \text{Porosity \%} = 11.713 &- 6.375 * \text{Power} \\ &- 3.633 * \text{Primary gas} \\ &+ 3.022 * \text{Feed rate} \end{aligned} \quad (5.5)$$

Here, all parameters are normalized and coefficients are given in the equation. In order to see the relative importance of the processing parameters, the coefficient of empirical equations 5.3, 5.4 and 5.5 were plotted in Figure 5.8a, b and c respectively. Figures 5.8a-c are **Pareto diagrams** where positive and negative sign of the coefficients

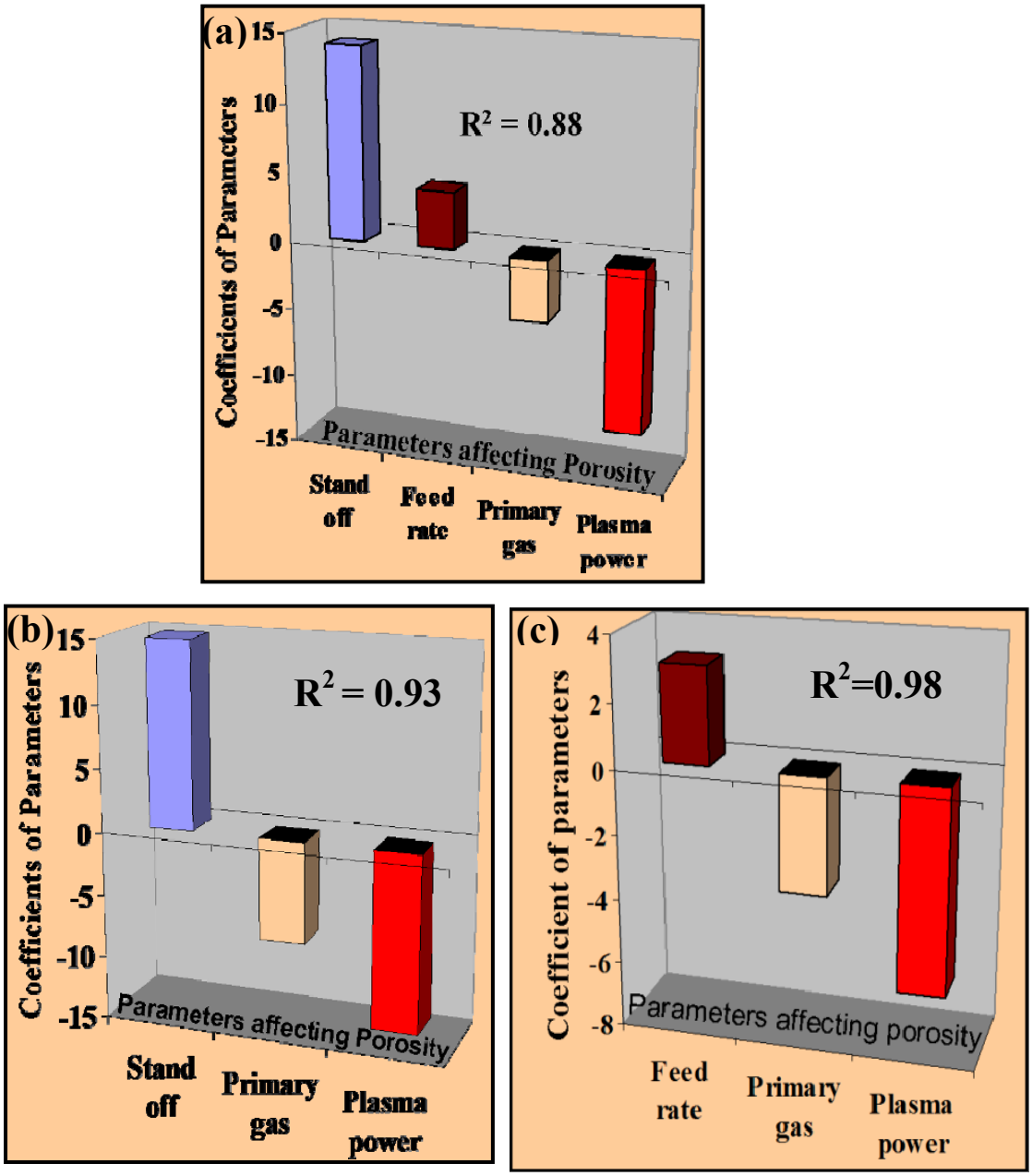

Figure 5.8: Pareto diagram showing the effects of process parameters on porosity of (a) A-SD coating (b) A4C-SD coating at constant feed rate (c) A8C-SD coating at constant stand-off distance.

indicates the nature of the effect and absolute value shows the extent of dominance on the porosity Pareto analysis is a statistical tool for identifying the variables which has most significant effect on the entire process. It works on 80/20 rule i.e. 80% of the effect is dominated by 20% causes [138]. Hence, Pareto analysis enables selection of the most effective plasma processing variable that would impact porosity of the coating.

As shown in Figure 5.8a, the stand-off and feed rate are on the positive side whereas plasma power and primary gas flow are on the negative side. This suggests that with the increase in stand-off and feed rate, porosity of the coating will increase while the increase in plasma power and primary gas flow rate will result in porosity decrease. The most critical parameter which affects the porosity in A-SD coating was stand-off distance with the positive and highest value of the coefficient (+13.544). The regression analysis using SPSS software indicated that stand-off distance is significant at 99.9% confidence level. The second most important parameter affecting the porosity is plasma power and is significant at 99.1% confidence level. Primary gas flow rate and feed rate are ranked third and fourth, to affect the porosity of the coating.

Similarly, in case of A4C-SD, Pareto diagram indicates that with the increase in stand-off distance, porosity of the coating increases while an increase in primary gas flow rate and plasma power causes a decrease in the porosity. The most sensitive parameter which affects the porosity was stand-off distance (Figure 5.8 (b) and is significant at 99.9% confidence level. The second most important parameter which affects the porosity of the free-standing coating sample is plasma power and is significant at 99.6%

confidence level. Primary gas flow rate is ranked last in terms of its sensitivity on the porosity of A4C-SD coating. Since powder feed rate was kept constant for synthesizing the A4C-SD coating, this has not been included in Pareto analysis.

Similarly, stand-off was kept constant in case of A8C-SD powder, Pareto diagram includes only feed rate, primary gas flow rate and plasma power (as shown in Figure 5.8 (c). Plasma power was found most critical parameter which affects the porosity and is significant at 99.6% confidence level. The second most important parameter which affects the porosity of the A8C-SD is primary gas flow rate which is significant at 99.8% confidence level. Since feed rate was kept constant for A4C-SD coating, Pareto analysis for A-SD and A8C-SD coatings indicates that feed rate is less sensitive than other chosen parameter. Hence there is less variation in the porosity of the coating due to the feed rate. However, lower porosity of the coating may be obtained at very low feed rate i.e. 1 g/min but that would not be economical process unless coating required is very thin ~ 25-50 μm. In the present case, coating thickness is ~ 400 μm and deposition time was between 4-5 minutes.

The most critical parameter which affects the porosity of A-SD and A4C-SD coatings was stand-off distance for (stand-off was same and kept constant the A8C-SD coating). A higher stand-off distance results in reduce impact velocity at the substrate and hence lower degree of flattening. In addition, longer flight time may also cause resolidification of molten droplets before reaching the substrate. These conditions ultimately lead to high porosity and hence degrade the hardness of the coating. A shorter

stand-off distance than 75 mm would result in overheating and oxidation of the substrate in addition to bounce back of molten particles. Azarmi et al. [139] carried out the optimization of atmospheric plasma spray process parameters using a design of experiment for Ni-based superalloys and found stand-off as the most critical parameter which affects the density of the coating. Pareto analysis revealed the sensitivity of individual process parameters on porosity of different coatings and hence provided the approach for further refining of the process parameters in order to produce a coating with specific density and microstructure.

It is recalled that optimization studies were carried out only on the spray dried powder and not ICP-1 powder due to limited availability of ICP-1 powder. The optimized plasma process parameters were used for synthesizing the coatings from ICP-1 powder as well as spray dried powder. Details of the microstructural characterization of synthesized coatings from both types of powders are summarized in chapter 6.

6. MICROSTRUCTURE OF Al_2O_3-CNT COMPOSITE COATING

Plasma sprayed Al_2O_3-CNT composite coatings were synthesized from spray dried powder and in situ CVD powder (ICP-1 powder). Optimized plasma process parameters shown in Table 6.1, have been used for synthesizing Al_2O_3-CNT coatings from both spray dried and ICP-1 powders. Microstructural details of coatings are discussed in the following section.

Table 6.1: Optimized plasma process parameters using spray dried powder

Current (A)	Voltage (V)	Primary Gas, Argon (slm)	Secondary Gas, Helium (slm)	Stand-off (mm) from the substrate	Powder feed rate (gram/min.)
850	40	56.6	59.5	75	3

6.1 Coatings Synthesized using Spray Dried Al_2O_3-CNT Powder

Two sets of the coatings were synthesized using spray dried powder: (i) coating synthesized at the optimized plasma process parameters with the "lowest" porosity (will be referred as high density (HD) coating) and (ii) Coating synthesized at those plasma process parameters which showed "highest" porosity (will be referred as low density (LD) coating). Two different plasma parameters were used in order to understand the effect of porosity on coating's mechanical properties (hardness, elastic modulus, fracture toughness, and wear resistance). The plasma processing parameters utilized for both (i.e. lowest and highest porosity) coatings are tabulated in Table 6.2.

Table 6.2: Plasma spray parameters for synthesis of Al_2O_3-CNT coatings with lowest and highest porosity.

Plasma process parameters for synthesizing **"lowest porosity"** coating					
Current (A)	**Voltage (V)**	**Primary Gas, Argon (slm)**	**Secondary Gas, Helium (slm)**	**Stand-off (mm) from the substrate**	**Powder feed rate (gram/min.)**
850	40	56.6	59.5	75	3
Plasma process parameters for synthesizing **"highest porosity"** coating					
Current (A)	**Voltage (V)**	**Primary Gas, Argon (slm)**	**Secondary Gas, Helium (slm)**	**Stand-off (mm) from the substrate**	**Powder feed rate (gram/min.)**
750	40	42.5	59.5	75	3

Figure 6.1 shows the plasma sprayed HD and LD coatings on steel substrates. The HD coating containing 0 wt.% CNT, 4 wt.% CNT, 8 wt.% CNT will be referred as HD-A-SD, HD-A4C-SD, and HD-A8C-SD respectively whereas LD coating containing 0 wt.% CNT, 4 wt.% CNT, 8 wt.% CNT will be referred as LD-A-SD, LD-A4C-SD, and LD-A8C-SD respectively. It is observed that with increasing CNT content, the color of the coating becomes darker. Figures 6.2a, b, and c show the cross-sectional view of HD-A-SD, HD-A4C-SD and HD-A8C-SD coatings respectively. Figures 6.2d, e, and f show the cross-sectional view of LD-A-SD, LD-A4C-SD, and LD-A8C-SD coatings respectively. Thicknesses of HD and LD coatings were in range of 400-450 μm. The coatings were uniform and adherent to the substrate. Porosity of HD and LD coatings was measured using Archimedes principle using water as the medium. The porosity content of

the coatings is tabulated in Table 6.3. It is observed that CNT reinforced coating has slightly lower porosity in both HD and LD coatings. The reason for lower porosity with higher CNT content is explained in section 5.4.

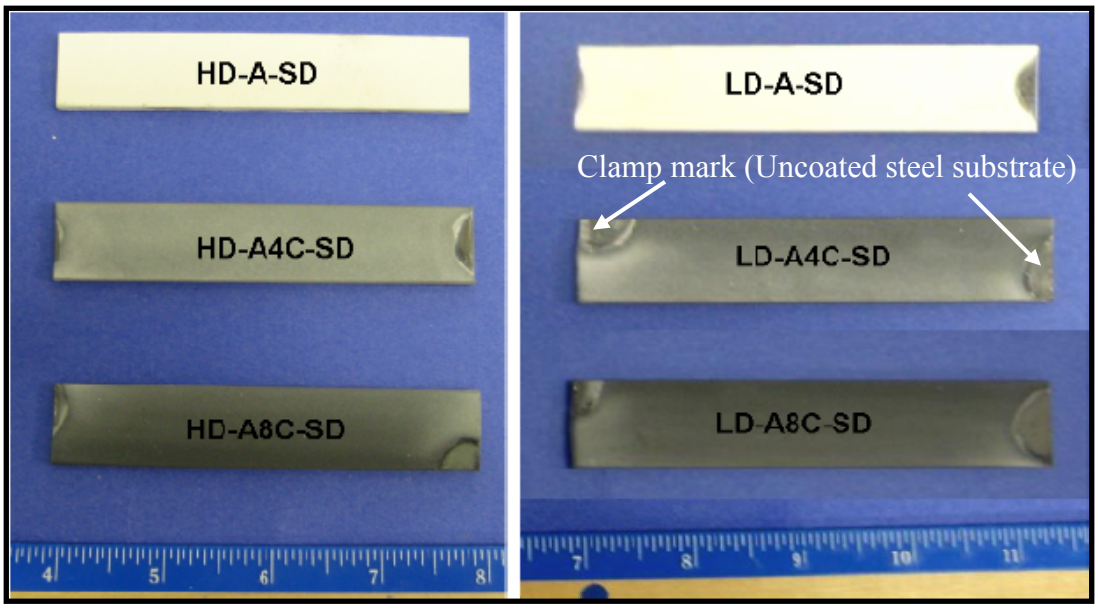

Figure: 6.1 Plasma sprayed high density (HD) and low density (LD) coating on an AISI 1020 steel coupon of size 100 x 19 x 3 mm^3. Marks at the both end of coating (as shown in figure) is due to fixture.

Retention of CNTs in plasma sprayed coatings was validated by Raman spectroscopy. Figure 6.3 shows the Raman spectra collected from the initial powder and CNT containing LD and HD coatings. Presence of D peak at 1350 cm^{-1} (corresponds to disordered graphite) and G peak at 1570 cm^{-1} (corresponds to stretching mode of graphite) confirms the retention of CNT structure in coatings.

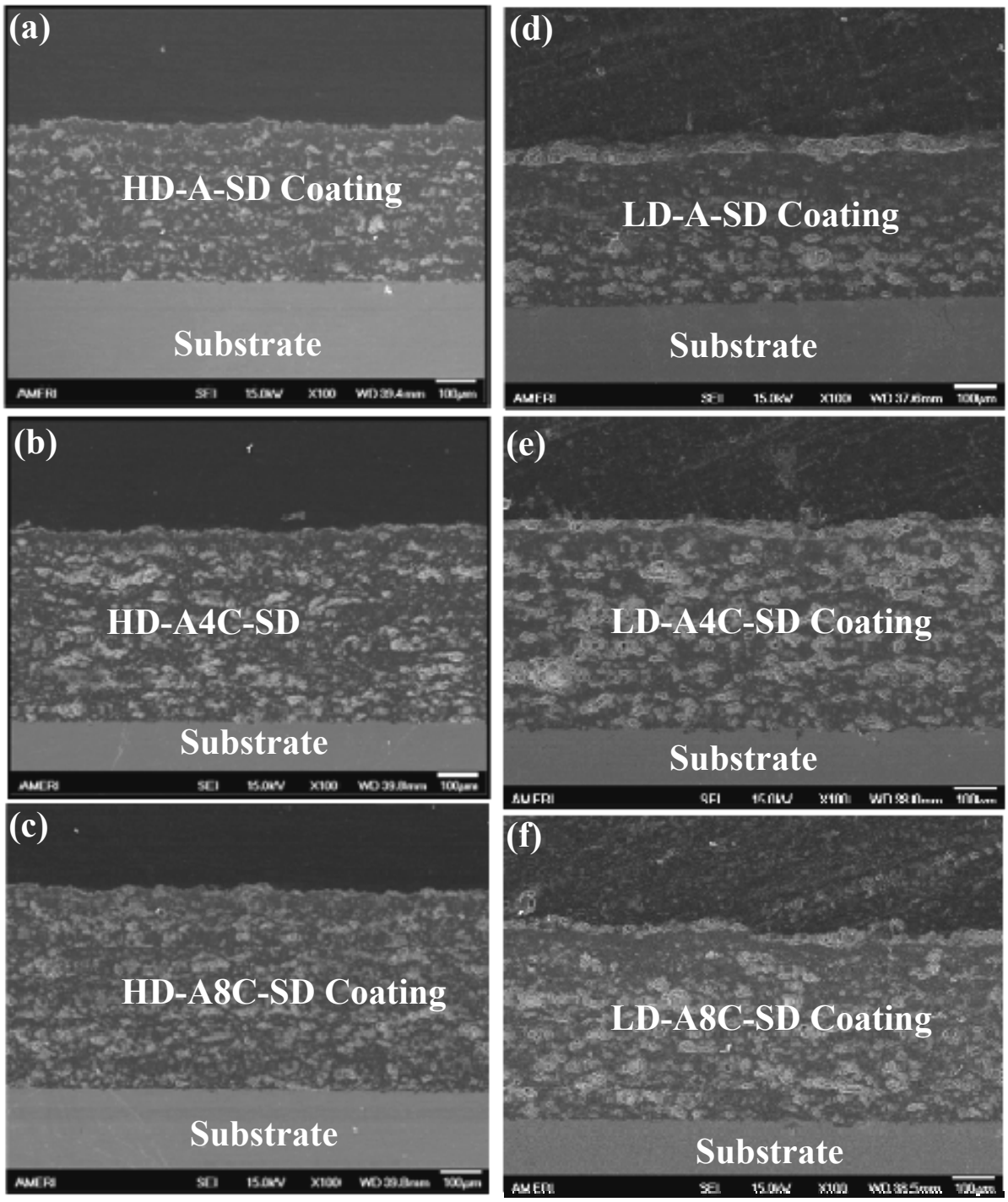

Figure 6.2: SEM image showing cross-sectional view of plasma sprayed (a) HD-A-SD coating (b) HD-A4C-SD coating (c) HD-A8C-SD coating (d) LD-A-SD coating (e) LD-A4C-SD coating (f) LD-A8C-SD coating. Thickness of all the synthesized coatings are in range of 400-450µm.

Table 6.3: Porosity (%) of HD and LD plasma sprayed coatings

*Porosity %			
	A-SD	**A4C-SD**	**A8C-SD**
HD Coating	4.2%	3.5%	3.0%
LD Coating	6.1%	5.6%	4.7%

*Error in porosity data was found ±0.3.

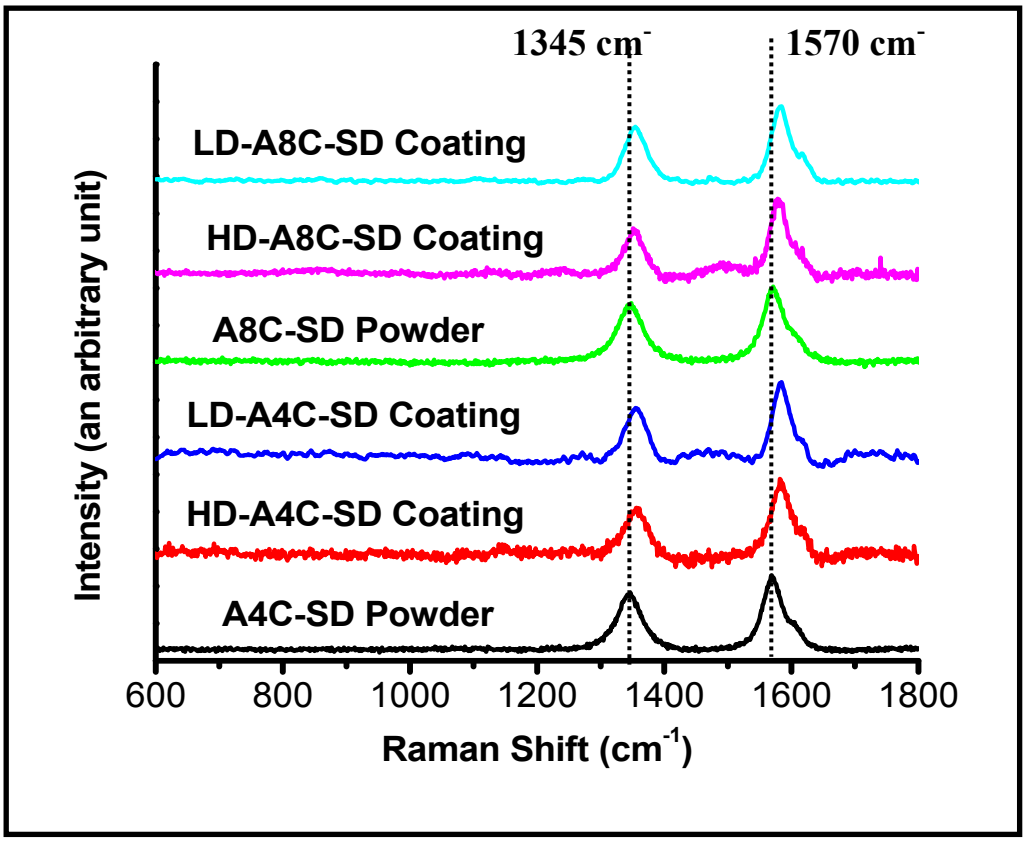

Figure 6.3: Raman spectrum of as received powder and plasma sprayed HD and LD coatings showing retention of CNTs in the coatings.

Table 6.4 shows the peak position (cm^{-1}) and ratio of intensity (I_D/I_G) of D and G peaks for A4C-SD and A8C-SD powders and high and low density coatings. . The intensity ratio of Raman peaks (I_D/I_G ratio) of powder and coatings obtained after plasma spraying are almost similar which indicates that there is no defect generation in the CNT structure. Both peaks show a slight shift towards higher wave number for CNT reinforced HD and LD coatings. The shift in the Raman spectrum of CNT has been correlated with tensile and compressive stress in nanotube [35, 140]. Tarantili et al. reported that position and full width at half-maximum (FHWM) of the Raman peak are sensitive to the strain present in the sample [140]. A shift towards larger wave numbers is observed if the sample is subjected to compression [140] . Shift of D and G peak towards higher wave number in case of plasma sprayed coating indicates the compressive force in CNTs, which may have developed due to solidification shrinkage of Al_2O_3. No experiments were done to measure the stress in the coatings.

Table 6.4: Position and ratio of intensity of D and G peaks obtained from Raman Spectroscopy of CNT reinforced powder (A4C-SD & A8C-SD) and coating (LD and HD).

Sample	**Position of D peaks**	**Position of G peaks**	**I_D/I_G**
A4C-SD Powder	1345	1570	0.853
HD-A4C-SD coating	1356	1582	0.849
LD-A4C-SD coating	1356	1582	0.886
A8C-SD Powder	1345	1570	0.931
HD-A8C-SD coating	1356	1582	0.935
LD-A8C-SD coating	1356	1582	0.957

SEM was further carried out on the fracture surface of CNT reinforced HD and LD coatings. Figures 6.4a-b show the fracture surface of HD-A4C-SD and HD-A8C-SD coating respectively whereas Figures 6.4c-d are the fracture surfaces of LD-A4C-SD and LD-A8C-SD coatings respectively.

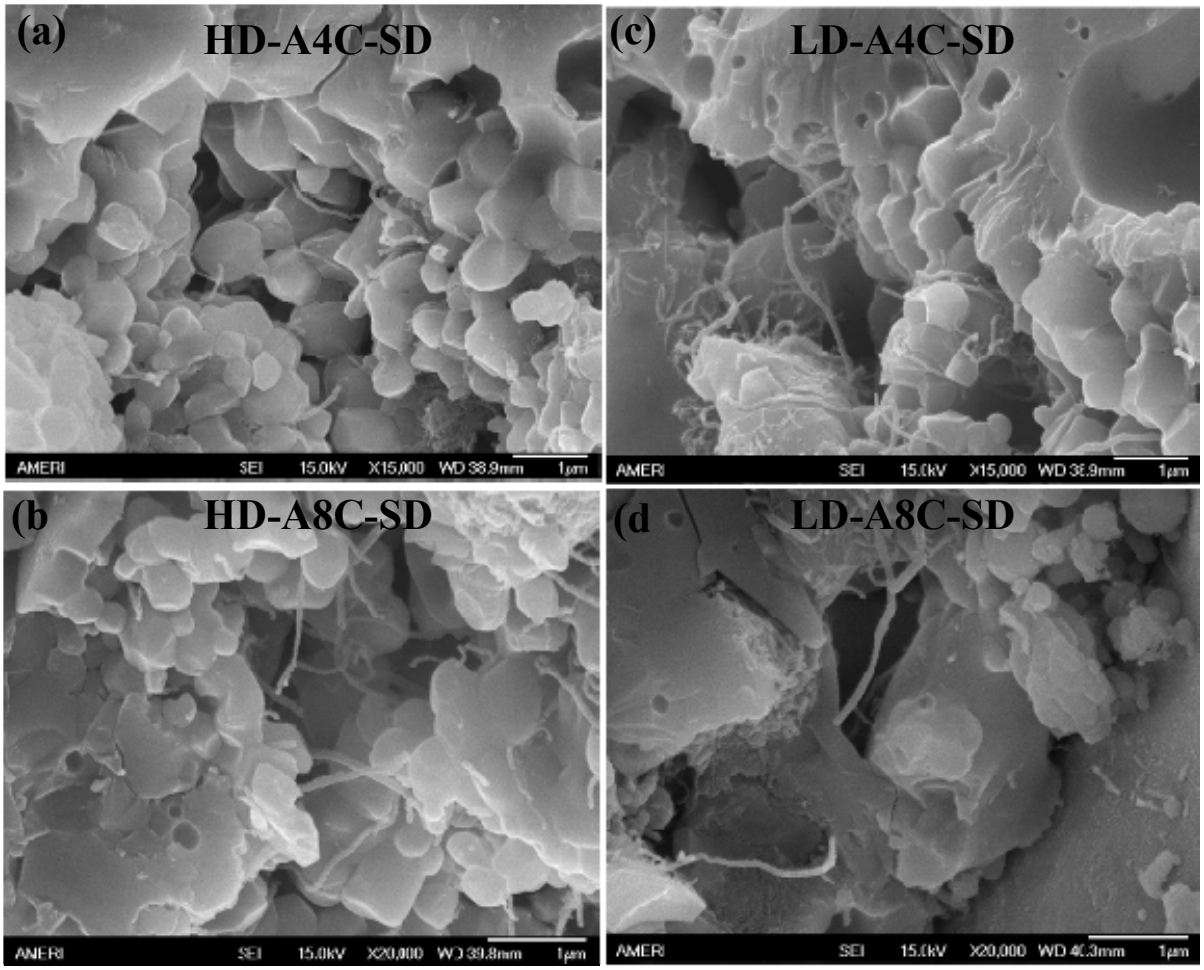

Figure 6.4: SEM image of fracture surfaces of (a) HD-A4C-SD coating (b) HD-A8C-SD (c) LD-A4C-SD coating (d) LD-A8C-SD coating showing CNTs in the Al_2O_3 matrix.

It is observed that CNTs are dispersed within Al_2O_3 splats. No agglomeration of CNTs was observed even for higher 8 wt. % of CNTs. It is expected that dispersed CNTs in the Al_2O_3 matrix will result in improving the fracture toughness and wear resistance of coatings. Al_2O_3-CNT coating was also synthesized using ICP-1 powder which is explained in the next section.

6.2 Coating Synthesized using CVD Al_2O_3-CNT (ICP-1) Powder

This coating was synthesized using optimized plasma process parameters which produced lowest porosity coating from spray dried powder. Due to lack of large amount of ICP-1 powder, plasma process parameters were not optimized for ICP-1 powder. Coating synthesized using ICP-1 powder will be referred as ICP-1 coating. Figure 6.5 shows the as-sprayed Al_2O_3 and ICP coatings. Similar to spray dried coating, color of ICP-1 coating also becomes darker due to CNT presence. Figures 6.6a and b show the cross-sectional view of Al_2O_3 and ICP-1 coatings, respectively. Coatings have a uniform thickness of 400 μm and are adherent to the substrate. Figure 6.7 shows the fracture surface of ICP-1 coating. It is observed that CNTs are dispersed in Al_2O_3 matrix. The measured porosity value for Al_2O_3 coating is ~6% (theoretical density: 3.99 g/cm^{-3}), while it is ~4% for ICP-1 (theoretical density: 3.93 g/cm^{-3}) coating. The lower porosity of ICP-1 coating is attributed to enhanced degree of melting of Al_2O_3 powder particle. Higher degree of melting in ICP-1 coating is attributed to excellent thermal conductivity of CNTs (~3000 W/m-K) [4] and its uniform dispersion on the Al_2O_3 powder surface.

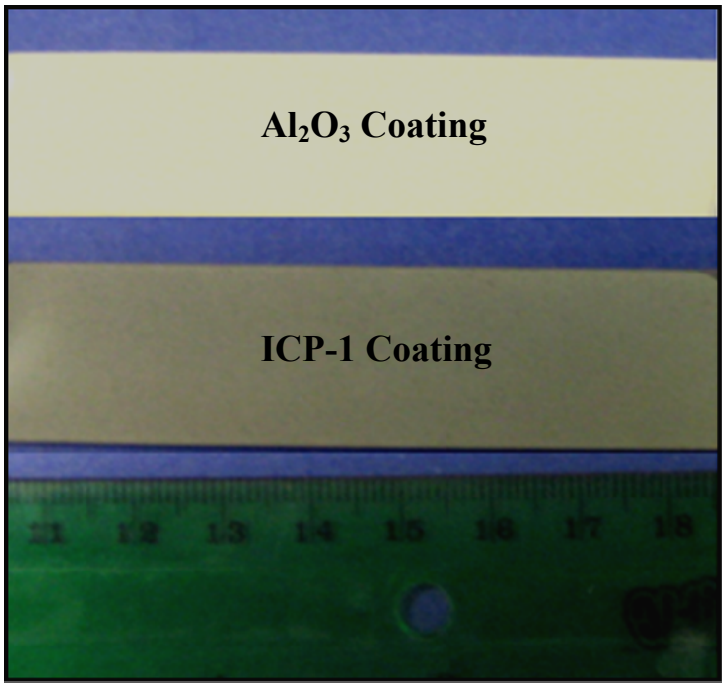

Figure: 6.5 Digital picture of plasma sprayed Al_2O_3 and ICP-1 coating

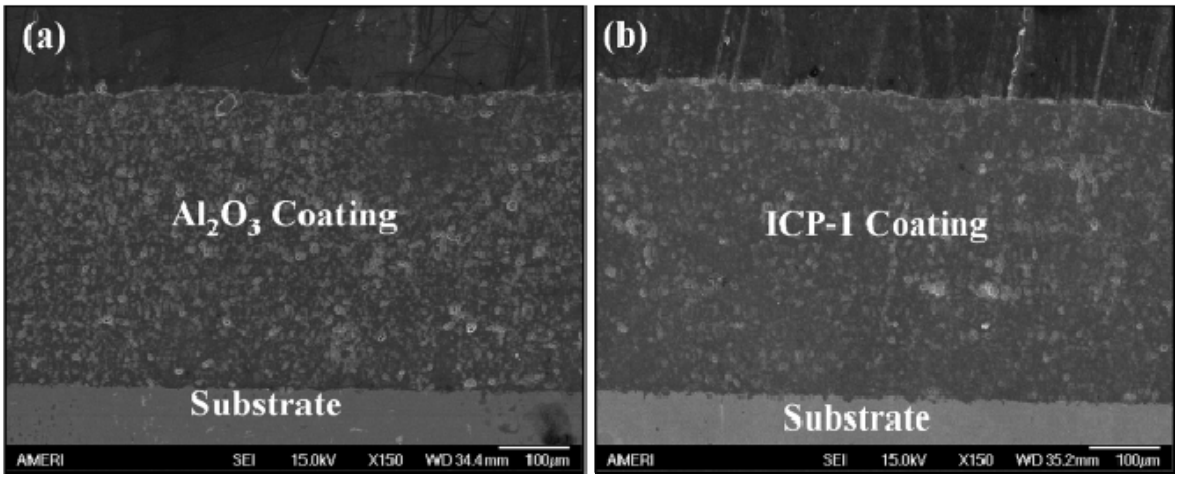

Figure 6.6 SEM image showing (a) cross-sectional view of plasma sprayed Al_2O_3 coating and (b) cross-sectional view of plasma sprayed ICP-1 coating

Mechanism for relatively lower porosity in CNT-reinforced coatings has already been explained in section 5.4 of this dissertation.

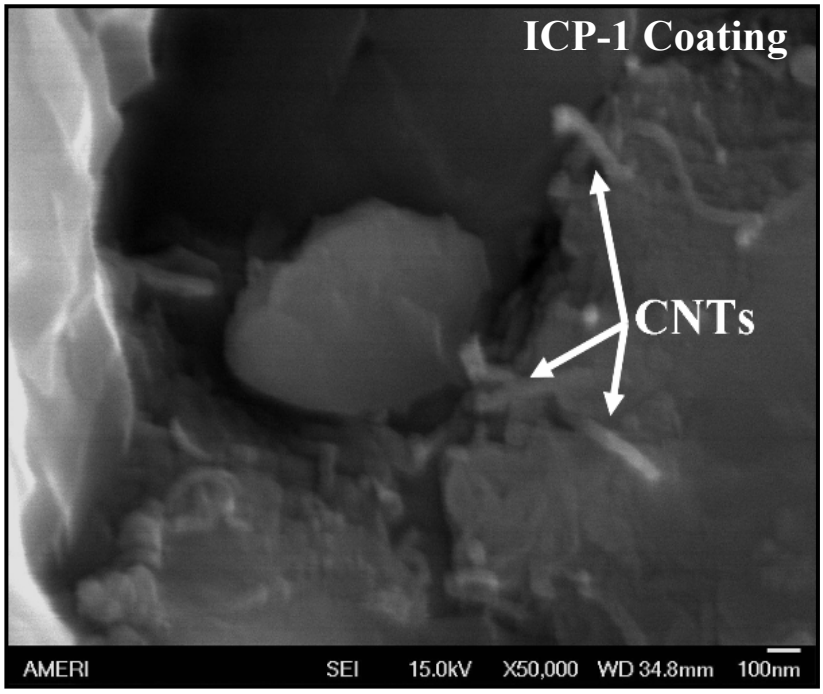

Figure 6.7: SEM image showing fracture surface of ICP-1 coating showing dispersed CNTs in the coating.

Figure 6.8 shows the Raman spectra for the ICP-1 powder and ICP-coating. I_D/I_G ratio was calculated for ICP-1 powder and coating which has been tabulated in Table 6.5. The presence of G peak confirms the retention of undamaged CNTs in the plasma sprayed ICP-1 coating. The I_D/I_G ratio for starting ICP-1 powder is 1.56 which decreased to 0.98 for plasma sprayed ICP-1 coating (Table 6.5). Reduction in I_D/I_G ratio indicates the higher degree of graphitization of CNTs in the ICP-1 coating. Several studies have confirmed the purification and graphitization of CNTs at high temperature [7, 141-144].

Huang et al. [143] performed high temperature (2000°C) annealing of CNT and found that purity

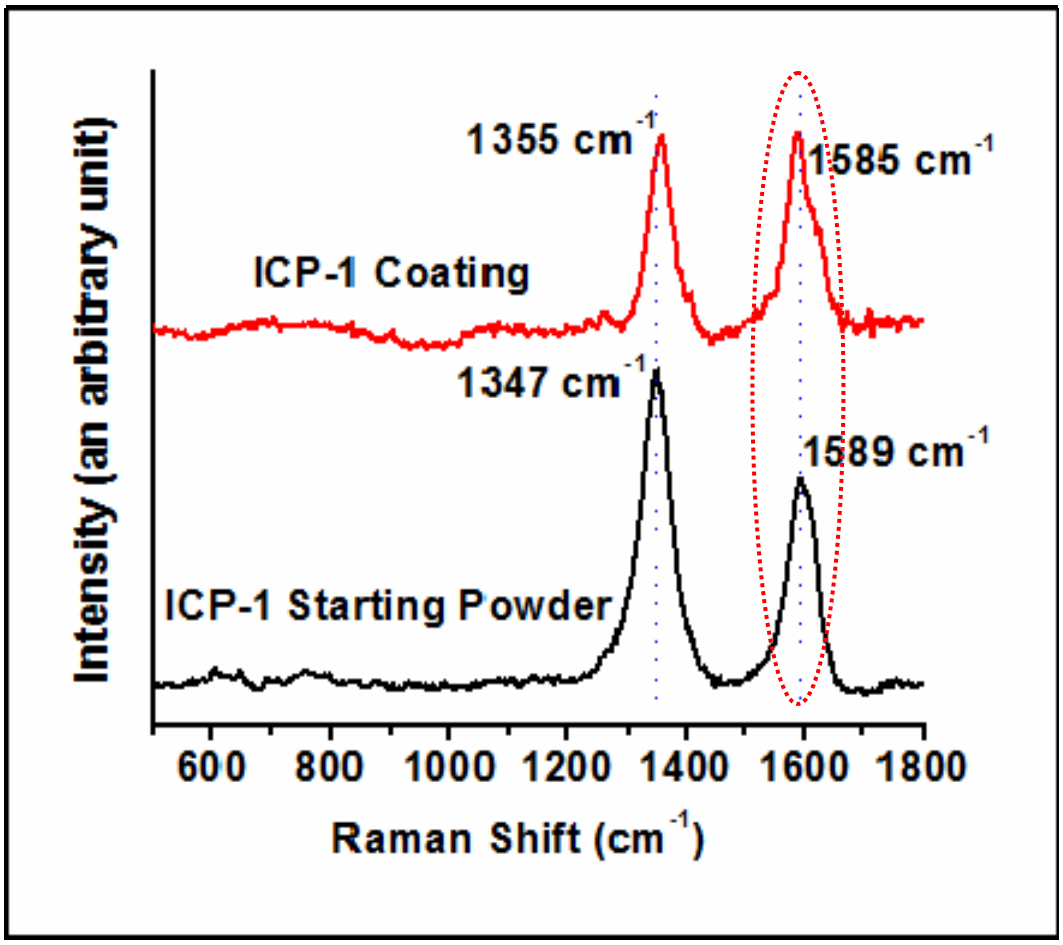

Figure 6.8: Raman spectrum of CVD Al_2O_3 powder and ICP-1 coating. Raman peaks suggest retention of CNTs and enhanced graphitization in the ICP-1 coating.

Table 6.5: Position and ratio of intensity of D and G peaks obtained from Raman Spectroscopy of ICP-1 powder, ICP-1 coating

Sample	**Position of D peaks**	**Position of G peaks**	**I_D/I_G**
ICP-1 Powder	1350	1594	1.56
ICP-1 Coating	1353	1589	0.98

of CNT increased resulting higher degree of graphitization. Figure 6.9a shows the CVD grown CNT with the catalyst particle in ICP-1 powder while Figure 6.9b shows the retained CNT in ICP-1 coating after plasma spraying. Inset image in Figure 6.9a is the IFFT image of CNT indicating the interlayer spacing of 3.86 Å for CVD grown CNT which decreased to 3.58 Å (inset image of Figure 6.9b) for the CNT in plasma sprayed ICP-1 coating.

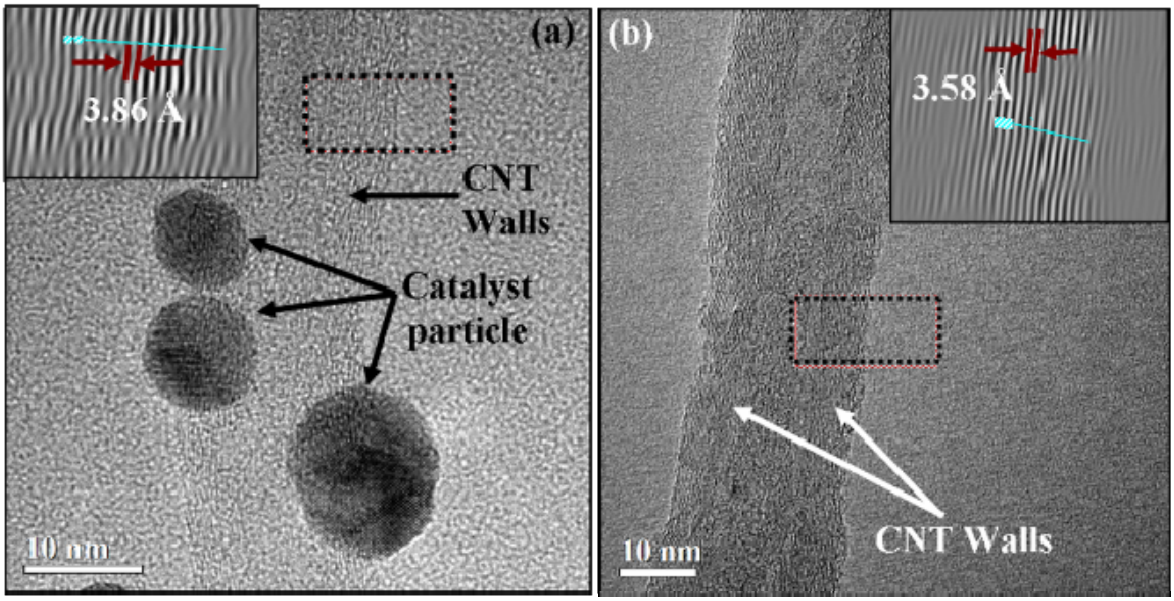

Figure 6.9: HRTEM images of (a) CVD grown CNT with catalyst particle in ICP-1 powder. Inset IFFT image shows the interlayer spacing between the CNT walls is 3.86 Å (b) CNT in plasma sprayed ICP-1 coating. Inset IFFT image shows the interlayer spacing between the CNT walls decreased to 3.58 Å.

To see the reproducibility in graphene wall's contraction, six samples were observed for ICP-1 powder. Similarly, six samples were observed for ICP-1 coating. All

samples exhibited contraction in the graphene wall spacing after the plasma spraying of ICP-1 powder. The average value of graphene wall spacing for CNTs in ICP-1 powder is 3.81± 0.06 Å while it was 3.48± 0.10 Å for CNTs in ICP-1 coating. A similar reduction in the interlayer spacing between the CNT walls (from 3.450 Å to 3.414 Å) was observed on increasing the annealing temperature from 1700°C to 2200°C [142]. This behavior is attributed to the diffusion of carbon atom at high temperature which causes growth of the graphene sheet. The growth of graphene sheet decreases the bulk surface area of the nanotube and ultimately decreases its free energy. To further minimize the free energy, interlayer spacing between the graphene layer contracts due to release of strain energy from highly curved sheet. Hence there is refinement of the graphene shell which ultimately leads to enhanced graphitization of CNT in ICP-1 coating. It is also observed nano-size catalyst particles are not present on the CNT surface in ICP-1 coating, which indicates possible sublimation of the catalyst in high temperature plasma and further refinement of the CNTs (Figure 6.9b).

Purification and graphitization of CNT was not observed in case of spray dried coating after plasma spraying. This is attributed to lower defect ratio of CNT in A4C-SD and A8C-SD powder which has a I_D/I_G ratio of 0.85 as compared to ICP-1 powder which has a high I_D/I_G ratio of 1.56. . Due to presence of high defect ratio of CNT in ICP-1 powder, there is a higher probability of purification at higher temperature as compared to CNTs in A4C-SD or A8C-SD powder which has a smaller defect ratio.

It is expected that uniformly dispersed CNTs in Al_2O_3 coatings synthesized from spray dried and ICP-1 powders will result in higher fracture toughness of coatings. Fracture toughness of coating has been discussed in next chapter.

7. FRACTURE TOUGHNESS OF COATINGS

7.1 Fracture Toughness of Coatings Synthesized from Spray Dried Powder

Fracture toughness of HD and LD coatings were measured using Anstis equation (as shown in Equation 7.1) [135],

$$K_c = \chi\left(\frac{E}{H}\right)^{1/2}\frac{P}{c^{3/2}} \tag{7.1}$$

P is the applied load, E is the elastic modulus, H is the Vickers hardness, c is the radial crack length (measured from center of indent), and χ (=0.016) is the calibration constant. For calculating the fracture toughness of the coating, elastic modulus of the coating was measured using nanoindentation technique in which elastic moduli of HD and LD coatings were mapped using nano dynamic mechanical analyzer (nano DMA). During modulus mapping in nanoDMA mode, a quasi static load (3 μN) is applied to berkovich tip with a dynamic load of 0.5 μN at a fixed frequency (200 Hz). Dynamic load is then analyzed to measure the amplitude and phase shift of the original signal. Equation of motion for sinusoidal force (F_0) can be given as (Equation 7.2)

$$F_0\sin(\omega t) = m\ddot{x} + C\dot{x} + kx \tag{7.2}$$

where m is the mass of sensor, k is the stiffness, and C is the damping of the system.

Displacement response is given as:

$$x = X\sin(\omega t - \phi) \tag{7.3}$$

Solution to the differential equation is as following:

$$X = \frac{F_o}{\sqrt{(k - m\omega^2)^2 + (C\omega)^2}}, \text{ and} \tag{7.4}$$

$$\phi = \tan^{-1} \frac{\omega C}{k - m\omega^2} \tag{7.5}$$

rearranging above equations, k and C can be found by:

$$k = \frac{F_0}{X} \frac{1}{\sqrt{1 + \tan^2 \phi}} + m\omega^2 \tag{7.6}$$

$$C = \sqrt{\frac{\left(\frac{F_0}{X}\right)^2 \tan^2 \phi}{1 + \tan^2 \phi}} \frac{1}{\omega} \tag{7.7}$$

Storage modulus (E') and loss modulus (E") can be calculated as following:

$$E' = \frac{k_s \sqrt{\pi}}{2\sqrt{A_c}} \tag{7.8}$$

$$E'' = \frac{\omega C_s \sqrt{\pi}}{2\sqrt{A_c}} \tag{7.9}$$

where, A_c is the contact area, which is dependent on the contact depth. Contact depth of the indenter is described through tip area function during instrument calibration.

Wide area (5μm x 5 μm) was selected for modulus mapping in order to see the role of CNT content and dispersion in contribution towards improved modulus of the plasma sprayed coatings. Instead of complex modulus, storage modulus has been taken as direct representative of the elastic modulus considering insignificant plastic deformation in ceramics. The storage modulus histograms from an average of 50,000 tests for HD and LD coatings are shown in Figure 7.1. Figures 7.1a-c show the storage modulus histograms for HD-A-SD, HD-A4C-SD, HD-A8C-SD coatings respectively. Figures 7.1d-f shows the storage modulus histograms for LD-A-SD, LD-A4C-SD,

LD-A8C-SD coatings respectively. Compared to HD coatings, the average elastic modulus of LD coatings shifted towards lower values which

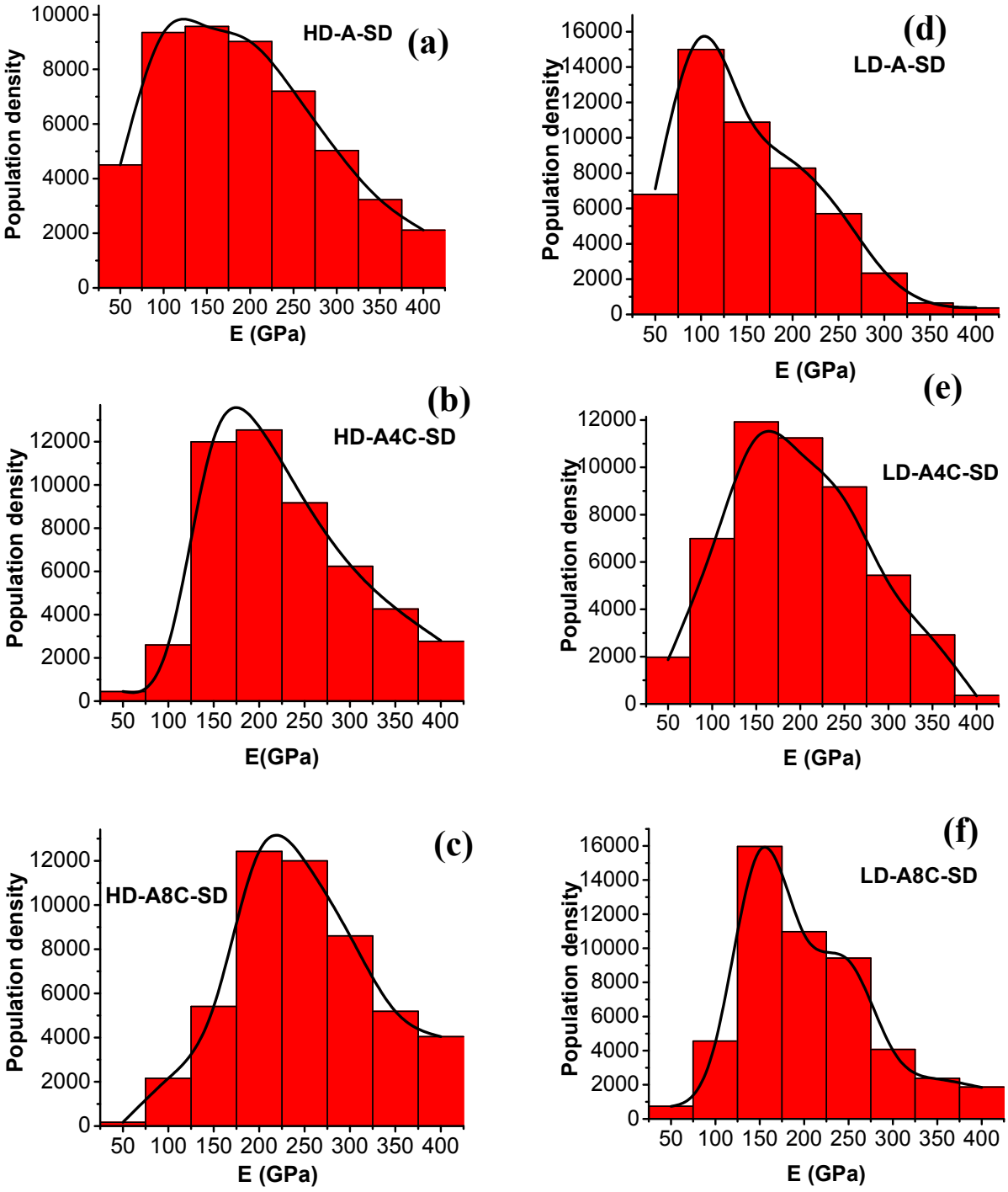

Figure 7.1: Storage modulus distribution for (a) HD-A-SD (b) HD-A4C-SD (c) HD-A8C-SD (d) LD-A-SD coating (e) LD-A4C-SD coating (f) LD-A8C-SD coating

is attributed to relatively higher porosity content in LD coatings (Table 6.1) as compared to HD coatings. Comparing among HD coatings, the average modulus for both CNT reinforced coating shifted to higher value than HD-A-SD coating, showing the reinforcement effect of dispersed CNTs. Higher average modulus of HD-A8C-SD (~227 GPa) coating than HD-A4C-SD coating (~180 GPa) is due to higher CNT content. Similar results are obtained for LD coatings. The increase in elastic modulus of CNT reinforced coatings is attributed to three major factors (i) higher elastic modulus of CNT (~1 TPa) [4, 7, 8, 26, 31, 38] (ii) homogeneous dispersion of CNT in the matrix ((iii) and relatively lower porosity in the coating (Table 6.3). Localized high values of modulus are attributed to the presence of CNTs at that location. The average value of elastic modulus for all coatings is tabulated in Table 7.1, which has been used for computing the fracture toughness.

Table 7.1: Average elastic modulus of HD and LD coatings obtained from nanoindentation technique in modulus mapping mode.

Elastic Modulus (GPa) of coatings			
	A-SD	**A4C-SD**	**A8C-SD**
HD Coating	**170±90**	**203±79**	**227±76**
LD coating	**129±70**	**173±74**	**180±78**

Fracture toughness was calculated using indentation cracking technique. Vickers indentation at 4 kg load was performed to develop the cracks in the coatings. Figures 7.2a-c show the Vickers indentations on the cross-section of HD-A-SD, HD-A4C-SD,

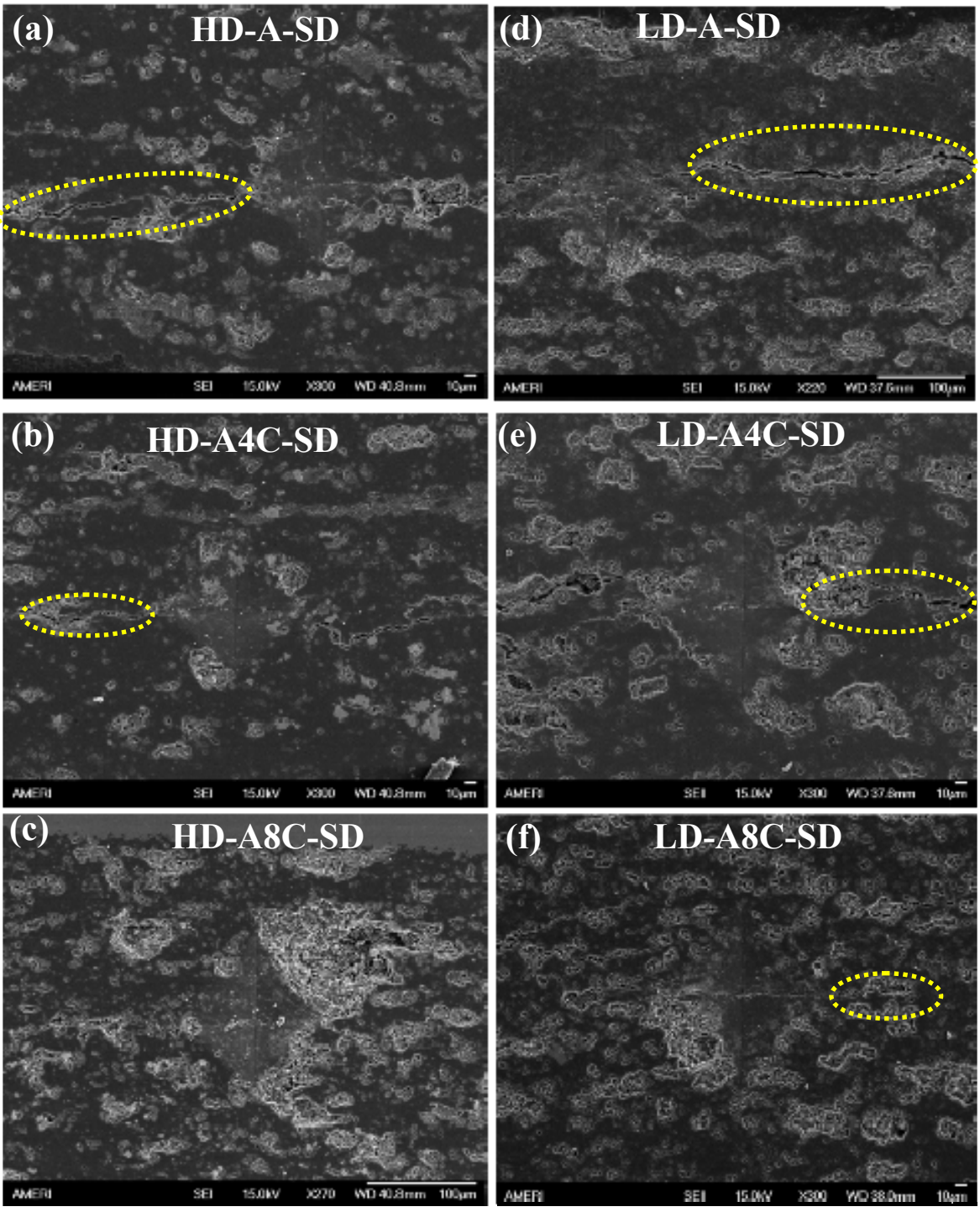

Figure 7.2: SEM image of Vickers indent at 4 kg load for (a) HD-A-SD, (b) HD-A4C-SD, (c) HD-A8C-SD, (d) LD-A-SD, (e) LD-A4C-SD, and (f) LD-A8C-SD coatings. All coatings showed radial cracks except HD-A8C-SD coating.

and HD-A8C-SD coatings respectively. Figures 7.2d-f shows the Vickers indentations on the cross-section of LD-A-SD, LD-A4C-SD, LD-A8C-SD coatings respectively. It is clearly seen in Figure 7.2 that large cracks developed in all LD coatings as compared to all HD coatings. No cracks were observed for HD-A8C-SD coating in Figure 7.2c. Indent edges in HD-A8C-SD coating were further magnified to observe if fine cracks developed in the coating. Figure 7.3 shows the high magnification SEM image of the indent corner on the cross section of HD-A8C-SD coating which shows a very fine radial crack (encircled).

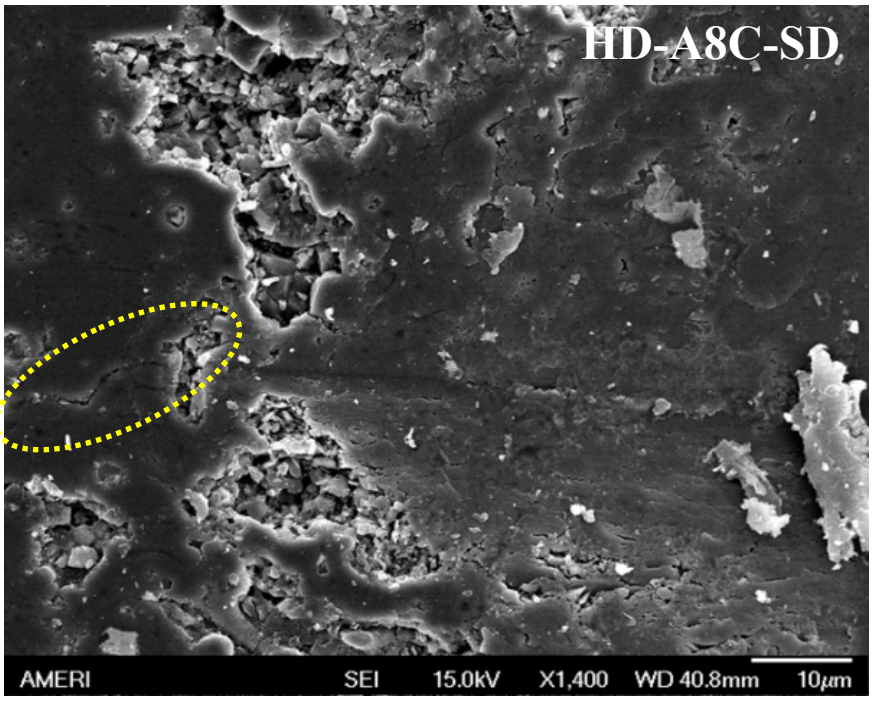

Figure 7.3: High magnification SEM image of Vickers indent at 4 kg load for (a) HD-A-8C-SD coating showing fine radial crack.

This is a clear indicator of the highest toughness of HD-A8C-SD coating. Table 7.2 summarizes the Vickers microhardness of HD and LD coatings. The relative improvement in microhardness value for HD coatings as compared to corresponding LD coatings of the same composition is attributed to lower porosity in HD coatings.

Table 7.2: Vickers microhardness of the HD and LD coatings

Microhardness (VHN) of HD and LD Coatings			
	A-SD	**A4C-SD**	**A8C-SD**
HD Coatings	1498±62	1606±53	1670±41
LD Coatings	1198±79	1345±59	1456±67

Comparing among HD coatings, there is ~7% and ~11% increase in the microhardness of HD-4C-SD and HD-A8C-SD coatings respectively as compared to HD-A-SD coating. Similarly, there is ~12%, and ~22% increase in the microhardness of LD-A4C-SD and LD-A8C-SD coatings respectively as compared to LD-A-SD coating. Improvement in the microhardness in CNT reinforced HD and LD coatings is attributed to the enhanced indentation resistance by presence of CNTs. Microhardness values listed in Table 7.2 have been used for calculating the fracture toughness of coating.

Fracture toughness values of HD and LD coatings are presented as bar chart in Figure 7.4. Fracture toughness of HD-A-SD, HD-A4C-SD and HD-A8C-SD coatings improved by 38, 36% and 73% respectively as compared to corresponding composition

among LD coatings. Highest improvement (~73%) in fracture toughness of HD-A8C-SD coating is attributed to the lowest porosity (~3%) in the coating. Equation 7.10 shows the exponential dependence of fracture toughness on the porosity [145].

$$K_{IC} = K_{ICd} e^{-bp} \tag{7.10}$$

K_{IC} is the fracture toughness (MPa.m$^{1/2}$), K_{ICd} is the fracture toughness for fully dense material, p is the apparent porosity in the material and b is the material constant.

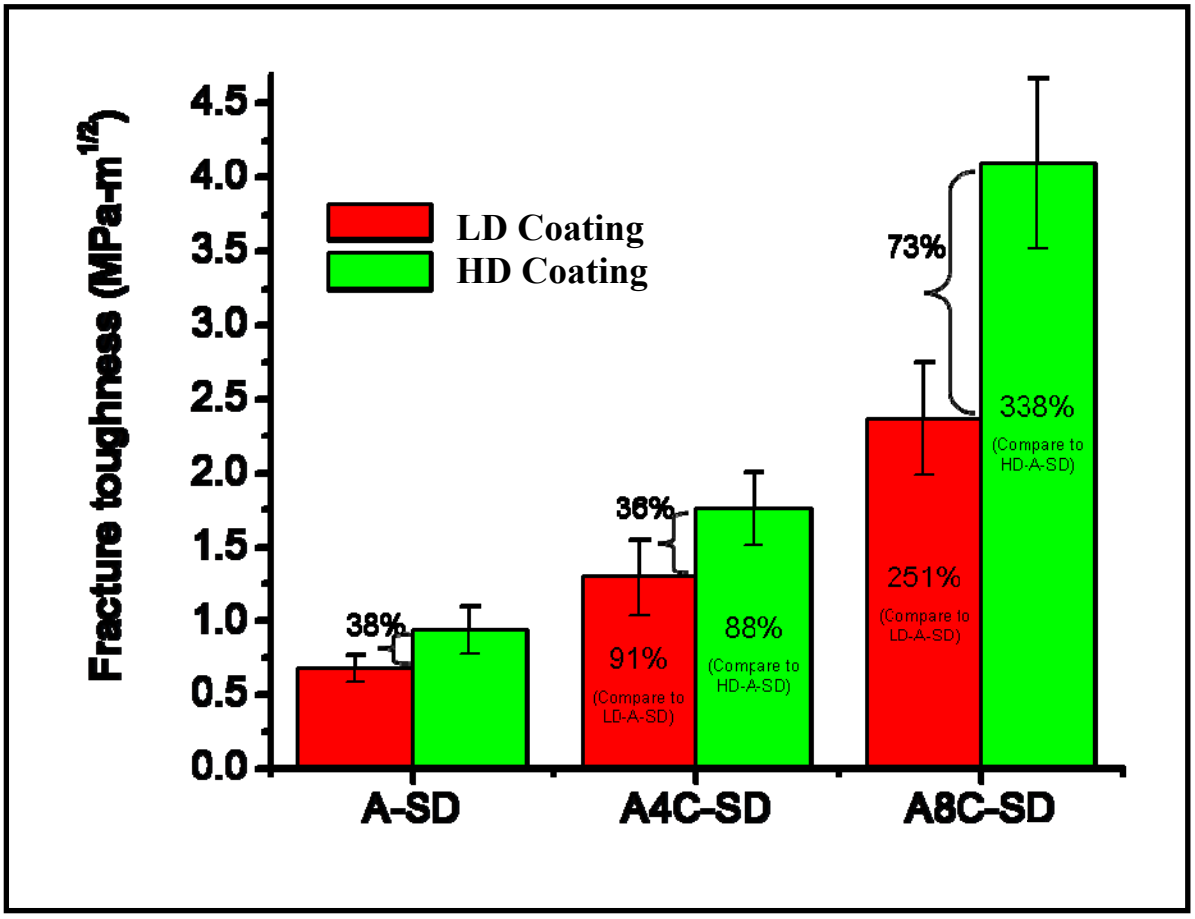

Figure 7.4: Fracture toughness of HD and LD coatings calculated using indentation cracking technique.

High and low density coatings exhibit improvement in the fracture toughness with an increasing CNT content. Among HD coatings, fracture toughness of HD-A8C-SD coating displayed tremendous improvement (~338 %) as compared to HD-A-SD coating. Among LD coatings, fracture toughness fracture toughness of LD-A8C-SD coating improved by ~251 % as compared to LD-A-SD coating. Several attempts have been made for enhancing the fracture toughness of Al_2O_3 by reinforcement of CNT. . Siegel et al. [36] reported that addition of 10 vol. % CNT to monolithic Al_2O_3 could lead to 24% increase in fracture toughness value while Zhang et al. [58] reported the 21.1% increase in fracture toughness by reinforcing 7.39 wt. % CNT to Al_2O_3. Balani et al. [4] from our research group showed improvement of 57% in fracture toughness by 8 wt. % CNT addition to Al_2O_3. However, synthesized Al_2O_3-8 wt. % CNT coating in their study was 94% dense [4]. In the present work the relative density of HD-A8C-SD coating is 96.5%, which has been achieved by optimizing the plasma processing parameters.

Significant improvement in the fracture toughness of CNT reinforced coatings is attributed to combined effect of lower porosity and excellent dispersion of CNTs in the Al_2O_3 matrix that promotes toughening mechanisms. SEM investigation inside the indentation crack elucidates the toughening mechanisms offered by CNTs. Figures 7.5a-b are high magnification SEM images within cracks of HD-A4C-SD and HD-A8C-SD coatings respectively. Figures 7.5c-d display high magnification SEM images of the cracks in LD-A4C-SD and LD-A8C-SD coatings respectively. CNT bridging between the splats resists the crack widening and propagation, and hence, contributes towards the toughening of CNT reinforced coating. Uniformly dispersed CNTs in Al_2O_3 matrix can

provide multiple sites of anchoring and bridging the splats resulting in uniform toughening. Crack deflection at CNT/Al_2O_3 interface is also observed in HD-A8C-SD and LD-A8C-SD coatings. Figure 7.6 shows that crack deflects to another direction after it interacts with CNT bridges. Such deflection results in dissipation of crack energy resulting in improved fracture toughness.

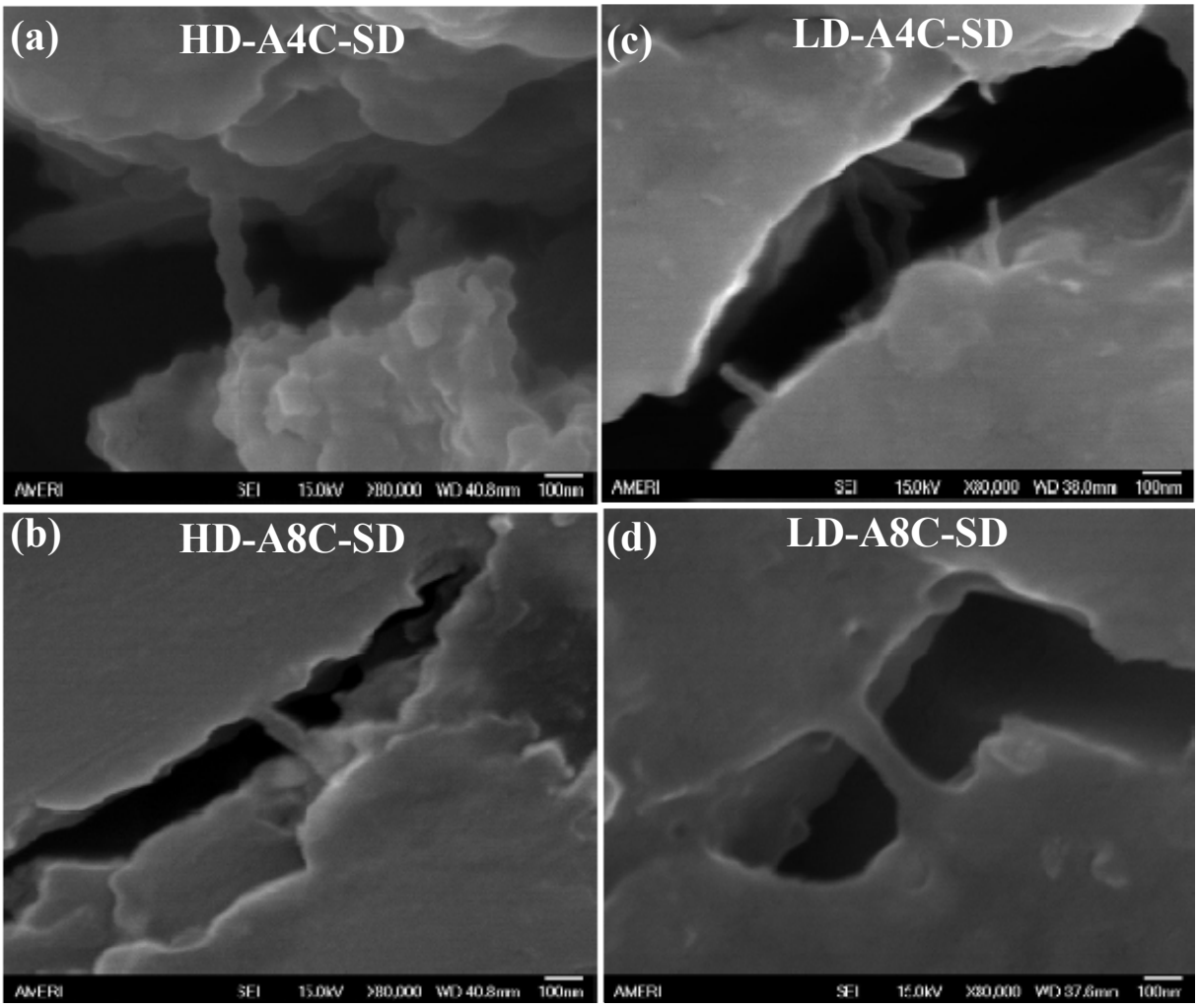

Figure 7.5: High magnification SEM image within the crack for (a) HD-A4C-SD coating (b) HD-A8C-SD coating (c) LD-A4C-SD coating (d) LD-A8C-SD coating showing CNT bridging inside the crack.

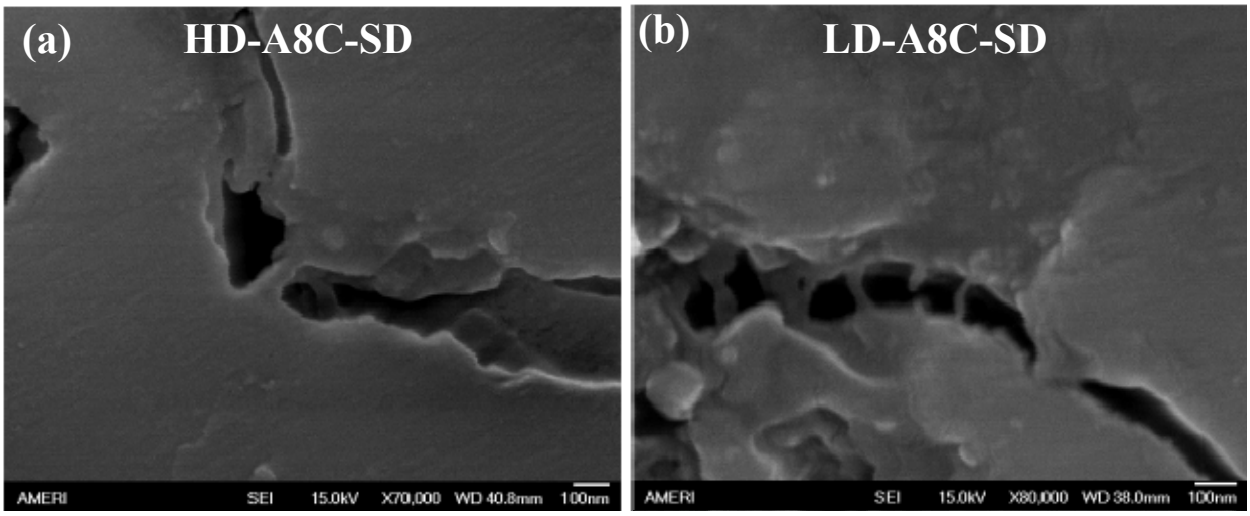

Figure 7.6: Crack deflections at Al_2O_3-CNT interface for (a) HD-A8C-SD coating (b) LD-A8C-SD coating

Figure 7.7 is the direct correlation between the porosity content,, CNT content and fracture toughness of HD and LD coatings. A percentage value inside the pyramid represents the porosity content in the coating. The effect of porosity on fracture toughness is observed along the x-axis. The combined effect of porosity and CNT reinforcement on fracture toughness can be seen along y-axis for HD and LD coatings in Figure 7.7. This clearly indicates that lower porosity in the coating in conjunction with uniformly dispersed CNT in the matrix plays an important role in enhancing the fracture toughness of coating. Fracture toughness of the ICP-1 coating was also evaluated which is explained in the following section.

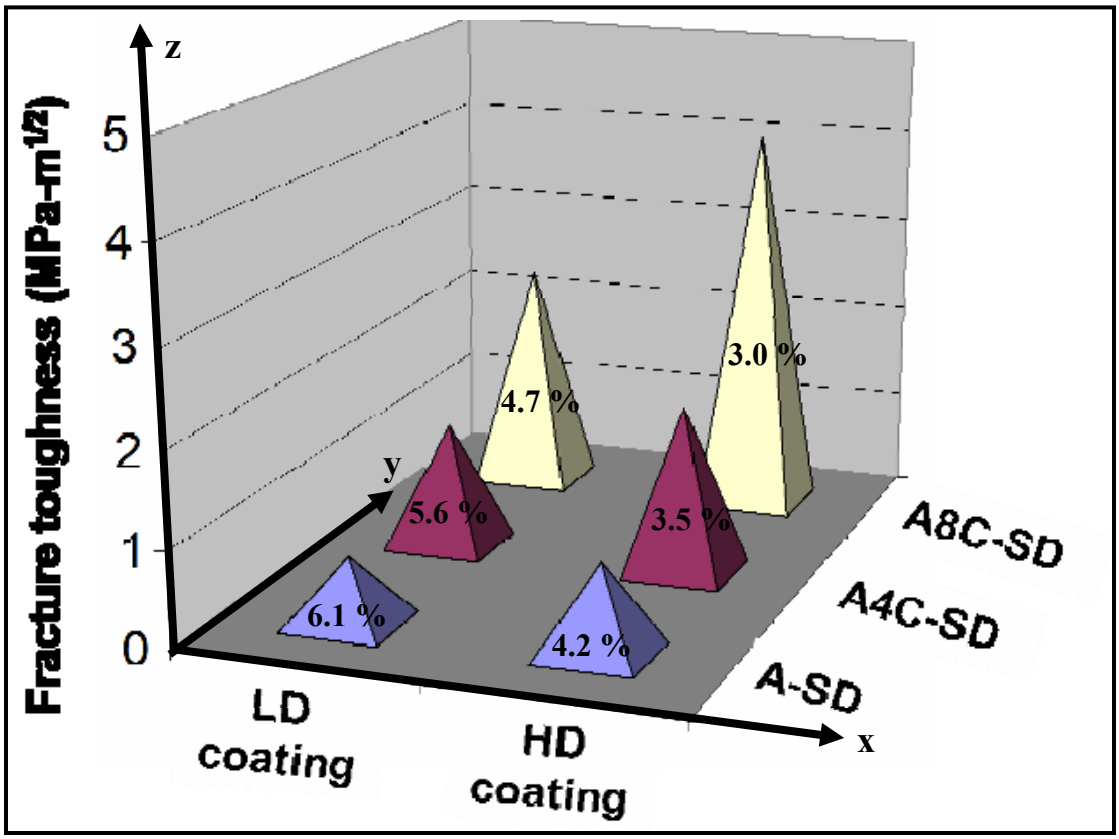

Figure 7.7: Effect of porosity and CNT reinforcement on fracture toughness of HD and LD coating. Percentage value shown inside the pyramid represents the porosity in the coating.

7.2 Fracture Toughness of ICP-1 Coating

Fracture toughness of ICP-1 coating was also measured using Anstis equation based upon the radial crack generation during Vickers indentation. Elastic modulus was calculated from the load-displacement curve obtained during Vickers indentation. An increase in 27% in elastic modulus value was observed for ICP-1 coating which is attributed to uniform dispersion of CNTs in Al_2O_3 matrix and strong bonding between

Al_2O_3/CNT. Strong bonding between matrix/reinforcement assists load transfer from the matrix to reinforcement and hence resists the selective elastic deformation of the matrix. An increase in 15% in microhardness value of ICP-1 coating was observed which is due to enhanced indentation resistance by CNT reinforcement to Al_2O_3 matrix. Elastic modulus and hardness obtained from Vickers indentation was used in calculating the fracture toughness of ICP-1 coating. An increase in 24% in relative fracture toughness of ICP-1 coating was observed by mere 1.5 wt. % CNT reinforcement. It should be recalled that relative improvement of 88% was observed by 4 wt. % CNT addition to Al_2O_3 matrix in HD-A4C-SD coating (Figure 7.4). A mere 1.5 wt. % CNT content in ICP-1 coating resulted in significant improvement in fracture toughness which is attributed to superior degree of CNT dispersion on each Al_2O_3 particle that promotes following toughening mechanisms: (i) crack bridging by CNT (ii) crack deflection at CNT interface (iii) strong CNT-Al_2O_3 interface.

Figure 7.8a shows the SEM image of the indent on ICP-1 coating showing the radial cracks generated at 4 kg load. Figure 7.8b shows the high magnification image within the crack which clearly shows the CNT bridging between the splats that resists the crack widening and hence contribute towards the toughening of ICP-1 coating. Figure 7.9 shows the CNT bridging between the Al_2O_3 splats. Thickening of the CNT diameter to ~100 nm (CVD grown CNT diameter: 15-50 nm) indicates the formation of Al_2O_3 layer on CNT surface. During plasma spraying, molten Al_2O_3 spreads over CNT surface by capillary action and freezes instantaneously due to very rapid cooling rate.

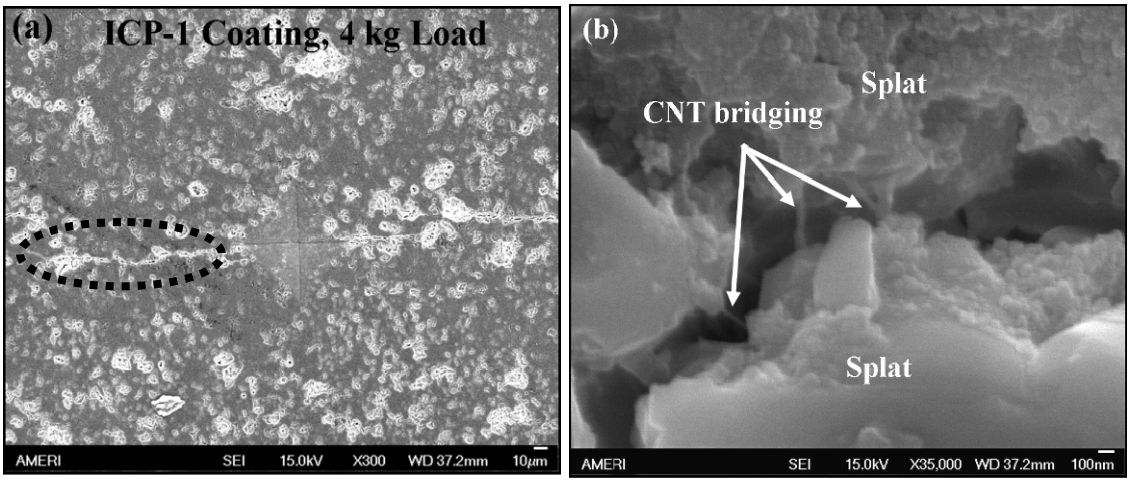

Figure 7.8: (a) SEM image of Vickers indent on ICP-1 coating at 4 kg load showing radial cracks (b) SEM image shows CNT bridging inside the crack.

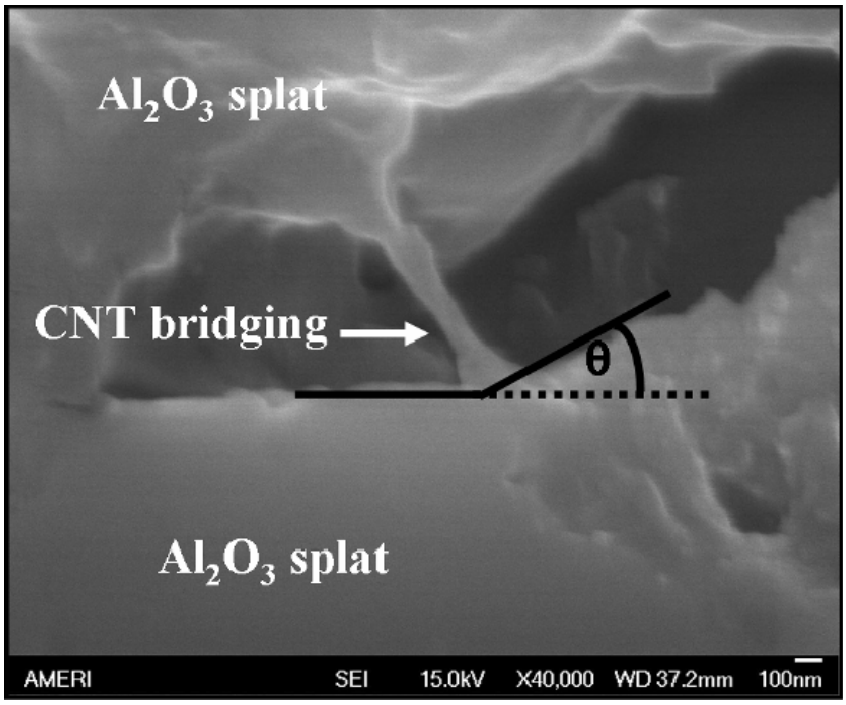

Figure 7.9: Crack deflection at the CNT bridge

(~4.6 *10^6 Ks^{-1}). Balani et al. [27] studied the wetting of CNT by molten Al_2O_3 and found coating formation on the CNT surface. Further, Figure 7.9 shows that a crack propagates to CNT and then deflects to another direction. The crack deflection angle (θ) was measured as 25 degree. Uniform dispersion of CVD grown CNTs on each Al_2O_3 particle and high surface area of CNT imparts uniform sites for energy release rate and high fracture toughness of ICP-1 coating.

In addition to crack bridging and crack deflection, strong CNT-Al_2O_3 interface is also regarded as another toughening mechanism. The bonding/interaction between CNT and matrix play an important role in stress transfer from the matrix to the CNT which ultimately affects the mechanical properties [7]. Figure 7.10a shows the TEM image of CNT-Al_2O_3 interface with corresponding SAED pattern as inset showing presence of α-Al_2O_3 phase. Figure 7.10b shows the high magnification HRTEM image of CNT-Al_2O_3 interface with lattice distortion. Lattice spacing of 2.165 Å corresponds to (006) plane of α-Al_2O_3. Inset in Figure 7.10b is the Fast Fourier transformed (FFT) image of the rectangular region which indicates the distortion of the lattice upon interaction with CNT. The interfacial lattice distortion suggested a possible reaction as presented in equation 7.11.

$$2Al_2O_3 + 6C \rightarrow Al_4C_3 + 3CO_2 \qquad (7.11)$$

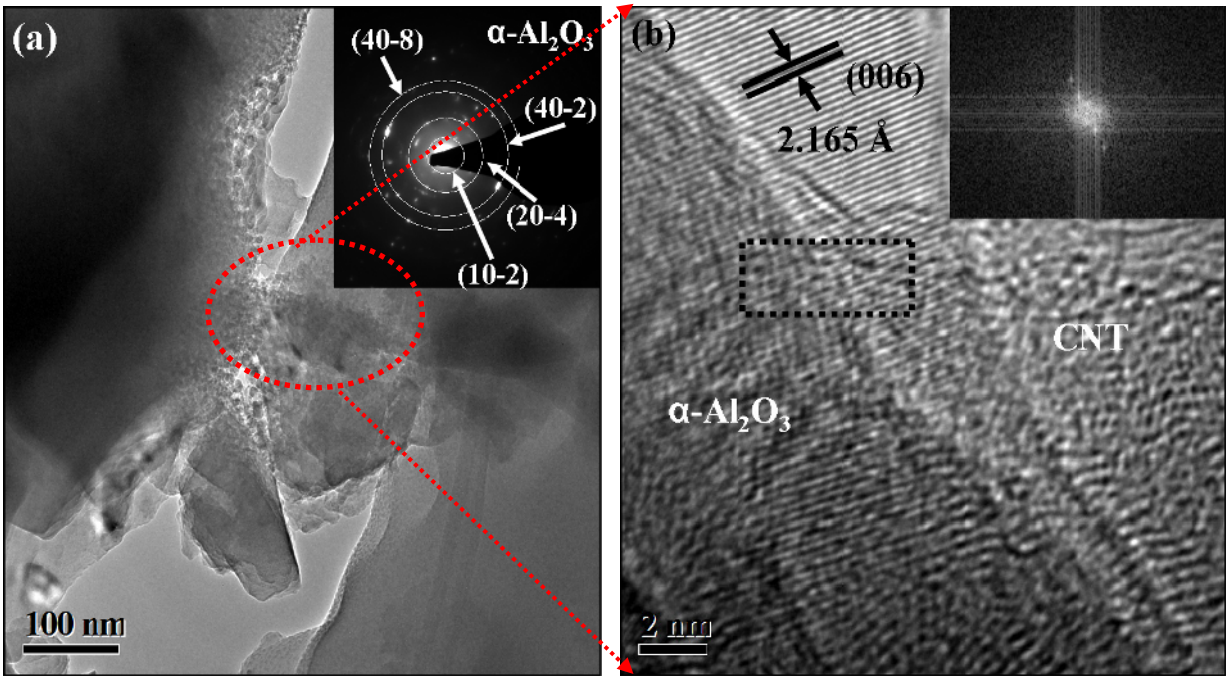

Figure 7.10: (a) TEM images of plasma sprayed ICP-1 coating shows the Al_2O_3-CNT interface. Inset image shows the SAED pattern indicating alpha alumina phase. (b) High magnification HRTEM image of Al_2O_3-CNT interface showing strong interaction between CNT and Al_2O_3. Inset image is the FFT image of the lattice structure showing overlap between CNT and Al_2O_3

Thermodynamic activity of Al_4C_3 (~6.89×10^{-19} at 2200 K, near the melting point of Al_2O_3) is very low, as computed from FactSage thermochemistry software [146]. Gibbs free energy of formation of Al_4C_3 is 700.2 kJ and 558.4 kJ at 2200 K and 2500 K respectively. These macroscopic thermodynamic computations suggest that no stable reaction product form between Al_2O_3 and C. However, atomic level interaction at Al_2O_3–CNT interface and pseudo-bonding between aluminum and carbon atoms has been confirmed by performed ab-initio studies [27]. Hence, it can be concluded that there is a

strong interaction between CNT and Al_2O_3 at the atomic interface which could contribute towards the toughening mechanism of the ICP-1 coating.

Similar toughening mechanisms (crack bridging by CNT, crack deflection at CNT/Al_2O_3 interface) were observed in both SD and ICP-1 coatings. But 24% improvement in the fracture toughness of ICP-1 coating by mere 1.5 wt. % CNT addition was very significant as compared to SD coatings and it attributed to uniform degree of CNT dispersion. It is recalled here, due to limitation of large scale synthesis of ICP-1 powder, optimization of plasma parameters were done on spray died powder and not on ICP-1 powder. It is envisaged that, optimized parameters for ICP-1 powder in conjunction with excellent CNT dispersion on each of the Al_2O_3 particle will lead to much enhanced fracture toughness of the coating.

Tribological behavior of coatings is dependent upon the material properties (E, H, K_{IC}), which is evident from Evans and Marshall equation [110] (represented as Equation 7.12).

$$V = P_n^{1.125} K_c^{-0.5} H^{-0.625} \left(\frac{E}{H}\right)^{0.8} S \qquad (7.12)$$

where, V is the wear volume (m^3), P_n is applied load (MPa), K_c is fracture toughness, H is the hardness, E is the elastic modulus (GPa) and S is the sliding distance (m). Tribological behavior of SD and ICP-1 coatings has also been evaluated at room and high temperature which will be discussed in the next two chapters.

8. ROOM TEMPERATURE TRIBOLOGICAL BEHAVIOR

8.1 Tribological Behavior of Coatings Synthesized from Spray Dried Powder

Figure 8.1 shows the cumulative wear weight loss as a function of sliding distance at a normal load of 30 N for high density (HD-A-SD, HD-A4C-SD, HD-A8C-SD) and low density (LD-A-SD, LD-A4C-SD, LD-A8C-SD) coatings. The cumulative wear weight loss increases with the increasing sliding distance and decreases with increasing CNT content for both type of coatings. Higher wear weight loss was observed for all compositions of LD coatings as compared to HD coatings.

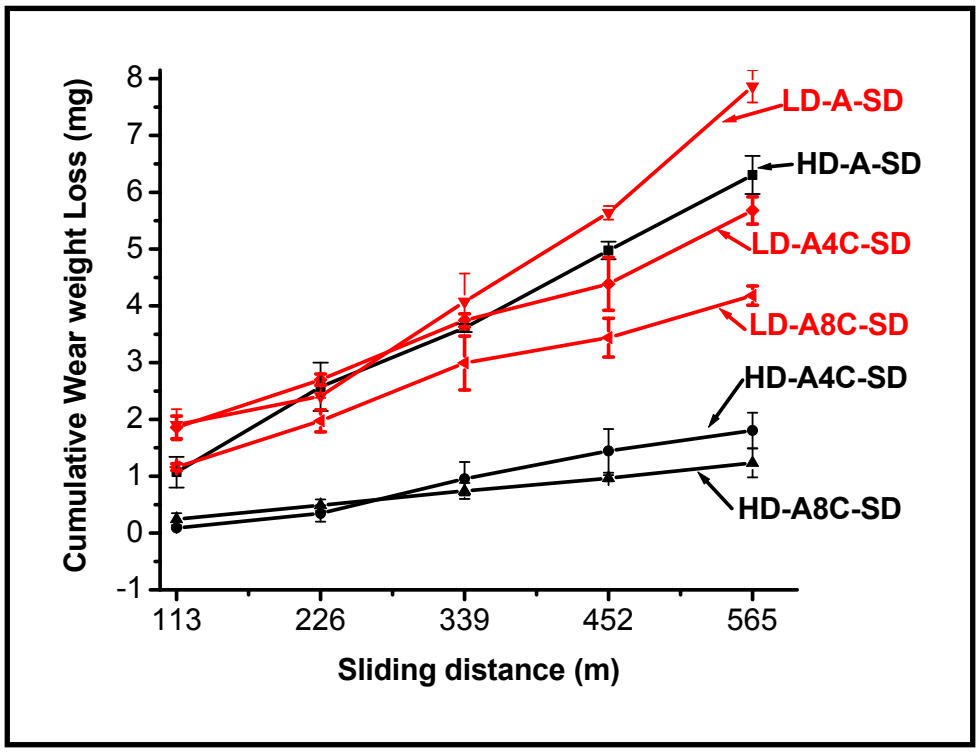

Figure 8.1: Cumulative wear weight loss of HD and LD coatings as function of sliding distance at normal load of 30N

Cumulative wear weight loss (at 565 m sliding distance) as a function of CNT content has been plotted in Figure 8.2. From Figure 8.2, following observations has been made.

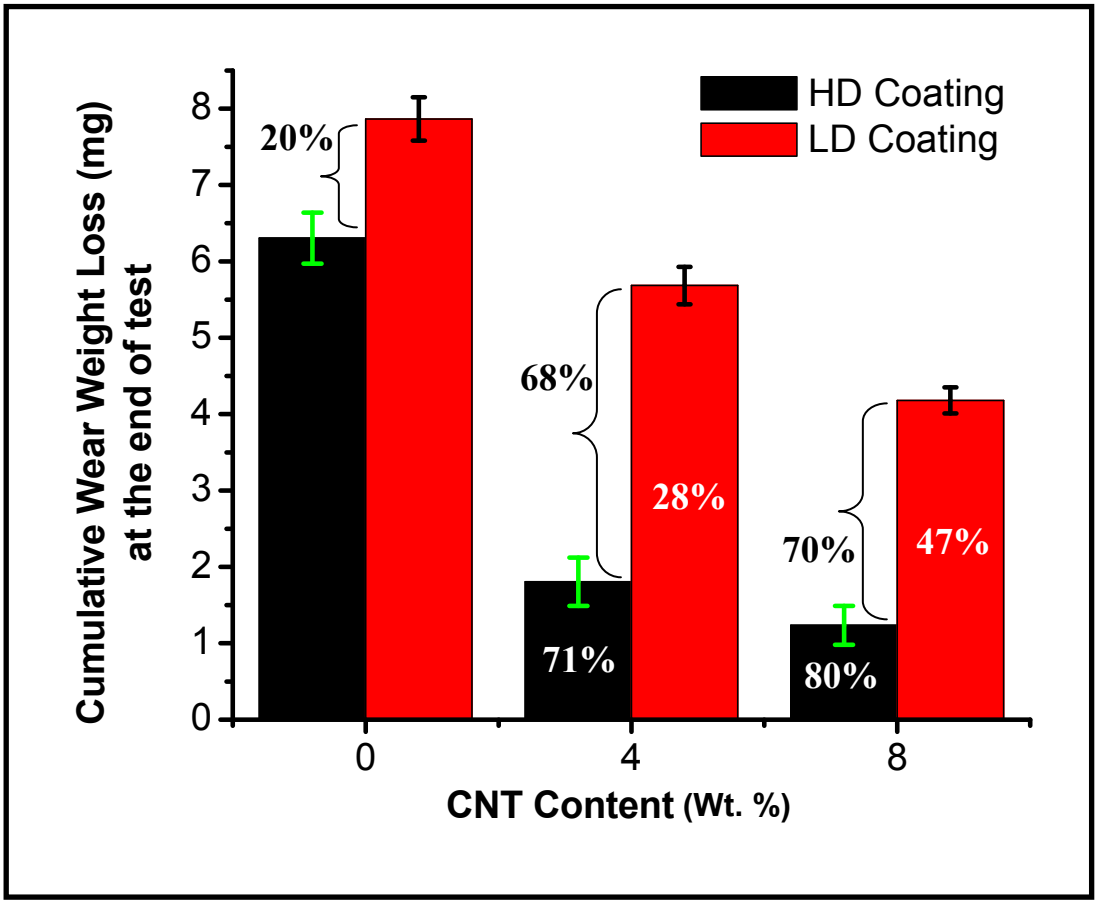

Figure 8.2: Cumulative wear weight loss of HD and LD coating as function of CNT content after the linear sliding distance of ~565 meters and at normal load of 30 N.

There is ~71% and ~80% improvement in the wear resistance of HD-A4C-SD and HD-A8C-SD coatings respectively as compared to HD-A-SD coating. Similarly, there is an improvement of ~28% and ~47% in the wear resistance of LD-A4C-SD and LD-A8C-SD coatings respectively as compared to LD-A-SD coating. Comparing between HD and LD coatings, there is an improvement of ~20% in wear resistance of HD-A-SD coating as

compared to LD-A-SD coating. HD-A4C-SD and HD-A8C-SD coatings displayed ~68% and ~70% improvement respectively as compared to low density coatings of similar compositions. It can be concluded that lower amount of porosity in the coating and CNT reinforcement to matrix enhances the wear resistance of plasma sprayed coatings when sliding against silicon nitride (Si_3N_4) counter body.

SEM observation of wear tracks was carried out to identify the wear mechanism in HD and LD coatings. Figure 8.3a-c shows the micrograph of wear surface of HD-A-SD, HD-A4C-SD and HD-A8C-SD coatings whereas Figure 8.3d-f represents the wear surface of LD-A-SD, LD-A4C-SD and LD-A8C-SD coatings. Wear surface of all coatings show rough surface. In addition, wear surface of all coatings show discontinuous smooth thin film, which is attributed to a possible tribochemical reaction. Tribochemical reaction has a critical role in wear behavior of ceramic material [147]. Formation of smooth, thin protective layer as result of tribochemical reaction can reduce the wear of coating surface against sliding [112, 147, 148].

Elemental X-ray mapping of the worn surface was carried out to identify the composition of the thin film. Figures 8.4a-c show the elemental X-ray maps of worn surface of HD-A-SD, HD-A4C-SD and HD-A8C-SD coating respectively. Figure 8.4a1, b1, c1 are the back scattered images of wear track of HD-A-SD, HD-A4C-SD and HD-A8C-SD coating respectively. Figures 8.4a2-a5 shows the distribution of silicon, aluminum, oxygen and nitrogen respectively. Figures 8.4b2-b6 and 8.4c2-c6 show the distribution of silicon, aluminum, oxygen, nitrogen and carbon. Presence of silicon and

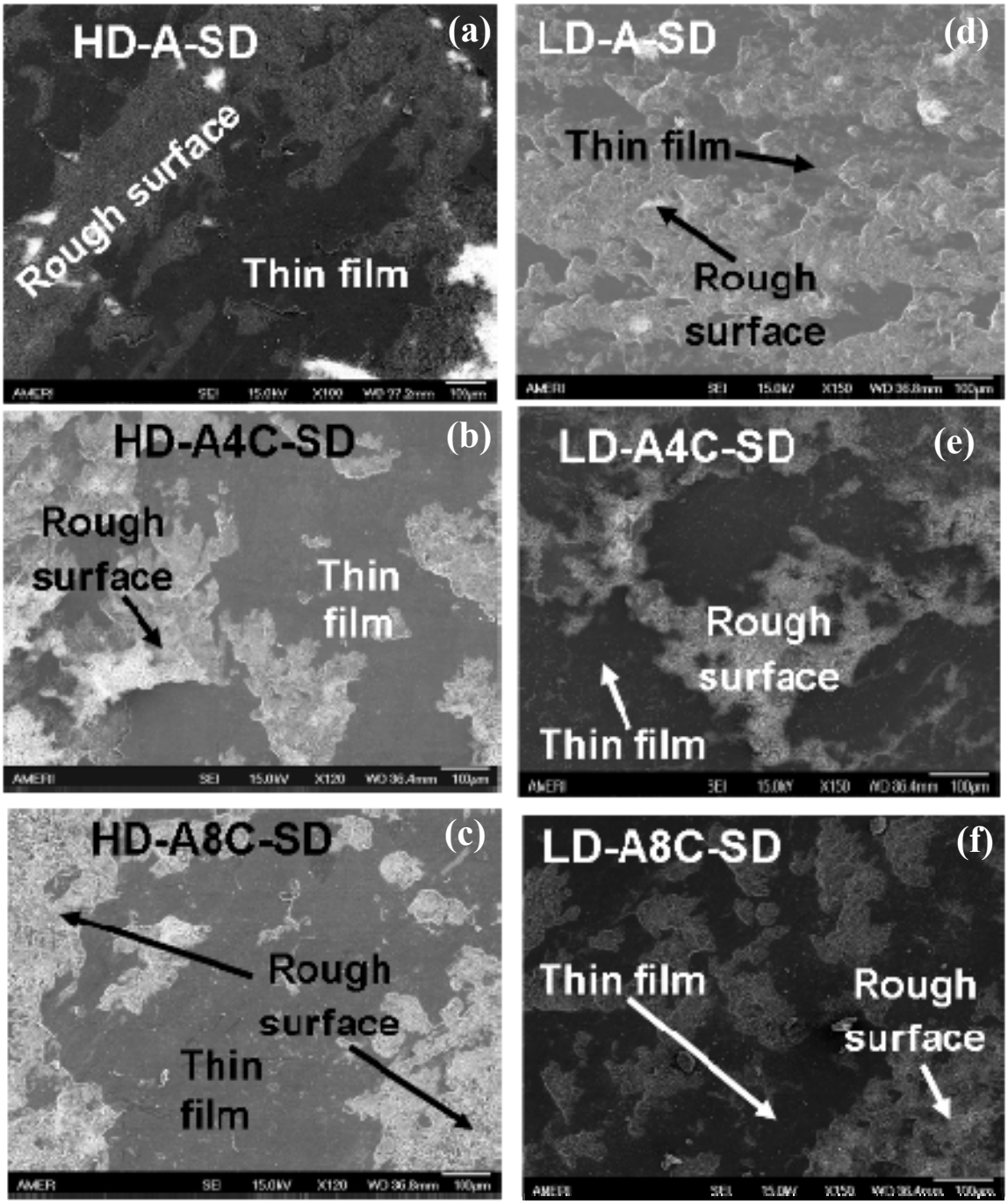

Figure 8.3: Wear surface topography after the linear sliding distance of ~565 meters and at normal load of 30 N for (a) HD-A-SD coating (b) HD-A4C-SD coating (c) HD-A8C-SD coating (d) LD-A-SD coating (e) LD-A4C-SD coating (f) LD-A8C-SD coating

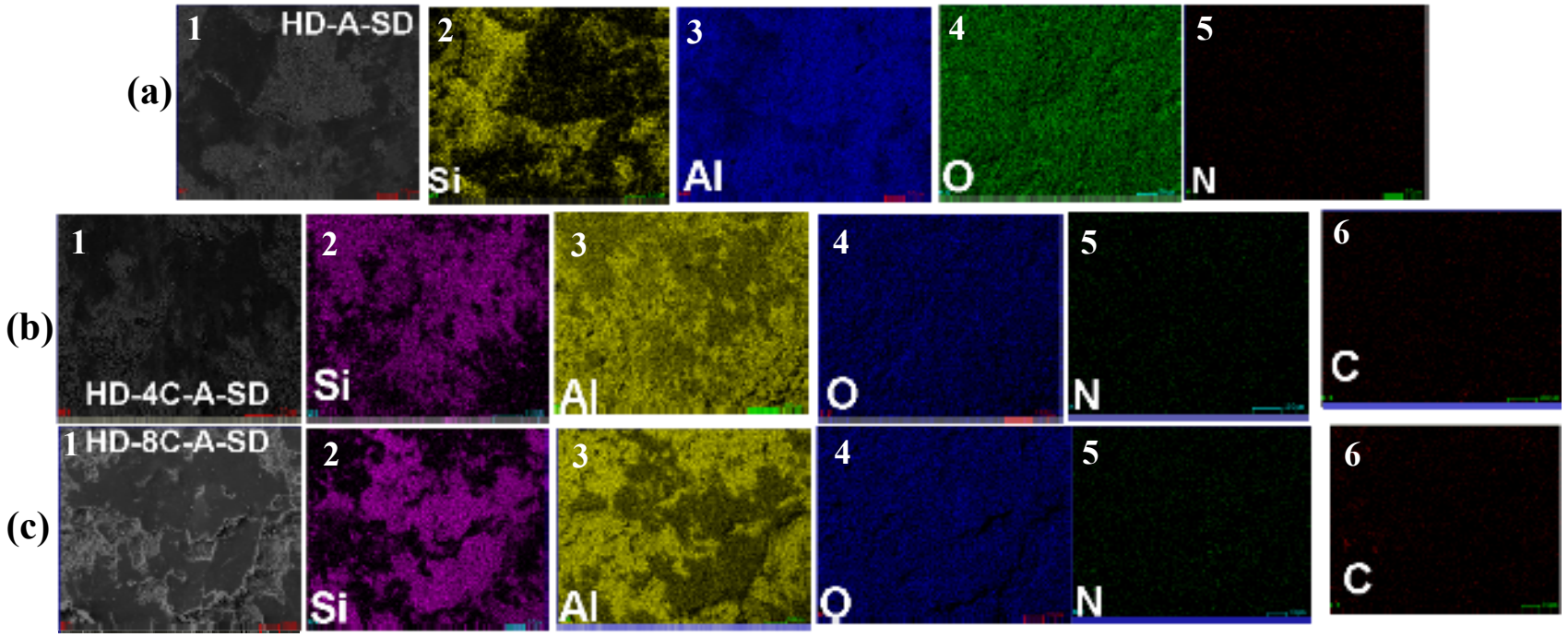

Figure 8.4: X-ray maps of wear track of (a) HD-A-SD coating (b) HD-A4C-SD coating (c) HD-A8C-SD coating. a1, b1, c1 are the back scattered image of wear track of HD-A-SD, HD-A4C-SD and HD-A8C-SD coatings respectively. a2-a5 shows the distribution of silicon, aluminum, oxygen and nitrogen respectively while b2-b6 and c2-c6 shows the distribution of silicon, aluminum, oxygen, nitrogen and carbon respectively.

nitrogen in the worn surface is as a result of transferred oxidation product of silicon nitride ball. In numerous studies [112, 147, 148], room temperature oxidation of Si_3N_4 is reported in the presence of moisture. Similar elemental X-ray mapping results were obtained for LD coatings but are not included here.

Lin et al. [112] studied the tribological behavior of titanium oxide (TiO_2) reinforced Al_2O_3 (Al_2O_3-3 wt. % TiO_2) coating against Si_3N_4 ball from room temperature to 873 K. They found that wear rate of coating was too small to be measured accurately at the room temperature and increased (~5.5×10^{-5} mm^3/Nm) with the increase in the temperature. Improved wear resistance at room temperature was attributed to the formation of protective silicon oxide (SiO_2) layer on the wear track. This protective SiO_2 layer was the result of the oxidation of Si_3N_4 (counter body) ball in the presence of the moisture. It was observed that, with the increasing temperature, the absorption tendency of moisture on the worn surface decreased and there was no more protective SiO_2 layer resulting in higher wear of the coating. Formation of the protective layer between the ball and the coating occurs due to tribochemical reaction which is caused by the moisture/oxygen absorption from the atmosphere [147].

A room temperature oxidation reaction of Si_3N_4 in the presence of moisture was analyzed with the help of FactSage thermochemistry software [146]. Equation 8.1 shows probable oxidation reaction at room temperature (298 K) and associated Gibbs free energy which indicates the formation of SiO_2 as the reaction product.

At 298 K : $Si_3N_4 + 75\ H_2O + 1000\ O_2 = 997\ O_2 + 3\ SiO_2 + 71\ H_2O + 2\ N_2$

$$\Delta G = -9.05 \times 10^7\ J \qquad (8.1)$$

The formation of SiO_2 film was experimentally validated by performing XPS analysis on the wear surface of the coatings. Figures 8.5a and b show XPS analysis of worn surfaces of HD-A-SD and HD-A8C-SD coatings. XPS analysis confirms the presence of Si 2p peak in the wear track of HD-A-SD and HD-A8C-SD coating. A peak near 103.5 eV indicates the 4+ oxidation state of the silicon and confirms the Si-O bond formation which corresponds to SiO_2 thin film. It was interesting to note that, there was no significant signal which can confirm the presence Si-N bond (near 102.5eV) [149]. Hence, the transferred thin film on the wear track is identified as SiO_2 film. The wear surface of counter body (Si_3N_4 ball) was also examined to further evaluate SiO_2 film formation.

Figures 8.6a-b show the unworn and worn surfaces of Si_3N_4 ball. Worn surface shows rough region indicating the wear phenomena. There was no transfer layer observed on the worn surface of Si_3N_4 ball. It has been confirmed by performing EDS and elemental X-ray mapping on the worn surface of the ball. Figure 8.6c shows the EDS spectra from the worn surface of ball. Highest intensity peak was observed for silicon. Table 8.1 shows the quantitative results of elements present in the worn surface of ball which showed small amount of oxygen and traces of aluminum.

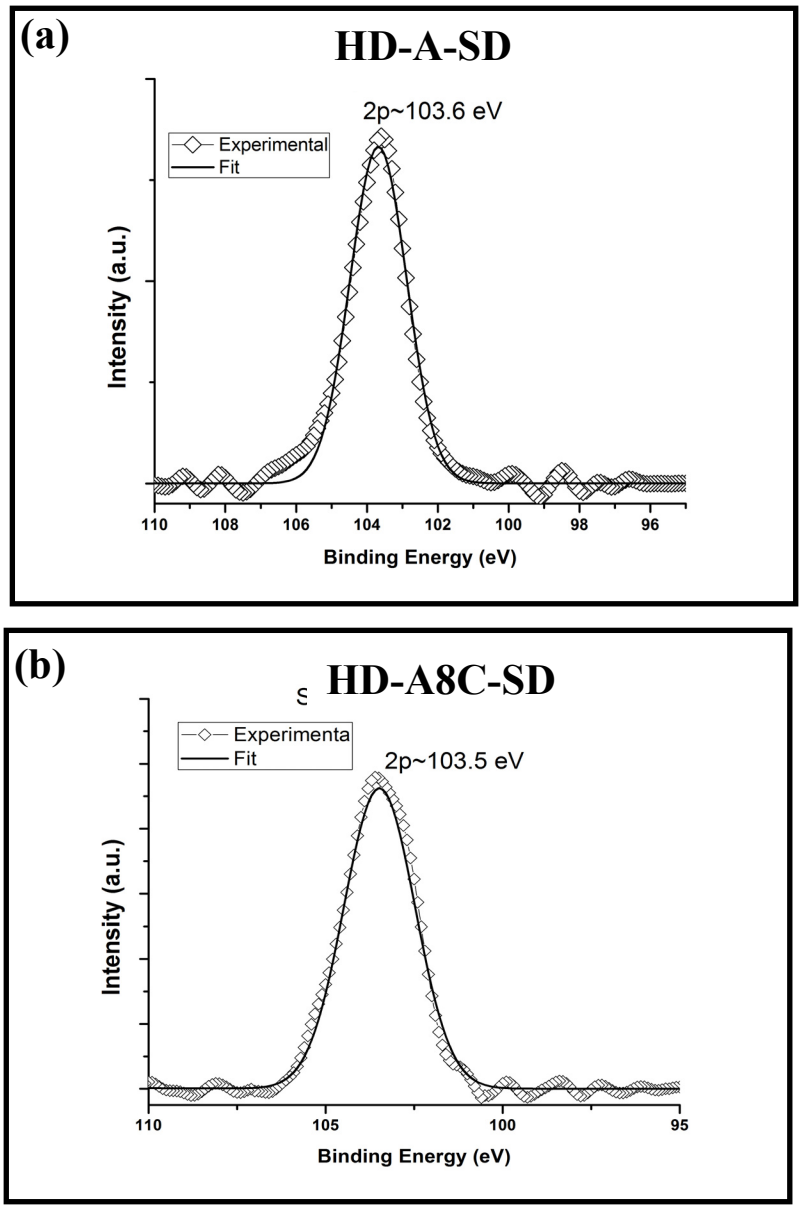

Figure 8.5: XPS spectra collected from (a) wear track of HD-A-SD coating (b) wear track of HD-A-8CSD coating. Both spectra show the major peak of Si 2p near ~103.5 ev confirming the presence of SiO_2 layer on the surface of wear track.

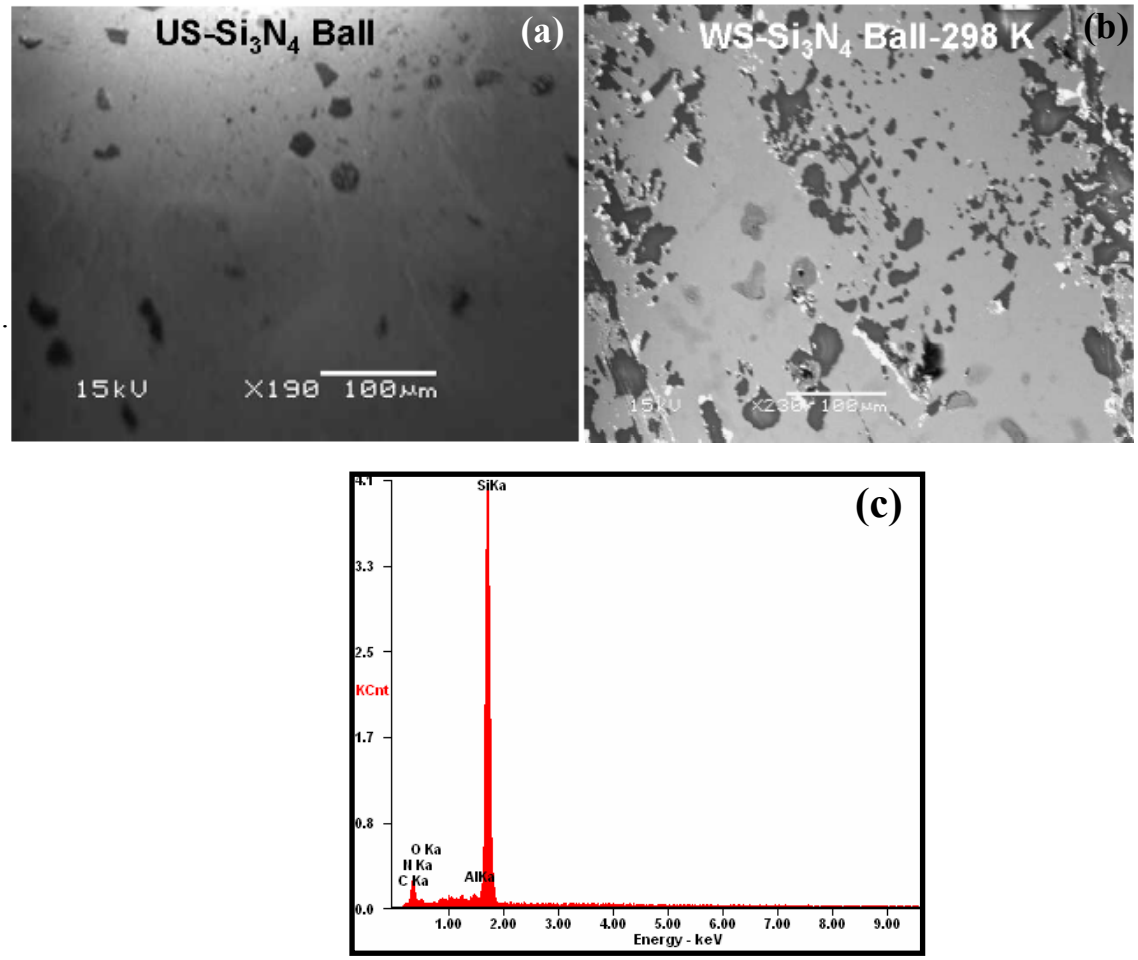

Figure: 8.6: (a) unworn surface (US) and (b) worn surface (WS) of Si_3N_4 ball after the room temperature wear test (c) EDS spectra collected on the worn surface of ball showing high intensity peak for silicon.

Table 8.1: Quantitative results of elements present on the worn surface of Si_3N_4 ball

Element	Wt.%	At.%
CK	07.24	12.68
NK	21.72	32.59
OK	02.74	03.59
AlK	**00.91**	**00.71**
SiK	67.38	50.42

Figure 8.7 is the elemental X-ray map of the worn surface of Si_3N_4 ball. Figure 8.7a represents the back scattered image of worn surface whereas Figures 8.7 b–f show the distribution of aluminum, silicon, carbon, nitrogen, and oxygen respectively. X-ray map further validates the negligible presence of aluminum on the worn surface of ball. Negligible presence of transfer layer from the coating to worn surface of ball further indicates the presence of protective layer (i.e. SiO_2 thin film) on the worn surface of coating caused lower wear weight loss of coating and hence no transfer layer on the ball. The percentage of area covered by the transferred thin film (SiO_2) on the worn surface of HD and LD coatings was measured from five to six wear track images using Image J software (http://rsbweb.nih.gov/ij/index.html). Table 8.2 shows the fraction of the area coverage of the transferred SiO_2 film on the wear track of HD and LD coatings. Table 8.2 indicates the slightly higher transfer of SiO_2 containing film in case of HD coatings as compared to LD coatings. Also, relatively higher transfer of SiO_2 containing film was observed in the wear track of CNT reinforced HD and LD coatings. Higher transfer of SiO_2 film in HD coatings as compared to LD coatings is attributed to the higher hardness of HD coatings (as shown in Table 7.2) which leads to more intense wear of Si_3N_4 ball. Similarly, CNT reinforced coatings have relatively higher hardness (as shown in Table 7.2) causes intense wear of Si_3N_4 ball. It is well known that transferred thin film to the wear track acts as a protective layer and can protect the surface effectively against further wear of coating [112, 147].

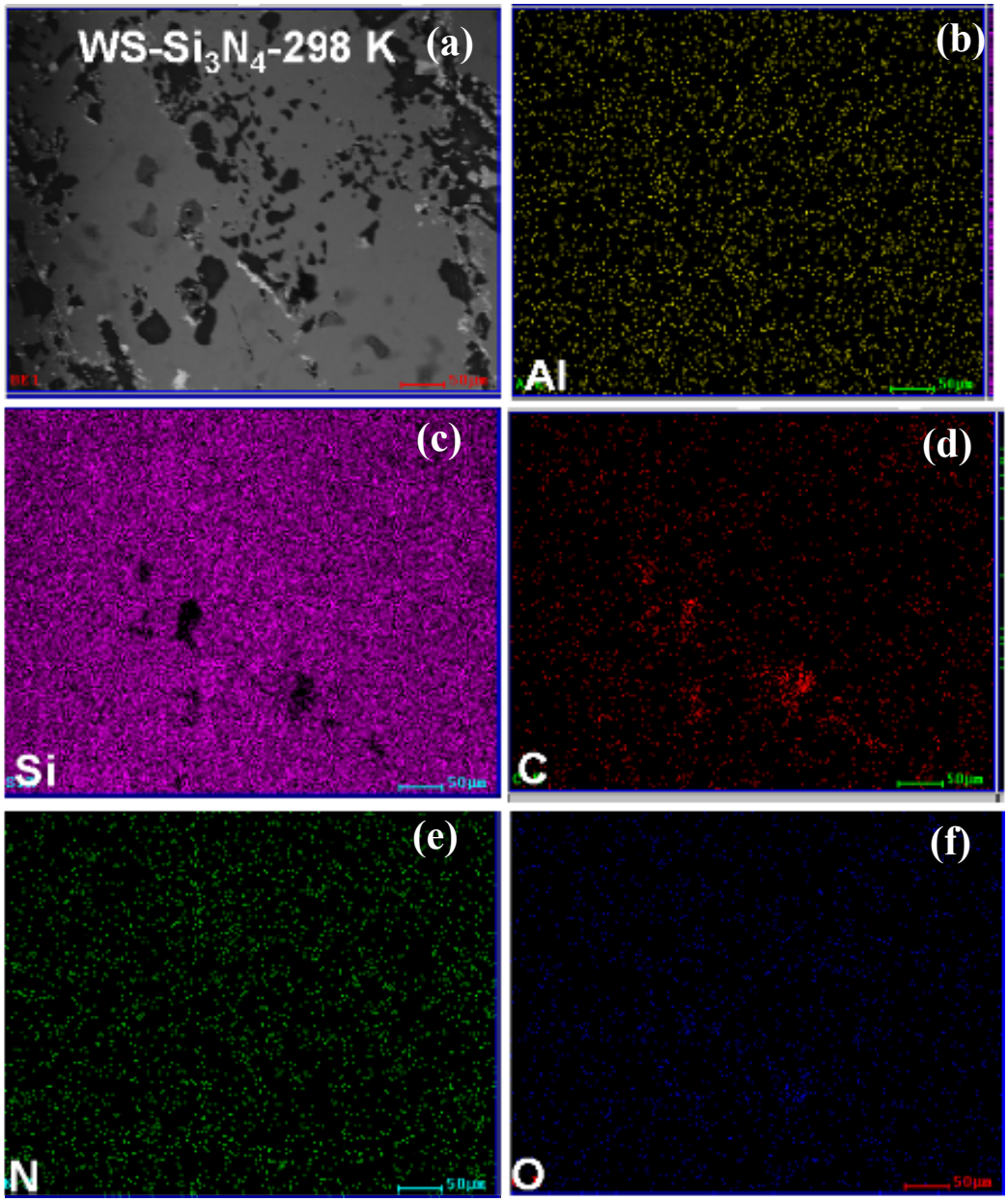

Figure 8.7: X-ray map of worn surface of Si_3N_4 ball after the room temperature (298 K) wear test showing (a) back scattered image of worn surface (b) distribution of aluminum(c) distribution of silicon (d) distribution of carbon (e) distribution of nitrogen (f) distribution of oxygen

Table 8.2: Area fraction of protective thin film

Area fraction of protective thin film	
HD-A-SD	0.63
HD-A4C-SD	0.69
HD-A8C-SD	0.76
LD-A-SD	0.56
LD-A4C-SD	0.61
LD-A8C-SD	0.7

Relatively higher amount of protective film on the wear surface of HD coatings is one of the reasons that lead to improvement in wear resistance of HD coatings as compared to LD coatings. The higher fraction of film in wear track of HD-A4C-SD (0.69) and HD-A8C-SD coating (0.76) compared to HD-A-SD coating (0.63) is one of the reasons for improvement in wear resistance of CNT reinforced coatings.

Other factors which are responsible for improvement in the wear resistance of the coatings include (i) higher hardness and (ii) improved fracture toughness. Evans and Marshall [110] has proposed the wear of ceramic material based on the fracture toughness value which is represented in equation (8.2);

$$V = P_n^{1.125} K_c^{-0.5} H^{-0.625} \left(\frac{E}{H}\right)^{0.8} S \qquad (8.2)$$

where, V is the wear volume (m^3), P_n is the applied load (MPa), K_c is the fracture toughness (MPa $m^{1/2}$), H is the hardness, E is the elastic modulus (GPa) and S is the sliding distance (m). Equation 8.2 shows that high fracture toughness of the material will result in improved wear resistance. It has been discussed in Chapter 7 that all HD

coatings have higher fracture toughness as compared to LD coatings. Hence, HD coatings display better wear resistance as compared to LD coatings. CNT reinforcements also offer the toughening mechanism which contributes towards the higher wear resistance of coating. Figures 8.8a and b show the CNT bridging between the splats in wear tracks of HD-A4C-SD and HD-A8C-SD coatings. Figures 8.8c and d show CNT bridges between the splats in wear tracks of LD-A4C-SD and LD-A8C-SD coatings. CNT bridging reduces the degree of material removal by resisting the crack propagation.

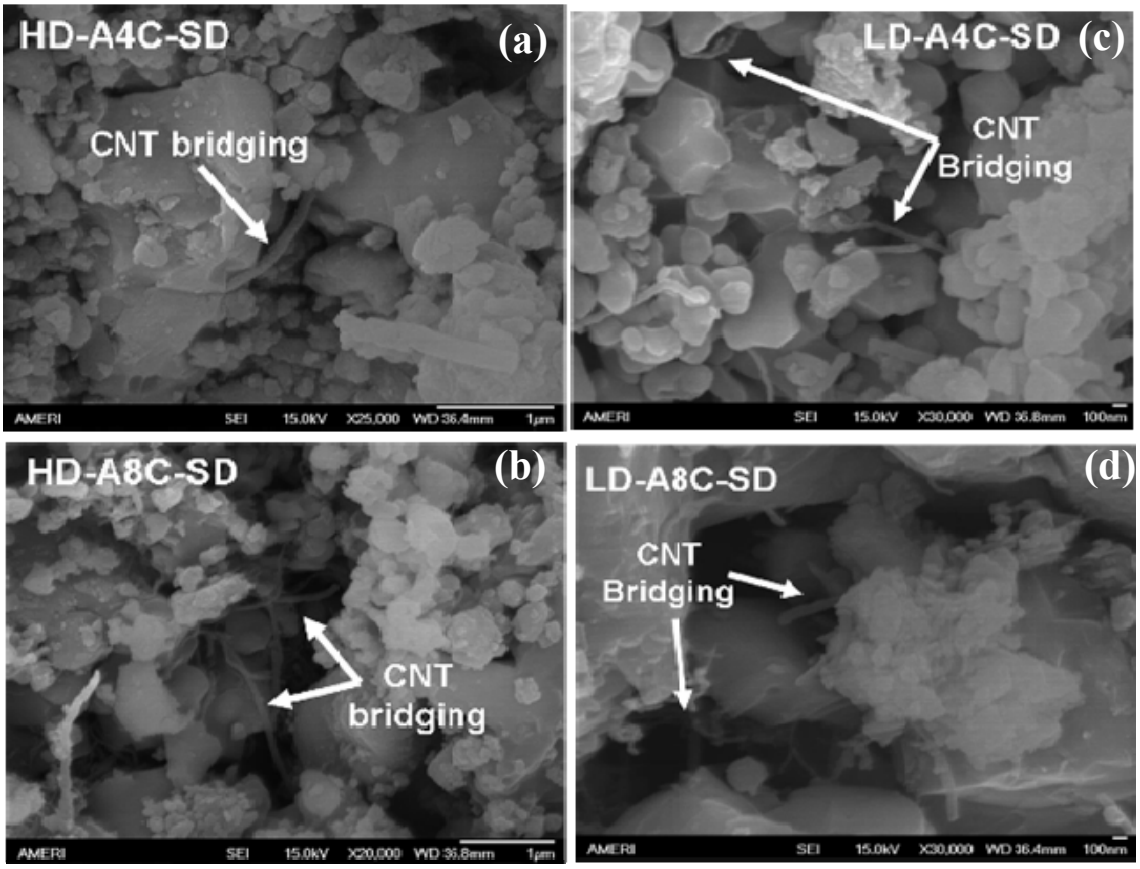

Figure 8.8: High magnification image of wear surface (a) HD-A4C-SD coating (b) HD-A8C-SD coating (c) LD-A4C-SD coating (d) LD-A8C-SD coating, showing the CNT bridging between the splats.

Figure 8.9a shows the average coefficient of friction (COF) for HD coatings with respect to sliding distance at 30 N load. Figure 8.9b is the average COF for LD coatings with respect to sliding distance at 30 N load.

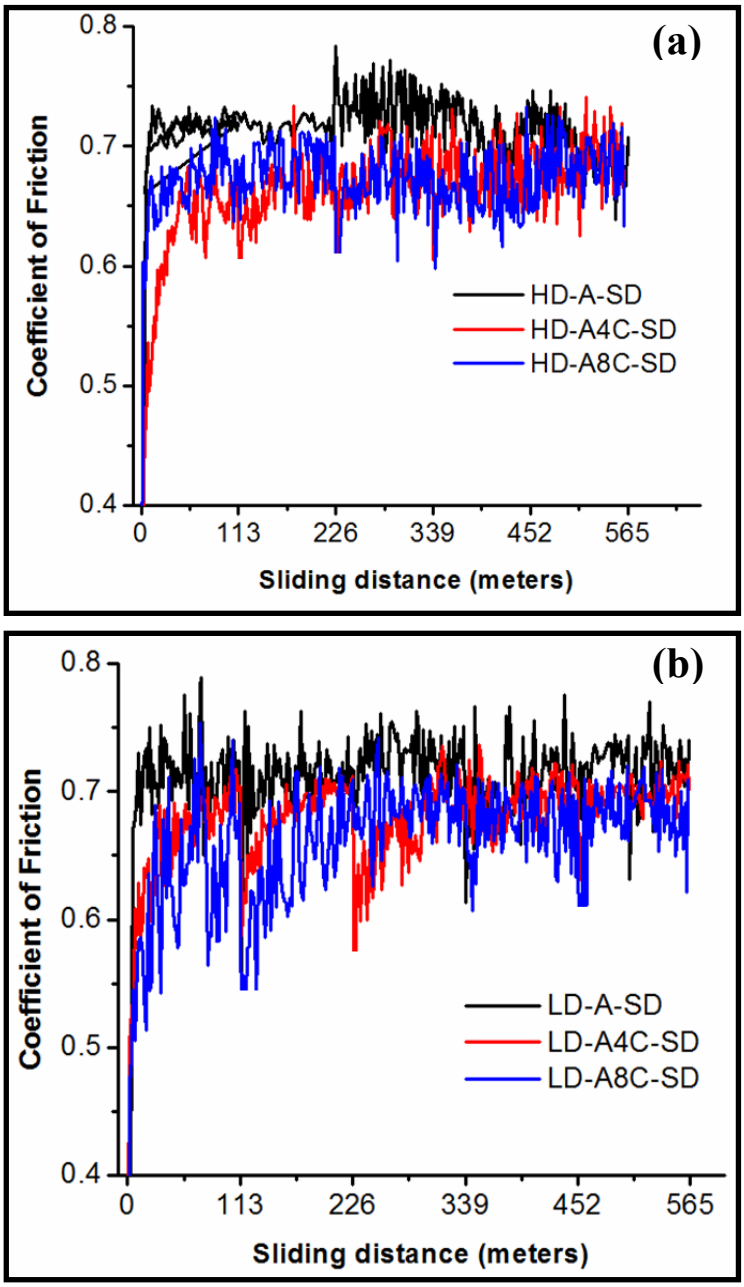

Figure 8.9: Coefficient of friction (COF) with sliding distance at normal load of 30 N for wear track of (a) HD coating (b) LD coating

Relatively higher spikes and fluctuation were observed for COF of LD coatings which are attributed to higher debris generation during wear condition. Since, relatively large area of the wear track in HD coatings is covered with protective film (Table 8.2), the amount of wear debris generation in wear track of HD coating is lower leading to less fluctuation in COF value. The average COF value for HD-A-SD wear track was found ~0.71 while it was ~0.67 and ~0.65 for HD-A4C-SD and HD-A8C-SD wear track. Average COF for wear track of LD (~0.73 for LD-A-SD, ~0.68 for LD-A4C-SD and ~0.69 for LD-A8C-SD) was found almost similar to COF for HD wear track. However, it can be seen that, CNT reinforced coating has slightly lower COF in both HD and LD coatings. Raman spectra were obtained from the unworn (US) and worn surfacez (WS) of HD-A4C-SD and HD-A8C-SD coatings as shown inFigure 8.10. Raman spectra showed the presence of D and G peaks in the worn surface of coating indicating retained CNT after the wear. Ratio of intensity of D and G peaks (I_D/I_G) has been calculated from the Raman spectra and is tabulated in Table 8.3. I_D/I_G ratio from the worn surface of both coatings is lower (I_D/I_G= 0.76 for HD-A4C-SD and 0.73 for HD-A8C-SD) as compared to unworn surface of coating (I_D/I_G= 0.84 for HD-A4C-SD and 0.93 for HD-A8C-SD). A lower I_D/I_G value indicates higher degree of graphitization in the wear surface which might be due to exposed graphene layer of CNTs by continuous abrading of the wear surface. Hence relatively lower COF was observed for CNT reinforced coating.

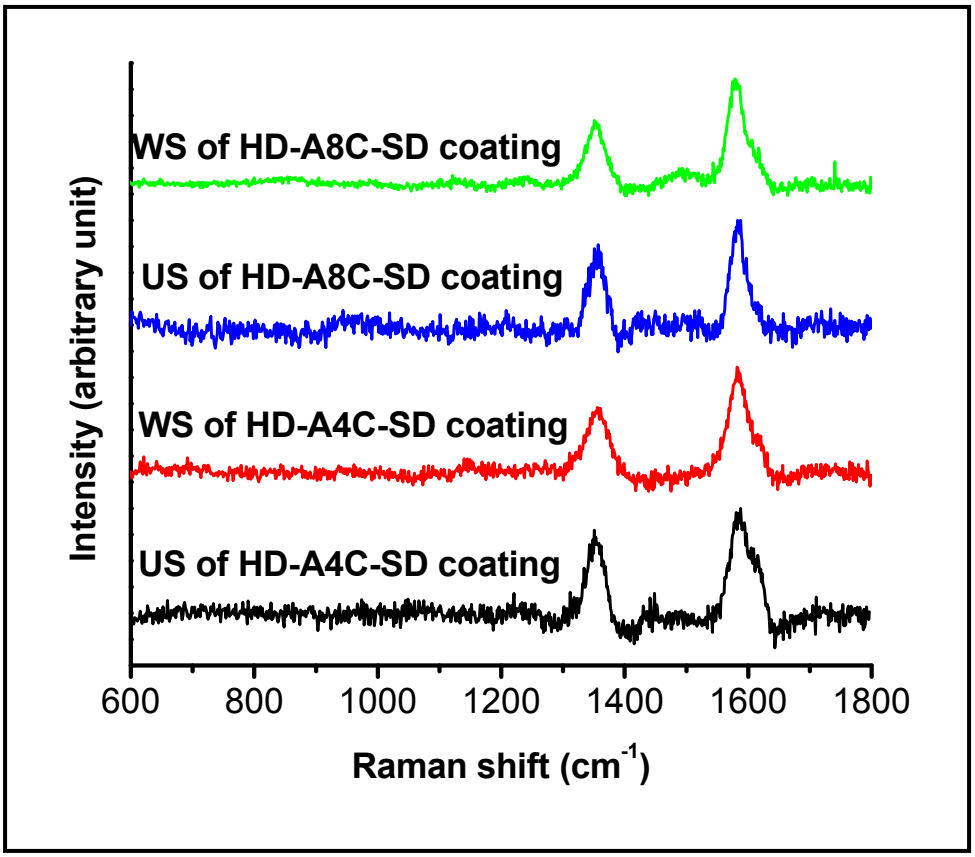

Figure 8.10: Raman spectra of unworn surface (US) and worn surface (WS) of HD-A4C-SD and HD-A8C-SD coating.

Table 8.3: Position and ratio of intensity of D and G peaks obtained from Raman Spectroscopy of unworn and worn surface of HD-A4C-SD and HD-A8C-SD coating.

Sample	**Position of D peaks**	**Position of G peaks**	**I_D/I_G**
US of HD-A4C-SD coating	1356	1582	0.84
WS of HD-A4C-SD coating	1361	1588	0.76
US of HD-A8C-SD coating	1356	1582	0.93
WS of HD-A8C-SD coating	1362	1584	0.73

Figure 8.11 is the graphical representation correlating porosity and wear resistance of HD and LD coatings. Percentage value written inside the pyramid represents the porosity in the coating. Lower porosity in the coating results in lower weight loss and hence higher wear resistance of the coating. Tailoring the porosity to a smaller value by optimizing the plasma process parameters leads to significant improvement in the wear resistance of coating. Thus, it becomes clear how plasma process parameters affect the coating's final property. Uniformly dispersed CNTs in the matrix also play an important role in enhancing the wear resistance of coating. Figure 8.11 shows that CNT reinforced coatings have higher wear resistance as compared to coatings without CNT.

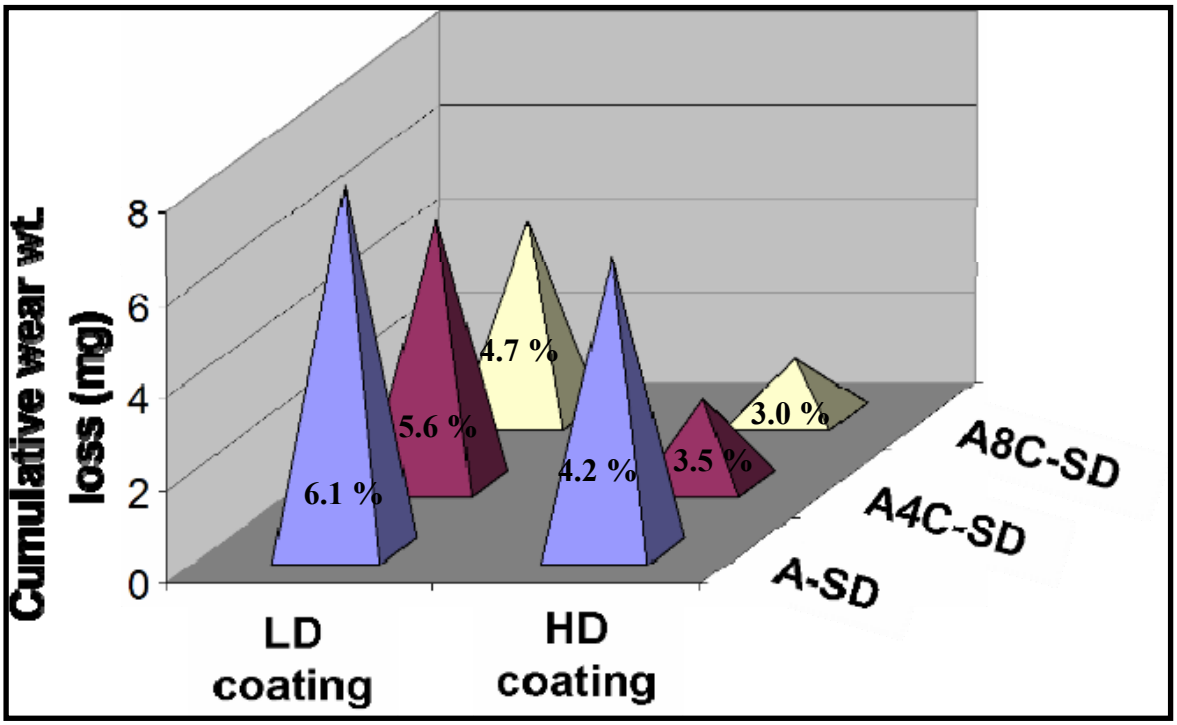

Figure 8.11: Effect of porosity on cumulative wear weight loss of HD and LD coating. Percentage value shown inside the pyramid represents the porosity in the coating.

8.2. Tribological Behavior of Coating Synthesized using CVD Al_2O_3-CNT (ICP-1) Powder

Figure 8.12 shows the cumulative wear weight loss as a function of sliding distance at different loads for Al_2O_3 and ICP-1 coatings. *It is highlighted that counter body used for wear test of ICP-1 coating is tungsten carbide (WC) ball and not Si_3N_4 ball as in the case of coatings synthesized from spray dried powder*. The difference in the counter body will lead to different tribochemical reaction and affect the wear behavior of ceramic material. Figure 8.12 shows that cumulative wear weight loss increases with the sliding distance and the load. There is almost no weight loss for both coatings at 10 N load suggesting that load is not high enough to cause wear in Al_2O_3 based coatings. The wear weight increases for 30 N and 50 N loads.

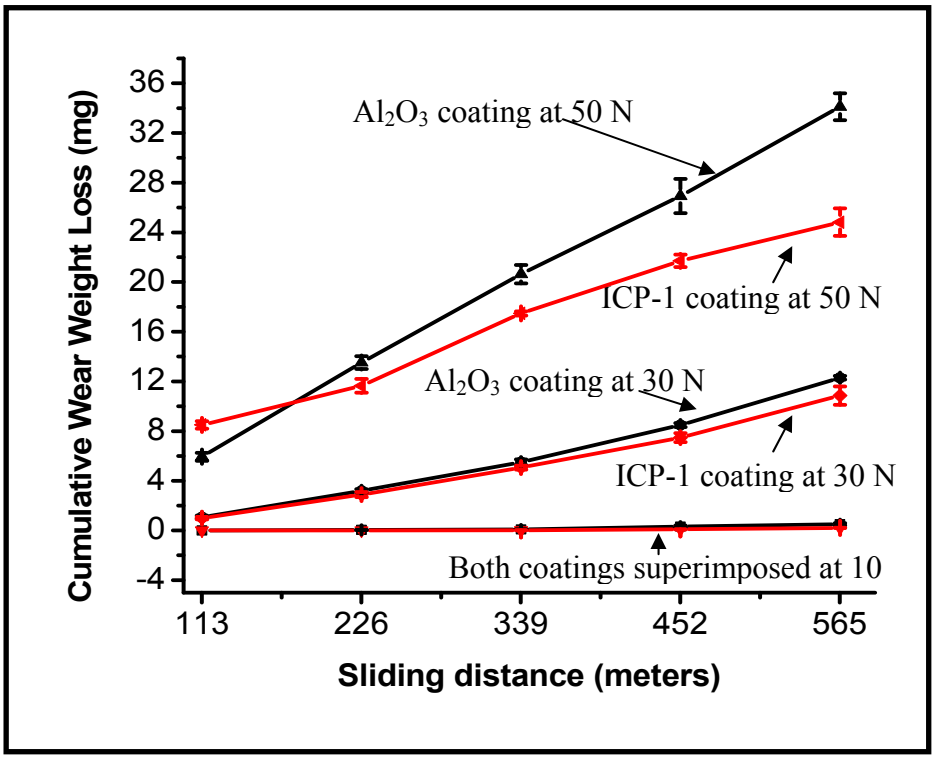

Figure 8.12: Cumulative wear weight loss of Al_2O_3 coating and ICP-1 coating at different loads.

Higher wear weight loss is observed for Al_2O_3 coating as compared to ICP-1 coating at 50 N load. It can be concluded that load and CNT reinforcement plays the major roles in wear behavior of both coatings. SEM observation of the wear track was carried out to identify the wear mechanism due to load and CNT reinforcement. At 30 N load, SEM image indicates the mild abrasive wear resulting in smoother surface (Figure 8.13a and b).

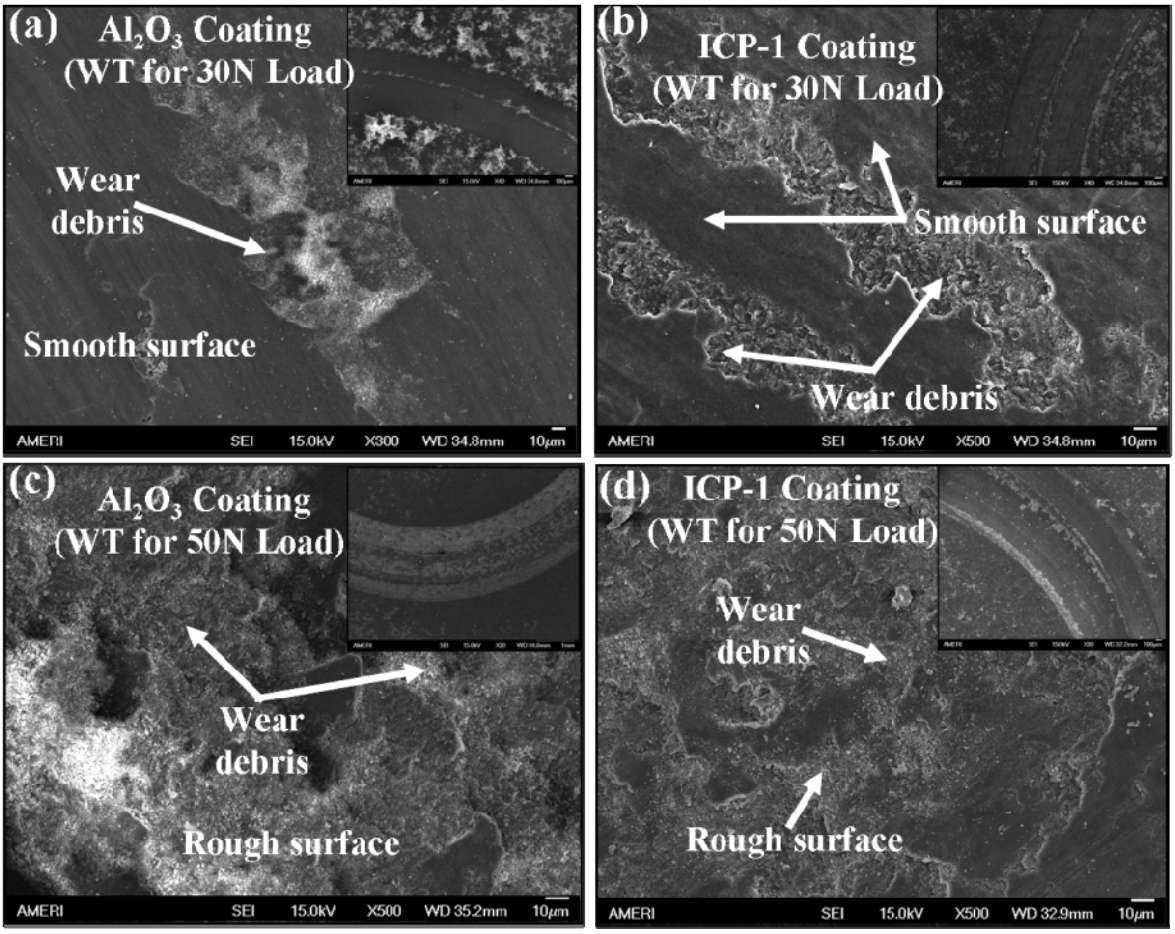

Figure 8.13: Wear surface topography after the linear sliding distance of ~565 meters (a) Al_2O_3 coating at 30 N load (b) ICP-1 coating at 30 N load (c) Al_2O_3 coating at 50 N load (d) ICP-1 coating at 50 N load. Each inset image shows the 3 mm wide wear track (WT) caused by tungsten carbide ball.

On the other hand severe abrasive wear results in rough surface which is seen in case of 50 N load (Figure 8.13c and d). The inset image in Figure 8.13a-b and in Figure 8.13c-d is 3 mm wide wear track left by WC ball at 30 N and at 50 N loads respectively. Occasional pull out of the material was observed in case of mild wear for 30 N load. In contrast, at 50 N load the surface was deeply grooved. This is attributed to pronounced contact stress between the WC ball and wear material at higher load. The higher contact stress favors cracking in the coating which ultimately leads to fracture. Hence it is expected the higher degree of material removal occurs at a higher load. Further, weak intersplat cohesion in plasma sprayed coating [28] may induce the debonding of interlinked splats and their detachment from the coating at the higher load.

It is recalled, wear surface of spray dried coating showed tribochemical SiO_2 film formation on the wear track when sliding against Si_3N_4 ball. Unlikely, for the case of ICP-1 coating, wear surface did not show any tribochemical film on the wear surface. This is in accordance with the literature results. Li et al. [150] studied the sliding wear behavior of titanium aluminide (TiAl) using steel and ceramic ball (Al_2O_3, Si_3N_4, WC). They found the strong influence of counter body on the wear behavior TiAl intermetallics. Though not much difference observed in wear loss against Si_3N_4 and WC ball, but, tribochemical film formation was observed on the wear track of TiAl intermetallics when slided against Si_3N_4 ball. No such type of film was observed on the wear track against WC ball [150].

Figure 8.12 shows the higher improvement in the wear resistance of ICP-1 coating at 50 N load (~27%) as compared to 30 N load (~12%). This can be correlated with the wear mechanism in conjunction with the effect of CNT reinforcement at higher load. Since, at 50 N load severe wear dominates and the material removal occurs by cracking followed by fracture, CNT reinforcement offers the toughening mechanism at higher load. CNT bridging plays an important role in deflecting the cracks (Figures 7.9 and 8.14) and hence reduces the degree of material removal at higher load by resisting the crack propagation. But in the case of mild wear, load (30 N) is not enough to generate the crack in the coating and hence the toughening mechanism is not very effective at lower load. It is also observed from Figure 8.12 that ICP-1 coating shows low cumulative wear weight loss as compared to Al_2O_3 coating (at 50 N load) except during initial 200 m of sliding distance. Initial wear loss in ICP-1 coating at 50 N load is due to higher surface roughness (2.93±0.61 μm) of ICP-1 coating than Al_2O_3 (1.43±0.38 μm) coating. Surface roughness plays an important role in wear loss of the material as surface asperities come in direct contact and gets abraded first.

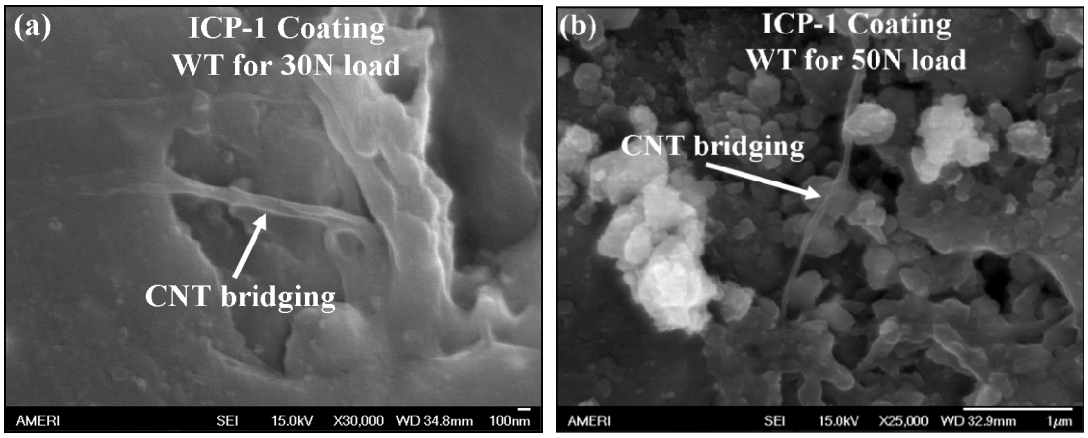

Figure 8.14: High magnification image of wear surface of ICP-1 coating at (a) 30 N load and (b) 50 N load, showing the CNT bridging between the splats.

From Evans and Marshall equation (Equation 8.2), it is very clear that higher fracture toughness of the material will result in enhanced wear resistance of the coating. Wear weight loss was computed from Equation 8.2 for both coatings at 30 N and 50 N loads. Improvement in "*computed"* and "*experimental"* wear resistance of ICP-1 coating at 30N and 50 N loads is tabulated in Table 8.4. There is 45% improvement in the *"computed"* wear resistance at 30 N load and 47% at 50 N load for ICP-1 coating over Al_2O_3 coating. However, the *experimental* results shows wear resistance improvement of 12% at 30N load and 27% 50N load for ICP-1 coating. Overestimation in the *computed* value of wear resistance improvement is attributed to surface roughness and surface asperities which were not taken care of in equation 8.2.

Table 8.4: Computed and experimental wear resistance of ICP-1 coating.

Load	**Improvement in wear resistance (%) (Computed value from Equation 8.2)**	**Improvement in wear resistance (%) (Experimental Value)**
30N	45	12
50N	47	27

Figure 8.15 shows the average COF with respect to sliding distance for both coatings at 10 N, 30 N and 50 N loads. It is recalled that for spray dried coating, continuous curve of COF was shown but for ICP-1 coating. Average COF values are shown in Fig. 8.15 due to difficulty in representing the large amount of data at three different loads (10 N, 30 N, 50 N) for both Al_2O_3 and ICP-1 coatings. It is observed that higher load induces the higher coefficient of friction. Highest value of COF for both coatings at 50 N load is attributed to rough wear surface which further validates the mechanism of severe abrasive wear and debris formation whereas lower value of COF at

30 N load is due to smoother wear surface indicating the mechanism of mild abrasive wear.

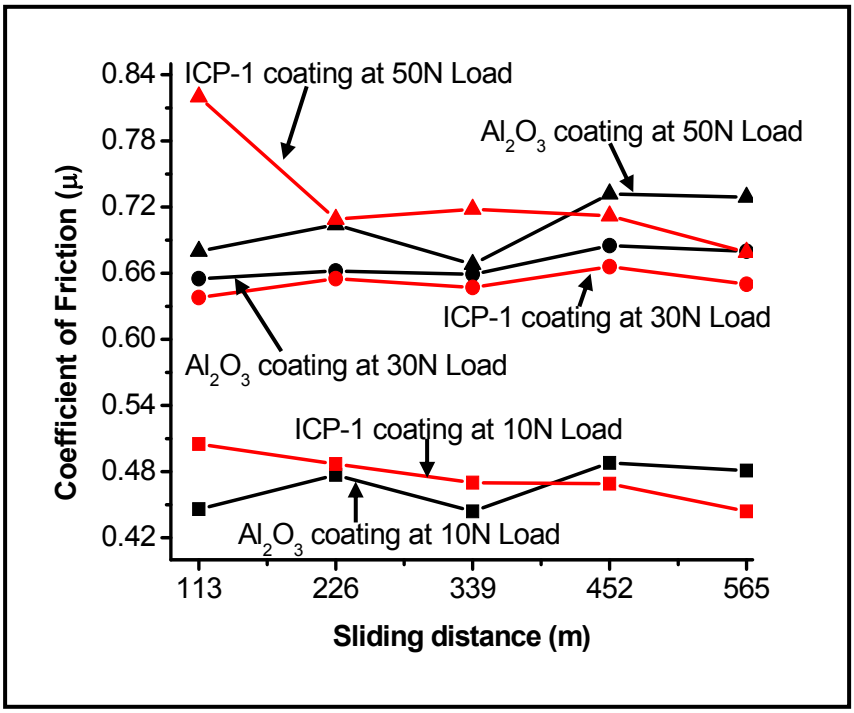

Figure 8.15: Average coefficient of friction (COF) with sliding distance at different loads for wear track of Al_2O_3 coating and ICP-1 coating

Effect of CNT reinforcement on COF at 10 N load was not significant as there was insignificant wear at the low load for both coatings (Figure 8.12). Raman spectra of ICP_1 coating show presence of D and G peaks in the wear track in Figure 8.16. Table 8.5 shows the I_D/I_G ratio for wear track of ICP-1 coating, which is almost similar for 30 N (I_D/I_G=0.87) and 50 N load (I_D/I_G =0.88). However, I_D/I_G ratios from wear track at both loads are lower as compared to unworn surface of ICP-1 coating (I_D/I_G=0.98). A lower I_D/I_G value indicates higher degree of graphitization within wear track. This might be due to exposed graphene layer of CNTs by continuous abrading of the wear surface. In the

case of 30 N load, graphitization in the wear track of ICP-1 coating resulted in slightly lower but uniform COF (0.63) than Al_2O_3 coating (COF=0.67). In contrast, COF for wear track of ICP-1 coating at 50 N load showed discontinuous behavior. COF for the wear surface of ICP-1 coating at 50 N load shows higher value (0.82) in the initial stage than Al_2O_3 coating (COF= 0.68). This behavior of ICP-1 coating can be understood in terms of two competing wear mechanism *viz.* (i) wear debris generation and (ii) graphitization in wear track due to contact pressure.

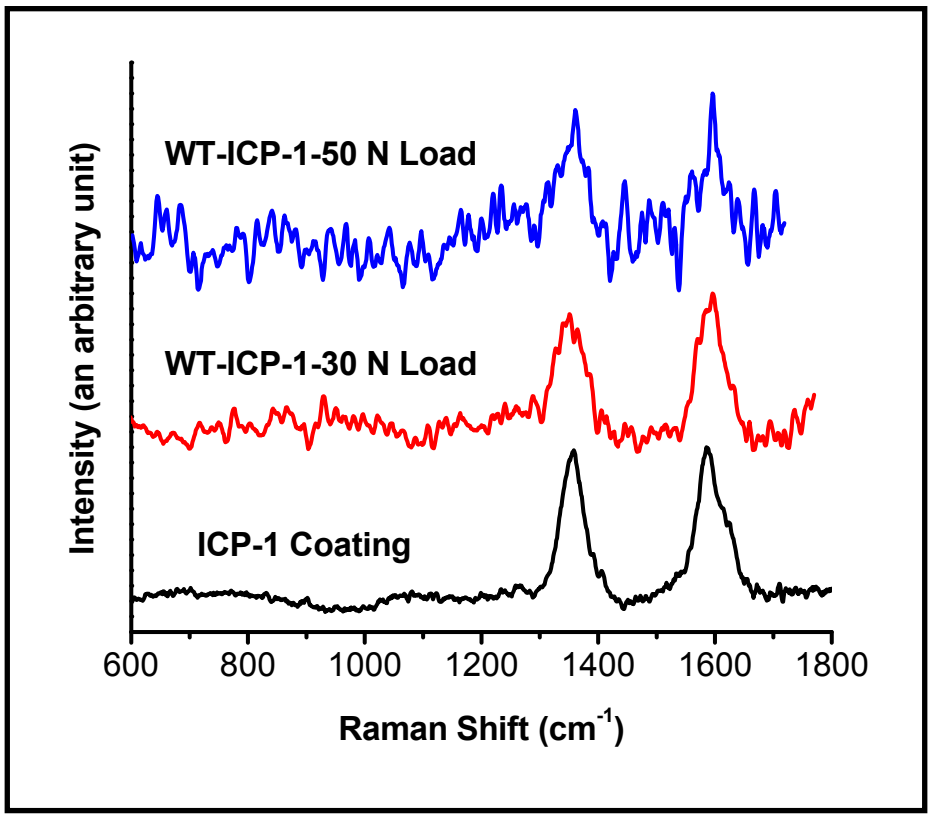

Figure 8.16: Raman spectrum of ICP-1 coating, wear track (WT) of ICP-1 coating at 30N, and 50N load. Raman peak of ICP-1 coating, and wear track of ICP-1 coating at both loads suggests enhanced graphitization of CNTs.

Table 8.5: Position and ratio of intensity of D and G peaks obtained from Raman Spectroscopy of ICP-1 coating and its wear track (WT) at 30N and 50N load.

Sample	**Position of D peaks**	**Position of G peaks**	**I_D/I_G**
ICP-1 Coating	1353	1589	0.98
ICP-1 WT-30N load	1349	1594	0.87
ICP-1 WT-50N load	1362	1598	0.88

Higher surface roughness of ICP-1 coating (2.93±0.61 μm) than Al_2O_3 coating (1.43±0.38 μm) lead to high wear debris generation in the wear track of ICP-1 coating and dominates graphitization in the initial stage, resulting in higher COF. However, as the wear time progresses wear process stabilizes slowly and graphitization dominates over the wear debris generation leading to reduction in COF**.**

Although optimization of plasma parameters was not done for ICP-1 coating due to lack of availability of ICP-1 powder, 1.5 wt. % of CNT addition in ICP-1 coating resulted ~24% improvement in the wear resistance. Enhanced wear resistance of ICP-1 coating is attributed to excellent CNT dispersion in Al_2O_3 matrix which promoted the toughening mechanism. Similar toughening mechanism was observed for spray dried coating which resulted ~71% and ~80% relative improvement in wear resistance of HD-A4C-SD and HD-A8C-SD coating respectively. In addition, tribochemical film formation was observed in the wear track of all spray dried coatings which further assisted in lowering the wear loss. The next chapter describes high temperature tribological behavior of CNT reinforced Al_2O_3 coatings.

9. HIGH TEMPERATURE TRIBOLOGICAL BEHAVIOR

In this chapter, tribological behavior of plasma sprayed Al_2O_3-CNT coatings at the elevated temperature is discussed. It should be emphasized that *no attempt has been made to study the high temperature tribological behavior of* Al_2O_3-CNT composite coating. Wear and friction behavior of the Al_2O_3-CNT composite coating at temperature ranging from 298 to 873 K is investigated using ball-on-disk tribometer.

9.1 High Temperature Tribological Behavior of Coatings Synthesized from Spray Dried Powder

Figure 9.1 shows the cumulative wear weight loss of high density (HD-A-SD, HD-A4C-SD, HD-A8C-SD) and low density (LD-A-SD, LD-A4C-SD, LD-A8C-SD) coatings at 298 K, 573 K and 873 K. Wear weight loss in Figure 9.1 is plotted after ~565 meters of linear sliding distance at a normal load of 30 N. The cumulative wear weight loss increases with the temperature for HD and LD coatings when sliding against Si_3N_4 counter body. Cumulative wear weight loss decreases with an increasing CNT content for HD and LD coatings at all temperatures. HD coatings show a lower weight loss for all compositions as compared to LD coatings. Table 9.1 is the summary of the improvement in wear resistance of CNT reinforced HD and LD coatings at all temperatures. The data from Table 9.1 is also presented graphically for a direct visual comparison in wear behavior between HD and LD coatings.

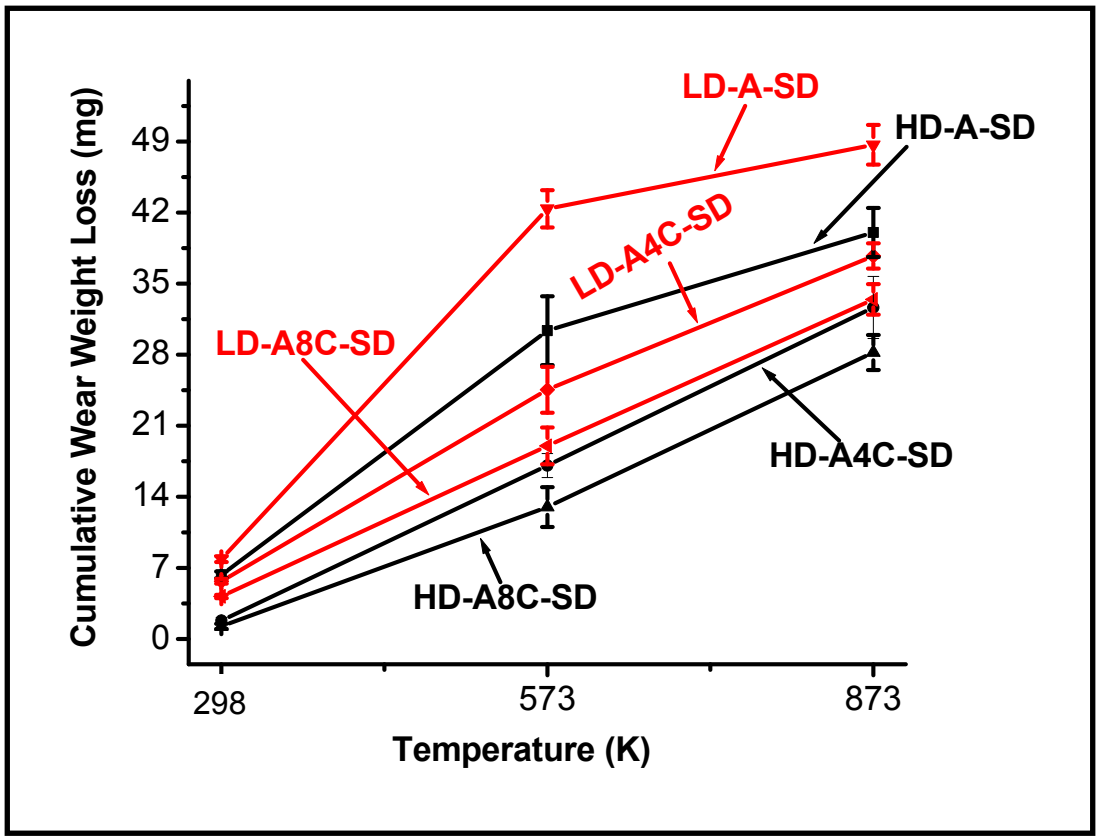

Figure 9.1: Cumulative wear weight loss of HD and LD coatings as function of different temperature at normal load of 30N and after a linear sliding distance of ~565 meters.

Wear comparison among HD and LD coatings is shown in Figure 9.2 as bar charts. Figure 9.2a shows cumulative wear weight loss of HD-A-SD and LD-A-SD coating as a function of temperature. Figure 9.2b shows the cumulative wear weight loss of HD-A4C-SD and LD-A4C-SD coating. Cumulative wear weight loss of HD-A8C-SD and LD-A8C-SD coatings as a function of temperature is shown in Figure 9.2c. Percentage (%) value shown near curly bracket in Figures 9.2a-c is the relative improvement in wear

Table 9.1: Improvement in the wear resistance of HD and LD coatings at temperatures from 298 K to 873 K.

Comparison among **HD** coatings	**Wear resistance of CNT reinforced *HD coating* improved by (%)**			
		298 K	**573 K**	**873 K**
	HD-A4C-SD coating (compared to HD-A-SD coating)	71	44	18
	HD-A8C-SD coating (compared to HD-A-SD coating)	81	57	30
Comparison among ***LD*** coatings	**Wear resistance of CNT reinforced *LD coating* improved by (%)**			
		298 K	**573 K**	**873 K**
	LD-A4C-SD coating (compared to LD-A-SD coating)	28	42	22
	LD-A8C-SD coating (compared to LD-A-SD coating)	47	55	31
Comparison between ***HD & LD*** coatings	**Compare to LD coating, wear resistance of HD coating improved by (%)**			
		298 K	**573 K**	**873 K**
	HD-A-SD	20	28	18
	HD-A4C-SD	68	30	13
	HD-A8C-SD	72	32	16

resistance of HD coatings as compared to LD coatings. The percentage value shown inside the black bar is the reduction in the wear resistance of that coating at elevated temperature as compared to same coating at 298 K. The percentage value shown inside the red bar is the reduction in the wear resistance of that coating at elevated temperature as compared to same coating at 298 K.

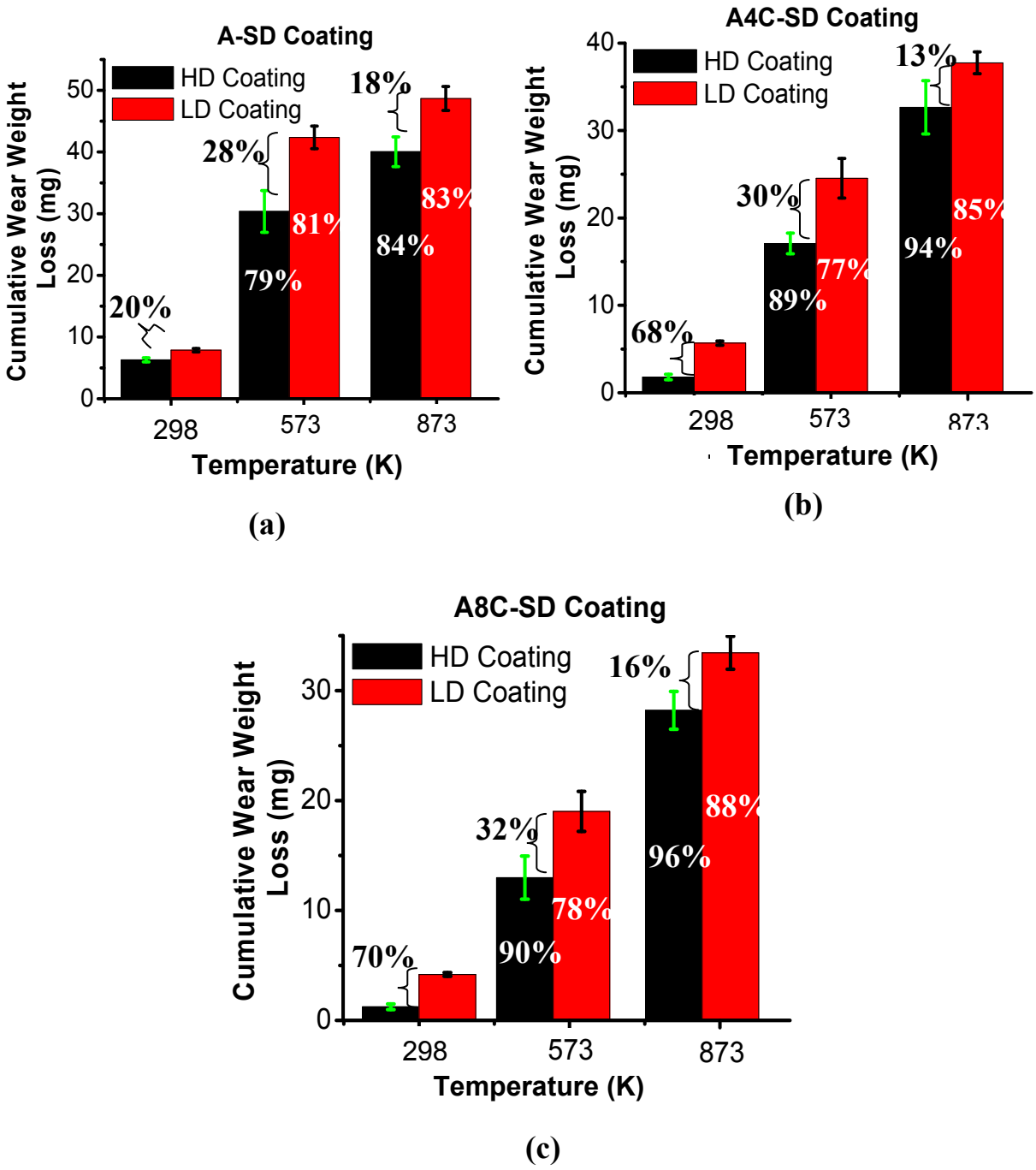

Figure 9.2: Cumulative wear weight loss (after linear sliding distance of ~565 meters) as function of temperature for (a) HD-A-SD and LD-A-SD coating (b) HD-A4C-SD and LD-A4C-SD coating (b) HD-A8C-SD and LD-A8C-SD coating

Fig 9.2 clearly indicates that temperature and CNT content has strong effects on wear behavior of HD and LD coatings against Si_3N_4 counter body. Wear surface of HD and LD coatings have been analyzed to understand the high temperature wear behavior. SEM observations of wear surface of HD and LD coatings at "873 K" are shown in Figure 9.3. Figures 9.3a-c show the SEM micrographs of wear surface of HD-A-SD, HD-A4C-SD and HD-A8C-SD coatings at 873 K respectively. Figures 9.3d-f represents the wear surfaces of LD-A-SD, LD-A4C-SD and LD-A8C-SD coatings at 873 K respectively. Wear surface of all HD and LD coatings at 873 K showed rough surface which indicates the phenomena of severe wear. Wear surfaces of HD and LD coatings did not show much difference in the morphology. Figure 9.3 also shows very "small amount" of discontinuous thin film observed in the wear surface of HD and LD coatings at ~873 K except LD-A-SD coating. Absence of thin film in the wear surface of LD-A-SD coating is due to relatively lower hardness of LD-A-SD coating (Table 7.2) resulting in lesser wear rate of Si_3N_4 ball and hence negligible amount of transfer layer from the ball to the coating. Distribution of thin film on the wear track has been observed by performing elemental X- ray mapping of the wear track. Figures 9.4a-c show the elemental X-ray mapping of the wear surfaces of HD-A-SD, HD-A4C-SD and HD-A8C-SD coating at 873 K respectively. Figures 9.4a1, b1, c1 are the back scattered images of wear tracks of HD-A-SD, HD-A4C-SD and HD-A8C-SD coatings respectively. Figures 9.4a2-a5 show the distribution of silicon, aluminum, oxygen and nitrogen respectively while 9.4b2-b6 and 9.4c2-c6 shows the distribution of silicon, aluminum, oxygen, nitrogen and carbon.

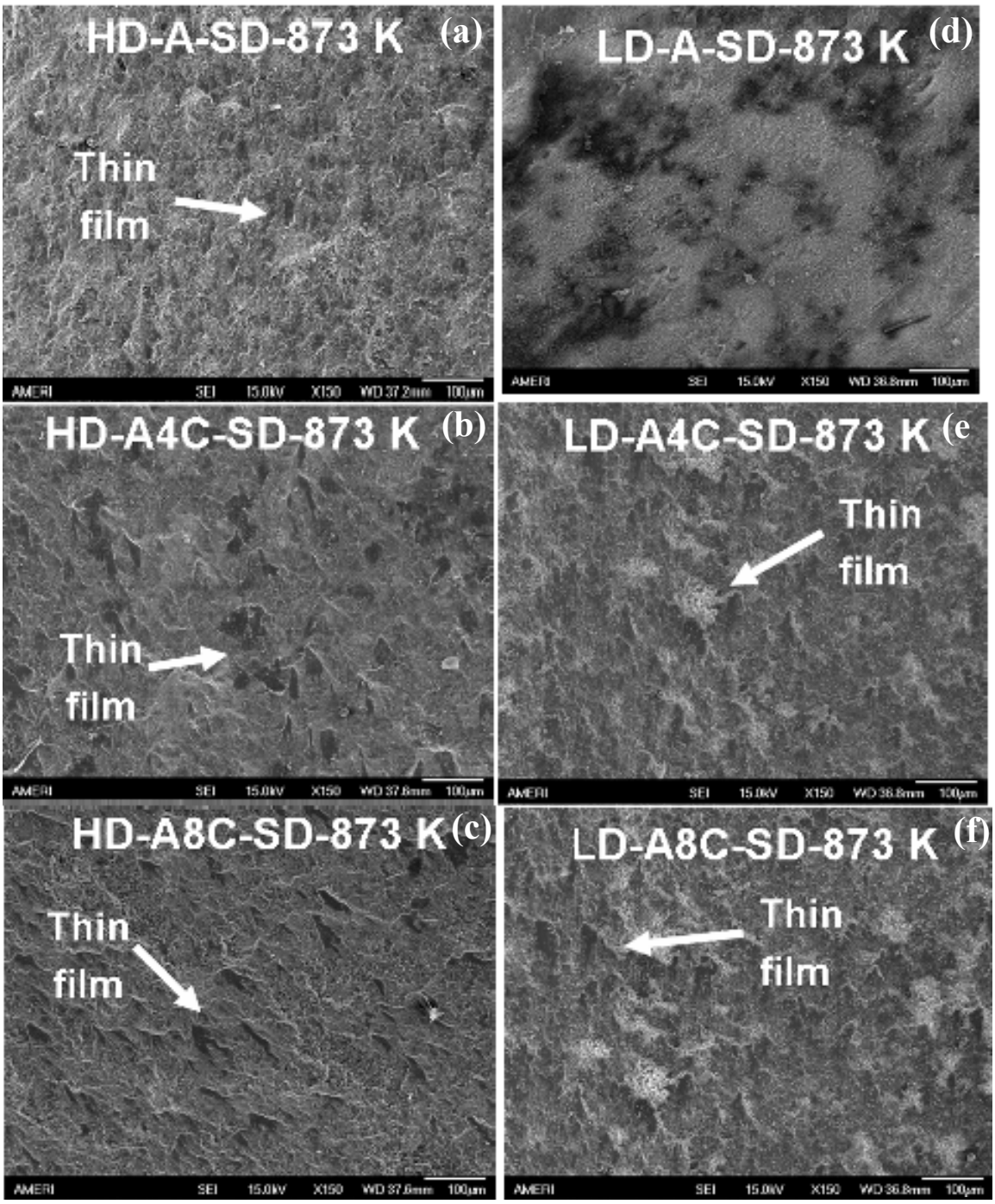

Figure 9.3: Wear surface topography at ~873 K and after the linear sliding distance of ~565 meters and at normal load of 30 N for (a) HD-A-SD coating (b) HD-A4C-SD coating (c) HD-A8C-SD coating (d) LD-A-SD coating (e) LD-A4C-SD coating (f) LD-A8C-SDcoating

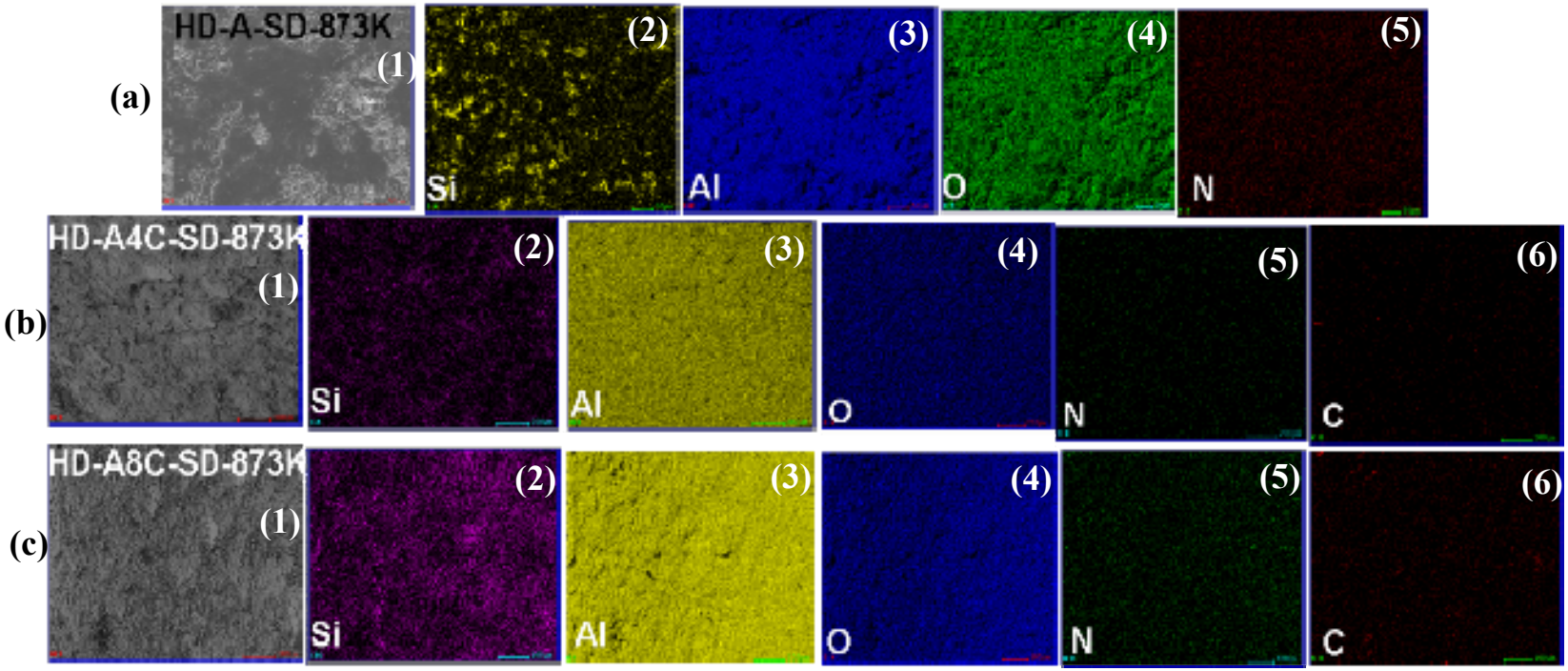

Figure 9.4: X-ray map of wear track of (a) HD-A-SD coating at 873 K (b) HD-A4C-SD coating at 873 K (c) HD-A8C-SD coating at 873 K. a1, b1, c1 are the back scattered image of wear track of HD-A-SD, HD-A4C-SD and HD-A8C-SD coatings respectively. a2-a5 shows the distribution of silicon, aluminum, oxygen and nitrogen respectively while b2-b6 and c2-c6 shows the distribution of silicon, aluminum, oxygen, nitrogen and carbon respectively.

X-ray map confirms the presence of silicon, nitrogen in the wear surface which is as results of tribochemical reaction with the Si_3N_4 ball.

High temperature oxidation reaction of Si_3N_4 in the presence of moisture was analyzed with the help of FactSage thermochemistry software [146]. Equation 9.1-9.4 shows oxidation reactions from 298 K to 1173 K and associated Gibbs free energy. Equation 9.1 and 9.2 indicates the formation of crystalline SiO_2 as the reaction product at 298 K and 573 K which changes to amorphous hydrated SiO_2 at 873 K. Increasingly negative Gibbs free energy with the increasing temperature confirms thermodynamic stability of amorphous hydrated SiO_2 formation at higher temperature (873 K).

At 298 K: $Si_3N_4 + 75\ H_2O + 1000\ O_2 = 997\ O_2 + 3\ SiO_2 + 71\ H_2O + 2\ N_2$
$\Delta G = -9.05 * 10^7$ J (9.1)

At 573 K : $Si_3N_4 + 75\ H_2O + 1000\ O_2 = 996\ O_2 + 3\ SiO_2 + 75\ H_2O + 2\ N_2$
$\Delta G = -1.58 * 10^8$ J (9.2)

At 873 K : $Si_3N_4 + 75\ H_2O + 1000\ O_2 = 996\ O_2 + 3\ SiO_2.\ n\ H_2O$ (amorphous) + $75\ H_2O + 2N_2$ $\Delta G = -2.36 * 10^8$ J (9.3)

At 1173 K : $Si_3N_4 + 75\ H_2O + 1000\ O_2 = 996\ O_2 + 3\ SiO_2.\ n\ H_2O$ (amorphous) + $75\ H_2O + 2N_2$ $\Delta G = -3.19 * 10^8$ J (9.4)

XPS analysis of the wear surface of HD-A-SD and HD-A8C-SD coating in Figure 9.5 confirmed that discontinuous thin film is composed of SiO_2. It should be noted that, equation 9.3 shows the formation of amorphous hydrated SiO_2 as reaction product at 873 K while XPS shows the presence of crystalline SiO_2. This is attributed to transformation of amorphous hydrated SiO_2 to crystalline SiO_2 below ~823 K [146].

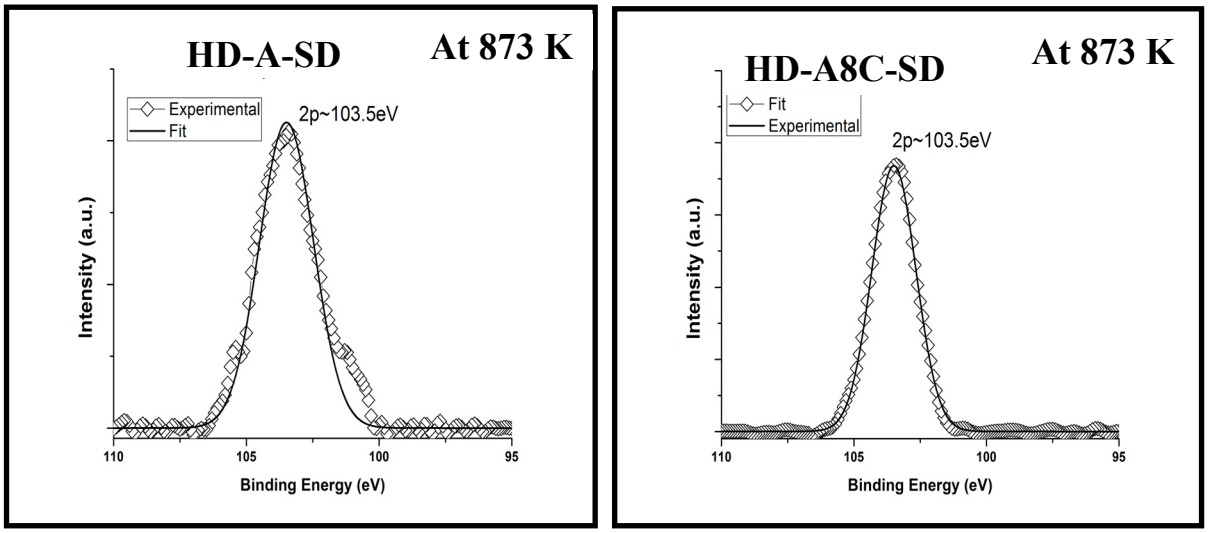

Figure 9.5: XPS spectra collected from (a) wear track of HD-A-SD coating (b) wear track of HD-A-8CSD coating. Both the spectra show the major peak of Si 2p near ~103.5 ev confirming the presence of SiO_2 layer on the surface of wear track.

It must be recalled most of the room temperature wear surfaces of HD and LD coatings were covered with protective tribochemical film that reduced the wear. In the case of high temperature, very small amount of protective tribochemical film SiO_2 film was found on the wear surfaces and hence result in higher wear loss. Si_3N_4 ball oxidizes in the presence of moisture and forms a protective film on the wear surface of coatings as a result of tribo-chemical reaction [112, 147]. However, with the increase in temperature, absorption tendency of moisture on the wear track decreases and there is reduced chance of tribochemical reaction to form a protective film. Hence severe wear occurs at high temperatures with a higher wear weight loss of the coatings.

Severe wear of the coating was also validated by examining the Si_3N_4 ball in post wear condition. It was expected that there will the more transferred layer from the coating to Si_3N_4 ball surface in severe wear conditions. Figure 9.6a shows unworn surface of the Si_3N_4 ball whereas Figures 9.6b and c show the worn surfaces of Si_3N_4 ball after the wear test at 298 K and 873 K respectively. Unworn surface shows a smoother surface whereas rough surface is observed for 298 K and 873 K. From Figures 9.6b and c, it can be concluded that wear surface of the ball at 873 K has higher transfer layer from the coating. Composition of the transfer layer has been identified by performing EDS and X-ray mapping on the worn surface of Si_3N_4 ball at 873 K. EDS spectrum of the worn ball surface at 873 K presented in Figure 9.6d shows high intensity peak for aluminum. Table 9.2 is the quantitative EDS analysis of elements which shows high weight percentage of aluminum and oxygen on the worn ball surface. This is indicator of higher amount of Al-rich transfer layer from the wear track to ball as a result of severe wear of coating.

Elemental X-ray mapping (Figure 9.7) shows the distribution of aluminum, oxygen, carbon, silicon and nitrogen on the worn surface of the ball at 873 K. Higher transfer layer from the coating to ball suggest severe wear of the coating. Severe wear of the coating at 873 K also has an adverse effect on the toughening mechanism offered by CNTs. Due to severe wear of coating, some of the reinforced CNTs might get exposed to an ambient temperature (873 K) resulting in oxidation of CNTs.

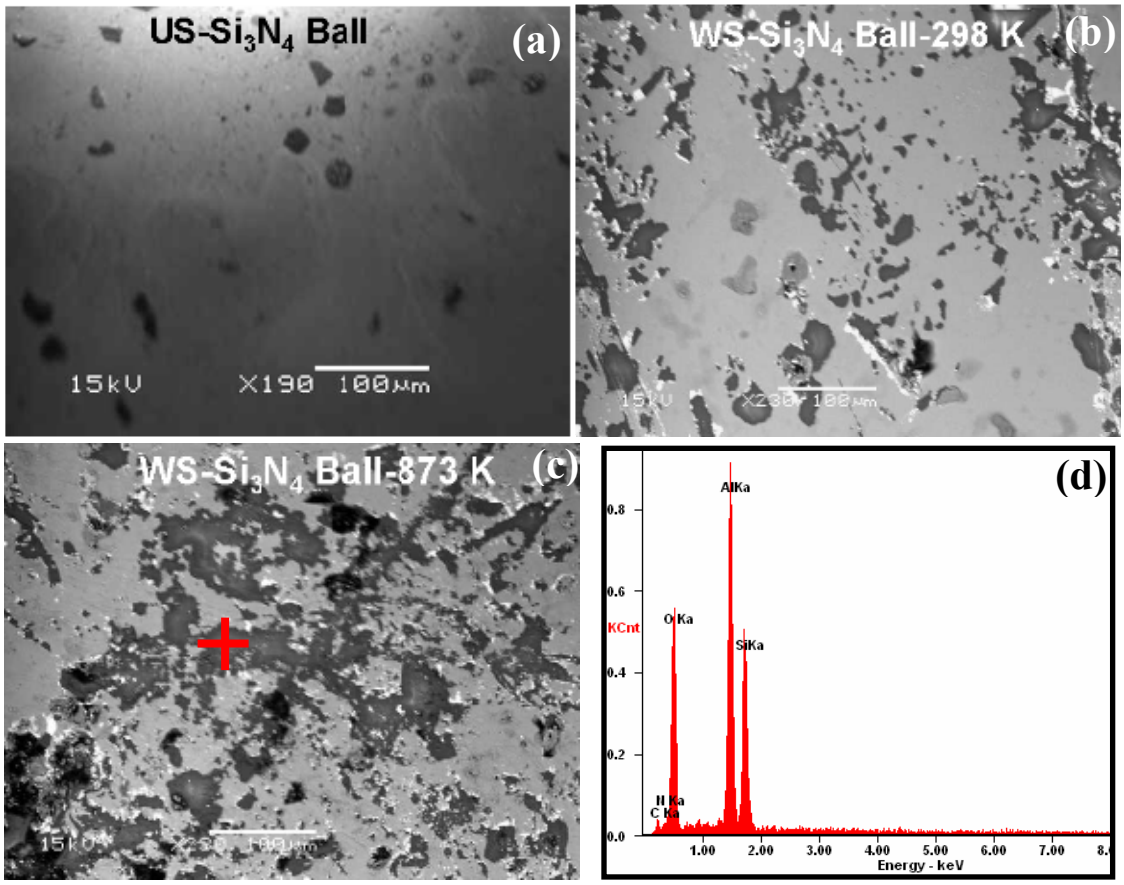

Figure: 9.6: (a) unworn surface (US) of Si_3N_4 ball (b) worn surface (WS) of Si_3N_4 ball after the wear test at 873 K (c) EDS spectra collected from the worn surface of ball

Table 9.2: Quantitative results of elements present on the worn surface of Si_3N_4 ball at 873 K.

Element	Wt. %	At. %
CK	04.81	07.81
NK	08.59	11.97
OK	36.62	44.65
AlK	**29.66**	**21.44**
SiK	20.33	14.12

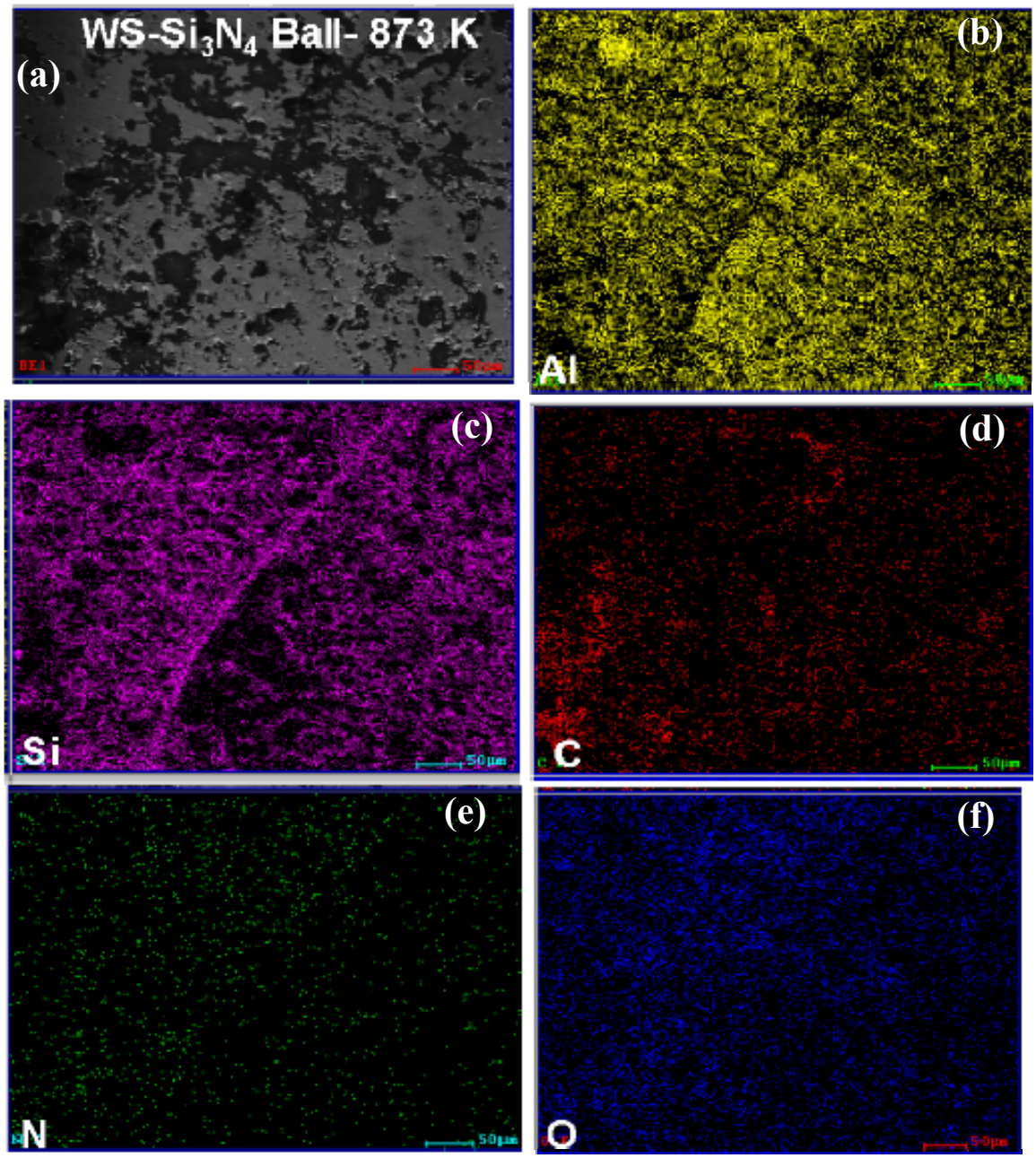

Figure 9.7: X-ray map of worn surface of Si_3N_4 ball after the wear test at 873 K showing (a) back scattered image of worn surface (b) distribution of aluminum(c) distribution of silicon (d) distribution of carbon (e) distribution of nitrogen (f) distribution of oxygen

Osswald et al.[151] monitored the oxidation of CNTs by Raman spectroscopy and concluded that oxidation of CNT occurs above 440°C with a severe rate at 550°C-600°C. Li et al. [152] also concluded that oxidation of CNTs occurs in the temperature range of 480°C-750°C in air. Oxidation of CNT might lead to defect generation in CNT structure which has been studied by collecting Raman spectra from the wear tracks of HD-A4C-SD and HD-A8C-SD coatings at 873 K. Figure 9.8 shows the Raman spectra for unworn and worn surfaces of HD-A4C-SD and HD-A8C-SD coatings at 873 K. I_D/I_G ratios in Table 9.3 were calculated from the spectra. I_D/I_G ratio was slightly higher for the wear surfaces of HD-A4C-SD and HD-A8C-SD coatings at 873 K as compared to unworn coating surface. Increased I_D/I_G ratio is the indication of more defects in the CNTs in the worn surface of HD-A4C-SD and HD-A8C-SD coatings which might be due to oxidation of CNTs at elevated temperature (873 K). This might degrade the toughening effect of CNT to some extent and lower the wear resistance.

It is well known that high temperature hardness of the ceramics decreases exponentially. Wang et al. [153] studied the temperature dependence of ceramic hardness and found that hardness of Al_2O_3 exponentially decreases with the increasing temperature (Equation-9.5)

$$H = H_0 e^{-aT} \tag{9.5}$$

where H_o and α are the constants determined from the experimental data, and T is the test

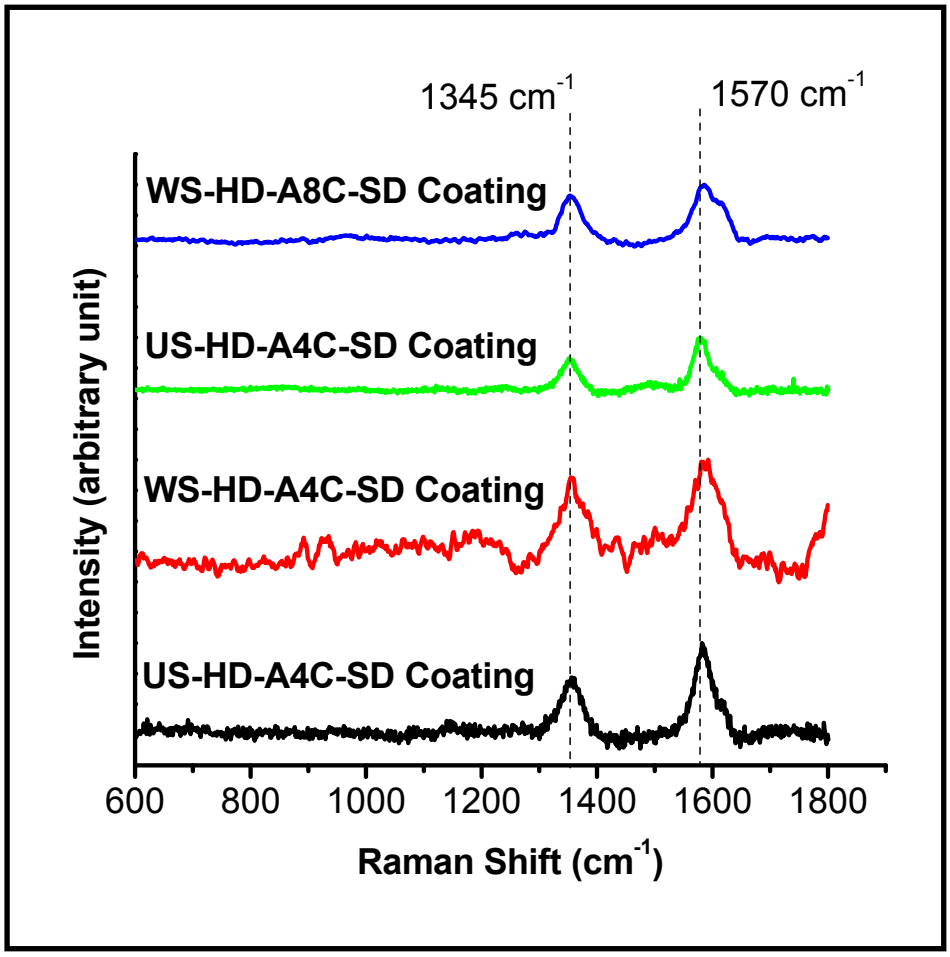

Figure 9.8: Raman spectrum of unworn surface (US) and worn surface (WS) of HD-A4C-SD and HD-A8C-SD coating at 873 K.

Table 9.3: Ratio of intensity of D and G peaks obtained from Raman Spectroscopy of unworn surface (US) and worn surface (WS) of HD-A4C-SD and HD-A8C-SD coating at 873 K.

Coating	I_D	I_G	I_D/I_G
US-HD-A4C-SD Coating	88	99	0.88
WS-HD-A4C-SD Coating	154	159	0.96
US-HD-A8C-SD Coating	191	200	0.95
WS-HD-A8C-SD Coating	247	251	0.98

temperature (°C). The hardness of Al_2O_3 reduces by ~29% at 300°C and 67% at 600°C [153]. It is expected that hardness of all HD and LD coatings decreases at the elevated test temperature resulting in more severe wear.

However, with the increasing CNT content, improvement in wear resistance was observed for HD and LD coatings at all temperatures as shown in Figure 9.9. Figure 9.9a shows cumulative wear weight loss of HD and LD coatings at 298 K. Figures 9.9b and c show cumulative wear weight loss of HD and LD coatings at 573 K and 873 K respectively. Relative increase in the wear resistance of CNT reinforced coating at higher temperature is attributed to higher fracture toughness of CNT reinforced coatings. Evans and Marshall equation (Equation 8.2) confirms that higher fracture toughness of material results to higher wear resistance of the coating [110]. CNT reinforcements also offer the toughening mechanisms which contribute towards the higher wear resistance of coating. Figures 9.10a and b show the CNT bridging between the splats in wear tracks of HD-A4C-SD and HD-A8C-SD coatings at 873 K. Figures 9.10 c and d show the CNT bridging between the splats in wear tracks of LD-A4C-SD and LD-A8C-SD coatings at 873 K. CNT bridging reduces the degree of material removal by resisting the crack propagation. It is true that oxidation of CNT may degrade the toughening effect to some extent and lower the wear resistance. However, our results indicate that CNT reinforced coatings displayed improved wear resistance even at higher temperature.

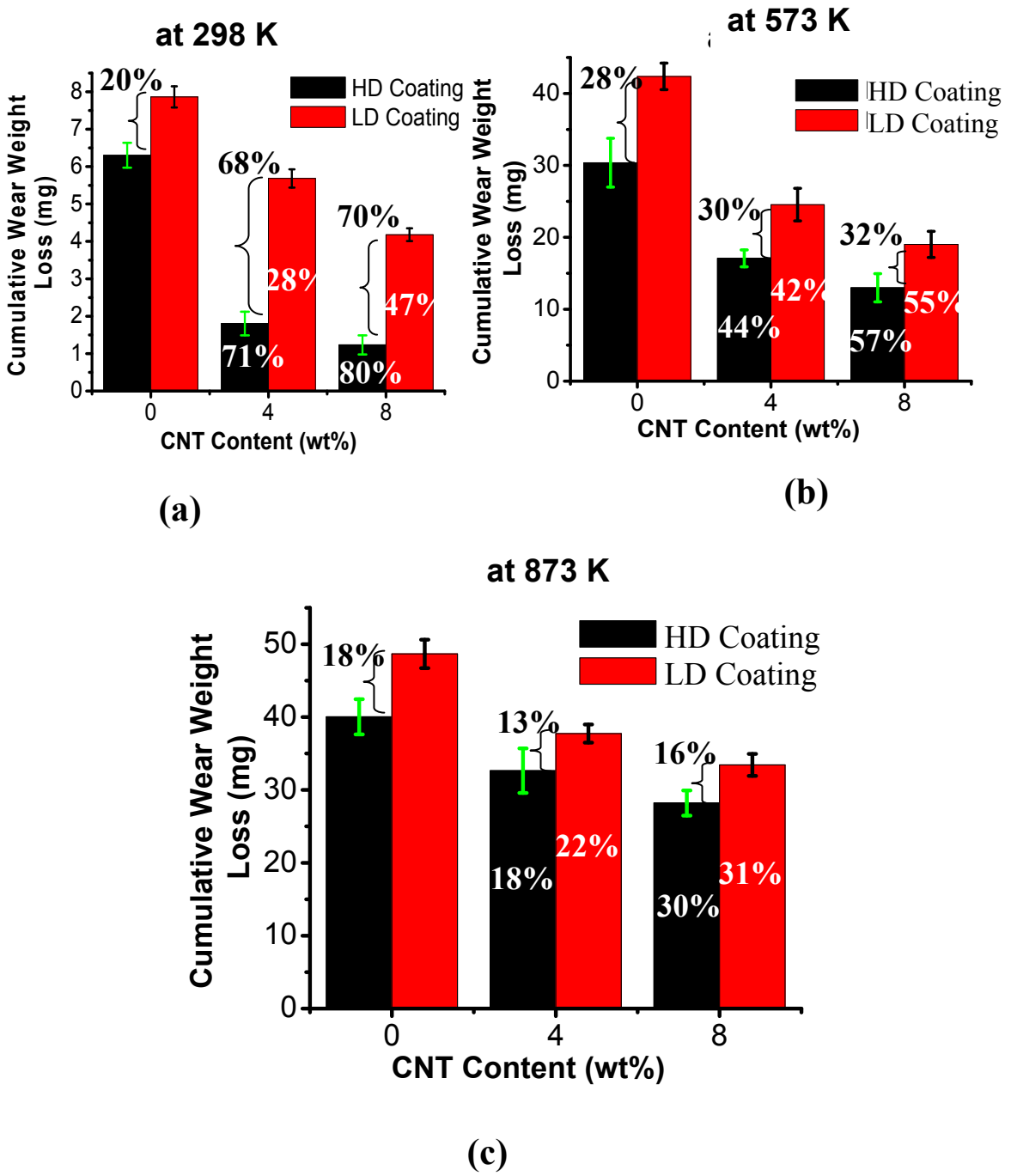

Figure 9.9: Cumulative wear weight loss (after linear sliding distance of ~565 meters) as function of CNT content for (a) HD-A-SD and LD-A-SD coating at 303 K (b) HD-A4C-SD and LD-A4C-SD coating at 573 K (b) HD-A8C-SD and LD-A8C-SD coating at 873 K

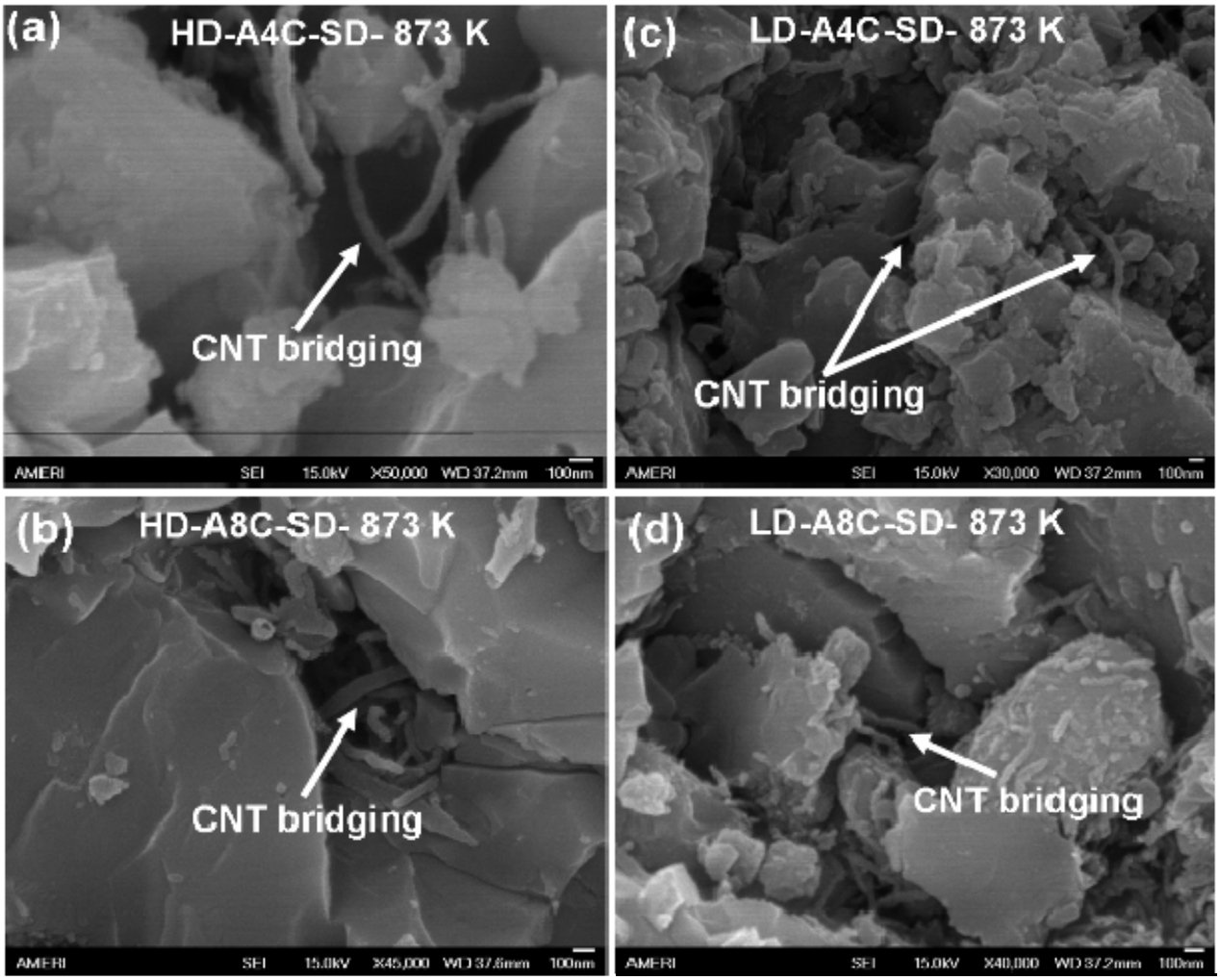

Figure 9.10: High magnification image of wear surface (a) HD-A4C-SD coating at 873 K (b) HD-A8C-SD coating at 873 K (c) LD-A4C-SD coating at 873 K (d) LD-A8C-SD coating at 873 K, showing the CNT bridging between the splats.

Coefficient of friction (COF) of all coatings was also evaluated at elevated temperatures. Figures 9.11a-c show COF plots of HD coatings at 298 K, 573 K and 873 K respectively. Figures 9.11d-f show COF plots of LD coatings at 298 K, 573 K and 873 K respectively.

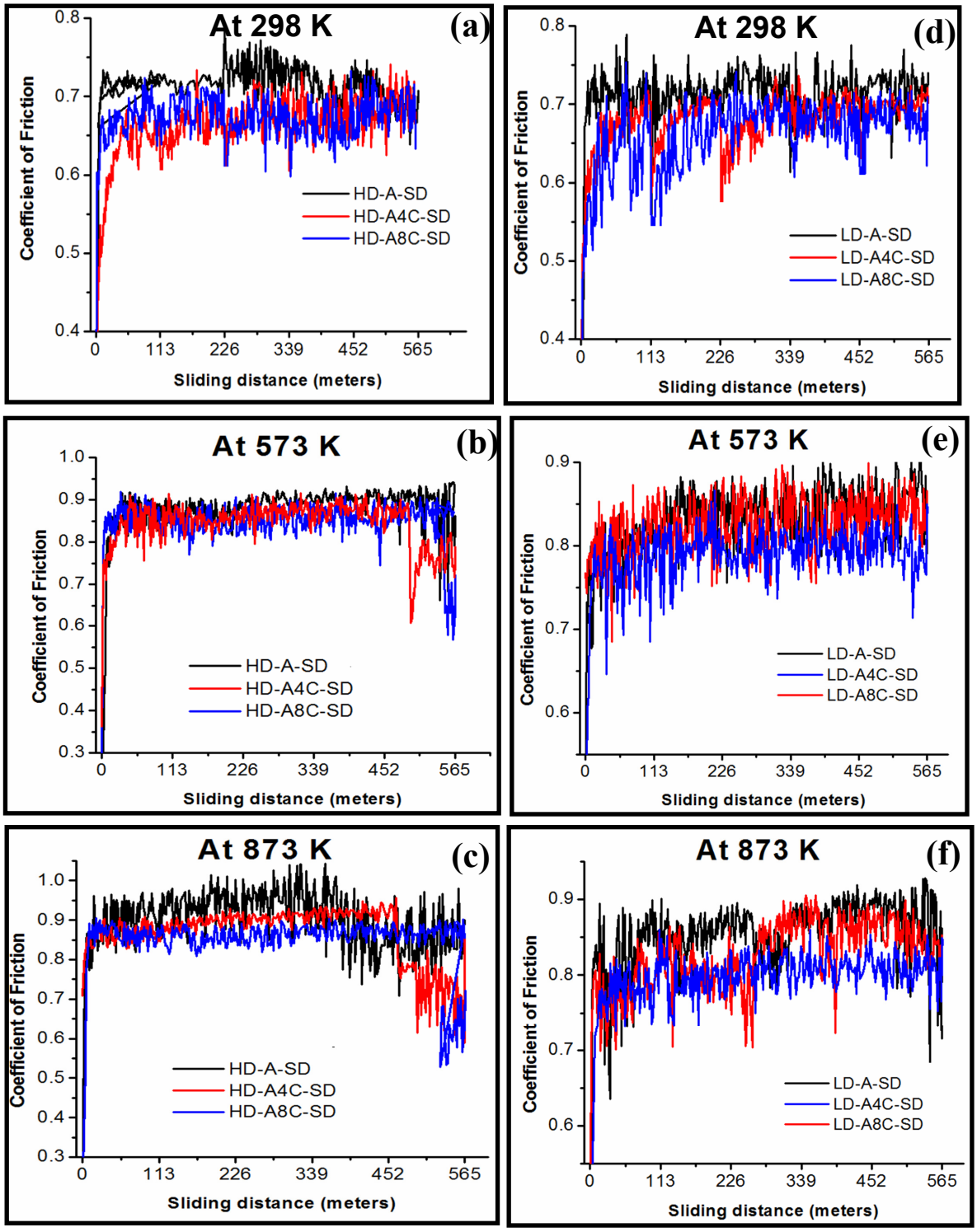

Figure 9.11: Coefficient of friction (COF) with sliding distance at normal load of 30 N for wear track of (a) HD coating at 298 K (b) HD coating at 573 K (c) HD coating at 873 K (d) LD coating at 298 K (e) LD coating at 573 K (f) LD coating at 873 K

Compared to COF curve at 298 K, slightly higher COF was observed for all HD and LD coating at elevated temperatures. This is attributed to higher wear loss and debris generation in all HD and LD coating resulting in higher COF at elevated temperatures. Further, higher fluctuations were observed in COF for LD coatings as compared to HD coatings for all temperatures. This is attributed to higher wear loss and debris generation and repeated formation and breakage of tribochemical film at elevated temperature. COF was marginally lower for CNT reinforced HD and LD coatings at elevated temperature which is attributed to the lubrication effect of graphite layers.

Figures 9.12 and 9.13 show the direct effect of porosity on the wear resistance of coatings at 573 and 873 K. Lower porosity in the coating resulted in lower wear weight

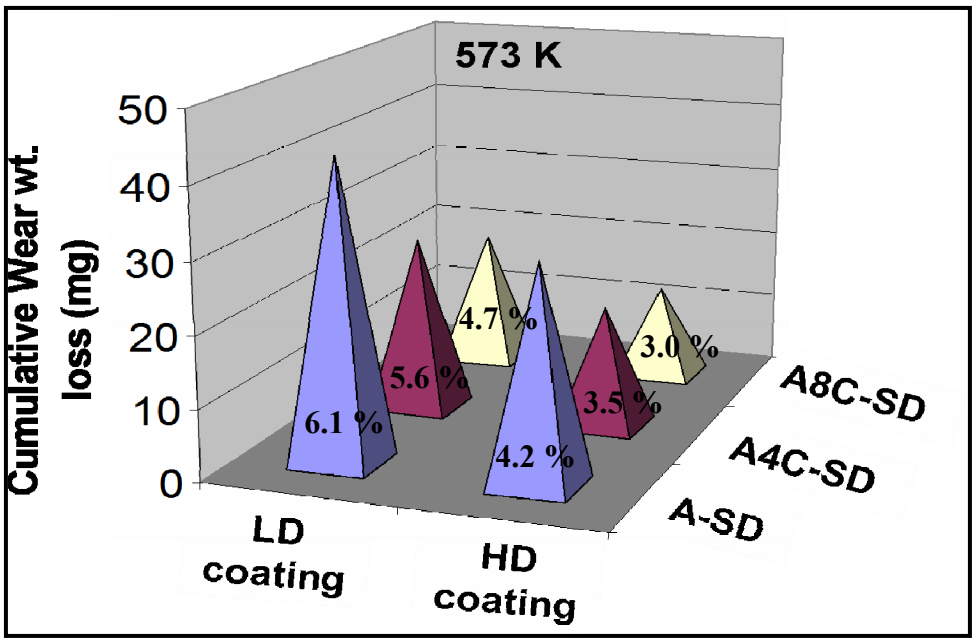

Figure 9.12: Effect of porosity on high temperature (573 K) wear weight loss of HD and LD coating. Percentage value shown inside the pyramid represents the porosity in the coating.

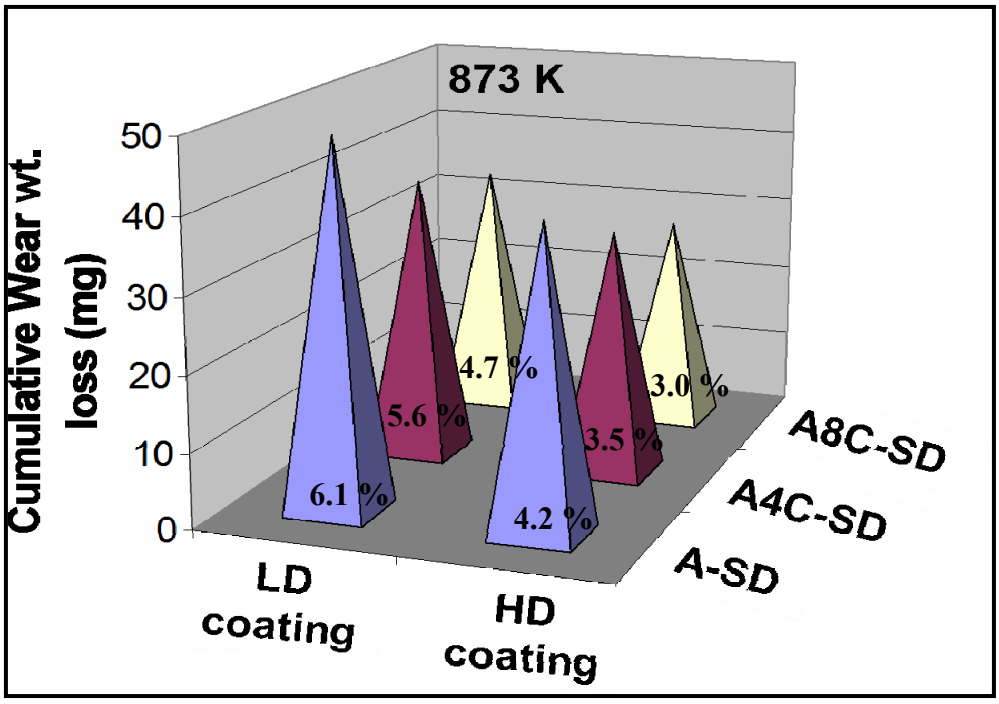

Figure 9.13: Effect of porosity on high temperature (~873 K) wear weight loss of HD and LD coating. Percentage value shown inside the pyramid represents the porosity in the coating.

loss at high temperatures. Hence, tailoring the porosity to lower level by optimizing plasma process parameters leads to higher wear resistance of coating even at higher temperature.

9.2 High Temperature Tribological Behavior of CVD Al_2O_3-CNT Coatings

Figure 9.14 shows the wear weight loss of Al_2O_3 and ICP-1 coatings at room temperature, 573 K and 873 K. It is emphasized that wear test for Al_2O_3 and ICP-1 coatings was conducted using WC ball as counter body. The weight loss increases with the temperature for Al_2O_3 coating while its decreases for ICP-1 coating. At room

temperature, relative improvement in the wear resistance of ICP-1 coating was found to be 12% while at 573 K and at 873 K, relative increase in the wear resistance of ICP-1 coating was found to be 56% and 82%, respectively. Wear surface of both coatings have been analyzed carefully to understand the high temperature tribological behavior of the coatings.

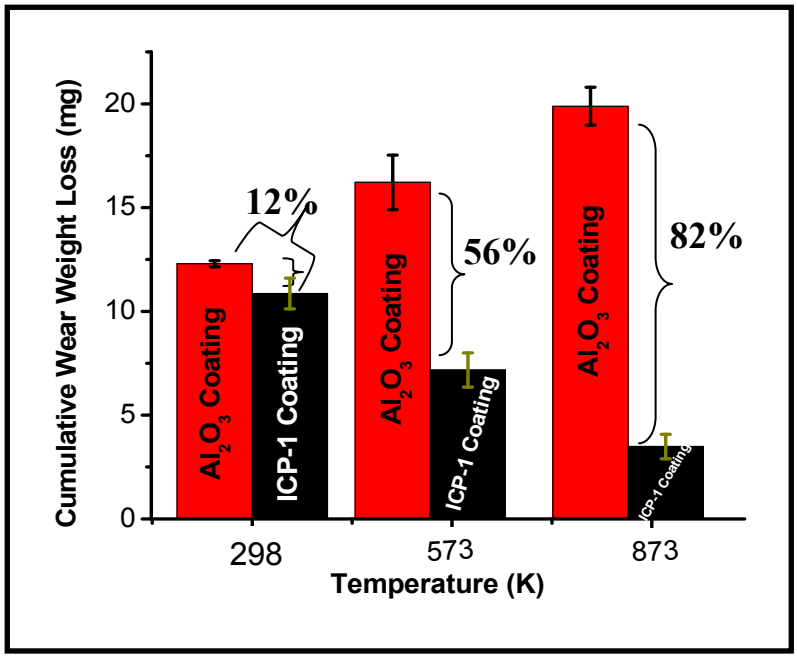

Figure 9.14: Wear weight loss of Al_2O_3 coating and ICP-1 coating at 298 K, 573 K and at 873 K. At 298 K, relative improvement in wear resistance of ICP-1 coating was 12% while at 573 K and at 873 K, relative increase in the wear resistance of ICP-1 coating was 56% and 82% respectively.

Figures 9.15a-c shows the micrographs of the wear surfaces of the Al_2O_3 coating sliding against WC ball at 298 K, 573 K and at 873 K respectively. Similarly, Figures 9.15d-f are the micrographs of the wear surface of the ICP-1 coating at 298 K, 573 K and

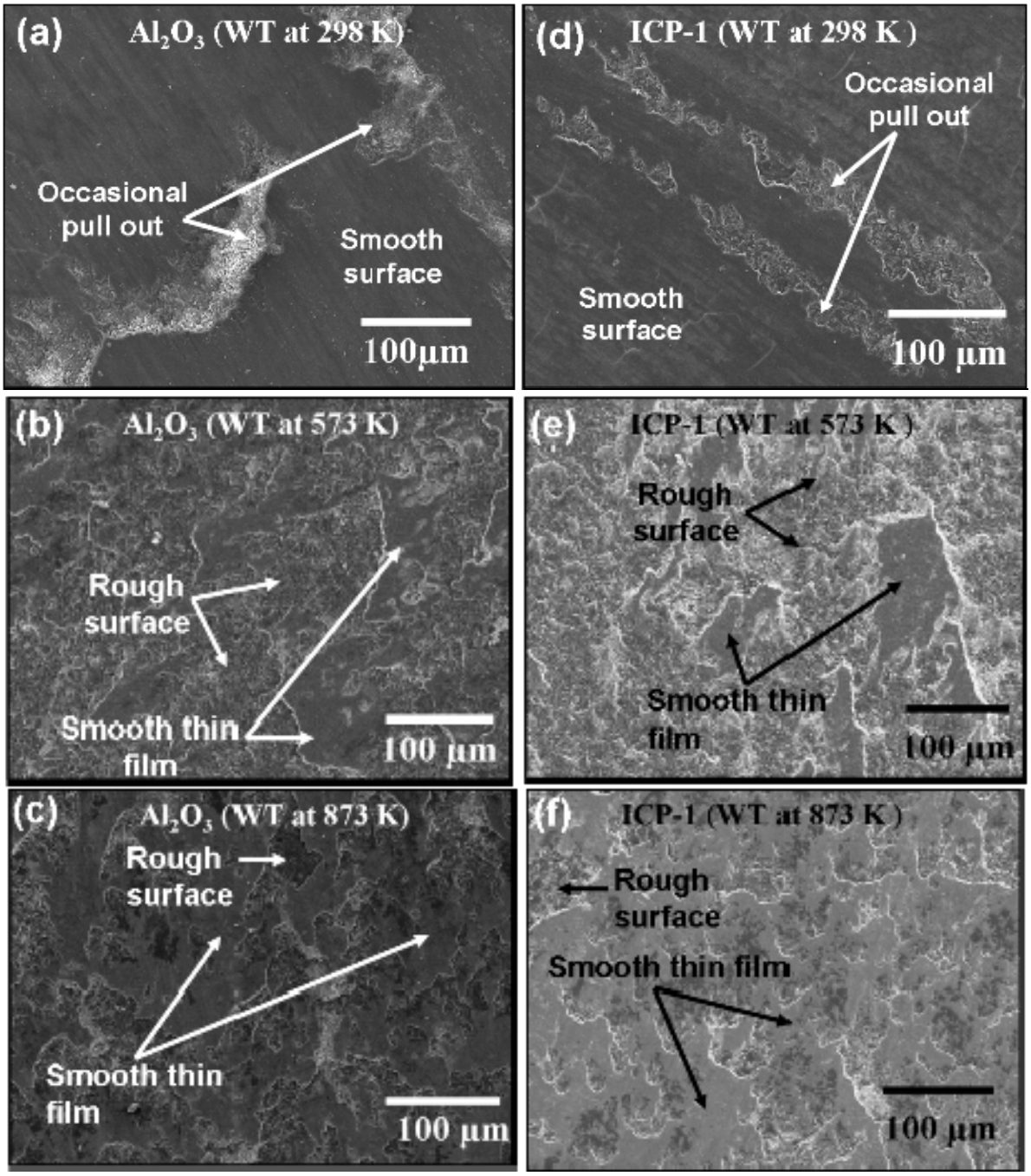

Figure 9.15: Wear surface topography after the linear sliding distance of ~565 meters (a) Al_2O_3 coating at 298 K showing smooth wear surface and occasional pull out (b) Al_2O_3 coating at 573 K showing rough surface and covered with smooth thin film (c) Al_2O_3 coating at 873 K showing rough surface and covered with smooth thin film (d) ICP-1 coating at 298 K showing smooth wear surface and occasional pull out (e) ICP-1 coating at 573 K showing rough surface and covered with smooth thin film (f) ICP-1 coating at 873 K showing rough surface and covered with smooth thin film

873 K respectively. SEM images in Figures 9.15 a and d show the mild wear occurs in both coatings at room temperature resulting in smoother surface. Occasional pull-out of lamellae was also observed at the room temperature. In contrast, wear surface had rough surface and was covered with discontinuous smooth thin film at elevated temperatures, as shown in Figures 9.15b, c, e, and f. Rough wear surface indicates the phenomena of severe wear while the discontinuous smooth thin film from due to tribochemical reaction at the elevated temperatures. Similar, wear phenomena has been observed for WC counterface. Figure 9.16a and b shows the unworn and worn surface of the WC ball. Compared to unworn surface, worn surface has rough region indicating the severe wear phenomena. Also, discontinuous thin film was also observed at the worn surface which might be due to tribochemical reaction.

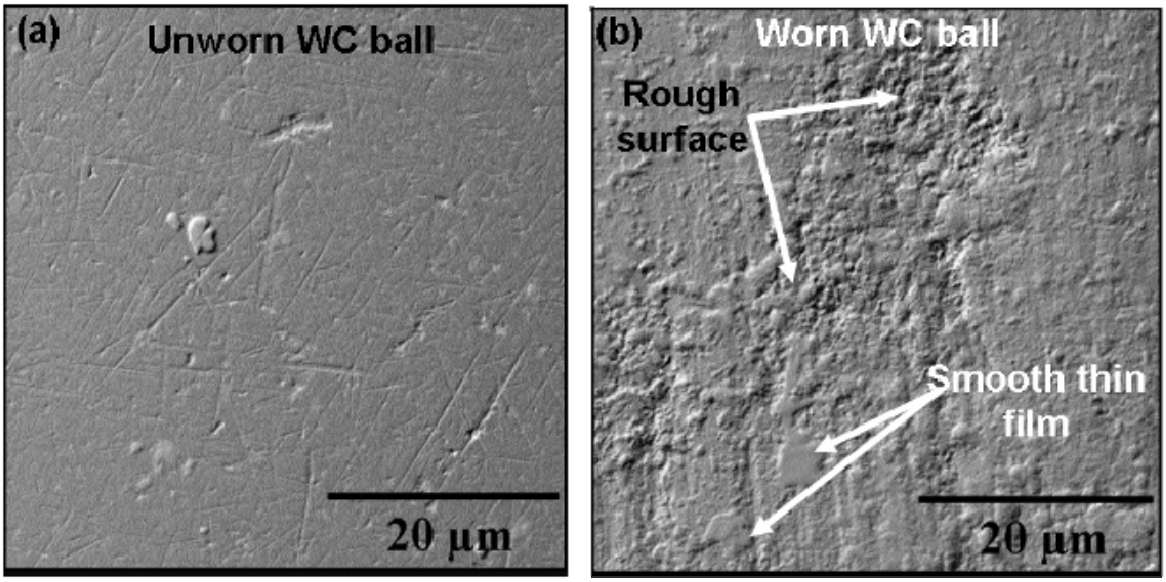

Figure 9.16: SEM micrograph of unworn WC ball (b) worn WC ball after wear at 873 K

Figure 9.17 shows the elemental X-ray maps of wear track of Al_2O_3 coating at 873 K. Figure 9.17a is the back scattered image of wear track and Figures 9.17b and c confirm the formation of thin film containing large amount of tungsten with traces of cobalt respectively. Presence of tungsten and cobalt in the wear track suggests that tungsten carbide ball oxidized at the elevated temperature and a layer was transferred to the wear surface of the coatings. Figures 9.17d and e showed the signature of aluminum (Al) and oxygen (O) respectively which has come from the Al_2O_3 matrix while Figure 9.17f showed the presence of carbon (C) which might have come from protective film of WC. Figure 9.18 is the elemental X-ray map of wear track of ICP-1 coating at 873 K. Figure 9.18a is the back scattered image of wear track and Figure 9.18b and c confirms the presence of tungsten and cobalt respectively in the wear track which is as a result of transferred oxidation product of tungsten carbide ball. Similar to wear track of Al_2O_3 coating, wear track of ICP-1 coating also gave the signature of Al (Figure 9.18d), O (Figure 9.18e), and C (Figure 9.18f). Similar phenomenon was observed at 573 K but only 873 K results are presented for the sake of brevity.

Oxidation reactions of WC-Co at room temperature and elevated temperature were analyzed with the help of FactSage thermochemistry software [146]. Equations 9.6-9.9 show probable oxidation reactions at difference temperatures and their associated Gibbs free energy. All reactions show formation of WO_3 as the reaction product. Moreover, Gibbs free energy becomes increasingly negative with the increasing temperature confirming thermodynamic stability of WO_3 formation. Oxidation product also shows the formation of cobalt tungstate ($CoWO_4$) complex oxide and gaseous

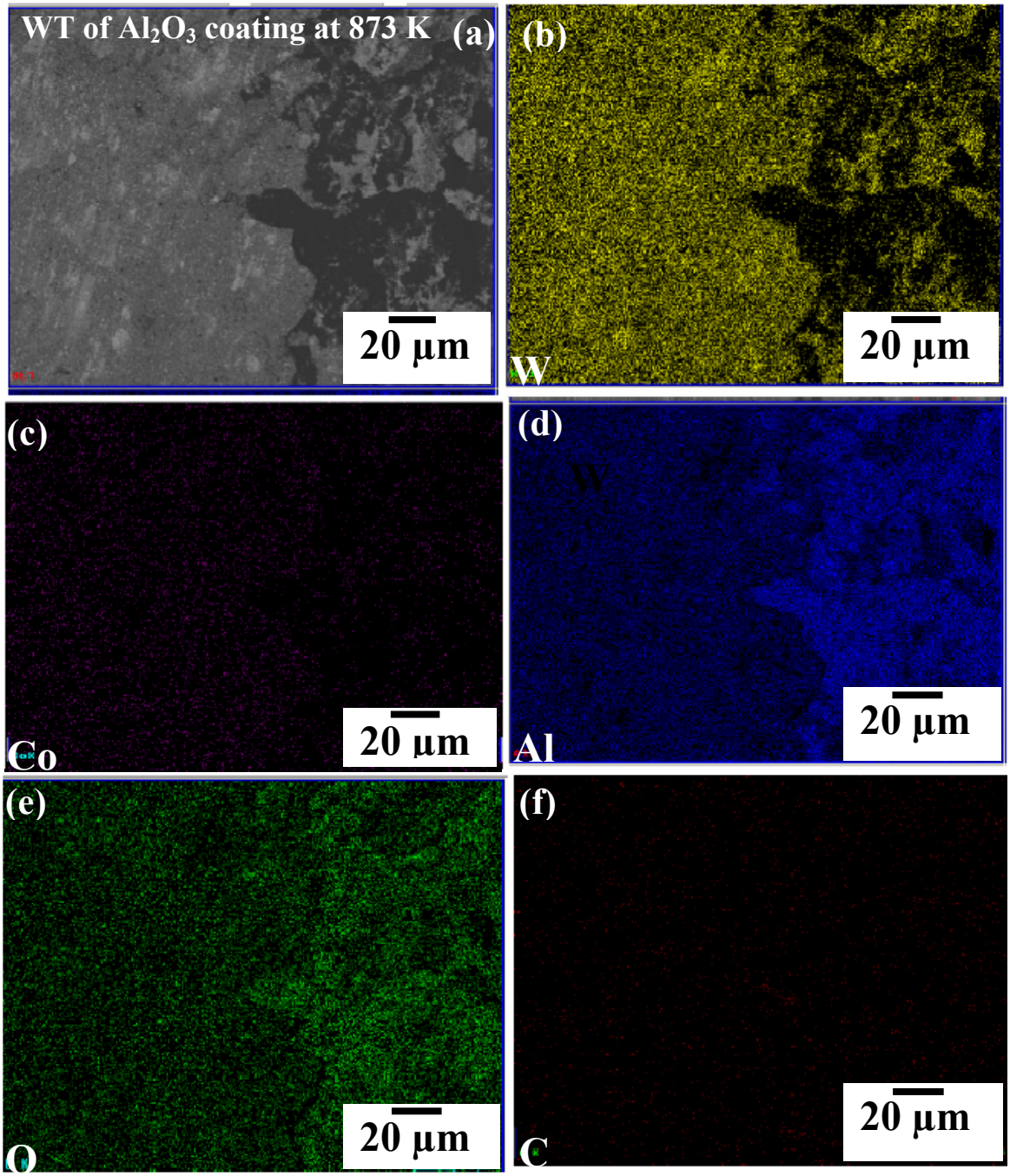

Figure 9.17: X-ray map of wear track of Al_2O_3 coating at 873 K showing (a) back scattered image of wear track (b) distribution of tungsten (c) distribution of cobalt (d) distribution of aluminum (e) distribution of oxygen (f) distribution of carbon.

.

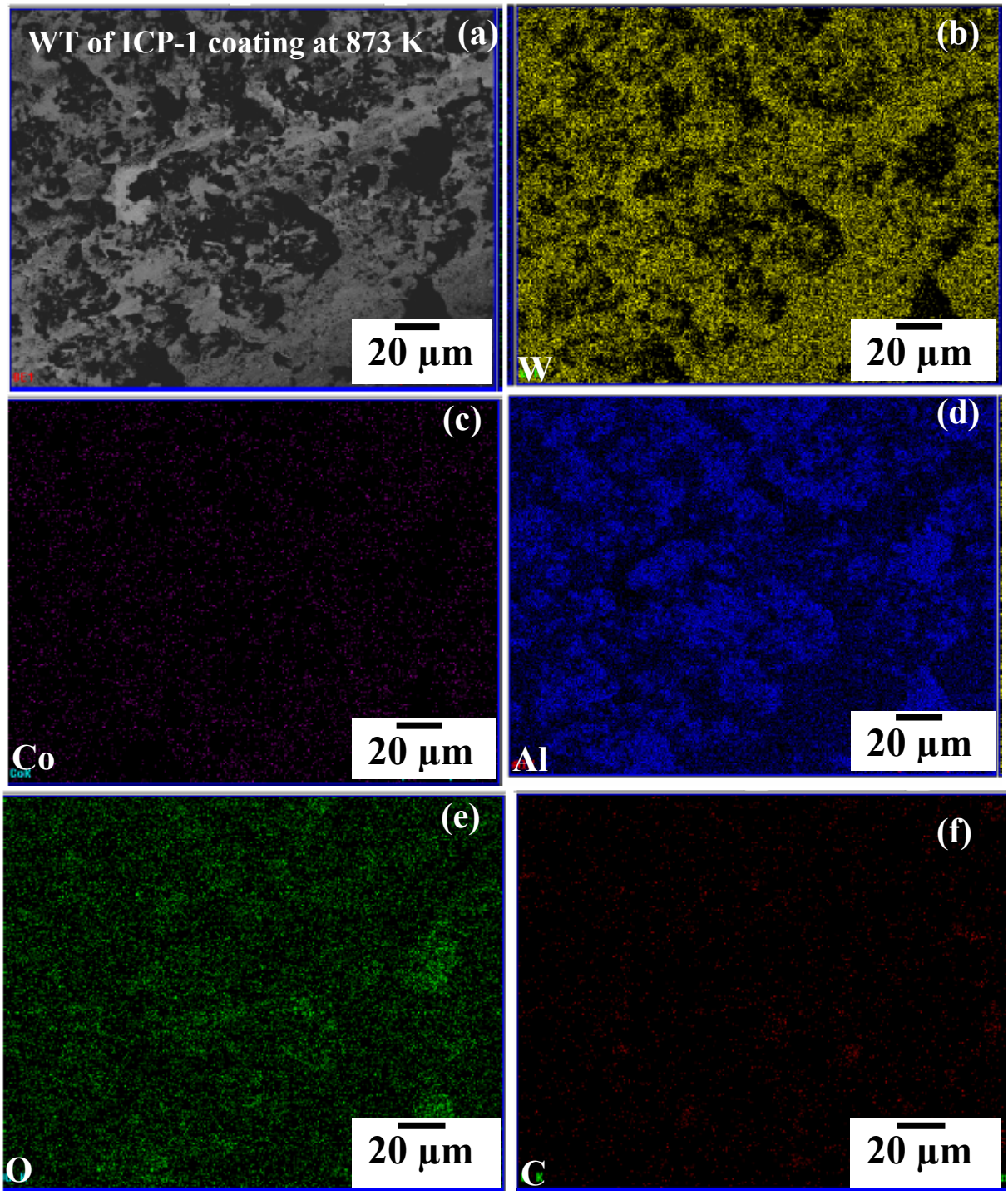

Figure 9.18: X-ray map of wear track of ICP-1 coating at 873 K showing (a) back scattered image of wear track (b) distribution of tungsten (c) distribution of cobalt (d) distribution of aluminum (e) distribution of oxygen (f) distribution of carbon.

carbon dioxide (CO_2). Voinovich et al. [154] mentioned that cobalt binder undergo more intensive oxidation and form complex oxide $CoWO_4$ with WO_3

At 298 K: $0.94\ WC + 0.06\ Co + 1000\ O_2 = 997.5\ O_2 + 0.93\ CO_2 + 0.88\ WO_3 + 0.06\ CoWO_4 \quad \Delta G = -45.1 * 10^3\ kJ$ (9.6)

At 573 K: $0.94\ WC + 0.06\ Co + 1000\ O_2 = 997.5\ O_2 + 0.93\ CO_2 + 0.88\ WO_3 + 0.06\ CoWO_4 \quad \Delta G = -88.7 * 10^3\ kJ$ (9.7)

At 873 K: $0.94\ WC + 0.06\ Co + 1000\ O_2 = 997.5\ O_2 + 0.93\ CO_2 + 0.88\ WO_3 + 0.06\ CoWO_4 \quad \Delta G = -141.1 * 10^3\ kJ$ (9.8)

At 1173 K: $0.94\ WC + 0.06\ Co + 1000\ O_2 = 997.5\ O_2 + 0.93\ CO_2 + 0.88\ WO_3 + 0.06\ CoWO_4 \quad \Delta G = -197.1 * 10^3\ kJ$ (9.9)

The formation of WO_3 film was experimentally validated by performing XPS analysis of the wear surface of the coatings at elevated temperature (873 K). XPS technique allowed measurement of the oxidation state of very thin layer on the wear track (EDS results also confirmed the presence of the W, Co and Al in the wear track). The XPS analysis on the worn surfaces (873 K) of Al_2O_3 and ICP-1 coatings reveals the presence of tungsten 6+ valence state as shown in survey and multiplex XPS data (Figure 9.19a & b). The major peak of W^{6+} ($4f_{7/2}$) was observed near 35.4 eV which is in good agreement with the reported literature value [155]. Because the tungsten is most stable in its 6+ oxidation state this confirm the formation of thin oxide layer of WO_3. It has been reported that the WC-Co has shown excellent wear resistant at ambient temperature and has poor high temperature oxidation resistant and degrade by forming oxide [156, 157]. A similar behavior is observed in the present study where WC degraded at 873 K to form a transfer layer on the coating.

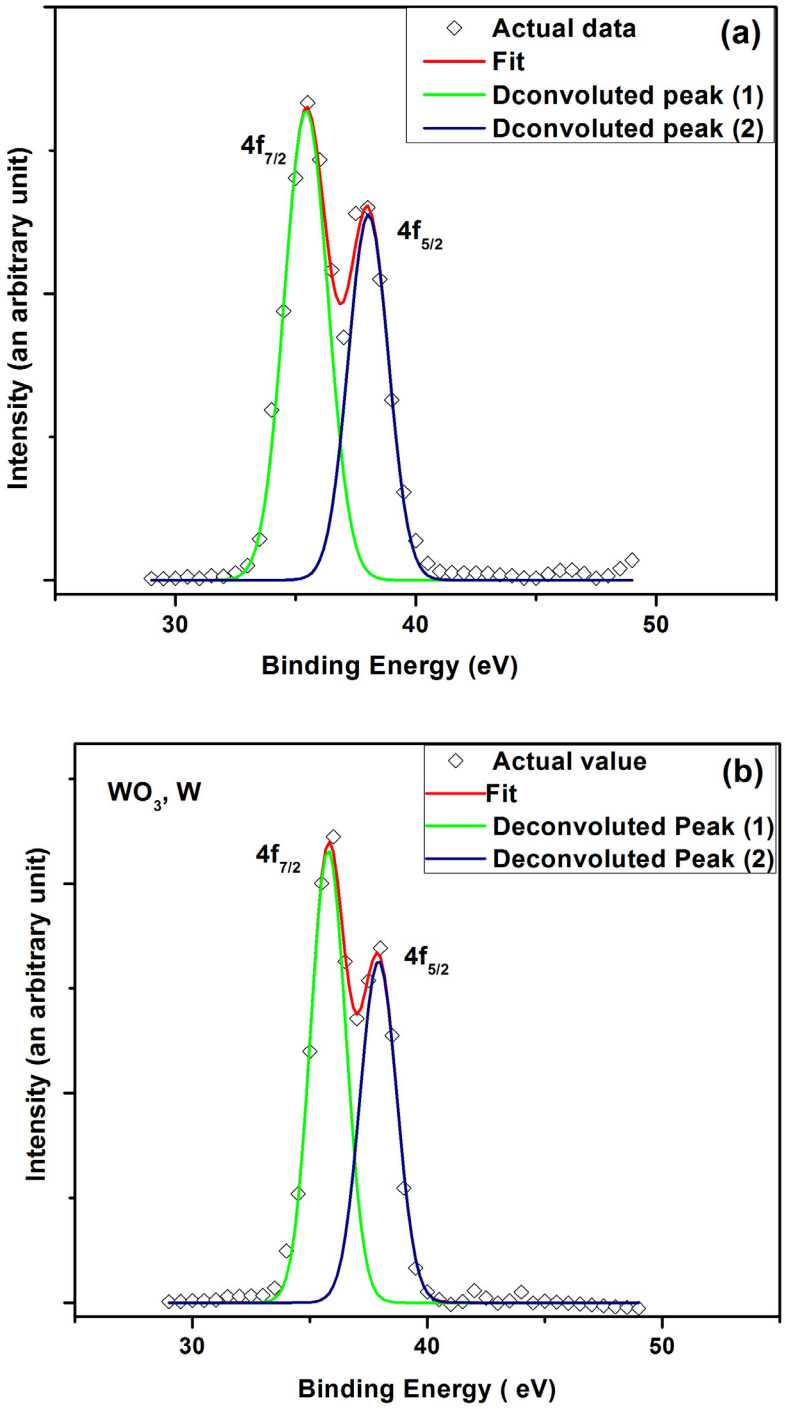

Figure 9.19: XPS spectra collected from (a) wear track of Al_2O_3 coating at 873 K (b) wear track of ICP-1 coating at 873 K. Both the spectra shows the major peak of W^{6+} ($4f_{7/2}$) confirming the formation of thin WO_3 layer on the surface of wear track.

The percentage of area covered by the transferred thin film (WO_3 and traces of Co) on the wear track of coating was measured from three or more wear track images using Image J software. Table 9.4 shows the fraction of the area coverage of the transferred WO_3 film on Al_2O_3 and ICP-1 coatings at different temperatures. From Table 9.4, it can be concluded that amount of transfer layer on the

Table 9.4: Area fraction of transferred thin film on the wear track*

	Area fraction of transferred thin film at 573 K	**Area fraction of transferred thin film at 873 K**
Wear track of Al_2O_3 Coating	0.20	0.52
Wear track of ICP-1 Coating	0.27	0.72

*No film formation was observed on the wear track at 298 K.

wear track increases with the increasing temperature for both coatings indicating the higher rate of tribo-oxidation reaction at the elevated temperature. Further, higher transfer of WO_3 containing film in case of ICP-1 coating is attributed to the higher hardness of ICP-1 coating which leads to more intense wear of WC ball. It is recalled that transferred thin film to the wear track acts as a protective layer and can protect the surface effectively against further wear of coating[112, 147]. This phenomenon dominates in the ICP-1 coating which shows the higher area fraction of the transfer film at 873 K and hence least wear (Figure 9.14).

Increasing weight loss of Al_2O_3 coating with temperature (as seen in Figure 9.14) can be understood in terms of two competing phenomenon: (i) hardness of Al_2O_3 coating

which decrease with temperature increase and (ii) presence of protective layer at the elevated temperature. Evans and Marshall equation [110] (Equation 8.2) clearly indicates that high fracture toughness of the material will result in enhanced wear resistance of the coating at room temperature. However, with the increase in temperature, elastic modulus and hardness both changes and can affect the wear property of the material. Gonzalez et al. [158] mentioned that elastic modulus of Al_2O_3 decreases very slowly up to about 600°C (873 K) and decreases more sharply above this temperature.

Recalling Equation 9.5 (i.e. temperature dependence of ceramic hardness), it is expected that hardness of Al_2O_3 coating decreases with the elevated temperature which will ultimately lead to high wear rate of the coating. Since, small area (20%) of wear surface of Al_2O_3 coating is covered with the protective layer at 573 K, severe wear occurs at the unprotected area due to reduced hardness. Ultimately, severe wear of unprotected surface dominates over the protective layer and hence total wear loss of the Al_2O_3 coating increased at 573 K in comparison to 298 K. In case of 873 K, even if the wear surface of Al_2O_3 coating is half (~52%) covered with protective layer, it is expected that there is drastic reduction (~67%) in hot hardness of Al_2O_3 coating at 873 K leading to severe wear in the unprotected area. The degree of material removal is more intense in case of 873 K than 573 K due to very low hardness of Al_2O_3 coating at 873 K. Hence, highest wear loss is observed for Al_2O_3 coating at 873 K.

In contrast, wear loss of ICP-1 coating shows a decreasing trend with the increasing temperature. Figure 9.20a shows the CNT bridging in the wear track of ICP-1

coating at 573 K. CNT bridges increases very likely coating cohesion (cohesion between splats) to reduce the wear loss. Even if the hardness of ICP-1 coating decreases at 573 K, ICP-1 coating has higher hardness (~15%) and higher elastic modulus than Al_2O_3 coating and relatively large part (27 %) of the wear surface is covered with the protective layer. CNT bridging was also observed in the wear track of ICP-1 coating at 873 K (Figure 9.20b). Further, 72% of the wear surface is covered with the protective layer in ICP-1 coating at 873 K. These two mechanisms dominate over the wear of the ICP-1 coating due to lower hardness at 873 K and hence overall wear resistance of ICP-1 coating increased at 873 K. Also, relative higher transfer of protective layer in the wear track of ICP-1 coating at the elevated temperature contributes towards the weight gain of the ICP-1 coating and hence shows lower wear loss.

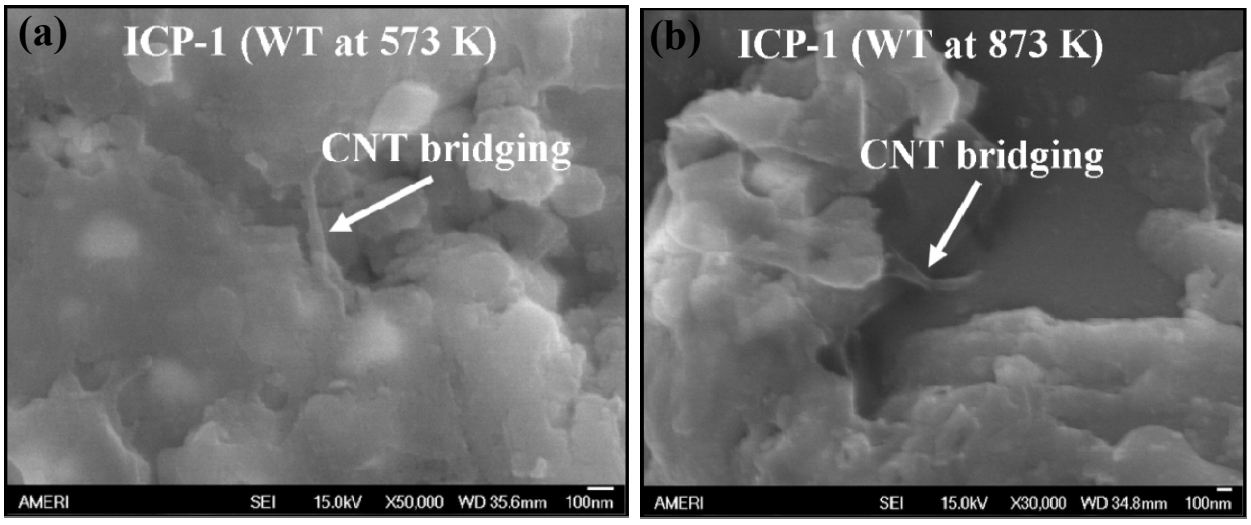

Figure 9.20: High magnification SEM image of wear track (WT) of (a) ICP-1 coating at 573 K and (b) ICP-1 coating at 873 K showing the CNT bridging between the splats.

The stability of CNT structure at elevated temperatures has been debated by several researchers. CNT oxidation at the elevated temperature can significantly degrade its mechanical properties [159]. Researchers have different opinion on the oxidation behavior of CNTs at elevated temperature [151, 160-162],which is already explained in section 9.1. It is recalled, oxidation of CNT occurs above 440°C with a severe oxidation at 550°C-600°C [151]. However, Zhang et al. [162] mentioned that oxidation resistance of CNTs depends on the degree of graphitization, content of the metallic catalyst particle, surface group and the local heat effects. Purified MWCNT exhibits higher activation energy for oxidation [162] (activation energy for oxidation of as-received MWCNT: 166.38 kJ/mol, activation energy for oxidation of purified CNT: 287.13 kJ/mol) resulting in improved oxidation resistance in air than as-received CNTs [162]. Similar finding was observed by Huang et al. [160], who mentioned that purified CNT is more stable towards oxidative destruction than the raw CNTs.

I_D/I_G ratio was calculated for the ICP-1 powder and for ICP-1 coating from Figure 6.8, which has been tabulated in Table 6.2. The I_D/I_G ratio for starting ICP-1 powder is 1.56 which decreased to 0.98 for plasma sprayed ICP-1 coating. Reduction in I_D/I_G ratio indicates the lower defect and high purity of CNTs in the ICP-1 coating. Several studies have confirmed the purification and graphitization of CNTs at high temperature [141, 144, 160, 161]. Huang et al. [160] performed high temperature (2000°C) annealing of CNT and found that purity of CNT increased resulting in higher degree of graphitization. High temperature annealing of CNTs leads to refinement of graphene shell structure [152] by (a) reducing the interlayer spacing between CNT walls and (b) by eliminating

the catalyst particle embedded in CNT i.e. by sublimation of catalyst particle. It is envisaged that higher degree of graphitization and purification of CNT also contributes towards the enhanced oxidation resistance of CNTs in ICP-1 coating.

In order to compare the defect generation/graphitization in the CNTs in wear track of spray dried coating and ICP-1 coating at elevated temperature (873 K), Raman spectrum was collected from the worn surface of ICP-1 coating at 873 K.

Figure 9.21 is the Raman spectra collected from worn surface of ICP-1 coating at 873 K and Table 9.5 is the calculated I_D/I_G ratio from the spectra. Lower I_D/I_G ratio was observed from worn surface of ICP-1 coating at 873 K (Table 9.5) which is opposite to worn surface of HD-A4C-SD and HD-A8C-SD coating at 873 K where higher I_D/I_G ratio was observed (Table 9.3). Lower I_D/I_G ratio in ICP-1 coating indicates the graphitization in the wear track while higher I_D/I_G ratio in the spray dried coating indicates more defect generation which might be due to oxidation of CNTs. This is a complex phenomenon to understand. Lower I_D/I_G ratio in ICP-1 coating might be due to combined effect of following facts: (i) enhanced oxidation resistance of CNTs in ICP-1 coating as explained in above section (ii) ~72% of the wear surface of ICP-1 coating is covered with protective layer resulting lesser chance of CNTs to get exposed in the ambient atmosphere (873 K) and (iii) continuous abrading of the wear surface might lead to exposed graphene layer of CNTs from the uncovered area of the wear track. However, compared to ICP-1 coating, slightly higher I_D/I_G ratio from the wear surface of HD-A4C-SD and HD-A8C-SD coating could be as a result of negligible presence of protective

layer on the worn surface of coating. This leads to severe wear of the coating as explained earlier and hence higher probability of CNTs to get exposed in the ambient atmosphere (873 K) causing more defect generation in CNT structure. Also, compared to ICP-1 coating, higher amount of CNT (4 wt. %, 8 wt. %) are present in spray dried coating. This might also lead to higher I_D/I_G ratio as there is higher probability of large amount of CNTs to be present in wear debris which is exposed to ambient atmosphere (873 K).

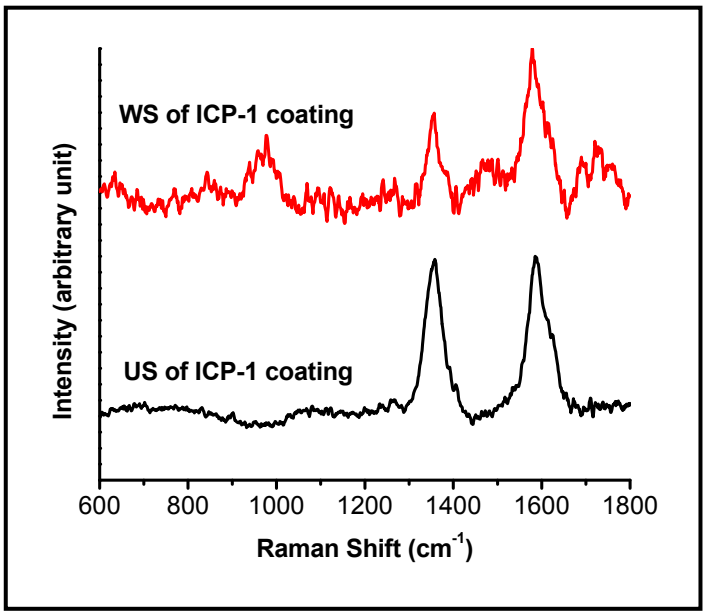

Figure 9.21: Raman spectra of unworn surface (US) and worn surface (WS) of ICP-1 coating at 873 K.

Table 9.5: Ratio of intensity of D and G peaks obtained from Raman Spectroscopy of unworn surface (US) and worn surface (WS) of ICP-1 coating at 873 K.

	Position of D peaks	Position of G peaks	I_D/I_G
US of ICP-1 Coating	1353	1589	0.98
WS of ICP-1 Coating	1354	1580	0.54

COF of Al_2O_3 and ICP-1 coatings as a function of sliding distance at room temperature are shown in Figure 9.22a. Coefficient of friction is almost similar (~0.7) for Al_2O_3 coating at room and elevated temperature. It is recalled that wear surface at the room temperature was smooth due to mild wear. Higher fluctuations were observed for COF of Al_2O_3 coating at 873 K (Figure 9.22b) which is attributed to the debris generation during severe wear condition. The large amount of wear debris dominates the protective film formation and hence results in higher fluctuations in COF for Al_2O_3 coating at 873 K. In contrast, ICP-1 coating has relatively large area (~72%) of wear surface covered with protective layer at 873 K. Hence, film formation dominates over wear debris generation leading to lesser fluctuation in COF value at 873 K (Figure 9.22b).

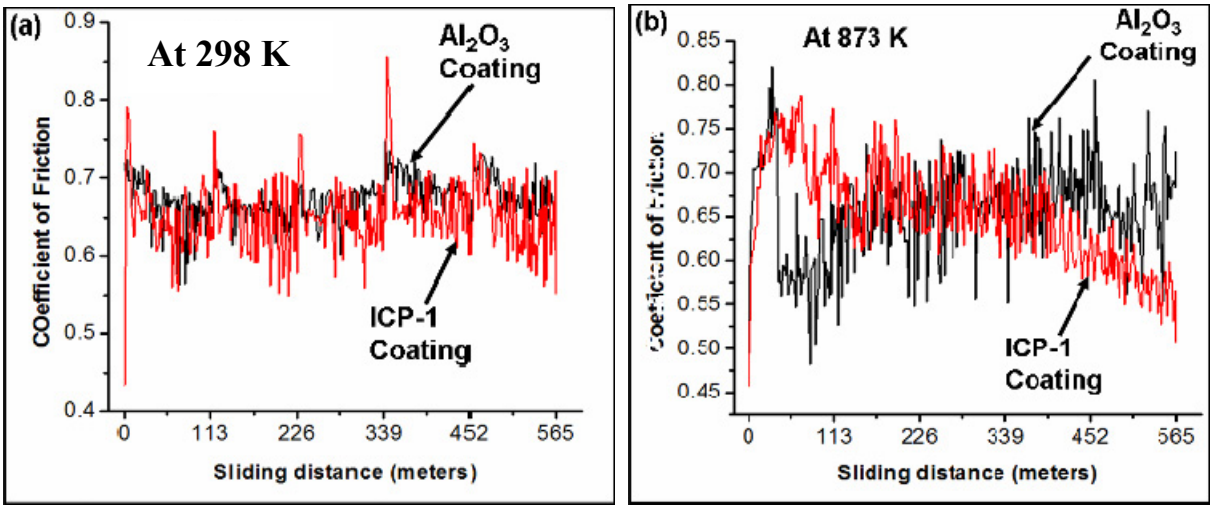

Figure 9.22: Coefficient of friction (COF) of wear track of Al_2O_3 and ICP-1 coating at (a) room temperature (RT) (b) elevated temperature (873 K)

It can be concluded that tribochemical film formation and CNT reinforcement play important roles at high temperature tribological behavior of HD and LD coatings. Counter body has significant effect in the tribochemical film formation. Protective film was observed on the wear track of ICP-1 coating when sliding against WC ball at elevated temperature. With the increasing CNT content, improvement in wear resistance was observed for both spray dried and ICP-1 coatings.

10. SPLAT FORMATION in Al_2O_3-CNT COATINGS

Splat is the smallest unit of microstructure of plasma sprayed coatings. The properties of the coatings are largely dependent on the splat morphology and their stacking. Incomplete melting and improper stacking of splats can result in porosity, poor adhesion at the inter-splat boundary, and micro-cracks, which can severely degrade the properties of the coatings. Hence splat formation and its morphology play the most significant role in dictating the coating properties. The splat morphology mainly depends on (i) feedstock material properties, (ii) in-flight thermal and kinetic state of the particle and (iii) substrate roughness and temperature. In this section, splat formation mechanism and morphology in high and low density Al_2O_3-CNT coatings is studied. The role of processing conditions and CNTs in splat formation is addressed. Single splat experiments were restricted to spray dried powder due to lack of CVD grown ICP powder. Splat experiments were conducted using the optimized plasma parameters for synthesizing HD and LD coatings. The aim of selecting these parameters was to understand the splat formation in HD and LD coatings which causes different level of porosity. Splats synthesized at HD coatings parameters will be referred as "HD splats" whereas splats synthesized at LD coating parameters will be referred as "LD splats". HD splats containing 0 wt. % CNT, 4 wt. % CNTs, 8 wt. % CNTs will be referred as HD-A-SD, HD-A4C-SD, and HD-A8C-SD respectively. LD splats containing 0 wt. % CNT, 4 wt. % CNTs, 8 wt. % CNTs will be referred as LD-A-SD, LD-A4C-SD, and LD-A8C-SD respectively. Plasma parameters for synthesizing both set of splats are tabulated in Table-10.1. In-flight particle temperature and velocity measured during the synthesis of

Table 10.1: Plasma process parameters for synthesizing HD and LD splats

Plasma process parameters for synthesizing "**HD" splat**					
Current (A)	**Voltage (V)**	**Primary Gas, Argon (slm)**	**Secondary Gas, Helium (slm)**	**Stand-off (mm) from the substrate**	**Powder feed rate (gram/min.)**
850	40	56.6	59.5	75	3
Plasma process parameters for synthesizing **"LD"** splat					
Current (A)	**Voltage (V)**	**Primary Gas, Argon (slm)**	**Secondary Gas, Helium (slm)**	**Stand-off (mm) from the substrate**	**Powder feed rate (gram/min.)**
750	40	42.5	59.5	75	3

HD and LD splats are tabulated in Table-10.2 and Table-10.3 respectively. Since splat morphology also depends upon the substrate roughness, polished (R_a = 0.03 μm) and grit blasted substrate (R_a = 2.40 μm) were considered as a variable. Two different substrate temperatures (453 K and 553 K) were selected to understand the effect of substrate preheating on the splat formation. Substrate conditions are tabulated in Table 10.4. It should be noted that HD and LD coatings were deposited on the grit blasted substrate (R_a = 2.40 μm) which was preheated to 453 K. Hence, similar substrate condition was kept for synthesizing the one set of splats.

Table 10.2: Measured in-flight particles temperature and velocity during synthesis of HD splat

	Temperature (K)	Velocity (m/s)
HD-A-SD	2745±9	338±0.66
HD-A4C-SD	2423±14	319±0.79
HD-A8C-SD	2397±12	314±0.84

Table 10.3: Measured in-flight particles temperature and velocity during synthesis of LD splat

	Temperature (K)	Velocity (m/s)
LD-A-SD	2495±11	275±0.81
LD-A4C-SD	2319±9	274±0.73
LD-A8C-SD	2306±7	271±0.64

Table 10.4: Substrate condition for synthesizing HD and LD splats

Substrate condition	
Substrate material	Plain carbon steel
Substrate roughness (Ra)	0.03, 2.40
Substrate preheat temperature (K)	453, 553

Splat formation can be optimized by experimentation but it requires extensive and time consuming experiments due to large number of processing variables involved in plasma spraying. Splat morphology simulation for the given processing variables can save considerable amount of time. In this study, splat morphology simulation has also been performed using SIMDROP (Simulent Drop 3.0, Simulent Inc, Toranto, Canada) and comparison has been made with the experimentally obtained splats. The single splat morphology has been correlated with fracture toughness and wear resistance of coatings.

10.1 Effect of Substrate Roughness on Splat Formation

Figures 10.1a and b show the HD-A-SD splats on grit blasted steel (R_a = 2.4 μm) and polished steel substrates (R_a = 0.03 μm) at an initial substrate temperature of 453 K. Due to difficulties in observing the splats on the rough substrate, even with the back scattered electron mode of SEM, splat studies are usually performed on the polished substrate. Similar reason has been mentioned in the literature [115, 163]. Fauchis et al. [115] reported that, 98% of the studies related to splat formation were conducted on the smooth substrate (R_a < 0.2 μm).

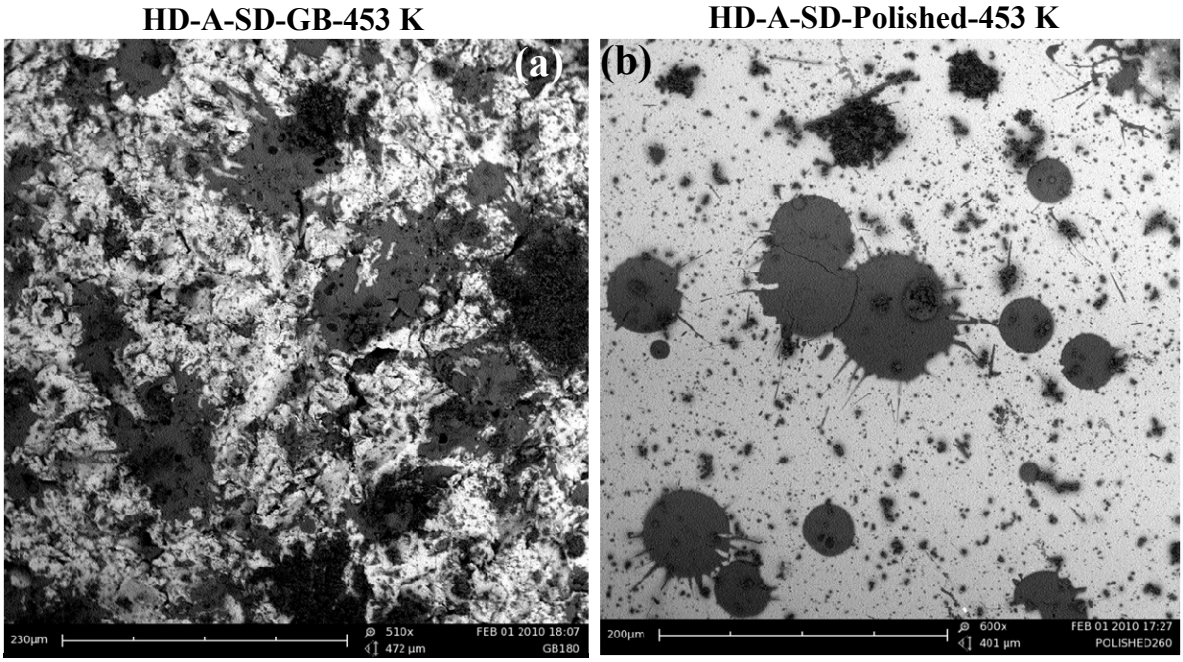

Figure 10.1: Plasma sprayed single splat of HD-A-SD on (a) grit blasted (GB) substrate (b) polished substrate, at initial substrate temperature of 453 K.

Comparing between Figures 10.1a and b, splats obtained on the grit blasted substrate are severely splashed and fragmented whereas splats on the smooth surface have a shape of disc type or disc with fingers. No fragmentation similar to rough grit

blasted surface was observed in Figure 10.1b. The reason behind severely splashed and fragmented splat on the rough substrate is that presence of surface irregularities increase the friction of flowing liquid droplet which leads to splash formation. Moreau et al. [164] studied the effect of surface roughness for molybdenum (Mo) single splat on the glass substrate with varying roughness (R_a) from 0.2 μm to 9.6 μm. A decrease in flattening degree from 7.4 on a smooth substrate to 3.9 on grit blasted substrate was observed, which was attributed to the surface asperities limiting the material flow [164]. Jiang et al. [165] also studied the single splat of Mo on grit blasted steel substrate (R_a = 3.4) and observed severe splashing of the splats, which was attributed to asperities and air pocket entrapped under the liquid droplet. These air pockets expand by the input of heat supplied by the liquid droplet and cause the breakup of splat into small pieces [165]. Apart from the substrate roughness,, the substrate temperature also affects the splat morphology [10, 115, 117]. The effect of substrate preheat temperature on splat formation is discussed in the next section. All single splat experiments presented here were done on smooth surface with R_a= 0.03 μm.

10.2 Effect of Substrate Temperature on Splat Formation

Figure 10.2 shows a matrix of splats obtained for HD and SD coatings for all three compositions at substrate temperature of 453 and 553 K. The aim of showing all HD and LD splats images together is to highlight the effect of substrate temperature and CNT content on the splat morphology. Figure 10.3 is the corresponding high magnification image of Figure 10.2. HD splat morphology changed from splashed and

fragmented to almost disc-shaped with an increase in substrate temperature from 453 to 553 K. Similar phenomena was observed in case of LD splats at 453 K and 553 K.

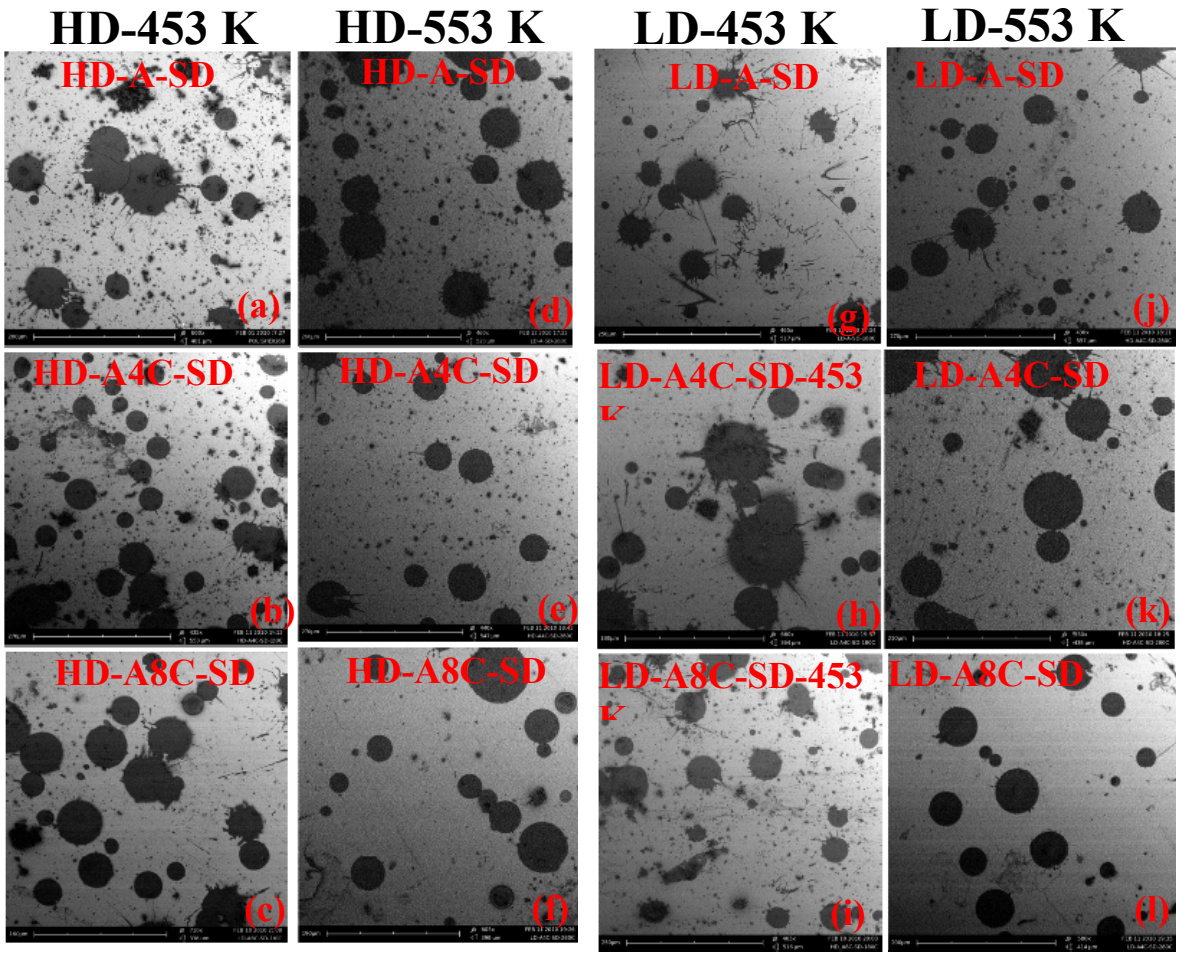

Figure 10.2: Low magnification image of plasma sprayed single splat on polished steel substrate for (a) HD-A-SD (b) HD-A4C-SD (c) HD-A8C-SD, at initial substrate temperature of 453 K (d) HD-A-SD (e) HD-A4C-SD (f) HD-A8C-SD, at initial substrate temperature of 553 K (g) LD-A-SD (h) LD-A4C-SD (I) LD-A8C-SD, at initial substrate temperature of 453 K (j) LD-A-SD (k) LD-A4C-SD (l) LD-A8C-SD at initial substrate temperature of 553 K.

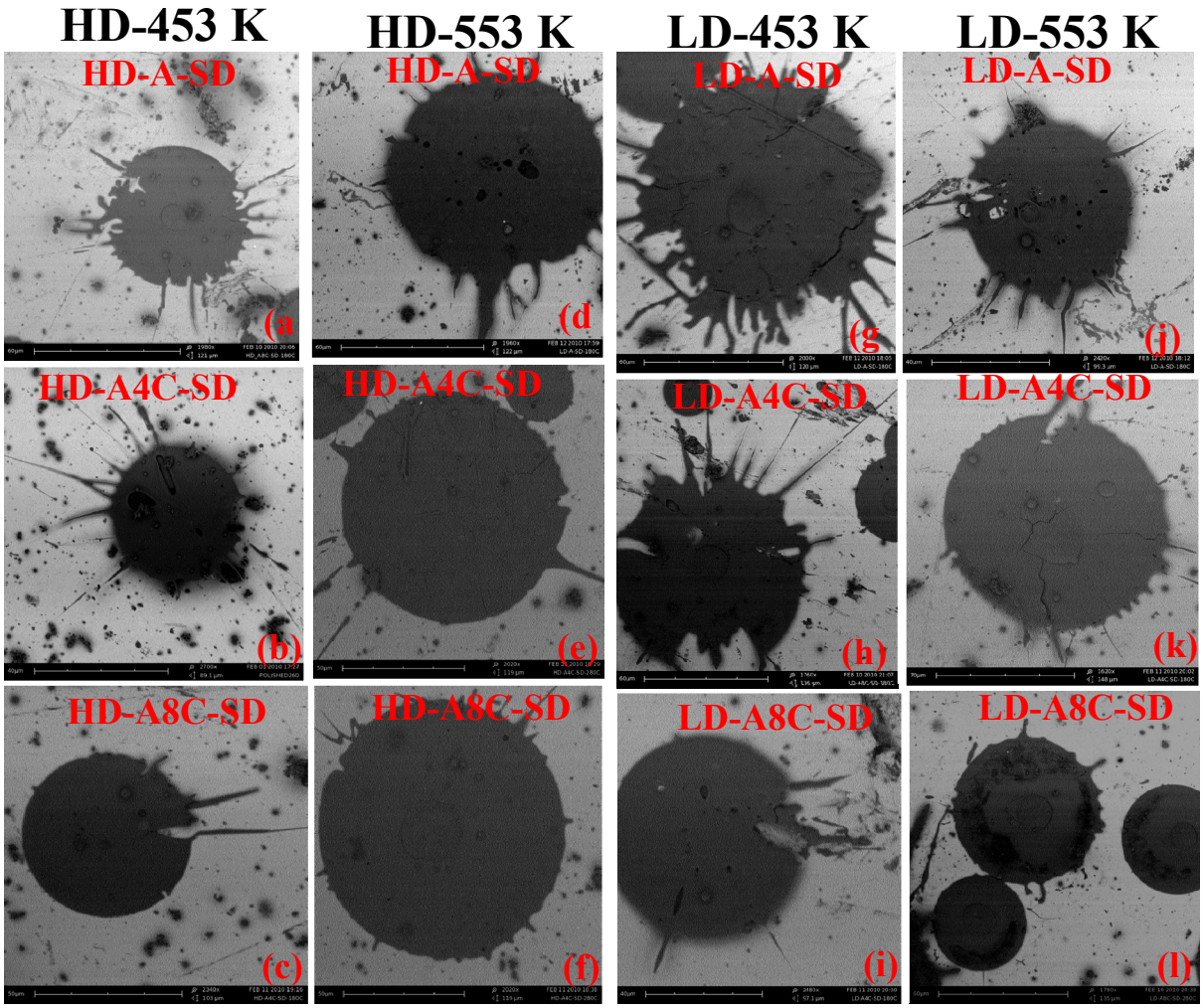

Figure 10.3: High magnification SEM image of plasma sprayed single splat on polished steel substrate for (a) HD-A-SD (b) HD-A4C-SD (c) HD-A8C-SD, at initial substrate temperature of 453 K (d) HD-A-SD (e) HD-A4C-SD (f) HD-A8C-SD, at initial substrate temperature of 553 K (g) LD-A-SD (h) LD-A4C-SD (I) LD-A8C-SD, at initial substrate temperature of 453 K (j) LD-A-SD (k) LD-A4C-SD (l) LD-A8C-SD at initial substrate temperature of 553 K.

An average splat diameter for each case is determined and plotted in Figure 10.4. Figures 10.4a and b shows the variation in splat diameter as a function of substrate preheat temperature for HD and LD splats respectively. Diameter of the fingered splat was calculated by measuring the radius of the splat from the center to the end of the finger. Splat diameter increases with an increasing substrate preheat temperature. The average length of the fingers radiating from the periphery of the splat reduced at higher substrate temperature as seen in Figure Figures 10.5a and b.

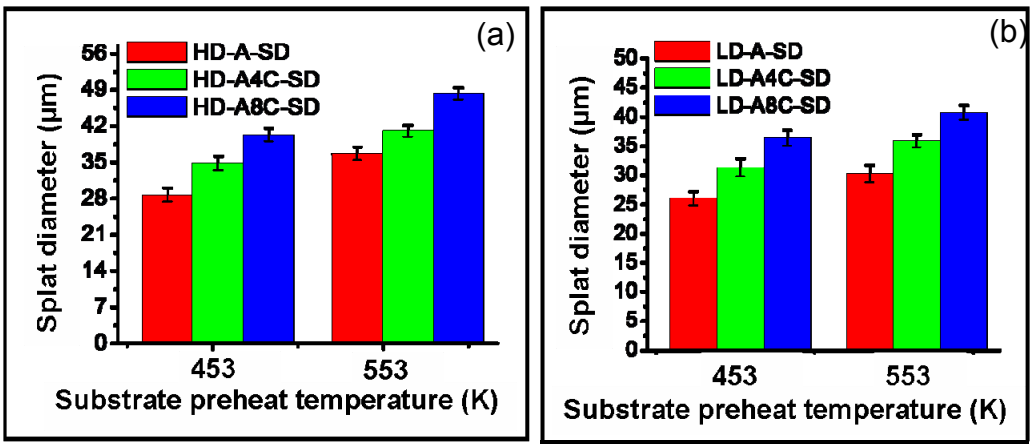

Figure 10.4 Variation in average splat diameter with function of substrate preheat temperature for (a) HD splats (b) LD splats

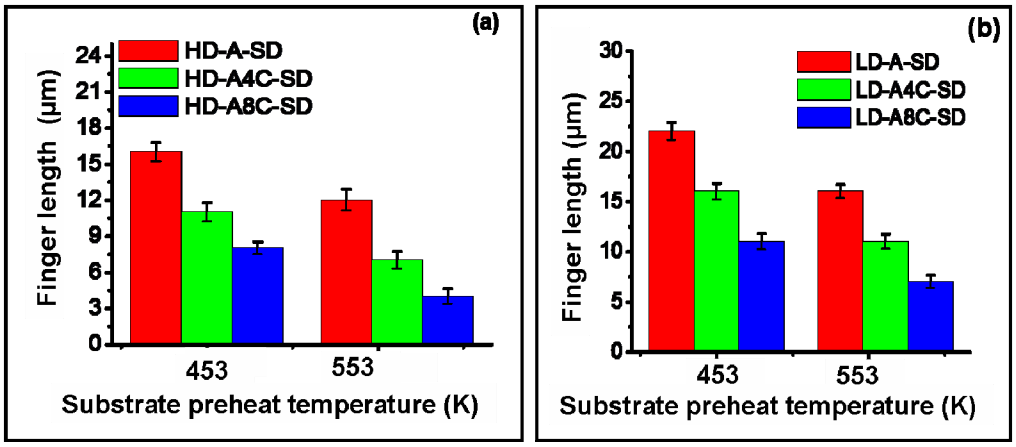

Figure 10.5 Variation in finger length with function of substrate preheat temperature for (a) HD splats (b) LD splats

Though there are few studies [10, 115, 117] which deal with the effect of substrate temperature on splats morphology, still the exact mechanism of splat formation is not completely known. The transition temperature at which splat morphology changes from splashed and fragmented disc to contiguous disc shape further complicates this issue. Vardelle et al. [166] mentioned that nucleation is delayed at higher substrate temperature and the splat remains in molten liquid stage until the spreading is completed. Fukomoto et al. [167] reported that above the transition temperature, solidification of the molten droplet slowed down causing more uniform solidification and hence it does not inhibit the droplet spreading. Splashing and finger formation phenomena at lower substrate temperature (453 K) can be related to localized solidification of the molten droplet which can obstruct the outward spreading liquid resulting in splashing and fingers formation. At higher substrate temperature (553 K), better contact and uniform heat conduction can lower the chance of localized solidification or even delay its initiation until the spreading is completed. This is a plausible reason for relatively higher splat diameter and smaller finger length at higher substrate temperature. Apart from the substrate temperature, CNT content can also affect the splat morphology which is discussed in the next section.

10.3 Effect of CNT Content on Splat Formation

Effect of CNT content on splat morphology can be observed at each substrate temperature for HD and LD splats. Among HD splats at 453 K (Figures 10.2a-c), lower degree of splashing has been observed with an increasing CNT content. Further, Figure 10.4a and b, suggest that with the increasing CNT content, splat diameter increased for

HD an LD splat respectively. Similarly, Figure 10.5a and b shows that with the increasing CNT content, finger length decreased for HD and LD splat respectively. To further see the effect of CNT content, splats geometry has been categorized into four different types as shown in Figures 10.6: (a) disc shape splat (b) splats with finger (c) fragmented splats and (d) splats having pores. Population density of these splats has been plotted as a function of CNT content. Figures 10.7 a-b shows the population density for four types of splat among HD splats at 453 K and 553 K respectively.

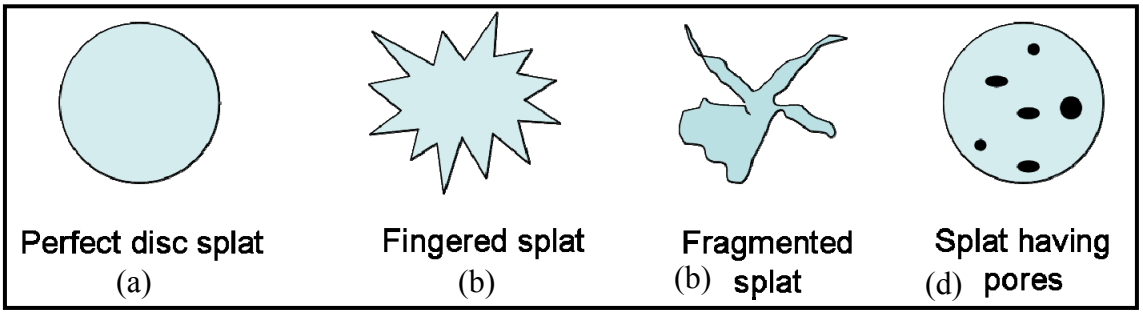

Figure 10.6: Schematic showing different morphology of splats

Similarly, Figures 10.7c-d shows the population density for different types of splat among LD splats at 453 K and 553 K respectively. It interesting to observe that with an increasing CNT content, percentage of disc shape splats increased for all the cases. Population density of splats with finger, fragmented splat and splat having void is lowest for highest (8 wt. %) CNT content. To understand the mechanism behind relatively higher splat diameter, lower finger length, and increased percentage of disc shaped splat, splats were observed in SEM at high magnification. Figures 10.8a-b shows the single splat of HD-A4C-SD and HD-A8C-SD at 453 K respectively while Figure 10.8c-d shows the single splat of LD-A4C-SD and LD-A8C-SD. It is observed that CNTs are well

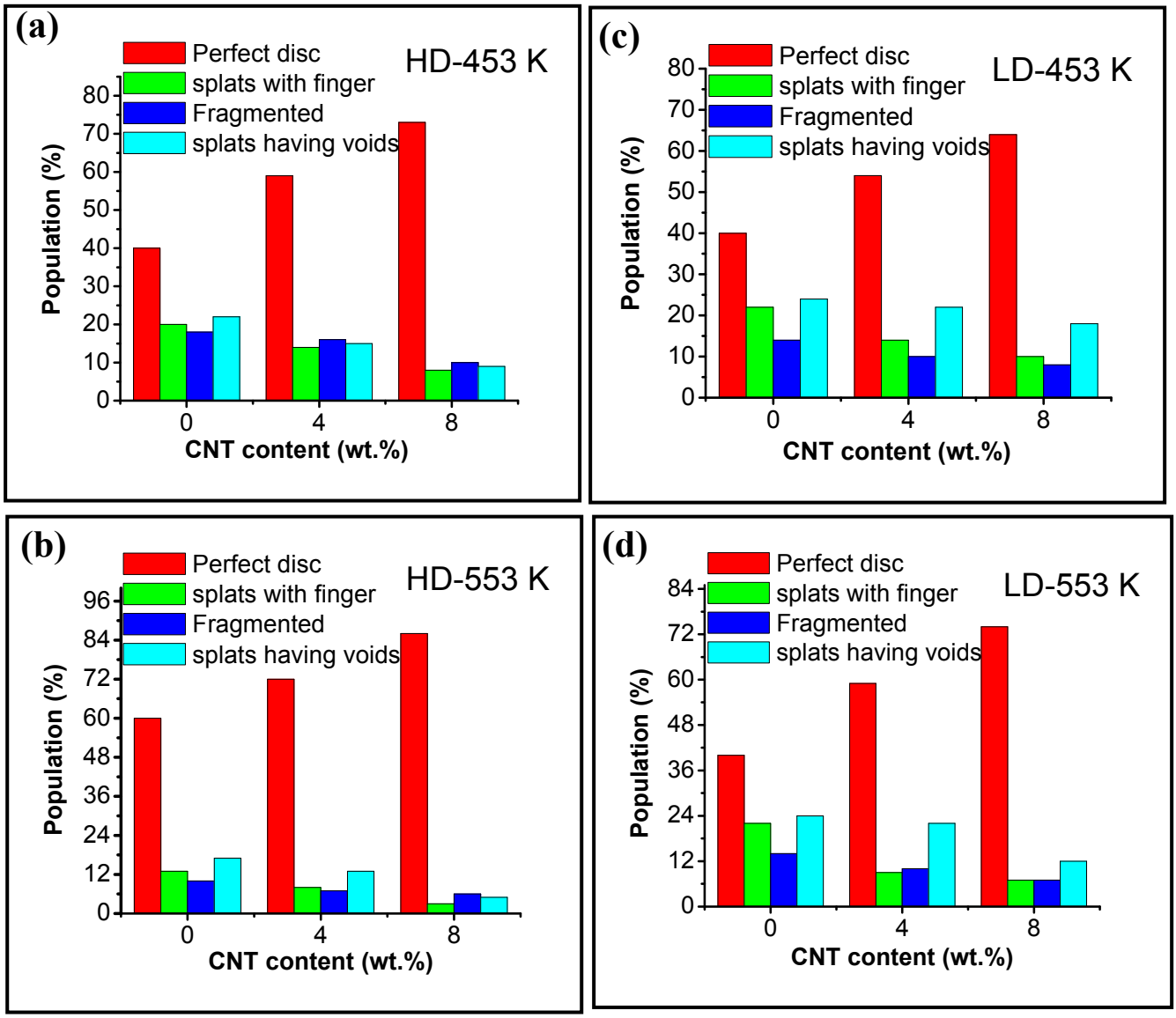

Figure 10.7: Population density of different type of splats as function of CNT content for (a) HD splats at 453 K (b) HD splats at 553 K (c) LD splats at 453 K (d) LD splats at 553 K

distributed in the splat matrix. Higher magnification images of HD-A4C-SD (Figure 10.9a) and HD-A8C-SD (Figure 10.9b) show the CNT agglomeration at the splat

periphery. Higher magnification images of LD-A4C-SD (Figure 10.9c) and LD-A8C-SD (Figure 10.9d) splat also show the CNT agglomeration at the splat periphery.

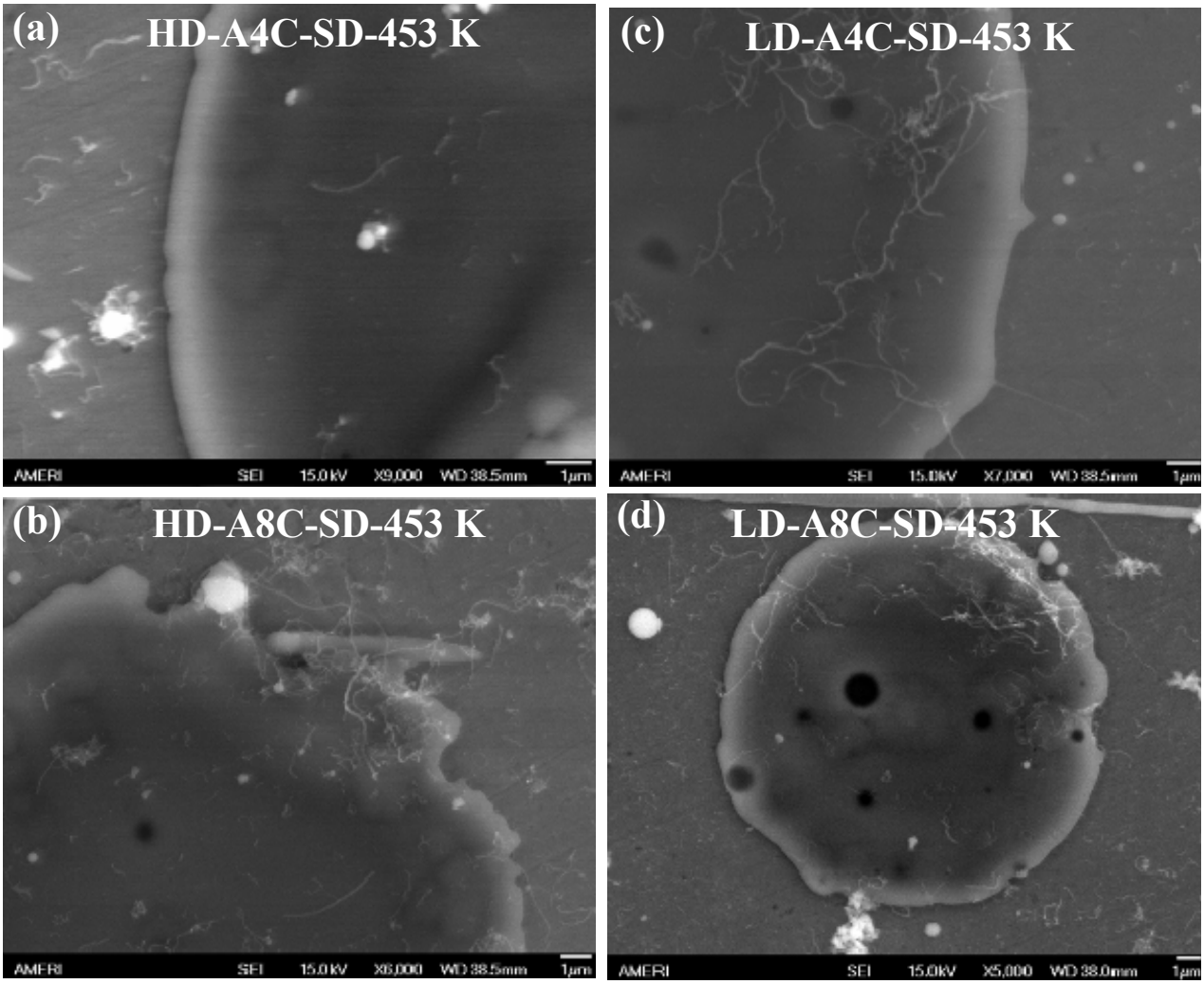

Figure 10.8: SEM image showing single splat of (a) HD-A4C-SD (b) HD-A8C-SD (c) LD-A4C-SD (d) LD-A8C-SD, at initial substrate temperature of 453 K.

There are two simultaneously competing phenomena can be observed with increasing CNT addition which are responsible for increased splat diameter and increased percentage of disc shaped splat.

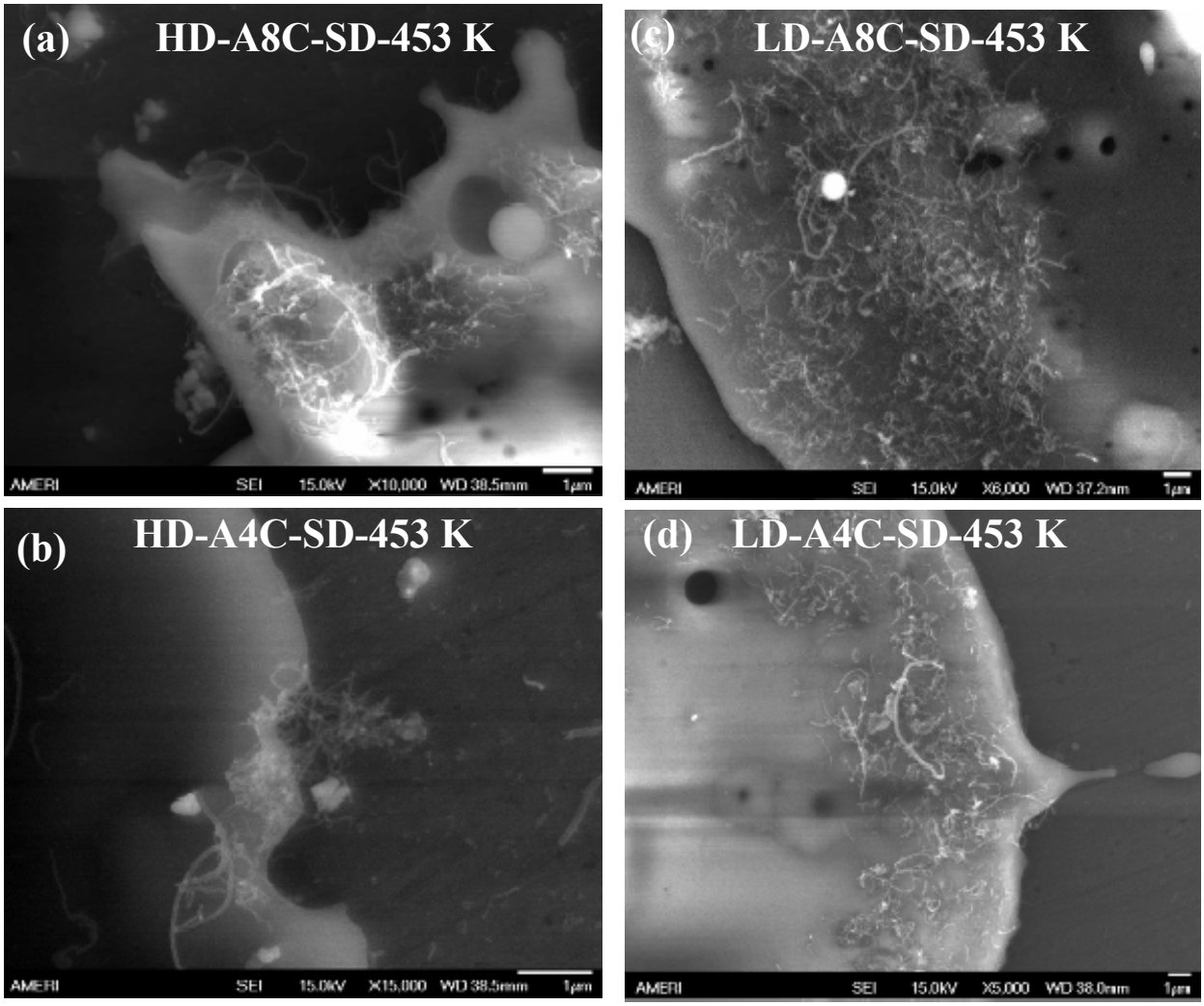

Figure 10.9: High magnification SEM image showing single splat of (a) HD-A4C-SD (b) HD-A8C-SD (c) LD-A4C-SD (d) LD-A8C-SD, at substrate temperature of 453 K

First, *"well distributed CNT*" in the melt (as shown in Figure 10.8) lead to enhanced heat content of the melt resulting lower viscosity of the melt. Heat capacity of C (graphite) is

larger than that for Al_2O_3. Specific heat for graphite is 2.145 $Jg^{-1}K^{-1}$ while for Al_2O_3 it is 1.358 $Jg^{-1}K^{-1}$ at measured in-flight particle temperature of 2400 K [146]. The higher heat content of the melt would increase the time required for heat loss to occur. Hence, localized solidification of the melt will be delayed which can cause the liquid instability. Delaying localized solidification of the melt results in enhanced spreading of the molten liquid resulting in higher splat diameter and smaller fingers size in CNT reinforced splat. (as shown in figure 10.3). Hence, relatively higher splat diameter was observed in case of CNT reinforced splat. Another competing factor is the "*agglomeration of CNT"* (as shown in Figure 10.9) in the periphery of the melt which might lead to increased viscosity. Increased viscosity of the melt will impede the further spreading of the melt and suppress fragmentation. Hence, higher percentage of disc shaped splat was observed in case of CNT reinforced HD and LD splats.

Thus, this is clear that CNT plays an important role in tailoring the splats shape and size which ultimately affect the coatings final property. The experimental optimization of splat geometry by varying in-flight temperature and velocity, CNT content and substrate conditions requires lots of effort and time. The computer simulation of splat can provide valuable information about processing conditions which can be feedback into experiments to save lot of time. Simulation of single splat is discussed in the following section.

10.4 Splat Simulation

Splat simulation was performed for HD and LD splats. Experimental data from the plasma spraying was used as the input parameters for simulations. Simulated splat morphology was compared with experimentally obtained splats. One of the major challenges encountered in simulation was the non availability of the materials properties, especially for CNT reinforced Al_2O_3. The availability of thermophysical properties of carbon nanotubes containing materials in the literature is a rarity. Hence some of the thermophysical properties of CNT reinforced Al_2O_3 were estimated based on the rule of mixtures. Table 10.5 shows the estimated values of the materials property for three materials (A-SD, A4C-SD, and A8C-SD), which were used as input for splat simulation using SIMDROP software.

Table 10.6 lists droplet size, droplet temperature, droplet velocity, substrate temperature and substrate roughness utilized as the input parameters for HD and LD splat simulations. The average powder size for each composition was assumed to be the droplet diameter. The powder size distribution for all compositions ranged between 24-30 μm in diameter (A-SD: 30±10 μm, A4C-SD: 26±7 μm, A8C-SD: 24±5 μm). The temperature and velocity of the particle were obtained experimentally using in-flight particle diagnostic sensor as listed in Tables 10.2 and 10.3. Substrate material was considered as plain carbon steel with the preheat temperature of 453 K. For the sake of brevity, simulation results at the substrate preheat temperature of 553 K are not included here. Roughness of the steel substrate was assumed as 0.03 μm for the simulation which was same as the polished steel substrate for splat experiment.

Table 10.5: Thermo-physical properties of A-SD, A4C-SD and A8C-SD.

S. No.	Property	Al_2O_3	Al_2O_3-4 wt. %CNT	Al_2O_3-8 wt. %CNT
1.	Density (kg/m^3)	3.99	3.85	3.72
2.	Liquid phase kinematic viscosity (m^2/s)	1.026D-5 at 2200 ^oC	$1.098x10^{-5}$ at 2200 ^oC	$1.1704x10^{-5}$ at 2200 ^oC
3.	Liquid phase thermal conductivity (W/m-K)	7.86 at 2054 ^oC	204.7 at 2054 ^oC	377 at 2054 ^oC
4.	Liquid Phase Specific Heat (Joule/Kg-K)	1358 at 2054 ^oC	1404 at 2054 ^oC	1444 at 2054 ^oC
5.	Liquid Phase Surface Tension (Kg/s^2)	0.69 at 2054 ^oC	0.69 at 2054 ^oC	0.69 at 2054 ^oC
6.	Solid Phase Thermal Conductivity (W/m-K)	36.16 at 25 ^oC 5.90 at 1039 ^oC	231.2 at 25 ^oC 202.9 at 1039 ^oC	401.9 at 25 ^oC 375.4 at 1039 ^oC
7.	Solid Phase Specific Heat (Joule/Kg-K)	772 at 25 ^oC 1273 at 1039 ^oC 1358 at 2054 ^oC	767.5 at 25 ^oC 1320 at 1039 ^oC 1404 at 2054 ^oC	763.6 at 25 ^oC 1361.8 at 1039 ^oC 1444 at 2054 ^oC
8.	Melting Point (^oC)	2054 ^oC	2054 ^oC	2054^oC
9.	Heat of Fusion (Joule/Kg)	$1.16x\ 10^6$	$1.16x\ 10^6$	$1.16x\ 10^6$

Table 10.6: List of molten droplet and substrate parameters used for simulation of HD and LD splats

	HD			LD		
	HD-A-SD	HD-A4C-SD	HD-A8C-SD	LD-A-SD	LD-A4C-SD	LD-A8C-SD
Initial particle radius (μm)	30	26	24	30	26	24
Particle temperature (K)	2745	2423	2397	2495	2319	2306
Particle velocity (m/s)	338	319	314	275	274	271
Initial substrate temperature (K)	453	453	453	453	453	453
Substrate roughness(μm)	0.03	0.03	0.03	0.03	0.03	0.03

As a consequence of the splat simulation, two output files are obtained: (i) substrate temperature vs. time (i.e. solidification curve) and (ii) volume fraction of the solid vs. time. These output files provide an idea about the solidification process. Simulation also results in creation of AVI files which visualizes the entire droplet impact on the substrate.

Figures 10.10a, c, and e are the simulated top views of HD-A-SD, HD-A4C-SD and HD-A8C-SD splats. All distances in the simulated view are in millimeters (mm). The simulation was performed at cells per radius (CPR) value of 15. The CPR is an indicator of the resolution. A CPR value of 15 is considered sufficient enough to produce relatively accurate results. Figures 10.10b, d, f are the SEM images of the splats of HD-A-SD, HD-A4C-SD and HD-A8C-SD at the same parameters which were used for the simulation. Relatively higher splashing was observed in simulated view of HD-A-SD (Figure 10.10a) which was also seen in the experimental result of HD-A-SD splat (Figure 10.10b).

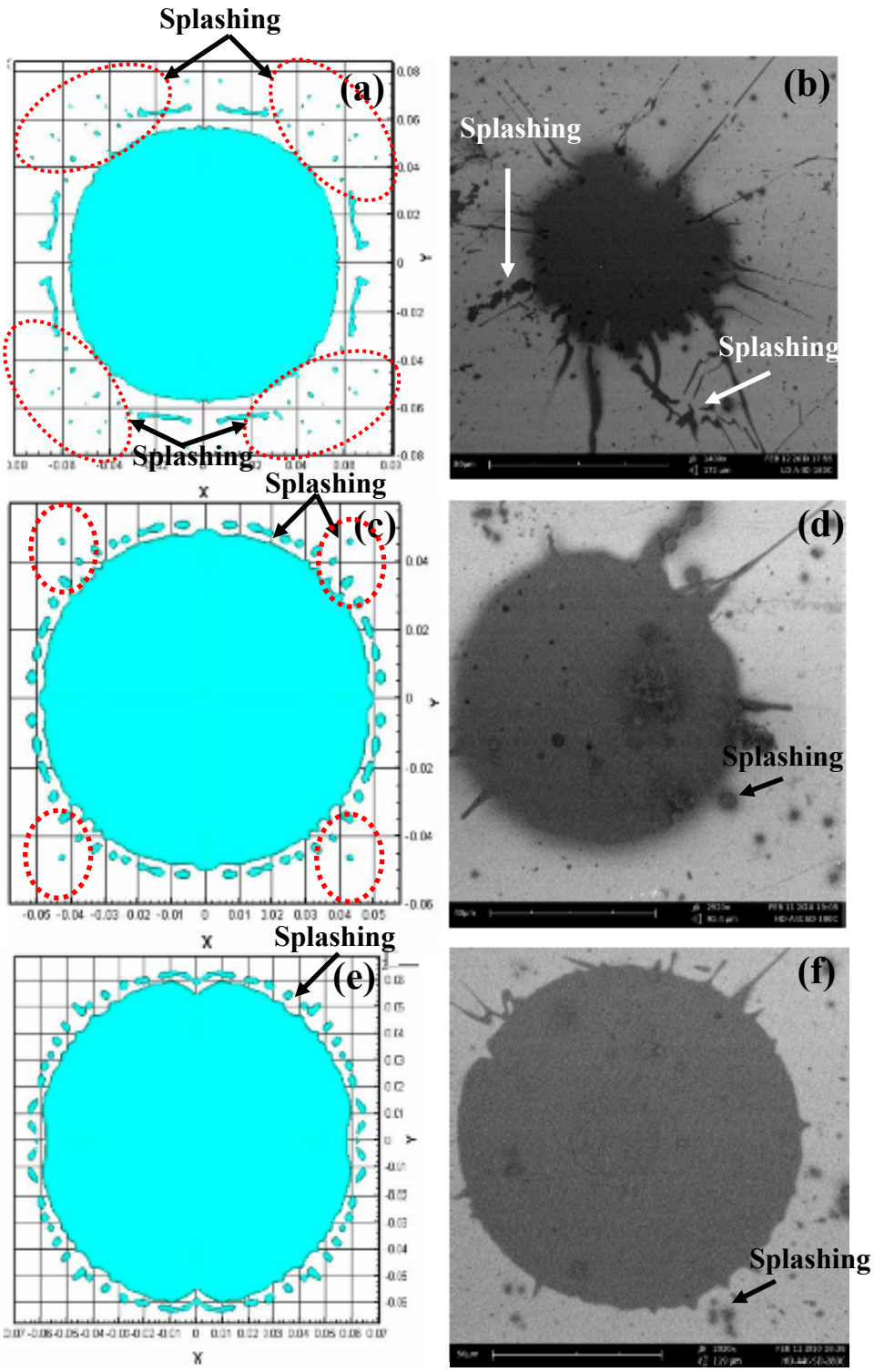

Figure 10.10: (a) Simulated top view of HD-A-SD splat (b) SEM image of experimentally obtained HD-A-SD splat (c) Simulated top view of HD-A4C-SD splat (d) SEM image of experimentally obtained HD-A4C-SD splat (e) Simulated top view of HD-A8C-SD splat (f) SEM image of experimentally obtained HD-A8C-SD splat

Lowest splashing of the droplet was observed in both simulated and experimental results of HD-A8C-SD splat (Figures 10.10c and f). Figure 10.11 shows the comparison between simulated and experimental splats for LD-A-SD, LD-A4C-SD and LD-A8C-SD. Higher splashing and finger formation was observed in simulated splat of LD-A-SD which matched well with the experimental result. Finger radiating outward from the periphery of the LD-A4C-SD and LD-A8C-SD splats were also observed in both experimental and simulated results. Since, splats obtained from the experiment and simulation matched well, it suggests that estimation of thermophysical properties of Al_2O_3-CNT by rule of mixture holds fairly good. Also, compared to LD splats, HD splats do not show finger formation. Such information when obtained from simulation can be very useful in synthesizing the coatings and its processing without performing the experiments. Of course, HD splats with less fingering are more desirable than fingered splats in LD coatings to synthesize dense microstructure of coating.

It was observed experimentally that splat diameter increases with an increasing CNT content. Also, HD splats have a larger splat diameter as compared to LD splats. In order to compare the experimental results with the simulated results, spreading ratio (D/D_0) for experimental and simulated splat were plotted for HD and LD splat. D is final diameter of splat and D_0 is the initial diameter of the droplet. Figure 10.12 shows the spreading ratio as a function of CNT content for HD and LD experimentally and simulated obtained splats. Both the experimental and simulation results show the similar increasing trend in spreading ratio as a function of CNT content for HD and LD splats.

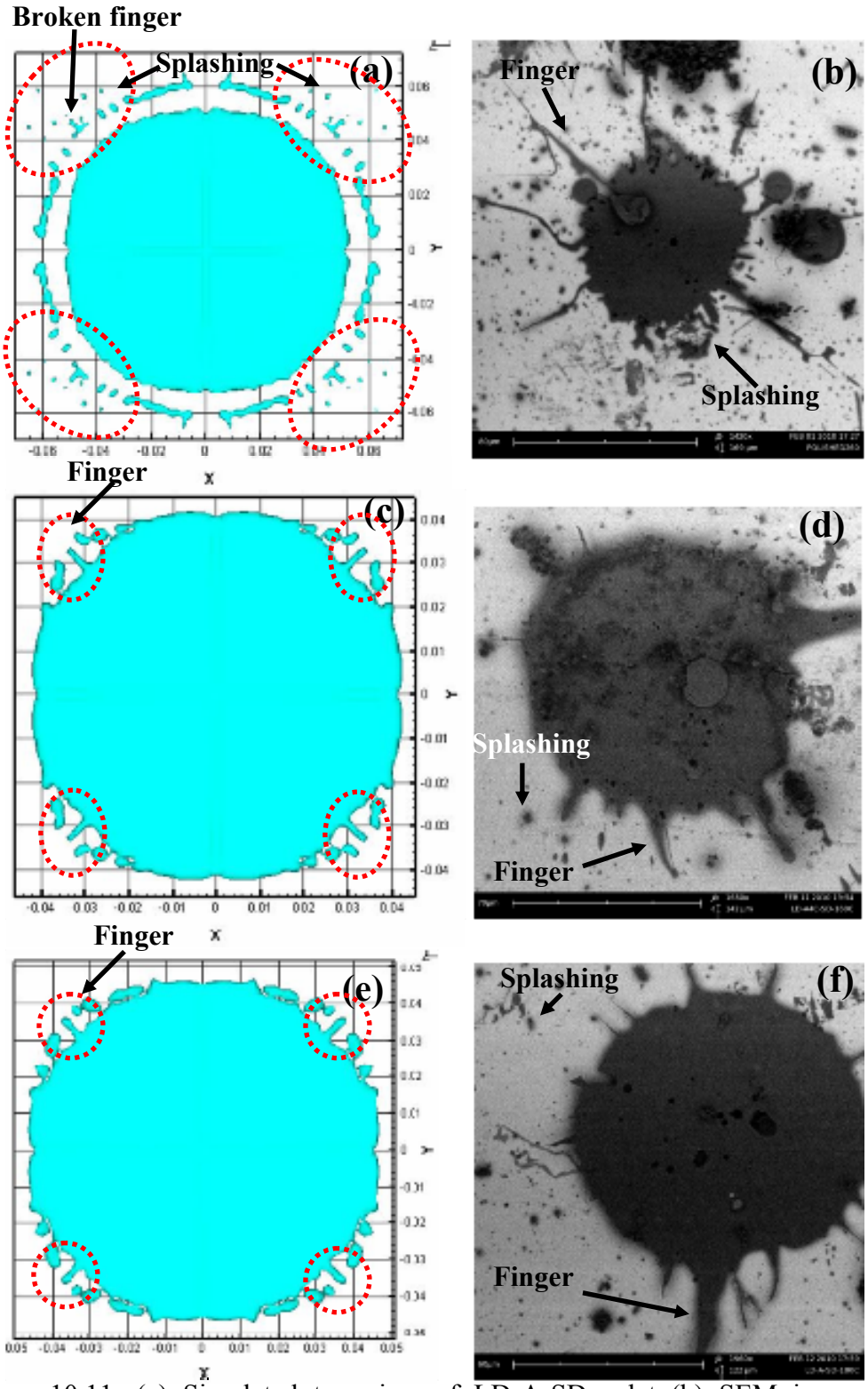

Figure 10.11: (a) Simulated top view of LD-A-SD splat (b) SEM image of experimentally obtained LD-A-SD splat (c) Simulated top view of LD-A4C-SD splat (d) SEM image of experimentally obtained LD-A4C-SD splat (e) Simulated top view of LD-A8C-SD splat (f) SEM image of experimentally obtained LD-A8C-SD splat

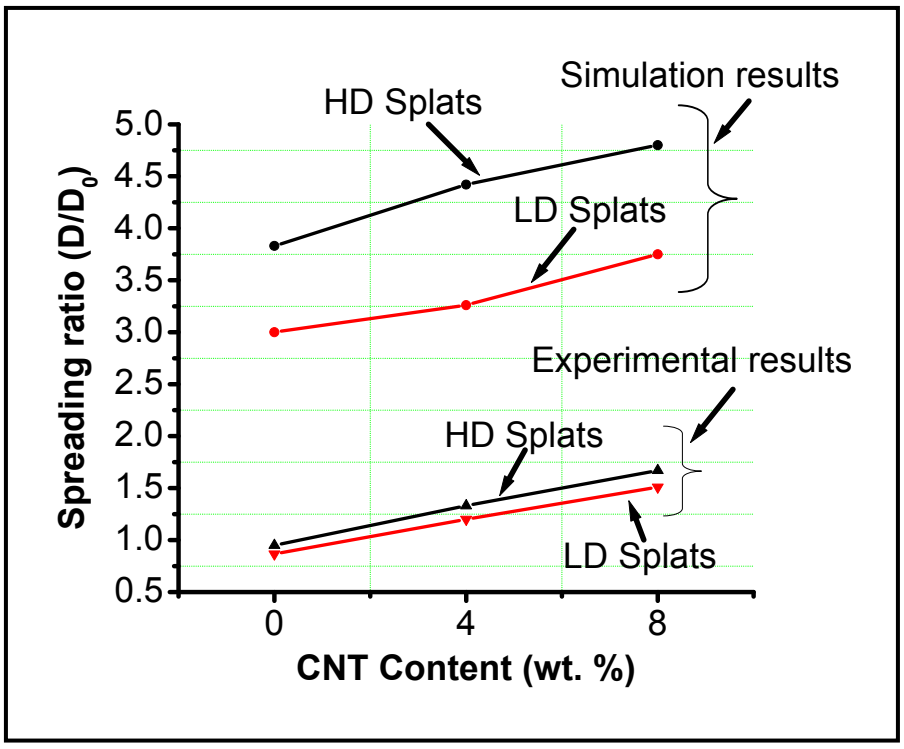

Figure 10.12: Spreading ratio as a function of CNT content for experimentally and simulated obtained HD and LD splats

Higher spreading ratio was observed for HD splats as compared to LD splats. However, experimentally obtained spreading ratio is lower than computed one due to initial powder characteristics. Spray dried powder, which contains ~30-40% of porosity, was used for synthesizing the splats. Due to presence of porosity, molten droplet size is expected to be much smaller resulting in smaller splat diameter and lower spreading ratio. During simulation, molten droplet size is assumed to be of as initial powder size which leads to larger diameter of splats as compared to experimentally obtained splats.

The solidification behavior during splat formation is studied as a function of time as shown in Figure 10.13. The discussion is restricted to solidification behavior of HD splats. Figures 10.13a-c show the simulated view of HD-A-SD, HD-A4C-SD and HD-A8C-SD splats at different intervals of time respectively. Solidification behavior can be

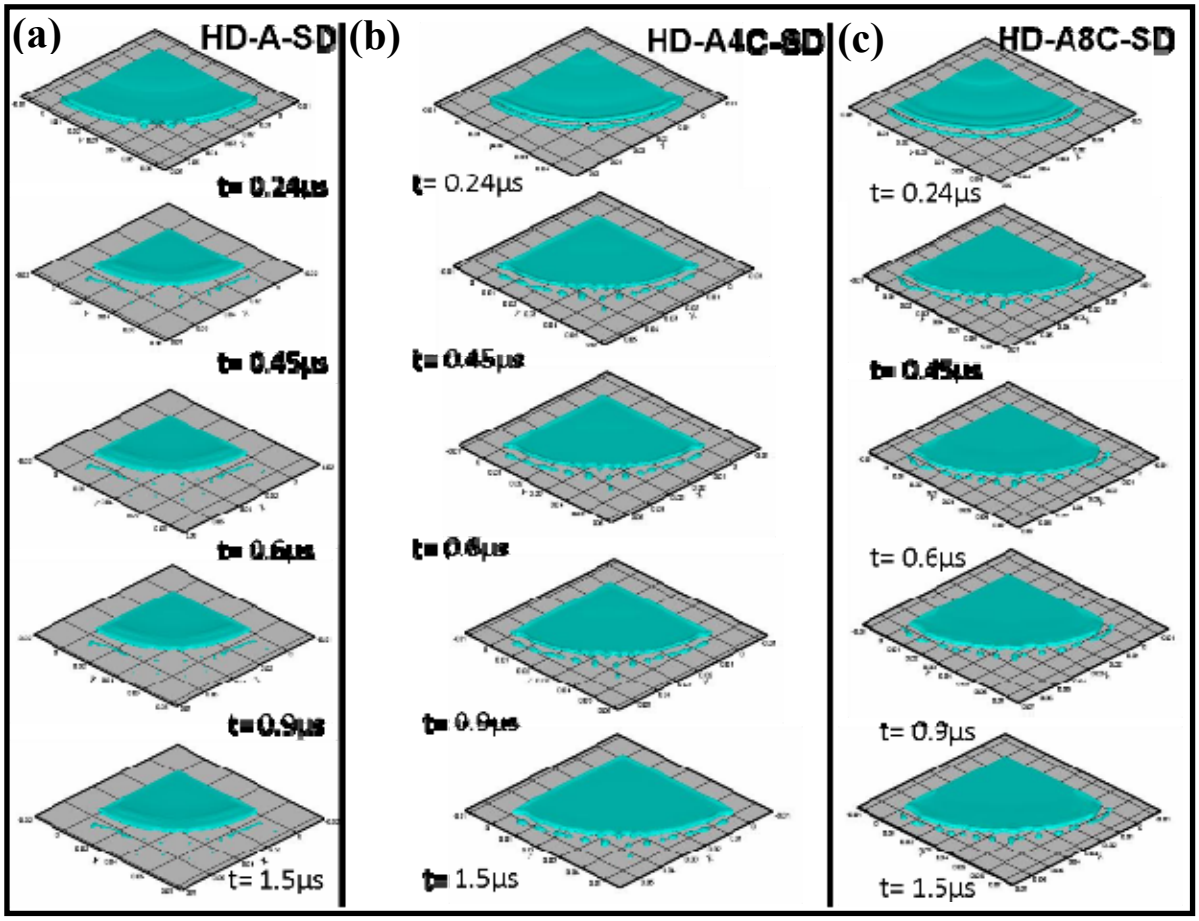

Figure 10.13: Simulated view at different interval of time for (a) HD-A-SD splat (b) HD-A4C-SD splat (c) HD-A8C-SD splat

explained with the help of volume percentage of solid at similar interval of time. Figure 10.14 shows the volume percentage of solid in HD-A-SD, HD-A4C-SD, and HD-A8C-

SD at different intervals. After 0.24 μs of the impact, the volume percentage of solid in HD-A-SD splat was 26% while it is 14% and 8% in HD-A4C-SD and HD-A8C-SD respectively. This indicates the delayed solidification process in CNT reinforced splat which is attributed to higher heat content of the melt due to CNT addition (as explained

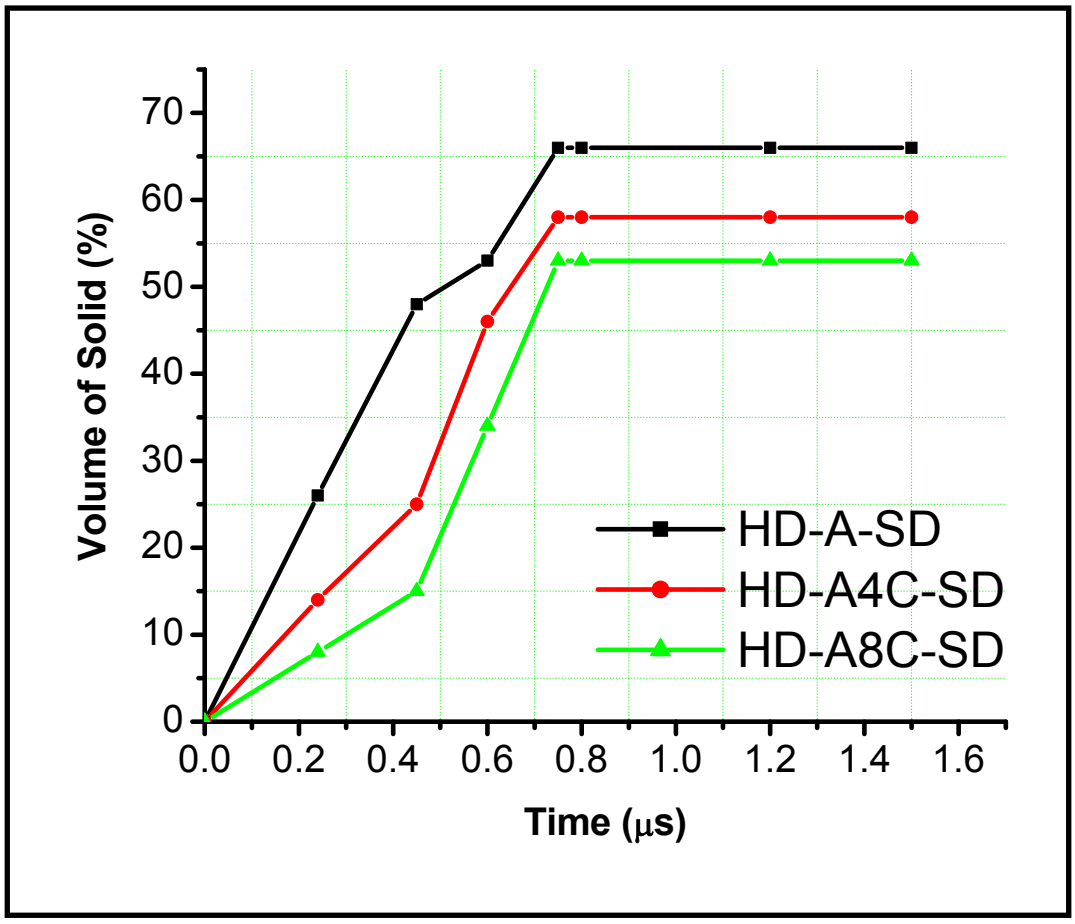

Figure 10.14: Volume percentage of solid as function of time for HD-A-SD, HD-A4C-SD and HD-A8C-SD splat

in section 10.3). After 0.45 μs of the impact, the volume percentage of solid in HD-A-SD splat was 48% while its 25% and 15% in HD-A4C-SD and HD-A8C-SD respectively.

Higher volume percentage of solid in HD-ASD splat after 0.45 μs of the impact resulted in higher splashing which can be seen in simulated view of HD-A-SD splat at 0.45 μs (Figure 10.13a). This has already been explained that rapid solidification of the melt leads to higher splashing due to spreading instability. Relatively lower splashing has been seen in case of HD-A4C-SD and HD-A8C-SD splat, as can be seen in the simulated view of HD-AC-SD (Figure 10.13b) and HD-A8C-SD (Figure 10.13c) at 0.45 μs. After 0.75 μs of the impact, the volume percentage of solid in HD-A-SD splat was 66%, while its 58% and 53% in HD-A4C-SD and HD-A8C-SD splat which become constant. Hence, there are no changes observed in simulated view of HD-A-SD, HD-AC-SD and HD-A8C-SD splat at later stages (i.e. at 0.9 μs and 1.5 μs). Time interval for splat formation was increased to from 1.5 to 5 μs in order to find the onset of complete solidification. Between 1.5 and 5 μs, small increment in volume fraction of solid was observed (ΔV=+ 2% for HD-A-SD splat, ΔV=+ 1.2% for HD-A4C-SD splat and ΔV=+ 0.91% for HD-A8C-SD splat) for all splats. These results indicate that complete solidification may be occurring in milliseconds, which is beyond the computing power. This is in accordance with the solidification of the molten droplet in actual plasma spraying. Typically, molten droplet solidify at a cooling rate of ~10^6 K/s in plasma spraying process [65, 66], which indicates that droplet solidification time is ~ 0.5 milliseconds considering in flight particle temperature ~2750 K.

Solidification behavior can also be understood from the solidification curves of HD-A-SD, HD-A4C-SD and HD-A8C-SD splats. Figure 10.15 shows the substrate temperature with time for HD-A-SD, HD-A4C-SD and HD-A8C-SD splats. Three

different stages in the solidification curve in Figure 10.15 are discussed here. Corresponding view of the simulated splat at a particular time is also superimposed to

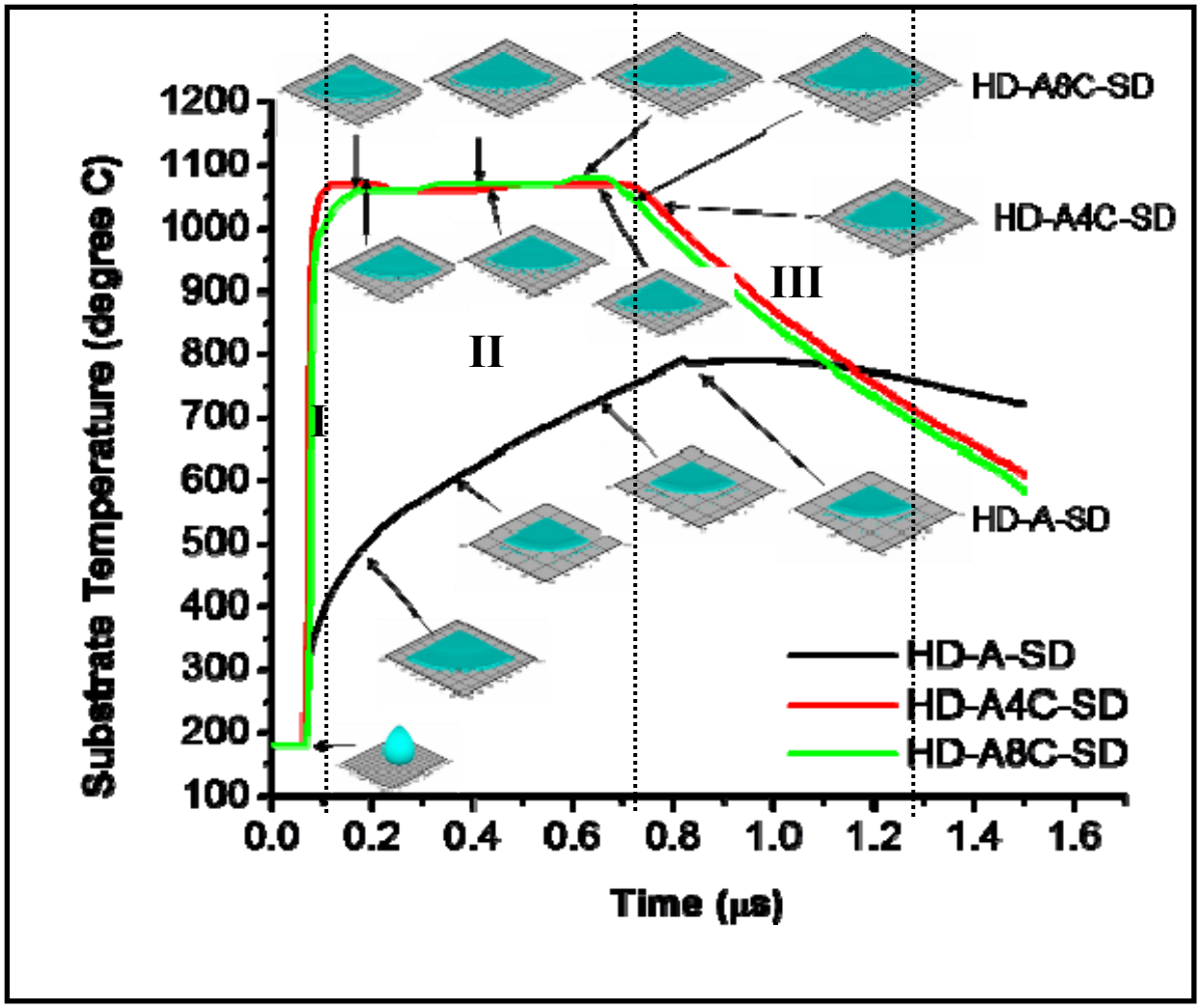

Figure 10.15: Substrate temperature as a function of time for HD-A-SD, HD-A4C-SD and HD-A8C-SD splat

better understand the solidification process. Stage I in Figure 10.16 shows a significant increase in the substrate temperature at 0.1 μs for HD-A-SD, HD-A4C-SD and HD-A8C-SD splats. This is attributed to the heat transfer from the molten droplet to substrate just

after its impact. Higher increase ($\Delta T = +650°C$) in the substrate temperature was seen for CNT reinforced splats which is attributed to higher heat content of CNT containing molten Al_2O_3 melt resulting in higher heat transfer to the substrate. During stage II, substrate temperature increases for HD-A-SD splats whereas substrate temperature remains constant for HD-A4C-SD and HD-A8C-SD splats. Increasing substrate temperature in case of HD-A-SD splat is due to higher rate of solidification (Figure 10.15) resulting in higher amount of heat energy release. Released latent heat of solidification will be absorbed by the substrate and substrate temperature will increase. However, CNT reinforced melt has higher heat content and remains molten for a long time. Hence no change in substrate temperature was observed during Stage II. In Stage III, substrate temperature decreased for all HD splats. However, lower rate of change (dT/dt) of temperature was observed for HD-A-SD as compared to HD-A4C-SD and HD-A8C-SD splat. This is attributed to additional radiation loss from CNTs because of their high emissivity (0.98) as compared to Al_2O_3 particle (emissivity 0.4) [4, 29].

It is concluded that splat simulation is an effective tool for simulating the plasma sprayed single splat morphology. This can contribute significantly towards optimization of splat morphology and can cut down the large number of experiments which involves lots of time and money. Next section discusses the correlation of splat with coating properties.

10.5 Correlation of Splat with Coating Properties

Splat morphology largely depends on the powder feedstock properties, substrate roughness and temperature and plasma processing parameters. Hence, varying plasma process parameters can leads to different kinds of splat morphologies which can affect the coating's property. This can be understood with the help of schematic shown in Figure 10.16. Variation in temperature and velocity of in-flight particles with varying plasma parameters results in different splat morphologies. Three different types of splats *viz* disc shape, fingered shape, and fragmented are shown in the schematic. Higher temperature and velocity of in-flight particles leads to disc shaped splats while lower temperature and velocity results to fingered and fragmented splats. Stacking of contiguous disc shaped splats can improve the bonding between splats and can minimize the porosity in the coating. The reverse is true for fingered and fragmented splat due to poor stacking. Hence, it can be concluded that adjusting the plasma parameters leads to different splats morphology which leads to different amount of porosity content in the coating.

Mechanical properties (hardness, elastic modulus, fracture toughness, wear resistance) of coatings can be significantly affected by the porosity as shown in Figure 10.16. Equation 10.1 shows the negative exponential dependence of hardness on porosity [137].

$$H = H_0 \exp(-ap) \tag{10.1}$$

H is the hardness of porous material, H_0 is the hardness for dense material, p is the apparent porosity in the material and a is the material constant.

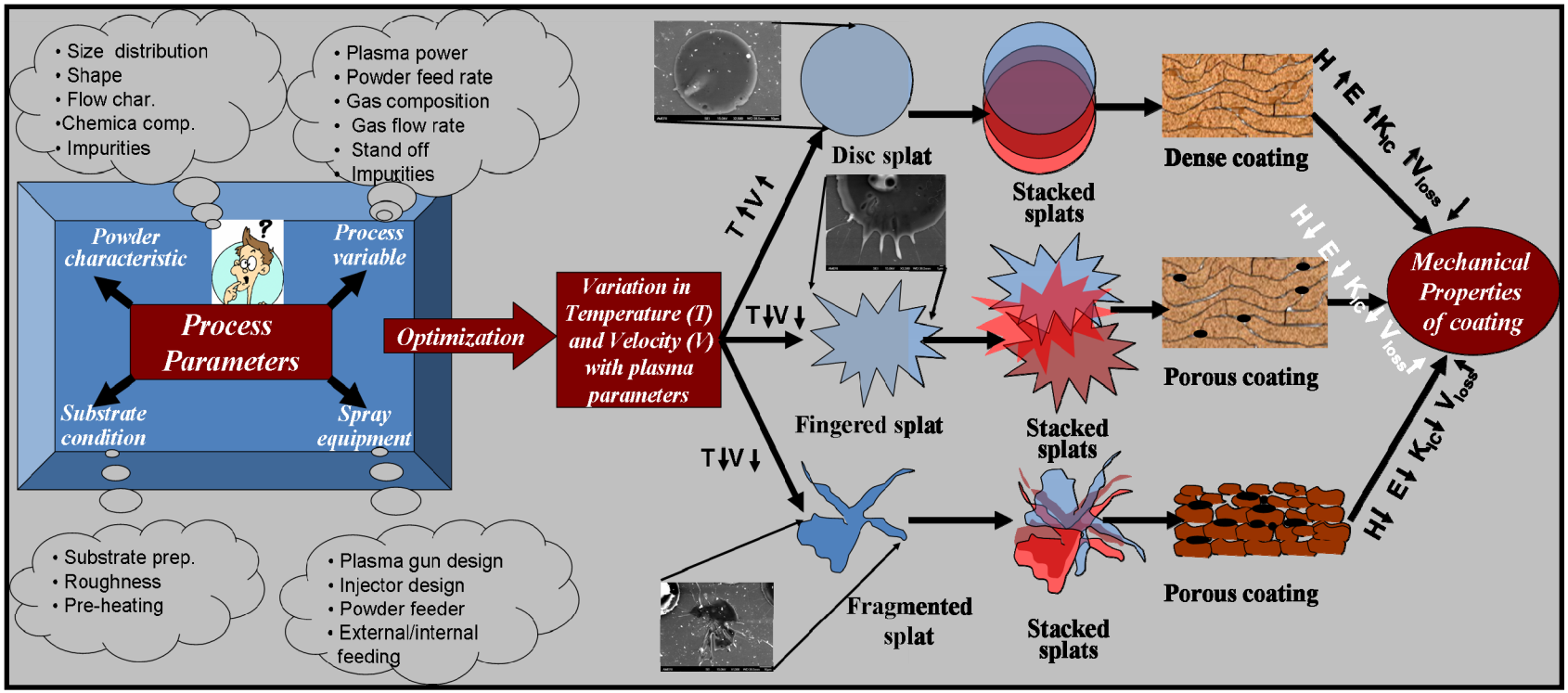

Figure 10.16: Schematic showing correlation between plasma parameters, splats morphology and mechanical properties of coating

It is recalled from Equation 1.1 and 7.10 which shows that elastic modulus and fracture toughness exponentially decrease with the porosity content. From the Evans and Marshall equation (Equation 8.2), it is obvious that, decrease in hardness, elastic modulus, and fracture toughness leads to lower wear resistance of coating. Hence it is concluded that porosity has an adverse effect on coating's mechanical properties which can be eliminated by optimizing the splat geometry. Optimized splats geometry can be achieved by optimizing plasma process parameters.

11. CONCLUSIONS

The *overall* objective of this dissertation has been achieved by developing ***process maps*** to synthesize high density CNT reinforced Al_2O_3 coatings by plasma spraying for improved mechanical and wear properties Process maps established correlations between plasma parameters, porosity, hardness, elastic modulus, fracture toughness, wear resistance and CNT content. A detailed list of conclusions regarding CNT dispersion in powder, process map development for coatings, and mechanical and tribological properties are summarized herewith.

CNT Dispersion in the Powder Feedstock

1. Spray drying and CVD techniques have proven to be effective in uniformly dispersing CNTs in Al_2O_3 matrix. The degree of CNT dispersion via CVD technique was more superior to spray drying. But CVD technique has limitation of large scale synthesis of composite powder. Spray drying technique can successfully synthesize Al_2O_3-CNT composite powder at large scale (e.g. several kilograms).

Process Map Development for Coatings

2. Process maps have been developed using spray dried Al_2O_3 powder with 0, 4 and 8 wt. % CNTs (A-SD, A4C-SD, A8C-SD). Correlations between plasma processing parameters to the particle's thermal and kinetic state and coating's porosity have also been established.

3. An empirical model using Pareto diagram was developed to link plasma processing parameters with the porosity of coating. Stand-off distance was found to be the most critical parameter for A-SD and A4C-SD coatings. In case of A8C-SD powder, plasma power was the most significant factor which affects the porosity, since stand-off distance was kept constant.

4. Significant effect of CNTs was observed on the thermal and kinetic history of in-flight particle. Lower temperature and velocity of in-flight A4C-SD (ΔT = -322 K, Δv = −19 m/s) and A8C-SD (ΔT = -348 K, Δv = −24 m/s) particles was observed as compared to A-SD particles. Lower temperature in CNT reinforced powder was due to higher radiation loss of CNT (emissivity: 0.98) as compared to A-SD (emissivity: 0.4). Lower velocity was attributed to the hollow tubular structure of CNTs that has larger drag resistance.

Mechanical Properties

5. Addition of 8 wt. % CNT increases the hardness of high density Al_2O_3 coating (HD-A-SD) from 1498 VHN to 1670 VHN. Same amount of CNT reinforcement improves the hardness of low density Al_2O_3 coating (LD-A-SD) from 1198 VHN to 1456 VHN. In case of ICP-1 coating, relative improvement of ~15% was observed in hardness. Improvement in the hardness of CNT reinforced coating was attributed to enhanced indentation resistance by CNT reinforcement to Al_2O_3 matrix.

6. Elastic modulus of HD-A-SD, HD-A4C-SD, and HD-A8C-SD coatings improved by 32%, 17%, and 26% respectively as compared to corresponding composition of LD coatings. Elastic modulus of HD-A8C-SD coating was 227±76 GPa which is ~34% improvement over HD-A-SD coating. Improvement in the elastic modulus of CNT reinforced coatings is attributed to combined effect of (i) higher modulus of CNT (ii) uniform CNT dispersion in the Al_2O_3 matrix, and (iii) improved coating density. In case of ICP-1 coating, an increase in ~27% in elastic modulus value was observed by mere 1.5 wt. % of CNT addition. This was attributed to superior degree of CNT dispersion in ICP-1 coating and strong bonding between Al_2O_3/CNT compared to spray dried coating.

7. Fracture toughness of HD-A-SD, HD-A4C-SD, and HD-A8C-SD coatings improved by 38%, 36%, and 73% respectively as compared to corresponding composition of LD coating. Highest improvement (~73%) in HD-A8C-SD coating is attributed to the combined effect of lowest porosity (~3%) and highest CNT content in the coating. Significant improvement in fracture toughness was attributed to uniform dispersion of CNTs in the Al_2O_3 matrix which promotes the toughening mechanism such as CNT bridging and crack deflection. Similar toughening mechanisms were observed in ICP-1 coating which caused 24% of relative improvement by mere 1.5 wt% of CNTs.

Room Temperature Tribological Properties

8. There was ~71% and ~80% relative improvement in the room temperature ball-on-disk sliding wear resistance of HD-A4C-SD and HD-A8C-SD coatings at 30 N load

respectively Similarly, relative improvement of ~28% and ~47% was observed in the room temperature wear resistance of LD-A4C-SD and LD-A8C-SD coatings at 30 N load respectively. Improvement of ~12% and 24% in room temperature wear resistance was observed for ICP-1 coating at 30 N and 50 N load respectively. Higher wear resistance of CNT reinforced coatings is attributed to: (i) higher hardness and fracture toughness (ii) CNT bridging between the splats in wear track and (iii) protective tribochemical film formation. Wear surface of SD coatings showed protective film (composed of SiO_2) on the wear surface when sliding against Si_3N_4 ball at room temperature. However, no protective film formation was observed on the wear surface of ICP-1 coating when sliding against WC ball at room temperature. Protective film on the wear surface as a result of tribochemical reaction reduced the wear of coating surface against sliding.

9. Coefficient of friction (COF) for HD-A-SD was ~0.71 which marginally reduced to ~0.67 and ~0.65 for HD-A4C-SD and HD-A8C-SD coatings respectively. Average COF for LD coatings (~0.73 for LD-A-SD, ~0.68 for LD-A4C-SD and ~0.69 for LD-A8C-SD) was found similar to COF for HD coatings. CNT reinforced coatings have slightly lower COF in both HD and LD coatings which is attributed to lubricating effect of CNTs due to graphitization. Similar lubricating effect was observed in ICP-1 coating at 30 N load which resulted in lower average COF (0.63) than Al_2O_3 (0.67).

High Temperature Tribological Properties

10. High temperatures wear of SD and ICP-1 coatings are pretty complex phenomena in terms of tribochemical film formation which has significant effect on the wear. Wear surface of SD coatings showed very less amount of protective film (composed of SiO_2) at higher temperature when sliding against Si_3N_4 ball. However, wear surface of ICP-1 coating showed higher amount of protective film (composed of WO_3) formation at higher temperature when sliding against WC ball. Among SD coatings, higher wear was observed with the increasing temperature. This was attributed to less amount of protective film (SiO_2) formation and lower hardness at higher temperature. With the increasing CNT content, improvement in the wear resistance was observed for SD coatings at higher temperature which was attributed to higher fracture toughness of CNT reinforced coating. ICP-1 coating showed improved wear resistance at higher temperature which was mainly due to higher amount of WO_3 protective film formation.

11. COF was higher (0.80-0.90) for all SD coatings at higher temperature as compared to room temperature coefficient of friction (0.65-0.73).

Processing-Splat –Property Correlation

12. The effect of plasma process variables on the splat morphology and porosity in the coating was established. Varying temperature and velocity of in-flight particles with plasma parameters result in different splat morphologies which generates different level of porosity in the coating. Higher in-flight temperature and velocity of the

particles resulted in contiguous disc shaped splat which can enhance the bonding between the splats and can reduce the porosity in the coating resulting enhanced mechanical properties of coating. CNT addition resulted in the increased splat diameter due to enhanced temperature of the melt. Splat simulation was carried out which matched well with experimentally obtained splats.

12. RECOMMENDATIONS FOR FUTURE WORK

In this current research, comprehensive process maps have been successfully developed to obtain high density plasma sprayed Al_2O_3-CNT coating with improved fracture and wear resistance. In addition, this work has also posed new research questions which need to be explored by future researchers. Some of the recommendations for further studies are listed below.

12.1 Process Map Development for CVD Al_2O_3-CNT Powder

In the current work, plasma parameters have been optimized using spray dried powder and most significant parameters affecting the porosity have been ranked in order of their criticality. A similar approach is recommended for developing process maps for CVD Al_2O_3-CNT powder to establish their reproducibility and correlation with mechanical and tribological properties. Such study is restricted by the lack of availability of CVD Al_2O_3-CNT powder in large amount.

12.2 Plasma Densification of Spray Dried Al_2O_3-CNT Powder

Though spray drying is an effective technique to uniformly disperse the CNT in the Al_2O_3 powder, spray dried agglomerates contains 30-40% of the porosity which can largely affect the coating's microstructure and properties. Plasma densification of the spray dried agglomerates can result in high density composite powder feedstock. Denser feedstock could further improve the density of coatings, which is the main objective of this study.

12.3 Adhesion and Bending Strength of Plasma Sprayed Coating

The failure of the plasma sprayed coating usually occurs at the coating/substrate interface or within coating. Hence the adhesion strength depends on the bonding between the first splat with the underlying substrate and inter-splat bonding. Adhesion strength of plasma sprayed coatings is usually measured by pull test (ASTM D4541-09), which is limited by the strength of the glue. It is recommended that novel techniques need to be developed for measuring adhesion strength. This includes multi-level tests as coating contains hierarchial microstructure. Nano or micro scratch technique should be adopted to evaluate the bonding between single splat and underlying substrate. The strength of the entire coating shall be estimated using four point bend test. During bending, crack is expected to propagate through entire coating thickness (inter-splat region) and along coating/substrate interface.

12.4 Fatigue Behavior of Plasma Sprayed Al_2O_3-CNT Coating

One of the major applications for plasma sprayed Al_2O_3-CNT is as wear resistant coatings on large propeller shafts in the marine industry. The rotation of shaft would lead to cyclic stresses in the coating. Hence it is recommended that fatigue behavior of plasma sprayed Al_2O_3-CNT shall be studied. CNT reinforced ceramic composites have never been evaluated for their fatigue properties. Such study would understand the role of CNT in preventing the crack propagation under cyclic loading.

LIST OF REFERENCES

1. Poyato R Vasiliev AL, Padture NP, Tanaka H, Nishimura T, *Aqueous colloidal processing of single-wall carbon nanotubes and their composites with ceramics.* Nanotechnology, 2006. **17**: p. 1770-1777.

2. Cha SI Kim KT, Lee KH, Mo CB, Hong SH, *Strengthening and toughening of carbon nanotube reinforced alumina nanocomposite fabricated by molecular level mixing process.* Scripta Materialia, 2005. **53**: p. 793–797.

3. Lei S Feng ZY, Chan Z, JI L., *Heterocoagulation System Assisted Adsorption of Carbon Nanotubes on Alumina for Toughening Ceramics.* Journal of Reinforced Plastics and Composites, 2008. **27**: p. 243-253.

4. Balani K Agarwal A, *Process map for plasma sprayed aluminum oxide–carbon nanotube nanocomposite coatings.* Surface & Coatings Technology, 2008. **202**: p. 4270-4277.

5. Balani K Zhang T, Karakoti A, Li WZ, Seal S, Agarwal A, *In situ carbon nanotube reinforcements in a plasma-sprayed aluminum oxide nanocomposite coating.* Acta Materialia, 2008. **56**: p. 571-579.

6. Vaidya A Srinivasan V, Streibl T, Friis M, Chi W, Sampath S, *Process maps for plasma spraying of yttria-stabilized zirconia: An integrated approach to design, optimization and reliability.* Materials Science and Engineering A, 2008. **497**: p. 239-253.

7. Xia Z Riester L, Curtin WA, Li H, Sheldon BW, Liang J, Chang B, Xu JM, *Direct observation of toughening mechanisms in carbon nanotube ceramic matrix composites.* Acta Materialia, 2004. **52**: p. 931-944.

8. Zhan GD Kuntz JD, Wan J, Mukherjee AK, *Single walled carbon nanotube as attractive toughening agents in alumina based nanocomposites.* Nature Materials, 2003. **2**: p. 38-42.

9. Balani K Harimkar SP, Keshri A, Chen Y, Dahotre NB, Agarwal A, *Multiscale wear of plasma-sprayed carbon-nanotube-reinforced aluminum oxide nanocomposite coating.* Acta Materialia, 2008. **56**: p. 5984-5994.

10. Sampath S Jiang XY, Matejicek J, Leger AC, Vardelle A, *Substrate temperature effects on splat formation, microstructure development and properties of plasma sprayed coatings Part I:Case study for partially stabilized zirconia.* Materials Science and Engineering A, 1999. **272**: p. 181-188.

11. Bianchi L Leger AC, Vardelle M, Vardelle A, Fauchais P, *Splat formation and cooling of plasma-sprayed zirconia.* Thin Solid Films, 1997. **305**: p. 35-47.

12. Mostaghimi J Pasandideh-Fard M, Chandra S, *Dynamics of Splat Formation in Plasma Spray Coating Process.* Plasma Chemistry and Plasma Processing, 2002. **22**: p. 59-84.

13. Jordan EH Gell M., *Nano crystalline ceramic and ceramic coatings made by conventional and solution plasma spray.* Nanomaterials technology for military vehicle structural applications, RTO-MP-AVT-122, 3-4 October, 2005.

14. Karagedov GR Lyakhov NZ, *Prepration and sintering of nanosized alpha Al2O3 powder.* NanoStructured Materials, 1999. **11**: p. 559–572.

15. Luo H Goberman D, Shaw L, Gell M, *Indentation fracture behavior of plasma-sprayed nanostructured Al2O3 /13wt.%TiO2 coatings.* Materials Science and Engineering A, 2003. **346**: p. 237-245.

16. Shaw LL Goberman D, Ren R, Gell M, Jiang S, Wang Y, Xiao DT, Strutt PR, *The dependency of microstructure and properties of nanostructured coatings on plasma spray conditions.* Surface and Coatings Technology, 2000. **180**: p. 1-8.

17. Wang Y Jiang S, Wang M, Wang S, Xiao TD and Strutt PR, *Abrasive wear characteristics of plasma sprayed nanostructured alumina/titania coatings.* Wear, 2000. **237**(2): p. 176-185.

18. Balani K Bakshi SR, Chen Y, Laha T, Agarwal A, *Role of powder treatment and carbon nanotube dispersion in the fracture foughening of plasma-sprayed aluminum oxide—carbon nanotube nanocomposite.* J. Nanosci. Nanotechnol., 2007. **7**: p. 1-10.

19. Friis M Persson C, *Control of Thermal Spray Processes by Means of Process Maps and Process Windows.* Journal of Thermal Spray Technology, 2003. **12**(1): p. 44-52.

20. Li JF Liao HL, Ding CX, Coddet C, *Optimizing the plasma spray process parameters of yttria stabilized zirconia coatings using a uniform design of experiments.* Journal of Materials Processing Technology, 2005. **160**: p. 34-42.

21. Srinivasan V Vaidya A, Streibl T, Friis M, Sampath S, *On the Reproducibility of Air Plasma Spray Process and Control of Particle State.* Journal of Thermal Spray Technology, 2006. **15**(4): p. 739-743.

22. Hu Y Shenderova O.A, Hu Z, Padgett C.W, Brenner D.W, *Carbon nanostructures for advanced composites.* Rep. Prog. Phys., 2006. **69**: p. 1847–1895.

23. Thomson K.E Jiang D, Ritchie R.O, Mukherjee A.K, *A preservation study of carbon nanotubes in alumina-based nanocomposites via Raman spectroscopy and nuclearmagnetic resonance.* Applied Physics A –Materials Science & Processing, 2007. **89**: p. 651–654.

24. Zhan GD Mukherjee AK, *Carbon nanotube reinforced alumina-based ceramics with novel mechanical, electrical, and thermal propertiess.* Int. J. Appl. Ceram. Technol., 2004. **1**: p. 161-171.

25. Zhang T Kumari L, Dua GH, Lia WZ, Wang QW, Balani K, Agarwal A, *Mechanical properties of carbon nanotube–alumina nanocomposites synthesized by chemical vapor deposition and spark plasma sintering.* Composites: Part A, 2009. **40**: p. 86-93.

26. Andrews R Jacques D, Qian D, Rantell T, *Multiwall Carbon Nanotubes: Synthesis and Application.* Acc. Chem. Res., 2002. **35**: p. 1008-1017.
27. Balani K Agarwal A, *Wetting of carbon nanotubes by aluminum oxide.* Nanotechnology, 2008. **19**(165701): p. 8pp.

28. Chen Y Balani K, Agarwala A, *Analytical model to evaluate interface characteristics of carbon nanotube reinforced aluminum oxide nanocomposites.* Appl. Phys. Lett., 2008. **92**(011916).

29. Chen Y Samant A, Balani K, Dahotre NB, Agarwal A, *Effect of laser melting on plasma-sprayed aluminum oxide coatings reinforced with carbon nanotubes.* Appl Phys A, 2009. **94**: p. 861-870.

30. Coleman JN Khan U, Blau WJ, Gun'ko YK, *Small but strong: A review of the mechanical properties of carbon nanotube–polymer composites.* Carbon, 2006. **44**: p. 1624-1652.

31. Delmottea JPS Rubioc A, *M echanical properties of carbon nanotubes: a fiber digest for beginners.* Carbon, 2002. **40**: p. 1729-1734.

32. Esawi A.M.K Farag M.M, *Carbon nanotube reinforced composites: Potential and current challenges.* Materials and Design, 2007. **28**: p. 2394–2401.

33. Flahaut E Peigney A, Laurent C, Marlie C, Chastel F, Rousset A, *Carbon nanotube–metal–oxide nanocomposites: microstructure, electrical conductivity and mechanical properties.* Acta mater., 2000. **48**: p. 3803-3812.

34. Lu JP, *Elastic properties of single and multilayered nanotubes.* J Phy Chem Solids, 1997. **58**: p. 1649-1652.
35. Schadler LS Giannaris SC, Ajayan PM, *Load transfer in carbon nanotube epoxy composites.* 1998. **73**: p. 3842-3844.

36. Siegel RW Chang SK, Ash BJ, Stone J, Ajayan PM, Doremus RW, Schadler LS, *Mechanical behavior of polymer and ceramic matrix nanocomposites.* Scripta mater., 2001. **44**: p. 2061-2064.

37. Treacy MMJ Ebbesen TW, Gibson JM, *Exceptionally high Young's modulus observed for individual carbon nanotubes.* Nature, 1996. **381**.

38. Wang X Padture N.P, Tanaka H, *Contact-damage-resistant ceramic/ single-wall carbon nanotubes and ceramic/graphite composites.* Nature materials, 2004. **3**: p. 539-544.

39. Yu M Lourie O, Dyer MJ, Moloni K, Kelly TF, Ruof RS, *Strength and breaking mechanism of multiwalled carbon nanotubes under tensile load.* Science, 2000. **287**: p. 637-640.

40. Mo CB Cha SI, Kim KT, Lee KH, Hong SH, *Fabrication of carbon nanotube reinforced alumina matrix nanocomposite by sol–gel process.* Materials Science and Engineering A, 2005. **395**: p. 124-128.

41. Sun J Gao L, *Development of a dispersion process for carbon nanotubes in ceramic matrix by heterocoagulation.* Carbon, 2003. **41**: p. 1063–1068.

42. Song YS Youn JR, *Influence of dispersion states of carbon nanotubes on physical properties of epoxy nanocomposites.* Carbon, 2005. **43**: p. 1378-1385.

43. Chen Y Balani K, Agarwal A, *Modified Eshelby tensor modeling for elastic property prediction of carbon nanotube reinforced ceramic nanocomposites.* Appl. Phys. Lett., 2007. **91**(031903).

44. Balani K Agarwal A, *Damping behavior of carbon nanotube reinforced aluminum oxide coatings by nanomechanical dynamic modulus mapping.* Journal of Applied Physics, 2008. **104 (063517)**: p. 1-6.

45. Jang BK Matsubara H, *Influence of porosity on hardness and Young's modulus of nanoporous EB-PVD TBCs by nanoindentation.* Materials Letters, 2005. **59**: p. 3462 – 3466.

46. Fan JP Zhuang DM, Zhao DQ, Zhang G, Wu MS, Wei F, Zhuang J, *Toughening and reinforcing alumina matrix composite with single-wall carbon nanotubes.* Applied Physics Letter, 2006. **89**: p. 121910 - 121910-3.

47. Dresselhaus MS Dresselhaus G, Saito R, Jorio A, *Raman spectroscopy of carbon nanotubes.* Physics Reports, 2005. **409**: p. 47-99.

48. Wong EW Sheehan PE, Lieber CM, *Nanobeam Mechanics: Elasticity, Strength, and Toughness of Nanorods and Nanotubes.* Science, 1997. **277**: p. 1971-1975.

49. Huang JY Chen S, Wang ZQ, Kempa K, Wang YM, Jo SH, Chen G, Dresselhaus MS, Ren ZF, *Superplastic carbon nanotubes.* Nature, 2006. **439**: p. 281.

50. Cho J Boccaccini AR, Shaffer SPM, *Ceramic matrix composites containing carbon nanotubes.* Journal of Material Science, 2009. **44**: p. 1934-1951.

51. Ning J Zhang J, Pan Y, Guo J, *Fabrication and mechanical properties of SiO2 matrix composites reinforced by carbon nanotube.* Materials Science and Engineering A, 2003. **357**: p. 392-396.

52. Shi XL Yang H, Shao GQ, Duan XL, Yan L, Xiong Z, Sun P, *Fabrication and properties of W–Cu alloy reinforced by multi-walled carbon nanotubes.* Materials Science and Engineering A, 2007. **457**: p. 18-23.

53. Wang Y Wu J, Wei F, *A treatment method to give sepearyed multi-walled carbon nanotubes with high purity, high crysatllization and a large aspect ratio.* Carbon, 2003. **41**: p. 2939-2948.

54. Lu KL Lagao RM, Chen YK, Green MLH, Harris PJF, Tsang SC, *Mechanical damage of carbon nanotubes by ultrasound.* Carbon, 1996. **34**: p. 814-816.

55. Duszova A Dusza J, Tomasek K, Blugan G, Kuebler J, *Microstructure and properties of carbon nanotube/zirconia composite.* Journal of the European Ceramic Society, 2008. **28**: p. 1023-1027.

56. Yamamoto G Omori M, Hashida T, Kimura H, *A novel structure for carbon nanotube reinforced alumina composites with improved mechanical properties.* Nanotechnology, 2008. **19**: p. 315708 (7pp).

57. Stojkovic D Zhang P, Crespi VH, *Smallest nanotubes: breaking the symmetry of sp3 bonds in tubular geometries.* Phys. Rev. Lett., 2001. **87**: p. 125502.

58. Zhang ZQ Liu B, Chen YL, Jiang H, Hwang KC, Huang Y, *Mechanical properties of functionalized carbon nanotubes.* Nanotechnology, 2008. **19**: p. 395702 (6pp).

59. Garg A Sinnott SB, *Effect of chemical functionalization on the mechanical properties of carbon nanotubes.* Chemical Physics Letters, 1998. **295**: p. 273-278.

60. Ahmad K Pan W, *Hybrid nanocomposites: A new route towards tougher alumina ceramics.* Composites Science and Technology, 2008. **68**: p. 1321–1327.

61. Bakshi SR Singh V, Seal S, Agarwal A, *Aluminum composite reinforced with multiwalled carbon nanotubes from plasma spraying of spray dried powders.* Surface & Coatings Technology, 2009. **203**: p. 1544-1554.

62. Balani K Agarwal A, McKechnie T, *Near net shape fabrication via vacuum plasma spray forming.* Trans. Indian Inst. Met., 2006. **59**: p. 237-244.

63. Balani K Anderson R, Laha T, Andara M, Tercero J, Crumpler E, et al, *Plasma-sprayed carbon nanotube reinforced hydroxyapatite coatings and their interaction with human osteoblasts in vitro.*

64. Balani K Anderson R, Laha T, Andara M, Tercero J, Crumpler E, et al, *Plasma-sprayed carbon nanotube reinforced hydroxyapatite coatings and their interaction with human osteoblasts in vitro.* Biomaterials, 2007. **28**: p. 618-624.

65. Fauchais P, *Understanding plasma spraying.* Journal of Physics D: Applied Physics, 2004. **37**: p. R86-R108.

66. Fauchais P Vardelle, Dussoubs B, *Quo vadis thermal spraying.* Journal of Thermal Spray Technology, 2001. **10**: p. 44-66.

67. Herman H Sampath S, Tiwari R, Neiser R, *Plasma spray forming of intermetallics and their composites.* Journal of Thermal Spray Technology, 1994. **3**: p. 294-296.

68. Laha T Kuchibhatla S, Seal S, Li W, Agarwal A, *Interfacial phenomena in thermally sprayed multiwalled carbon nanotube reinforced aluminum nanocomposite.* Acta mater., 2007. **55**: p. 1059-1066.

69. Cheang P Khor KA, *Addressing processing problems associated with plasma spraying of hydroxyapatite coatings.* Biomaterials, 1996. **17**: p. 537-544.

70. Cizek J Khor KA, Prochazka Z, *Influence of spraying conditions on thermal and velocity properties of plasma sprayed hydroxyapatites.* Materials science and Engineering C, 2007. **27**: p. 340-344.

71. Khan NA Lu J, *manipulation of air plasma spraying parameters for the production of ceramic coatings.* Journal of materials processing technology, 2009. **209**: p. 2508-2514.

72. Sato T Solonenko OP, Nishiyama H, *Optimization for plasma spraying processes by numerical simulation.* Thin solid film, 2002. **407**: p. 54-59.

73. Westergard R Erickson LC, Axen N, Hawthrone HM, Hogmark S, *The erosion and abrasion characteristics of alumina coatings plasma sparyed under different spraying conditions.* Tribology International, 1998. **31**: p. 271-279.

74. Leblanc L Moreau C, *The long term stability of plasma spraying.* Journal of Thermal Spray Technology, 2002. **11**: p. 380-386.

75. Li JF Liao H, Normand B, Cordier C, Maurin G, Foct J, Coddet C, *Uniform design method for optimization of process parameters of plasma sprayed TiN coatings.* Surface and Coatings Technology, 2003. **176**: p. 1-13.

76. Pierlot C Pawlowski L, Bigan M, Chagnon P, *Design of experiments in thermal spraying: A review.* Surface & Coatings Technology, 2008. **202**: p. 4483-4490.

77. Baik KH Grant PS, *Process Study, Microstructure, and Matrix Cracking of SiC Fiber Reinforced MoSi2 Based Composites.* Journal of Thermal Spray Technology, 2001. **10**: p. 584-591.

78. Mawdsley JR Su YJ, Faber KT, Bernecki TF, *Optimization of small-particle plasma-sprayed alumina coatings using designed experiments.* Materials Science and Engineering A, 2001. **308**: p. 189-199.

79. Sampath S Jiang X, Kulkarni A, Matejicek J, Gilmore DL, Neiser RA, *Development of process maps for plasma spray: case study for molybdenum.* Materials Science and Engineering A, 2003. **348**: p. 54-66.

80. Guessasma S Montavon G, Coddet C, *Modeling of the APS plasma spray process using artificial neural networks: basis, requirements and an example.* Computational Materials Science, 2004. **29**: p. 315-333.

81. Dyshlovenko S Pierlot C, Pawlowski L, Tomaszek R, Chagnon P, *Experimental design of plasma spraying and laser treatment of hydroxyapatite coatings.* Surface & Coatings Technology, 2006. **201**: p. 2054-2060.

82. Lin BT Jean MD, Chou JH, *Using response surface methodology for optimizing deposited partially stabilized zirconia in plasma spraying.* Applied Surface Science, 2007. **253**: p. 3254-3262.

83. Dwivedi G Wentz T, Sampath S, Nakamura T, *Assessing Process and Coating Reliability Through Monitoring of Process and Design Relevant Coating Properties.* Journal of Thermal Spray Technology, 2010. **19**: p. 695-712.

84. Plackett RL Burman JP, *The design of optimum multifactorial experiments.* Biometrika, 1946. **33**: p. 305-325.

85. Jaworski R Pawlowski L, Roudet F, Kozerski S, Maguer AL, *Influence of Suspension Plasma Spraying Process Parameters on TiO2 Coatings Microstructure.* Journal of Thermal Spray Technology, 2008. **17**: p. 73-81.

86. Jaworski R Pawlowski L, Roudet F, Kozerski S, Petit F, *Characterization of Mechanical Properties of Suspension Plasma Sprayed TiO2 Coatings Using Scratch Test.* Surface and coating technology, 2008. **202**: p. 2544-2553.

87. Mohammadi Z Ziaei-Moayyed AA, Sheikh-Mehdi AM, *Grit blasting of Ti–6Al–4V alloy: optimization and its effect on adhesion strength of plasma-sprayed hydroxyapatite coatings.* Journal of Materials Processing Technology, 2007. **194**: p. 15-23.

88. Box GEP Draper NRD, *Empirical Model Building and Response Methodology, Wiley, New York, USA*. 1987.

89. Kingswell R Scott KT, Wassell LL, *Optimizing the vacuum plasma spray deposition of metal, ceramic, and cermet coatings using designed experiments.* Journal of Thermal Spray Technology, 1993. **2**(2): p. 179-185.

90. Fang KT Shiu CX, Pan JX, *Uniform designs based on Latin squares*. Statistica Sinica, 1999. **9**: p. 905-912.

91. Fang KT Wang Y, *Number-Theoretic Methods in Statistics, Chapman & Hall London.* 1994.

92. Wang Y Fang KT, *Application of number theoretic methods in statistical analysis.* Science in China Series A, 1996. **26**: p. 1-10.

93. Fang Y, *Relationship between uniform design and orthogonal design, The Third International Chinese Statistical Association Statistical Conference, Beijing.* 1995.

94. Winker P Fang KT, *Optimal U-type design. In: H.Niederreiter, P. Zinterhof, and P. Hellekalek, Editors, Monte Carlo and Quasi Monte Carlo methods 1996, Springer, Berlin.* 1998: p. 436-448.

95. Balani K Gonzalez G, Agarwal A, Hickman R, O'Dell JS, Seal S., *Synthesis, microstructural characterization, and mechanical property evaluation of vacuum plasma sprayed tantalum carbide.* Journal of American Ceramics Society, 2006. **89**: p. 1419-1425.

96. Sun J Gao L, Jin XH, *Reinforcement of alumina matrix with multi-walled carbon nanotubes.* Ceramic International, 2005. **31**: p. 893-896.

97. Sun J Gao L, *Colloidal processing of carbon nanotube/alumina composites.* Chemistry of materials, 2002. **14**: p. 5169–5172.

98. An JW You DH, Lim DS, *Tribological properties of hot-pressed alumina-CNT composites.* Wear, 2003. **255**: p. 677-681.

99. Fan JP Zhao DQ, Wu MS, Xu ZN, Song J, *Preparation and microstructure of multi-wall carbon nanotubes-toughened Al2O3 composite.* Journal of American Ceramic Society, 2006. **89**: p. 750-753.

100. Zhu Y Shi L, Zhang C, Yang XZ, Liang J, *Preparation and properties of alumina composites modified by electric field-induced alignment of carbon nanotubes.* Applied Physics A: Materials Science & Processing, 2007. **89**: p. 761-767.

101. Jiang DT Thomson K, Kuntz JD, Ager JW, Mukherjee AK, *Effect of sintering temperature on a single-wall carbon nanotube-toughened alumina-based nanocomposite.* Scripta Materialia, 2007. **56**: p. 959-962.

102. Yamamoto G Omori M, Hashida T, *Preparation of Carbon Nanotube-Toughened Alumina Composites.* Water dynamics: 5th International Workshop on Water Dynamics. AIP Conference Proceedings, 2008. **987**: p. 83-85.

103. Wei T Fan ZJ, Luo GH, Wei F, *A new structure for multi-walled carbon nanotubes reinforced alumina nanocomposite with high strength and toughness.* Materials Letters, 2008. **62**: p. 641-644.

104. Estili M Kawasaki A, *An approach to mass-producing individually alumina-decorated multi-walled carbon nanotubes with optimized and controlled compositions.* Scripta Materialia, 2008. **58**: p. 906-909.

105. Kim SW Chung WS, Sohn KS, Son CY, Lee S, *Improvement of flexure strength and fracture toughness in alumina matrix composites reinforced with carbon nanotubes.* Materials Science and Engineering A, 2009. **517**: p. 293-299.

106. Zhang SC Fahrenholtz WZ, Hilmas GE, Yadlowsky EJ, *Pressureless sintering of carbon nanotube–Al2O3 composites.* Journal of the European Ceramic Society, 2010. **30**: p. 1373-1380.

107. Park KH Katoh Y, Kishimoto H, Kohyama A, *Evaluation of dual-ion irradiated b-SiC by means of indentation methods.* Journal of Nuclear Materials, 2002. **307-311**: p. 1187-1190.

108. Riester L Bridge RJ, Breder K, *Characterization of Vickers, Berkovich, Spherical and Cube Cornered Diamond Indenters by Nanoindentation and SFM.* Materials Research Bulletin, 1998. **45**.

109. Quinn GD Bradt RC, *On the Vickers indentation fracture toughness test.* Journal of American Ceramic Society, 2007. **90**: p. 673-680.

110. Evans AG Marshall B, *Wear Mechanism in Ceramics, Fundamentals of Friction and Wear of Materials.* 1981: p. 439.

111. Lim DS You DH, Choi HJ, Lim SH, Jang H, *Effect of CNT distribution on tribological behavior of alumina–CNT composites.* Wear, 2005. **259**: p. 539-544.

112. Lin X Zenga Y, Ding C, Zhang P, *Effects of temperature on tribological properties of nanostructured and conventional Al_2O_3–3 wt.% TiO_2 coatings.* Wear, 2004. **256**: p. 1018-1025.

113. Lim DS You DH, Choi HJ, Lim SH, Jang H, *Effect of CNT distribution on tribological behavior of alumina–CNT composites.* Wear, 2005. **259**: p. 539-544.

114. Ouyang JH Sasaki S, *Tribological characteristics of low-pressure plasma-sprayed $A1_2O_3$ coating from room temperature to 800°C.* Tribology International, 2005. **38**: p. 49-57.

115. Fauchais P Fukumoto M, Vardelle M, Vardelle M, *Knowledge Concerning Splat Formation: An Invited Review.* Journal of Thermal Spray Technology, 2004. **13**: p. 337-360.

116. Mostaghimi J Chandra S, *Splat formation in plasma-spray coating process.* Pure Appl. Chem., 2002. **74**: p. 441–445.

117. Sampath S Jiang X, *Splat formation and microstructure development during plasma spraying: deposition temperature effects.* Materials Science and Engineering A, 2001. **304–306**: p. 144–150.

118. Sobolev VV, *Formation of splat morphology during thermal spraying.* Materials Letters, 1998. **36**: p. 123-127.

119. Kulkarani AA Goland A, Herman H, Allen AJ, IIavsky J, Long GG, Carlo FD, *Advanced microstructural characterization of plasma-sprayed zirconia coatings over extended length scales.* Journal of Thermal Spray Technology, 2004. **14**: p. 239-250.

120. Li CJ Li CX, Wang M, *Effect of spray parameters on the electrical conductivity of plasma-sprayed La1−xSrxMnO3 coating for the cathode of SOFCs.* Surface and Coatings Technology, 2005. **198**: p. 278-282.

121. Sharma A Gambino RJ, Sampath S, *Anisotropic electrical properties in thermal spray metallic coatings.* Acta Materialia, 2006. **54**: p. 59-65.

122. Ghafouri-Azar R Mostaghimi J, Chandra S, Charmchi M, *A Stochastic Model to Simulate the Formation of a Thermal Spray Coating.* Journal of Thermal Spray Technology, 2002. **12**: p. 53-69.

123. Fukumoto M Huang Y, Ohwatari M, Coddet C, *Thermal Spray, Meeting the Challenge of the 21st century, ASM International, Metals Park, OH.* 1998: p. 401.

124. Pasandideh-Fard M Qiao YM, Chandra S, Mostaghimi J, *Capillary effects during droplet impact on a solid surface.* Physics of Fluids, 1996. **8**: p. 650-660.

125. Bennett T Poulikakos D, *Heat Transfer aspects of splat-quench solidification: modeling and experiment.* J. Mater. Sci., 1994. **29**: p. 2025-2039.

126. Zhao Z Poulikakos D, Fukai J, *Heat transferand fluid dynamics during the collision of a liquid droplet on a substrate—I Modeling.* Int. J. Heat Mass Transfer, 1996. **39**: p. 2271–2789.

127. Bussmann M Chandra S, Mostaghimi J, *Modeling the Splash of a Droplet Impacting a Solid Surface.* Physics of Fluids, 2000. **12**.

128. Bussmann M. Mostaghimi J Chandra S, *On a Three-Dimensional Volume Tracking Model of Droplet Impact.* Physics of Fluids, 1999. **11**: p. 1406-1417.

129. Pasandideh-Fard M Chandra S, Mostaghimi J, *1st International Thermal Spray Conference, Montreal, Quebec pp. 125.* 2000.

130. Pasandideh-Fard M Chandra S, Mostaghimi J, *A Three-Dimensional Model of Droplet Impact and Solidification.* Int. J. of Heat Mass Transfer, 2002. **45**: p. 2229-2242.

131. Pasandideh-Fard M Pershin V, Chandra S, Mostaghimi J, *Splat Shapes in a Thermal Spray Coating Process: Simulations and Experiments.* Journal of Thermal Spray Technology, 2002. **11**: p. 206-217.

132. Altman IS, *On principle inadequacy of the Plank distribution to the spectrum of the small particle thermal radiation.* Physics Letters A, 1999. **256**: p. 122-124.

133. Goberman D Sohn YH, Shaw L, Jordan E, Gell M, *Microstructure development of Al2O3–13wt.%TiO2 plasma sprayed coatings derived from nanocrystalline powders.* Acta Materialia, 2002. **50**: p. 1141-1152.

134. Yin Z Tao S, Zhou X, Ding C, *Preparation and characterization of plasma-sprayed Al/Al2O3 composite coating.* Materials Science and Engineering A, 2008. **480**: p. 580-584.

135. Anstis GR Chantikul P, Lawn BR, Marshall DB, *A Critical Evaluation of Indentation Techniques for Measuring Fracture Toughness: Direct Crack Measurements.* Journal of the American Ceramic Society, 1981. **64**: p. 533-538.

136. Ortega-Cervantez G Rueda-Morales G, Ortiz-López J, *Cold-wall CVD carbon nanotube synthesis on porous alumina substrates.* Journal of Materials Science: Materials in Electronics, 2009. **20**: p. 403-407.

137. Luo J Stevens R, *Porosity-dependence of elastic moduli and hardness of 3Y-TZP ceramics.* Ceramic International, 1999. **25**: p. 281-286.

138. Vemuri MK Chavala AR, Anil R, Sethunarayanan T, Seshadri V, International Engineering Management Conference, 2004: p. 765-769.

139. Azarmi F Coyle TW, Mostaghimi J, *Optimization of Atmospheric Plasma Spray Process Parameters using a Design of Experiment for Alloy 625 coatings.* Journal of Thermal Spray Technology, 2008. **17**(1): p. 144-155.

140. Tarantili P.A. Andreopoulos A.G., Galiotis C., *Real-Time Micro-Raman Measurements on Stressed Polyethylene Fibers. 1.Strain Rate Effects and Molecular Stress Redistribution.* Macromolecules, 1998. **31**: p. 6964-6976.

141. Andrews R Jacquesa D, Qianb D, Dickey EC, *Purification and structural annealing of multiwalled carbon nanotubes at graphitization temperatures.* Carbon, 2001. **39**: p. 1681-1687.

142. Ci L Zhu H, Wei B, Xu C, Wu D, *Annealing amorphous carbon nanotubes for their application in hydrogen storage.* Applied Surface Science, 2003. **205**: p. 39-43.

143. Huang W Wang Y, Luo G, Wei F, *99.9% purity multi-walled carbon nanotubes by vacuum high-temperature annealing.* Carbon, 2003. **41**: p. 2585-2590.

144. Ouldriane SD Szostak K, Frackowiak E, Be´guin F, *Annealing of template nanotubes to well-graphitized multi-walled carbon nanotubes.* Carbon, 2006. **44**: p. 799-823.

145. Corrêa MC Moraesa SB, Elias CN, Filho JD, Oliveirab LG, *Mechanical Properties of Alumina-Zirconia Composites for Ceramic Abutments.* Materials Research, 2004. **7**: p. 643-649.

146. FACTSAGE Thermodynamic Equilibrium Software version 5.0, Center for Research in Computational Thermochemistry of the Ecole Polythechnique at the Universite´ de Montre´al and GTT-Technologies, GmbH, Aachen, Germany, 2001.

147. Kim SS Chae YH, Kim DJ, *Tribological characteristics of silicon nitride at elevated temperatures.* Tribology Letters, 2000. **9**: p. 227-232.

148. Li J Xiong D, *Tribological behavior of graphite-containing nickel-based composite as function of temperature, load and counterface.* Wear, 2009. **266**: p. 360-367.

149. Oh YS Cho WS, Kim CS, Lim DS, Cheong DS, *XPS investigation of Si3N4/SiC nanocomposites prepared using a commercial polymer.* Journal of American Ceramic Society, 1999. **82**: p. 1076-1078.

150. Li CX Xia J, Dong H, *Sliding wear of TiAl intermetallics against steel and ceramics of Al2O3, Si3N4 and WC/Co.* Wear, 2006. **261**: p. 693–701.

151. Osswald S Havel M and Gogotsi Y, *Monitoring oxidation of multiwalled carbon nanotubes by Raman spectroscopy.* Journal of Raman Spectroscopy, 2007. **38**: p. 728-736.

152. Ci L Zhu H, Wei B, Xu C, Wu D, *Annealing amorphous carbon nanotubes for their application in hydrogen storage.* Applied Surface Science, 2003. **205**: p. 39-43.

153. Wang HL Hon MH, *Temperature dependence of ceramics hardness.* Ceramics International, 1999. **25**: p. 267-271.

154. Voitovich VB Sverdel VV, Voitovich RF and Golovko EI, *Oxidation of WC-Co, WC-Ni and WC-Co-Ni hard metals in the temperature range 500~800°C.* Int. J. of Refractory Metals & Hard Materials, 1996. **14**: p. 289-295.

155. Ho SF Contarini S, Rabalais J.W, *Ion-Beam-Induced Chemical Changes in the Oxyanions (MOn-y) and Oxides (MOx)Where M = Cr, Mo, W, V, Nb, and Ta.* J. Phys Chem., 1987. **91**: p. 4779-4788.

156. Newkirk AE, *The oxidation of tungsten carbide.* Journal of American Chemical Society, 1955. **77**(17): p. 4521-4522.

157. Sverdel VB Voitovich RF, Golovko EI, *Oxidation of WC-Co, WC Ni and WC-Co-Ni hard metals in the temperature range 500–800°C.* International Journal of Refractory Metals and Hard Materials, 1996. **14**(4): p. 289-295.

158. Gonzalez ES Miranda P, Martinez JJM, Guiberteau F, Pajares A, *Temperature dependence of mechanical properties of alumina up to the onset of creep.* J. Europ. Ceram. Soc., 2007. **27**: p. 3345–3349.

159. Morisada Y Maeda M, Shibayanagi T, Miyamoto Y, *Oxidation resistance of multiwalled carbon nanotubes coated with silicon carbide.* J. Am. Ceram. Soc., 2004. **87**: p. 804-808.

160. Huang W Wang Y, Luo G, Wei F, *9 9.9% purity multi-walled carbon nanotubes by vacuum high-temperature annealing.* Carbon, 2003. **41**: p. 2585-2590.

161. Li C Wang D, Liang T, Wang X, Wu J, Hu X and Liang J, *Oxidation of multiwalled carbon nanotubes by air: benefits for electric double layer capacitors.* Powder Technology, 2004. **142**: p. 175-179.

162. Zhang XX Deng CF, Xu R, Wang DZ, *Oxidation resistance of multi-walled carbon nanotubes purified with sulfuric and nitric acids.* J Mater. Sci., 2007. **42**: p. 8377–8380.

163. Fauchais P Vardelle M, Vardelle A, Bianchi L, *Plasma Spray: Study of the Coating Generation.* Ceramic International, 1996. **22**: p. 295-303.

164. Moreau C Gougeon P, Lamontagne M, *Influence of Substrate Preparation on the Flattening and Cooling of Plasma Sprayed Particles."* J. Therm. Spray Technol., 1995. **4**: p. 25-36.

165. Jiang X Matejicek J, Sampath S, *Substrate temperature effects on the splat formation, microstructure development and properties of plasma sprayed coatings Part II: case study for molybdenum.* Materials Science and Engineering A, 1999. **272**: p. 189-198.

166. Vardelle A Themelis NJ, Vardelle M, Fauchais P, *Transport and Chemical Rate Phenomena in Plasma Sprays.* J. High Temp. Mater., 1997: p. 295-314.

167. Fukumoto M Katoh S, Okane I, in: A. Ohmori (Ed.), *Proceeding of the Integrated Thermal Spray Conference, Kobe Japan, May, 1995, Japan High Temperature Society, Japan, 1995.* 1995: p. 353–358.

APPENDIX

This section provides a list of publication in peer reviewed journals directly related to this study.

List of publications in peer reviewed journals:

1. *Anup Kumar Keshri*, Jun Huang, Virendra Singh, Wonbong Choi, Sudipta Seal and Arvind Agarwal, "*Synthesis of Aluminum Oxide Coating with Carbon Nanotube Reinforcement Produced by Chemical Vapor Deposition for Improved Fracture and Wear Resistance"*, ***Carbon*** Vol. 48 (2010) 431-442

2. *Anup Kumar Keshri***,** Jun Huang, Wonbong Choi, and Arvind Agarwal, "*Intermediate Temperature Tribological Behavior of Carbon Nanotube Reinforced Plasma Sprayed Aluminum Oxide Coating", **Surface and Coatings Technology*** Vol. 204 (2010) 1847-1855

3. *Anup Kumar Keshri*, Riken Patel, and Arvind Agarwal "*Comprehensive Process Maps to Synthesize High Density Plasma Sprayed Aluminum Oxide Composite Coatings with Varying Carbon Nanotube Content"*, Manuscript conditionally accepted to ***Surface and Coatings Technology*** *(2010)*

4. *Anup Kumar Keshri*, Kantesh Balani, Srinivasa Rao Bakshi, Virendra Singh, Tapas Laha, Sudipta Seal and Arvind Agarwal, *"Structural Transformation in Carbon Nanotubes During Thermal Spraying"*, ***Surface and Coatings Technology*** Vol. 203 (2009) 2193-2201 **(Ranked 5th among TOP 25 articles in Surface and Coatings Technology journal for April-June 2009)**

5. *Anup Kumar Keshri*, Srinivasa Rao Bakshi, Yao Chen, Tapas Laha, Xiaohua. Li, Cesar Levy and Arvind Agarwal, *Nanomechanical Behavior of Plasma Sprayed PZT Coatings"*, ***Surface Engineering*** Vol. 25[4] (2009) 270-275

6. Debrupa Lahiri, Francois Rouzaud, Tanisha Richard, *Anup Kumar Keshri,* Srinivasa Rao Bakshi, Lidia Kos and Arvind Agarwal, "*Boron Nitride Nanotube Reinforced Polylactide-Polycaprolactone Copolymer Composite: Mechanical Properties and Cytocompatibility with Osteoblasts and Macrophages in vitro"* ***Acta Biomaterialia*** doi:10.1016/j.actbio.2010.02.044

7. Debrupa Lahiri, Virendra Singh, *Anup Kumar Keshri,* Sudipta Seal and Arvind. Agarwal, "*Carbon nanotube toughened hydroxyapatite by spark plasma sintering: microstructural evolution and multi-scale tribological properties",* ***Carbon*** Vol. 48 (2010) 3103-3120

8. Riken Patel, *Anup Kumar Keshri*, George S. Dulikravich and Arvind Agarwal, "*An Experimental and Numerical Algorithm for Near Net Shape Fabrication of Thin Walled Ceramic Structures by Plasma Spray Forming"*, ***Journal of Materials Processing Technology*** Vol. 210 (2010) 1260-1269

9. Debrupa Lahiri, Francois Rouzaud, Sabnam Namin, *Anup Kumar Keshri*, Nicolaos Tsoukias, Lidia. Kos, Arvind Agarwal, "Effect of CNT Addition in Polylactide-Caprolactone Copolymer on Mechanical Strengthening and Interaction with Human Osteoblast Cells in- vitro" ***ACS Applied Materials and Interfaces*** Vol. 1 (2009) 2470-2476

10. Debrupa Lahiri, *Anup Kumar Keshri*, Srinivasa Rao Bakshi, Arvind Agarwal, "Dual Strengthening Mechanism Induced by Carbon Nanotube in Roll Bonded Aluminum Matrix Composite",***Materials Science and Engineering A,*** Vol. 523 (2009) 263-270

11. Srinivasa R. Bakshi, Yao Chen, Timothy Price, Deen Zhang, *Anup Kumar Keshri*, D. Graham McCartney, Phil Shipway and Arvind Agarwal, "*Microstructure and Wear Properties of Aluminum/Aluminum-Silicon Composite Coatings Prepared by Cold Spraying*", ***Surface and Coatings Technology*** Vol. 204 (2009) 503-510

12. Srinivasa R. Bakshi, *Anup Kumar Keshri*, Virendra Singh, Sudipta Seal, Arvind Agarwal, *"Interface in Carbon Nanotube Reinforced Aluminum Silicon Composites: Thermodynamic Analysis and Experimental Verification"*, ***Journal of Alloys and Compounds*** Vol. 481 (2009) 207-213

13. Kantesh Balani, *Anup Kumar Keshri,* Debrupa Lahiri, Jorge E. Tercero and Arvind Agarwal, "*Nano-scratching of Hydroxyapatite Reinforced with Aluminum Oxide and Carbon Nanotubes*", ***JOM,*** Vol. 61 (2009) 63-66

14. Kantesh Balani, Sandip P. Harimkar, *Anup K Keshri*, Yao Chen, Narendra B. Dahotre and Arvind Agarwal, "*Multiscale wear of plasma-sprayed carbon-nanotube-reinforced aluminum oxide nanocomposite coating"* ***Acta Materialia***, Vol. 56, (2008) 5984-5994.

15. Yao Chen, Shobit Omar, *Anup Kumar Keshri*, Kantesh Balani, Krishnamurthy Babu, Juan C Nino, Sudipta Seal and Arvind Agarwal, "*Ionic conductivity of plasma-sprayed nanocrystalline yttria-stabilized zirconia electrolyte for solid oxide fuel cells*" ***Scripta Materialia,*** 60 (2009) 1023–1026

List of Paper Submitted to Peer Reviewed Journal:

1. Debrupa Lahiri, Ana Paula Benaduce, Francois Rouzaud, John Solomon, *Anup Kumar Keshri*, Lidia Kos, Arvind Agarwal, "*Wear Behavior and In-vitro Cytotoxicity of Wear Debris Generated from Hydroxyapatite-Carbon Nanotube Composite Coating"* Submitted to ***Journal of Biomedical Materials Research Part A***

CARBON 48 (2010) 431–442

available at www.sciencedirect.com

ScienceDirect

journal homepage: www.elsevier.com/locate/carbon

Synthesis of aluminum oxide coating with carbon nanotube reinforcement produced by chemical vapor deposition for improved fracture and wear resistance

Anup K. Keshri [a], Jun Huang [b], Virendra Singh [c], Wonbong Choi [b], Sudipta Seal [c], Arvind Agarwal [a,]*

[a] *Plasma Forming Laboratory and High Temperature Tribology Laboratory, Mechanical and Materials Engineering, 10555 West Flagler Street, EC 3464, Florida International University, Miami, FL 33174, USA*

[b] *Nanomaterials and Device Laboratory, Mechanical and Materials Engineering, 10555 West Flagler Street, EC 3464, Florida International University, Miami, FL 33174, USA*

[c] *AMPAC and Nanoscience Technology Center, 4000 Central FL Blvd, AMPAC, Eng 1 Room 381, University of Central Florida, Orlando, FL 32816, USA*

ARTICLE INFO

Article history:
Received 24 April 2009
Accepted 16 August 2009
Available online 19 September 2009

ABSTRACT

Chemical vapor deposition (CVD) was used to achieve a homogeneous dispersion of carbon nanotubes (CNTs) on aluminum oxide (Al_2O_3) powder. This powder was plasma sprayed onto a steel substrate to produce a 96% dense Al_2O_3 coating with CNT reinforcement. Addition of 1.5 wt.% CNTs showed a 24% increase in the relative fracture toughness of the composite coating. The improvement in the fracture toughness is attributed to uniform dispersion of CNTs and toughening mechanism such as CNT bridging, crack deflection and strong interaction between CNT/Al_2O_3 interfaces. Wear and friction behavior of the CNT reinforced Al_2O_3 coating under dry sliding condition was investigated by ball-on-disk tribometer. With the increasing normal loads from 10 to 50 N, the wear volume loss and coefficient of friction of the coating increased, owing to transition from the mild to severe wear. Wear resistance of the Al_2O_3–CNT composite coating improved by ~27% at 50 N. Coefficient of friction at 50 N was dependent on the competing phenomena of wear debris generation and graphitization due to pressure.

1. Introduction

Since the discovery of carbon nanotubes (CNTs), they have attracted much attention as potential reinforcement for composites due to their excellent mechanical, electrical, and thermal properties [1–6]. However, the natural tendency of CNTs to exist as agglomerates due to their strong surface forces [7–9], limits their application as uniformly dispersed reinforcement. Researchers have attempted molecular level mixing [10], sol–gel process [11,12], heterocoagulation [13,14], spray drying [15,16] and CVD [7,17] to effectively disperse the CNTs in the ceramic matrix. All of these CNT dispersion techniques have evinced varying degree of success with some limitations.

Molecular level mixing has shown promising results to achieve homogeneous dispersion of CNTs in the Al_2O_3 matrix [10]. However, this process requires functionalization of CNT which introduce defects and deteriorate its properties. Elastic modulus of CNTs decreases gradually with increasing functionalization due to introduction of sp^3 hybridized sites [16].

* *Corresponding author:* Fax: +1 305 348 1932.
E-mail address: agarwala@fiu.edu (A. Agarwal).
0008-6223/$ - see front matter © 2009 Elsevier Ltd. All rights reserved.
doi:10.1016/j.carbon.2009.08.046

Surface & Coatings Technology 204 (2010) 1847–1855

Contents lists available at ScienceDirect

Surface & Coatings Technology

journal homepage: www.elsevier.com/locate/surfcoat

Intermediate temperature tribological behavior of carbon nanotube reinforced plasma sprayed aluminum oxide coating

Anup Kumar Keshri [a], Virendra Singh [b], Jun Huang [c], Sudipta Seal [b], Wonbong Choi [c], Arvind Agarwal [a,*]

[a] Plasma Forming Laboratory and High Temperature Tribology Laboratory, Mechanical and Materials Engineering, Florida International University, Miami, FL 33174, USA
[b] AMPAC and Nanoscience Technology Center, 4000 Central FL Blvd, AMPAC, Eng 1 Room 381, University of Central Florida, Orlando 32816, USA
[c] Nanomaterials and Device Laboratory, Mechanical and Materials Engineering, Florida International University, Miami, FL 33174, USA

ARTICLE INFO

Article history:
Received 4 September 2009
Accepted in revised form 20 November 2009
Available online 1 December 2009

Keywords:
High temperature wear
Carbon nanotubes
Aluminum oxide
Plasma spray
Tribochemical reaction
Coefficient of friction

ABSTRACT

Tribological behavior of plasma sprayed carbon nanotube (CNT) reinforced aluminum oxide (Al_2O_3) composite coatings was examined at room temperature, 573 K and 873 K using tungsten carbide (WC) ball-on-disk tribometer. The weight loss due to wear of Al_2O_3 coating was found to be increasing with the temperature while Al_2O_3-CNT coating showed a decreasing trend in the weight loss with the temperature. Relative improvement in the wear resistance of Al_2O_3-CNT coating compared to Al_2O_3 coating was found to be 12% at room temperature which gradually increased to ~56% at 573 K and ~82% at 873 K. Protective layer as a result of tribo-chemical reaction was observed on the wear track of both of the coatings. The improvement in the wear resistance of Al_2O_3-CNT coating was attributed to three phenomena *viz.* (i) higher hardness at the elevated temperature as compared to Al_2O_3 coating, (ii) larger area coverage by protective film on the wear surface at the elevated temperature and (iii) CNT bridging between splats. The coefficient of friction (COF) of Al_2O_3 coating was nearly constant at room and elevated temperature whereas COF for Al_2O_3-CNT coating decreased at the elevated temperature (873 K).

1. Introduction

Carbon nanotubes (CNTs) have attracted much attention as a potential reinforcement for the enhancement of toughness [1–6] and wear resistance [7–10] of the ceramic matrix due to their remarkable mechanical [11–15] and thermal properties [16,17]. In the past, researchers have addressed the tribological behavior of CNT reinforced aluminum oxide (Al_2O_3) composite [7–10]. An et al. [8] studied the effect of 4 wt.% CNT addition on tribological behavior of hot pressed Al_2O_3 and observed that relative wear weight loss decreased by 45% with CNT addition. However, the wear resistance of the composite significantly decreased with the addition of 10 wt.% CNT which was attributed to inhomogeneous dispersion of the CNT and poor cohesion between CNT and Al_2O_3 matrix. Another study on tribological performance of Al_2O_3-CNT by Lim et al. [10] showed that wear weight loss continuously decreased with an increase in CNT content up to 12 wt.%. This was attributed to the enhanced dispersion of CNT in Al_2O_3 composite which was achieved by tape casting followed by lamination and hot pressing. Balani et al. [9] reported an improvement of 49 times in the sliding wear resistance by the addition of 8 wt.% CNT to Al_2O_3. Such improvement was attributed to a uniform dispersion of nanotubes, CNT bridging between the splats and enhanced densification by CNTs. All these studies investigated tribological behavior of the Al_2O_3-CNT coating at room temperature. However, no attempt has been made to study the tribological behavior of CNT-reinforced ceramic composites at elevated temperature; though there are some studies [18,19] that provide an insight into the tribological characteristics of Al_2O_3 without CNT reinforcement at the elevated temperature.

Ouyang et al. [19] studied the tribological characteristics of low-pressure plasma sprayed Al_2O_3 coating from room temperature to 800 °C and found a transition from mild to severe wear with the increasing temperature. At room temperature, Al_2O_3 coating exhibited low friction (0.17) and wear rate (1.07×10^{-5} mm^3/Nm) when sliding against Al_2O_3 ball. However, when temperature is increased above 400 °C, coefficient of friction (COF) and wear of the Al_2O_3 coating increased rapidly and reached a maximum (COF: 1.52, wear rate: 2.97×10^{-4} mm^3/Nm) at 800 °C. Similar result was found by Lin et al. [18] who studied the tribological behavior of Al_2O_3–3 wt.% TiO_2 coating against silicon nitride (Si_3N_4) ball from room temperature to 873 K. They found that wear rate of coating was too small to be measured accurately at the room temperature which increased (~5.5×10^{-5} mm^3/Nm) with the increase in the temperature. Improved wear resistance at room temperature was attributed to the formation of protective silicon oxide (SiO_2) layer on the wear track. This protective SiO_2 layer was the result of the oxidation of Si_3N_4 (counter body) ball in the presence of the moisture. It was observed

* Corresponding author. Tel.: +1 305 348 1701; fax: +1 305 348 1932.
E-mail address: agarwala@fiu.edu (A. Agarwal).

0257-8972/$ – see front matter © 2009 Elsevier B.V. All rights reserved.
doi:10.1016/j.surfcoat.2009.11.032

Comprehensive Process Maps to Synthesize High Density Plasma Sprayed Aluminum Oxide Composite Coatings with Varying Carbon Nanotube Content

Anup Kumar Keshri, Riken Patel, and Arvind Agarwal*
Plasma Forming Laboratory
Mechanical and Materials Engineering
Florida International University, Miami, FL 33174, USA

Abstract

Comprehensive process maps have been developed to synthesize "high density" plasma sprayed Aluminum oxide (Al_2O_3) composite coatings with 0, 4 and 8 wt. % carbon nanotube (CNT) reinforcement. These process maps correlate the key processing parameters such as plasma power, powder feed rate, primary gas flow rate, and stand-off distance to the temperature and velocity of the in-flight particles and finally to the density and microhardness of coatings. Relative importance of each significant process parameters was also investigated by making *"Pareto diagrams"*. Stand-off distance followed by the plasma power were found to be most sensitive parameters which affects the density of the plasma sprayed Al_2O_3-CNT composite coatings. Process maps showed that CNTs has significant effect on altering the temperature and velocity of in-flight particles. Higher thermal conductivity of CNTs alters the heat transfer phenomena during the coating build up which assists in densification.

Surface and Coatings Technology (2010), in press

Surface & Coatings Technology 203 (2009) 2193–2201

Contents lists available at ScienceDirect

Surface & Coatings Technology

journal homepage: www.elsevier.com/locate/surfcoat

Structural transformations in carbon nanotubes during thermal spray processing

Anup Kumar Keshri [a], Kantesh Balani [a,b], Srinivasa R. Bakshi [a], Virendra Singh [c], Tapas Laha [a,d], Sudipta Seal [c], Arvind Agarwal [a,*]

[a] Mechanical and Materials Engineering, Florida International University, Miami, FL 33174, USA
[b] Materials and Metallurgical Engineering, Indian Institute of Technology, Kanpur, India
[c] Mechanical, Materials and Aerospace Engineering, University of Central Florida, Orlando 32816, USA
[d] Materials and Metallurgical Engineering, Indian Institute of Technology, Kharagpur, India

ARTICLE INFO

Article history:
Received 6 December 2008
Accepted in revised form 9 February 2009
Available online 23 February 2009

Keywords:
Carbon nanotubes (CNTs)
Plasma spraying (PS)
High-velocity oxy fuel spraying (HVOF)
Cold spraying (CS)
Plasma spraying of liquid precursor (PSLP)

ABSTRACT

This study compares the interaction of carbon nanotubes (CNTs) with the flame/energy sources during different thermal spray processes *viz.* plasma spraying (PS), high-velocity oxy fuel spraying (HVOF), cold spraying (CS), and plasma spraying of liquid precursor (PSLP). CNTs were successfully retained as reinforcement in metal and ceramic composite coatings in all thermal spray processes except PSLP. The retention of CNT structure is attributed to micron size metal/ceramic powder which acts as a carrier and thermal shield against high heat in plasma spraying (PS) and high-velocity oxy fuel spraying (HVOF). However, vaporization of CNTs occurred in PSLP under the intense heat of the plasma which is attributed to phase transformation in unshielded CNTs.

1. Introduction

Carbon nanotubes (CNTs) have attracted much attention as reinforcement for composites, by virtue of their remarkable mechanical, electrical and thermal properties [1–4]. This allotrope of carbon possesses almost five times elastic modulus (~1 TPa) and 100 times tensile strength (~150 GPa) than those of high strength steels [5–7]. This ultrahigh strength of CNTs makes them potential reinforcement for composite materials. CNT reinforcement increases the strength and stiffness of metals and polymers, and improves the fracture toughness [8,9] and thermal conductivity [10] of ceramics. Some of the key processing techniques used in synthesis of CNT reinforced metal and ceramic composites are conventional powder metallurgy techniques [11,12], electro and electroless plating from CNT containing electrolytic baths [13,14], spark plasma sintering [15,16], and mechanical alloying [17].

In the last five years, our research group has utilized thermal spray techniques (*plasma spraying, high-velocity oxy fuel spraying, and cold spraying*) to synthesize CNT reinforced metal and ceramic composite coatings [9,18–30]. Laha et al. successfully synthesized CNT reinforced Al–23 wt.% Si composite coating via *plasma* and *HVOF spraying* using blended powder [18]. HVOF deposited coating resulted in improved density (96.8%) and elastic modulus in comparison with plasma sprayed composite [18]. Laha et al. also studied the interfacial phenomena between the Al–Si alloy matrix and the CNT reinforcement in composites synthesized by plasma spraying and HVOF spraying techniques [20]. Formation of SiC as interfacial reaction product was observed in both spraying techniques. However, the thickness of SiC layer in plasma spraying was greater than that of HVOF due to higher processing temperature in plasma spraying. The formation of SiC layer improved the wettability and interfacial adhesion between MWCNT reinforcement and Al–Si matrix [20].

Balani et al. synthesized CNT reinforced Al_2O_3 coating via *plasma spraying* using spray dried composite powder with varying CNTs content [9,21]. Spray dried powder resulted in improved CNTs dispersion and mechanical properties as compared to the blended powder. Addition of 8 wt.% CNTs to Al_2O_3 matrix resulted in fracture toughness of 5.04 ±0.58 MPa $m^{1/2}$ which is 57% improvement over Al_2O_3 coating without reinforcement [21]. The same coating also displayed improvement in pin-on-disc wear resistance by 49 times as compared to coating without reinforcement [22]. Balani et al. concluded retention of CNT network as anchor indicating the survivals of CNTs in harsh plasma spraying environment. In a separate study, Balani et al. synthesized CNT reinforced hydroxyapatite (HA) bioceramic coating through *plasma spraying* [23]. Fracture toughness improvement of 56% was observed for HA–4 wt.% CNT composite coating which is attributed to CNTs distribution and anchoring of CNTs to form bridge structure. Reinforcement of CNTs showed improvement in precipitation and mineralization of apatite onto CNT surface [23]. Plasma sprayed HA–4 wt.% CNT coating displayed an improvement in wear resistance (1.5 times) as compared to HA coating

* Corresponding author. Tel.: +1 305 348 1701; fax: +1 305 348 1932.
E-mail address: agarwala@fiu.edu (A. Agarwal).

0257-8972/$ – see front matter © 2009 Elsevier B.V. All rights reserved.
doi:10.1016/j.surfcoat.2009.02.013

Nanomechanical behaviour of plasma sprayed PZT coatings

A. K. Keshri[1], S. R. Bakshi[1], Y. Chen[1], T. Laha[1,2], X. Li[1], C. Levy[1] and A. Agarwal*[1]

Nanomechanical properties of the plasma sprayed lead zirconate titanate (PZT) coating have been investigated using nanoindentation technique. PZT coating processed at higher plasma power of 32 kW exhibited lower elastic modulus E of 98 GPa compared with the modulus (113 GPa) of the coating processed at plasma power of 20 kW. The variation in the elastic modulus is attributed to the fine porosity of the PZT coating, which is formed during plasma spraying. Porosity increases by evaporation of PbO phase during plasma spraying. Overall effective elastic modulus of both coatings is computed using micromechanics models and compared with the experimentally obtained values. Hashin–Shtrikman and rule of mixtures models predict values that closely match with nanoindentation values.

Keywords: Plasma spray, PZT, Nanoindentation, Elastic modulus, Porosity

Introduction

Lead zirconate titanate (PZT) is a piezoelectric material, which is widely used as sensors and actuators.[1,2] The miniaturisation of actuators requires fabrication of PZT in the form of thin films and coatings. There are several methods available for the synthesis of PZT coating. Crystalline PZT coatings have been prepared by various methods such as digital metalorganic chemical vapour deposition,[3] vacuum evaporation,[4] aerosol deposition,[5] pulsed laser deposition,[6] radio frequency magnetron sputtering[7,8] and sol–gel deposition.[9–11] PZT films prepared by sol–gel are limited in thickness and usually fall in the range below 1 μm. Deposition of thicker layer usually results in cracks[12] and inferior mechanical properties.

Sherrit *et al.*[13] successfully fabricated PZT glass composite (thickness, 80–250 μm) by plasma spraying technique. Evaporation of lead oxide was a major problem during plasma spraying of PZT, which lead to compositional inhomogeneities. In addition, the presence of porosity (30–40%) in PZT films made poling difficult.[13] Piezoelectric charge coefficient of plasma sprayed PZT film ranged from 0·47 to 1·1 pC/N and dielectric constant from 58 to 20. Plasma sprayed PZT films displayed piezoelectric nature, albeit small. Haessler *et al.*[14] studied the structure and electrical properties of PZT thick films (~200 μm) produced by plasma spraying. Because of the high temperature during the plasma spraying process, the $PbZrO_3$ in the PZT particles melts incongruently and PbO partly evaporates. EDX results showed an inhomogeneous distribution of the phases in the sprayed film due to lead oxide evaporation.

To comprehensively understand the factors influencing piezoelectric coefficients, the mechanical properties of these PZT coatings are extremely important. Elastic modulus is one of the important properties for the membrane structure, which can influence the stiffness of the structure.[15] Bahr *et al.*[16] studied the mechanical deformation of spin coated PZT thin films (600 nm) using continuous indentation technique. PZT film exhibited a hardness value between 5 and 8 GPa, which is slightly lower than the hardness of bulk PZT, ~9 GPa. The elastic modulus of the bulk PZT (~135 GPa) and thin PZT film (130–160 GPa) were also measured by nanoindentation. Zheng *et al.* also studied the nanoindentation behaviour of spin coated $Pb(Zr_{0·52}Ti_{0·48})O_3$ ferroelectric thin films (300–500 nm).[17] Hardness (~12 GPa) and elastic modulus (~150 GPa) of the PZT film were higher than those of the bulk PZT material. PZT coating synthesised using sol–gel process displayed an average elastic modulus and hardness value of ~121 and 13 GPa respectively.[18] Vincent *et al.* fabricated the soft and hard PZT films on alumina substrate by screen printing process.[19] Elastic modulus measured by nanoindentation was 52 ± 8 GPa for soft PZT film and 20 ± 7 GPa for hard PZT film.[19] Elastic modulus values were strongly influenced by porosity in the film.

It is observed that there is much research on nanomechanical properties of PZT film fabricated by sol–gel, screen printing and spin coating processes,[16–19] but nanomechanical properties of plasma sprayed PZT coatings have never been investigated.[13,14] Motivated by these considerations, the objective of the present work is to synthesise PZT coating via plasma spray technique and measure the nanomechanical properties of the plasma sprayed PZT coatings using nanoindentation technique. The correlation

[1]Department of Mechanical and Materials Engineering, Florida International University, Miami, FL 33174, USA
[2]Department of Metallurgical and Materials Engineering, Indian Institute of Technology, Kharagpur, India

*Corresponding author, email agarwala@fiu.edu

Published by Maney on behalf of the Institute
Received 19 August 2008; accepted 5 October 2008
DOI 10.1179/026708408X375307

Acta Biomaterialia xxx (2010) xxx–xxx

Contents lists available at ScienceDirect

Acta Biomaterialia

journal homepage: www.elsevier.com/locate/actabiomat

Boron nitride nanotube reinforced polylactide–polycaprolactone copolymer composite: Mechanical properties and cytocompatibility with osteoblasts and macrophages in vitro

Debrupa Lahiri [a], Francois Rouzaud [b], Tanisha Richard [a], Anup K. Keshri [a], Srinivasa R. Bakshi [a], Lidia Kos [b], Arvind Agarwal [a,*]

[a] Mechanical and Materials Engineering, Florida International University, Miami, FL 33174, USA
[b] Biological Sciences, Florida International University, Miami, FL 33174, USA

ARTICLE INFO

Article history:
Received 17 November 2009
Received in revised form 22 February 2010
Accepted 24 February 2010
Available online xxxx

Keywords:
Biodegradable polymer composite
Boron nitride nanotube
Mechanical properties
Viability
Cytotoxicity

ABSTRACT

Biodegradable polylactide–polycaprolactone copolymer (PLC) has been reinforced with 0, 2 and 5 wt.% boron nitride nanotubes (BNNTs) for orthopedic scaffold application. Elastic modulus of the PLC–5 wt.% BNNT composite, evaluated through nanoindentation technique, shows a 1370% increase. The same amount of BNNT addition to PLC enhances the tensile strength by 109%, without any adverse effect on the ductility up to 240% elongation. Interactions of the osteoblasts and macrophages with bare BNNTs prove them to be non-cytotoxic. PLC–BNNT composites displayed increased osteoblast cell viability as compared to the PLC matrix. The addition of BNNTs also resulted in an increase in the expression levels of the *Runx2* gene, the main regulator of osteoblast differentiation. These results indicate that BNNT is a potential reinforcement for composites for orthopedic applications.

1. Introduction

Biodegradable polymers are classified as the second generation bio-implant materials [1] due to their advantages over the first generation metallic and ceramic implants because they do not leave undesired foreign elements in the body, even when implant removal is not feasible. One of the main applications of the biodegradable polymers is as temporary scaffolds in bone tissue engineering [2–5]. Amongst the biodegradable polymers, the most commonly used for biomedical applications are poly-ε-caprolactone (PCL) and polylactic acid (PLA), because of their excellent bioresorbability and biocompatibility. There are some basic differences between PLA and PCL, from both the mechanical properties and the chemistry point of view. PLA is a brittle, crystalline polymer with high strength and low elongation at the fracture point. PLA degrades at a faster rate through enzymatic or alkali hydrolysis [2]. On the other hand, PCL is a semi-crystalline polymer of elastomeric nature. It shows hydrophobic nature and degrades at a slower rate [6]. PCL and PLA can thus be used to form a series of copolymers with tailored combinations of strength, deformability and the degradation rate, suitable for the intended bio-applications [2,7–10].

PLC copolymer scaffolds are proposed for the bone and cartilage tissue regeneration in this study. However, the PLC scaffold has elastic modulus and tensile strength that do not match with the properties of the bone tissue or cartilage. Subchondral, trabecular and cortical bone tissues show higher elastic modulus [11], whereas cartilage shows higher tensile strength [12] than PLC. Researchers have used several reinforcements for improving the mechanical properties of PCL, PLA and copolymers. These reinforcements include hydroxyapatite (HA) [3,4,13–16], organic phases like polysaccharides, starch, cellulose, etc. [17–21], silk fibers [22,23] and carbon nanotubes (CNT) [24–27]. The biocompatibility of the reinforcement is a major concern. Since reinforcement may remain within the living tissues for a longer time after the biodegradable matrix is absorbed, it is desired that minimum amount of second phase should be added to obtain maximum increase in the mechanical properties. These requirements necessitate that the second phase material must have excellent mechanical properties and biocompatibility. Studies have reported significant improvement in the mechanical properties of PLA, PCL and PLC copolymer with the addition of carbon nanotubes [13,24–27]. However, it must be noted that biocompatibility of CNTs is still being debated and actively researched [28–32]. Motivated by this scenario, we propose in this study the application of a novel material, boron nitride nanotube (BNNT), as the second phase reinforcement for the biodegradable PLC copolymer.

* Corresponding author. Tel.: +1 305 348 1701; fax: +1 305 348 1932.
E-mail address: agarwala@fiu.edu (A. Agarwal).

1742-7061/$ - see front matter © 2010 Acta Materialia Inc. Published by Elsevier Ltd. All rights reserved.
doi:10.1016/j.actbio.2010.02.044

Please cite this article in press as: Lahiri D et al. Boron nitride nanotube reinforced polylactide–polycaprolactone copolymer composite: Mechanical properties and cytocompatibility with osteoblasts and macrophages in vitro. Acta Biomater (2010), doi:10.1016/j.actbio.2010.02.044

CARBON 48 (2010) 3103–3120

available at www.sciencedirect.com

ScienceDirect

journal homepage: www.elsevier.com/locate/carbon

Carbon nanotube toughened hydroxyapatite by spark plasma sintering: Microstructural evolution and multiscale tribological properties

Debrupa Lahiri [a], *Virendra Singh* [b], *Anup K. Keshri* [a], *Sudipta Seal* [b], *Arvind Agarwal* [a,*]

[a] *Plasma Forming Laboratory and Nanomechanics and Nanotribology Laboratory, Mechanical and Materials Engineering, 10555 West Flagler Street, EC 3464, Florida International University, Miami, FL 33174, USA*

[b] *AMPAC and Nanoscience Technology Center, 4000 Central FL Blvd, AMPAC, Eng 1 Room 381, University of Central Florida, Orlando 32816, USA*

ARTICLE INFO

Article history:
Received 8 January 2010
Accepted 23 April 2010
Available online 23 May 2010

ABSTRACT

Carbon nanotube (CNT) reinforced hydroxyapatite (HA) composite synthesized using spark plasma sintering is investigated in this study. Quantitative microstructural analysis suggests that CNTs play a role in grain boundary pinning and are responsible for the improved densification and retention of nanostructure throughout the thickness of the sintered pellet. HA crystal forms coherent interface with the CNT, resulting in a strong interfacial bond. The uniform distribution of 4 wt.% CNTs in the HA matrix, good interfacial bonding and fine HA grain size help to improve the fracture toughness by 92% and elastic modulus by 25% as compared to the HA matrix without CNT. Toughening mechanisms have been explained in terms of interfacial shear strength and pull-out energy of CNT from the HA matrix. CNT plays a major role in improving the wear resistance of HA matrix at both macro- and nano-scale. It is concluded that graphene layer removal from the CNT surface occurs during macro-wear, but not for nano-wear. Thus, the coefficient of friction (CoF) in HA–CNT decreases in macro-wear due to lubrication available through delaminated graphene layers.

1. Introduction

Hydroxyapatite (HA) is an attractive material for bone substitution and reconstruction owing to its chemical composition ($Ca_{10}(PO_4)_6(OH)_2$), crystal structure and calcium to phosphate ratio (1.67), which is very similar to that of apatite found in the human skeletal system [1–3]. Because of its unique bioactive and osteoconductive properties, HA has been clinically tested and accepted for orthopedic applications. However limited stability of HA causes its dissociation into tricalcium phosphate (TCP) and tetracalcium phosphate, during prolonged exposure at high temperature processing [1,4]. Further, the mechanical properties of HA are insufficient for major load bearing implants. The fracture toughness of dense HA (1 MPa $m^{0.5}$) is just half of the minimum reported fracture toughness of cortical bone (2–12 MPa $m^{0.5}$) [3]. Poor wear resistance of HA is another drawback for its successful application in orthopedic implants [2,3,5–7].

Nanocrystalline HA has been utilized by several researchers [8–12] to overcome some of these limitations. The development of nanoparticles has been accompanied by the need for a suitable processing technique to retain the fine grain size. Spark plasma sintering (SPS) has proved to be a promising technique for the sintering of nanoceramics [13–17]. Due to simultaneous application of pressure, electrical current, and rapid heating rate, SPS offers better densification of

* *Corresponding author:* Fax: +1 305 348 1932.
E-mail address: agarwala@fiu.edu (A. Agarwal).
0008-6223/$ - see front matter
doi:10.1016/j.carbon.2010.04.047

Journal of Materials Processing Technology 210 (2010) 1260–1269

Contents lists available at ScienceDirect

Journal of Materials Processing Technology

journal homepage: www.elsevier.com/locate/jmatprotec

An experimental and computational methodology for near net shape fabrication of thin walled ceramic structures by plasma spray forming

Riken R. Patel[a], Anup Kumar Keshri[a], George S. Dulikravich[b], Arvind Agarwal[a,*]

[a] Plasma Forming Laboratory, Department of Mechanical and Materials Engineering, Florida International University, 10555 West Flagler Street, EC 3464, Miami, FL 33174, United States

[b] Multidisciplinary Analysis, Inverse Design, Robust Optimization and Control Laboratory, Department of Mechanical and Materials Engineering, Florida International University, 10555 West Flagler Street, EC 3464, Miami, FL 33174, United States

ARTICLE INFO

Article history:
Received 27 October 2009
Received in revised form 15 January 2010
Accepted 13 March 2010

PACS:
44.05.+e
44.10.+i
44.15.+a
44.25.+f
44.27.+g
44.35.+c
45.10.−b
47.11.Df
47.11.Fg
52.77.Fv
81.05.Je

Keywords:
Near net shape
Plasma spray forming
Ceramic
Aluminum oxide
Computation
Algorithm

ABSTRACT

Near net shape (NNS) fabrication by plasma spray forming (PSF) is a rapid prototyping technique to fabricate engineering components having axi-symmetric geometry out of ceramics and refractory metals which are difficult to manufacture by conventional techniques. This study establishes an experimental and computational protocol to manufacture thin walled ceramic (Al_2O_3) structures on the graphite mandrel (substrate) via plasma spray forming. The combination of experimental and computational approaches reduces currently used empirical methods for the similar purpose. Thermal profiles generated during plasma spraying of Al_2O_3 on the graphite mandrel for various mandrel designs and cooling conditions were computed by solving the conjugate problem of computational fluid dynamics and 3D unsteady heat transfer. Entire plasma spraying booth was modeled as per actual dimensions to consider the effect on the thermal profile of the mandrel/coating system. The computed temperature profile was compared with the experimentally measured temperature. The corresponding thermal stresses in the mandrel and spray deposited Al_2O_3 layer were computed. Computed thermal stresses were compared with the fracture strength of Al_2O_3 to prevent cracking of the spray formed structure during spraying and its successful removal from the mandrel. An optimum temperature increase rate (TIR) during plasma spray forming is defined for the successful deposition and removal of the freestanding ceramic structure.

1. Introduction

Near net shape (NNS) forming by plasma spray technique is a rapid manufacturing process that provides feasibility of fabricating axi-symmetric, free standing, thin walled (~1 mm) contoured structures from ceramics, metal matrix composites, intermetallics and refractory metals which are difficult to manufacture by conventional techniques like casting, forging or powder metallurgy (Agarwal et al., 2002; Fang and Xu, 2002). Researchers have demonstrated the feasibility of fabricating free-standing components using several combinations of mandrels/substrates and coatings in the following studies. Agarwal et al. (2002) synthesized nanostructured Al_2O_3 free standing cylindrical structures of thickness 0.4–0.6 mm on 6061 aluminum mandrel by PSF. Complex geometries like nozzles, cones and cylinders of thickness up to 3 mm of nickel and yttria–8 wt.% zirconia (Devasenapathi et al., 2002) and free standing annular ring structure of 20 mm diameter, 8 mm width and 3 mm thickness of Al_2O_3–40 wt.% TiO_2 composite (Gopalakrishnan et al., 2003) were also fabricated. Radially symmetric, free-standing yttria stabilized zirconia conical structures of 1.2 mm thickness (Fogarassy et al., 2004) and thin walled tungsten (W) nozzle liner and non-eroding rhenium (Re) throat on reusable graphite mandrel (Balani et al., 2006) were manufactured using PSF technique. Free standing HfC rings of 12 mm diameter (Agarwal et al., 2001), thin walled zero erosion refractory metal/ceramic nozzles inserts for solid rocket propulsion (Hickman et al., 2001)

* Corresponding author. Tel.: +1 305 348 1701; fax: +1 305 348 1932.
E-mail address: agarwala@fiu.edu (A. Agarwal).

0924-0136/$ – see front matter © 2010 Elsevier B.V. All rights reserved.
doi:10.1016/j.jmatprotec.2010.03.012

ARTICLE

Carbon Nanotube Reinforced Polylactide–Caprolactone Copolymer: Mechanical Strengthening and Interaction with Human Osteoblasts in Vitro

D. Lahiri,[†] F. Rouzaud,[†] S. Namin,[§] A. K. Keshri,[†] J. J. Valdés,[†] L. Kos,[†] N. Tsoukias,[§] and A. Agarwal*,[†]

Mechanical and Materials Engineering, Biological Sciences, and Biomedical Engineering, Florida International University, Miami, Florida 33174

ABSTRACT This study proposes the use of carbon nanotubes (CNTs) as reinforcement to enhance the mechanical properties of a polylactide–caprolactone copolymer (PLC) matrix. Biological interaction of PLC–CNT composites with human osteoblast cells is also investigated. Addition of 2 wt % CNT shows very uniform dispersion in the copolymer matrix, whereas 5 wt % CNT shows severe agglomeration and high porosity. PLC–2 wt % CNT composite shows an improvement in the mechanical properties with an increase in the elastic modulus by 100% and tensile strength by 160%, without any adverse effect on the ductility up to 240% elongation. An in vitro biocompatibility study on the composites shows an increase in the viability of human osteoblast cells compared to the PLC matrix, which is attributed to the combined effect of CNT content and surface roughness of the composite films.

KEYWORDS: PLA-PCL copolymer • carbon nanotube • biodegradable scaffold • strengthening • osteoblast • viability

1. INTRODUCTION

The rapid advancement in the field of tissue engineering and regenerative medicine has led to an increased interest in the use of biodegradable polymers as scaffold material. Biodegradable polymers have been used extensively for multiple bone fixation, repair of osteochondral defects, and ligament and tendon reconstruction (1). Poly-lactic acid (PLA) and poly-ε-caprolactone (PCL) are used as scaffold materials for their excellent bioresorbability and biocompatibility. PLA is a crystalline and brittle polymer with high strength and low elongation at break value. It degrades easily at a faster rate through enzymatic or alkali hydrolysis (2). In contrast, PCL is a semicrystalline polymer of elastomeric nature, which is hydrophobic and degrades at a slower rate (3). PCL is therefore a suitable comonomer of PLA for the preparation of a series of copolymers with mechanical properties ranging from elastomeric to rigid. PLA–PCL copolymer (PLC) has good elongation characteristics, which makes it interesting for bioapplications where both elasticity and degradability are required (4). Hence, copolymerization of PLA and PCL provides a controlled way to adjust the degradation rate, suitable for the intended application (2).

It is equally important that the copolymer should possess excellent mechanical properties as the scaffold material. One of the most effective methods of increasing the mechanical properties (elastic modulus and tensile strength) of a polymer is by reinforcing with a second-phase material. Hence, researchers have used different types of second-phase materials for mechanical strengthening of PLA, PCL, and their copolymers (PLC) (5–16). Among all of these, carbon nanotubes (CNT) seem to be the reinforcement with most potential, due to their very high mechanical properties (Young's modulus 0.2–1 TPa, tensile strength 11–63 GPa) (17, 18) and fiberlike structure. A recent study by Usui et al. (19) demonstrated that multiwalled carbon nanotubes (MWCNT) have very good bone-tissue compatibility and help in the bone repair by accelerating its growth. Further, CNTs get closely integrated in the grown bone without toxic effect. All these findings have caused carbon nanotubes to be the suitable second-phase reinforcement for biodegradable polymers in orthopedic scaffold applications.

Researchers have studied the effect of CNT addition on the mechanical strengthening for PLA (20–23) and PCL (24–26). However, there is currently no report available on a PLC copolymer–CNT composite. Biocompatibility of the CNT-reinforced PLC copolymer composite is another very important issue for scaffold application. Zhang et al. (27) reported that the presence of MWCNTs in PLA inhibits fibroblast cell growth due to less attachment of the cells on the composite surface, although they were not able to establish the cause. Another in vitro study showed that osteoblasts grown on PLA–CNT composite exhibit higher viability and metabolic activity, suggesting it to be a favorable environment for the cells (28). The biocompatibility for PLC–CNT composite is yet to be established, as there are no reports available on biostudies of PCL–CNT and PLC–CNT

† Mechanical and Materials Engineering.
‡ Biological Sciences.
§ Biomedical Engineering.
Received for review June 19, 2009 and accepted October 4, 2009
DOI: 10.1021/am900423q

Published on Web 10/20/2009

Materials Science and Engineering A 523 (2009) 263–270

Contents lists available at ScienceDirect

Materials Science and Engineering A

journal homepage: www.elsevier.com/locate/msea

Dual strengthening mechanisms induced by carbon nanotubes in roll bonded aluminum composites

D. Lahiri[a], S.R. Bakshi[a], A.K. Keshri[a], Y. Liu[b], Arvind Agarwal[a,*]

[a] Nanomechanics and Nanotribology Laboratory, Mechanical and Materials Engineering, Florida International University, Miami, FL 33174, USA
[b] Advanced Materials Engineering Research Institute, Mechanical and Materials Engineering, Florida International University, Miami, FL 33174, USA

ARTICLE INFO

Article history:
Received 14 May 2009
Received in revised form 28 May 2009
Accepted 4 June 2009

Keywords:
Al–CNT composite foil
Roll-bonding
Dislocation density
Strain hardening
Dispersion

ABSTRACT

The dual role of carbon nanotubes (CNTs) in strengthening roll bonded aluminum composites has been elucidated in this study. An increase in the elastic modulus by 59% has been observed at 2 vol.% CNT addition in aluminum, whereas tensile strength increases by 250% with 9.5 vol.% CNT addition. CNTs play a dual role in the strengthening mechanism in Al–CNT composite foil, which can be correlated to the degree of dispersion of CNTs in the matrix. Better CNT dispersion leads to improvement of elastic properties. In contrast, CNT clusters in the aluminum matrix impede dislocation motion, causing strain hardening and thus improvement in the tensile strength. Dislocation density of the composites has been computed as a function of CNT content to show the effect on strain hardening of the metal matrix–CNT composite.

1. Introduction

Carbon nanotubes (CNTs) have found an increasing interest as reinforcement for aluminum matrix due to their excellent mechanical properties. Elastic modulus of CNT has been reported to vary between 200 and 1250 GPa [1,2], depending on different morphologies. Since the first study by Kuzumaki et al. [3], Al–CNT composite has been successfully processed through different techniques. Most of such investigations have dealt with the powder metallurgy route, often assisted with severe plastic deformation process [4–9]. Researchers have also explored thermal spray methods [10–12], magnetic sputtering [13], liquid infiltration [14], and high pressure torsion [15] for preparing Al–CNT composites. Dispersion of nanotubes is the most critical step towards enhancement of mechanical properties of the composite. Improved degree of CNT dispersion in Al matrix has been achieved through molecular level mixing [9,16] and growing CNT on Al powder particles through chemical vapor deposition [5] prior to consolidation. This improvisation has resulted in 350% increase in the strength [16], proving the role of better dispersion in enhancement of mechanical properties of the composite. Most of the above-listed processing technique involves high temperature for consolidation, which might result in inducing some damage to CNTs. Hence a room temperature technique, like roll bonding, could be a viable option for processing soft, ductile matrix, e.g., Al or Cu based CNT reinforced composites.

Roll bonding is already an established process for mechanical strengthening of aluminum [17,18]. This technique has been successfully used for fabrication of metal (Cu) [19] and ceramic (SiC) [20] reinforced aluminum matrix composites. Choi et al. [8] have shown the positive effect of severe deformation on good dispersion and alignment of CNTs in Al matrix. Li et al. [21] has published the only report on processing of Cu matrix–CNT composite through roll-bonding route. In that study, SWCNTs were acetone sprayed on 10 μm thick Cu foils and then 19 such foils, with intermediate layers of CNTs, were roll bonded to form the composite, with 13% increase in strength. But, till date, processing of Al–CNT composite through roll-bonding route has not been reported. Hence, in the present study, Al–CNT composites have been synthesized by roll-bonding technique.

Another aspect of interest is the role of CNTs in the strengthening mechanism of metal matrix. Apart from enhancement in elastic modulus, it has also been concluded that CNTs obstruct dislocation movement, thus creating high dislocation density in the metal matrix composites in case of soft matrix like Al [8], Mg [22–25], Cu [26] and lead free solder (SnAgCu) alloy [27]. Dislocation pile ups are created due to mismatch in the elastic modulus of CNT and the soft metal matrix [22–24,27]. This, in turn, increases the strain hardening of the matrix metal during plastic deformation. But, till date no report is available on the "quantification" of dislocation density and strain hardening of the composite induced by CNTs.

* Corresponding author.
E-mail address: agarwala@fiu.edu (A. Agarwal).

0921-5093/$ – see front matter © 2009 Elsevier B.V. All rights reserved.
doi:10.1016/j.msea.2009.06.006

Surface & Coatings Technology 204 (2009) 503–510

Contents lists available at ScienceDirect

Surface & Coatings Technology

journal homepage: www.elsevier.com/locate/surfcoat

Microstructure and wear properties of aluminum/aluminum–silicon composite coatings prepared by cold spraying

Srinivasa R. Bakshi [a], Di Wang [a], Timothy Price [b], Deen Zhang [b], Anup K. Keshri [a], Yao Chen [a], D. Graham McCartney [b], Philip H. Shipway [b], Arvind Agarwal [a,*]

[a] Department of Mechanical and Materials Engineering, Florida International University, Miami, FL 33174, USA
[b] School of Mechanical, Materials and Manufacturing Engineering and Management, University of Nottingham, University Park, Nottingham, NG7 2RD, UK

ARTICLE INFO

Article history:
Received 14 May 2009
Accepted in revised form 17 August 2009
Available online 21 August 2009

Keywords:
Aluminum coating
Metal matrix composite
Wear
Delamination
Cold spraying

ABSTRACT

Composite coatings containing aluminum and aluminum–11.6 wt.% silicon eutectic alloy phases of varying compositions were fabricated using cold spraying. Coating contained a uniform distribution of the two phases. The hardness of the coatings increased as the volume fraction of Al–Si in the coating increased. The length to width ratio of the splats was found to be larger for Al particles compared to Al–Si particles. Dry sliding ball-on-plate wear tests indicated that the wear volume loss was similar for the Al and Al/Al–Si composite coatings in spite of the increase in microhardness. This discrepancy is explained by the inter-splat delamination mechanism. The coefficient of friction of aluminum coating reduced on Al–Si addition.

1. Introduction

Cold gas dynamic spraying or, more simply, cold spray is a coating technology which involves the acceleration and impact of solid particles on a substrate to form a coating. Typical cold sprayed coating thicknesses range between 100–1500 μm. The particles are accelerated in a supersonic gas jet which can be produced by the use of a converging–diverging de Laval nozzle [1]. Particles impinging on a substrate will either rebound from the substrate (with or without causing erosion), or bond with the substrate depending on the material type and particle velocity on impact with the substrate. In this way, coating formation is provided via plastic impact at high velocity (300–1200 m/s) and a temperature much below the melting point of the starting powder (ambient temperature to 700 °C). Bonding occurs due to rapid and significant deformation under high pressures and strain rates. It has been observed that for a range of metals, particle deposition only occurs when the particle velocity exceeds a critical value. It has been widely reported that many metallic materials such as Cu, Al, Ni, Ti, Fe- and Ni-based alloys can be readily deposited by cold spray [2–6] and recently there has been a growing interest in the use of cold spray to deposit composite coatings.

A disadvantage of the process is that it is believed that only materials that are plastically deformable can form a coating. Dispersion of hard and brittle phases in a ductile matrix has been achieved by co-deposition of powder mixtures. Examples include TiO_2–Zn [7], WC–Co [8,9], Al_2O_3–Cu [10], TiB_2–Cu [11], Al–SiC [12] and Al_2O_3–Al [12,13], Cr_3C_2–Ni [14] and SiC–Al–Si [15]. The majority of these studies have been aimed at investigation of the coating microstructure and deposition characteristics. Although a suitable distribution of reinforcement phase was obtained in most of the cases, only a few attempts have been made to study the effect on the mechanical properties of the composites. Kim et al. [9] found that the cold sprayed nanosized WC–Co coatings had extremely high hardness of around 2050 VHN. Phani et al. [10] found that addition of nano-alumina inhibited grain growth of nanocrystalline copper coatings and an increase in the hardness was observed. Hall–Petch hardening was found to occur and be the dominant mechanism of hardening. Wolfe et al. [14] have carried out preliminary wear experiments on cold sprayed Cr_3C_2–Ni coatings and found that the wear resistance was slightly better than 4140 steel substrate. Guo et al. [16] have studied the dry sliding wear of cold sprayed tin–bronze coatings and found that the wear properties deteriorated on annealing the coatings although it was observed that the porosity decreased. However, despite its importance in terms of engineering applications of cold spray coatings; there have been limited studies on the wear behavior of cold sprayed ceramic–metal composite deposits.

Two of the main applications of cold spraying are deposition of wear resistant coatings and repair of defective structural components. Aluminum–silicon alloys and its composites are important materials for applications in the automobile industry. One of the main reasons for their use is their excellent wear resistance. Clarke and Sarkar have

* Corresponding author. Tel.: +1 305 348 1701; fax: +1 305 348 1932.
E-mail address: agarwala@fiu.edu (A. Agarwal).

0257-8972/$ – see front matter © 2009 Elsevier B.V. All rights reserved.
doi:10.1016/j.surfcoat.2009.08.018

Journal of Alloys and Compounds 481 (2009) 207–213

Contents lists available at ScienceDirect

Journal of Alloys and Compounds

journal homepage: www.elsevier.com/locate/jallcom

Interface in carbon nanotube reinforced aluminum silicon composites: Thermodynamic analysis and experimental verification

Srinivasa R. Bakshi[a], Anup K. Keshri[a], Virendra Singh[b], Sudipta Seal[b], Arvind Agarwal[a,*]

[a] Plasma Forming Laboratory, Department of Mechanical and Materials Engineering, Florida International University, 10555 West Flagler Street, EC 3464, Miami, FL 33174, USA
[b] AMPAC and Nanoscience Technology Center, University of Central Florida, Orlando, FL 33816, USA

ARTICLE INFO

Article history:
Received 13 January 2009
Received in revised form 10 March 2009
Accepted 11 March 2009
Available online 21 March 2009

Keywords:
Metal matrix composites
Surfaces and interfaces
Carbon nanotubes
Thermodynamics
Carbide

ABSTRACT

Interface in carbon nanotubes (CNTs) reinforced aluminium–silicon composites are studied via thermodynamic and kinetic analysis. A pseudo-phase diagram has been generated based on the thermodynamic calculations to predict the type of carbide (Al_4C_3 or SiC) that would form at the matrix–CNT interface as a function of matrix composition and processing temperature. The pseudo-phase diagram is useful in high temperature processes like thermal spray forming. Critical thickness values for carbide nucleation suggest the formation of Al_4C_3 with Al–11.6 wt.% Si alloy and SiC with Al–23 wt.% Si alloy. Thermodynamic calculations show that the amount of Al_4C_3 increases with an increase in the CNT content. The computed results perfectly agree with the results obtained by XRD, SEM of fracture surface and high-resolution transmission electron microscopy (HRTEM) observations on Al–11.6 wt.% Si and Al–23 wt.% Si alloy reinforced with CNT.

1. Introduction

Light weight and high strength metal matrix composites reinforced with carbon fibers have been used for many automobile and space applications [1–3]. In recent years, the focus has shifted to reinforcement of metal matrix composites with carbon nanotubes (CNTs) due to their strengths in excess of 100 GPa and stiffness of 1000 GPa which makes them superior to carbon fibers [4,5]. The major challenge has been to disperse and align the nanotubes in the metal matrix and the fabrication of bulk composites having the above-mentioned characteristics. Cha et al. [6] have shown extraordinary improvement of the yield strength (~200% increase for 10 vol.% CNT addition) in copper–CNT composites fabricated by the molecular mixing method. The increase in the strength was attributed to the uniform dispersion of CNTs. Choi et al. [7] have fabricated aluminium–CNT composites by extrusion of ball milled powders. Young's modulus and yield strength increased by ~49% and ~46%, respectively, for the 4 vol.% CNT containing composite.

The fiber–matrix interface plays an important role in strengthening of the composite. The applied stress is transferred to the high strength reinforcement through the interfacial layer. So a strong interface would make the composite very strong but at the expense of ductility of the composite. A weak interface would lead to lower strength and inefficient utilization of fiber properties by facilitating pullout phenomena at low loads due to interface failure. Interfacial reactions and degree of wetting of the reinforcement (fibers) also affect the properties of the composite [8–10]. Formation of aluminum carbide (Al_4C_3) has been observed at the interface in liquid metal infiltrated aluminum silicon alloy composites reinforced with carbon fibers containing 7 wt.% [11] and 13 wt.% Si [12]. Vidal-Setif et al. have shown reduction in strength and premature failure of 75 vol.% carbon fiber reinforced A357 alloy due to formation of Al_4C_3 and presence of brittle Si particles [13]. So formation of Al_4C_3 needs to be avoided. This can be done by either by controlling the chemistry of the matrix or by using coated carbon fibers [14,15].

Recently there has been a lot of interest in fabrication of aluminum matrix composite reinforced with carbon nanotubes. Bulk aluminium–CNT composites have been fabricated using various processes like cold isostatic pressing followed by hot extrusion [16], pressureless infiltration technique [17] and thermal spraying [18–20] to name a few. *In general, less attention has been devoted to the interfacial reaction between the metal matrix and CNT.* It has been reported by some authors that no reaction product is observed [7,21]. It is very important to understand the interaction between metals and the new forms of carbon namely CNTs, from theoretical and practical viewpoint. Carbon nanotubes are made by rolling a sheet of graphene onto itself and hence outer shell is made up of the basal plane. So they could be quite stable chemically. Zhong et al. have shown from the changes occurring in the intensity of (1 1 1) peak of the XRD pattern of Cobalt, after a 10-h annealing treatment with various forms of carbon at 1000 °C, that the interaction of layered graphite was the lowest followed by single walled CNT,

* Corresponding author. Tel.: +1 3053481701; fax: +1 3053481932.
E-mail address: agarwala@fiu.edu (A. Agarwal).

0925-8388/$ – see front matter © 2009 Elsevier B.V. All rights reserved.
doi:10.1016/j.jallcom.2009.03.055

The Nano-scratch Behavior of Biocompatible Hydroxyapatite Reinforced with Aluminum Oxide and Carbon Nanotubes

Kantesh Balani, Debrupa Lahiri, Anup K. Keshri, S.R. Bakshi, Jorge E. Tercero, and Arvind Agarwal

Hydroxyapatite (HA) reinforced with sub-micrometer Al_2O_3 and carbon nanotubes (CNTs) has been synthesized as a coating on the Ti-6Al-4V substrate via plasma spraying. The addition of Al_2O_3 and CNTs to HA has shown improvement in the hardness and elastic modulus by 65% and 50%, respectively, when compared to HA. Consequently, HA-Al_2O_3-CNT coatings have been nano-scratched to understand their wear performance. Reinforcement of HA by Al_2O_3 shows a decrease in the wear volume by more than 13 times, whereas HA-Al_2O_3-CNT coating demonstrated further wear volume reduction of five times compared to that of HA-Al_2O_3 coating.

INTRODUCTION

Biocompatibillity of hydroxyapatite (HA) has been established by various researchers because of its chemical structure similar to that of bone and teeth (Ca/P ratio of 1.66).[1,2] Application of HA as a structural material is limited because of its brittleness and low fracture toughness (~0.4 MPa $m^{1/2}$).[1,3] Hence arises the need to reinforce the HA without hampering its biocompatibility. Introduction of ceramics (e.g., ZrO_2, Al_2O_3, mullite, Ni_3Al, and SiC,) with better mechanical properties has been applied to enhance the energy absorption by HA matrix.[2-6] It becomes a special concern to retain the biocompatibility of the composite while reinforcing secondary materials to improve mechanical properties of HA matrix.[2,4] Extensive interfacial reaction between HA and ZrO_2 to form tricalcium phosphate (TCP) limits its utilization.[4] Toxicity of SiC_w restricts its reinforcement in HA matrix.[7] Alumina (Al_2O_3), being a bioinert material, has shown much promise.[2,8] Reinforcement with carbon nanotubes (CNTs) has shown fracture toughness enhancement by up to three times, HA crystallinity increase by 27%, bending strength of up to 180 MPa, without deterioration of the coating's biocompatibility.[1,7] In addition, apatite precipitation has been observed on the CNT surface endorsing non-toxicity of human fiber osteoblasts in the CNT reinforced HA coating.[1] Consequently, macro-scale pin-on-disk wear resistance improvement of up to 1.5 times was also observed in CNT reinforced HA matrix.[3]

The current work focuses on the synergistic effect of secondary reinforcements such as sub-micrometer Al_2O_3 (150 nm particle size) and CNTs in attaining enhanced fracture toughness and wear resistance of HA matrix. HA coatings reinforced with Al_2O_3 and CNTs are synthesized using plasma spraying, and wear resistance of HA-Al_2O_3-CNT biocomposites is quantified using nano-scratching by evaluation of its wear volume. Since our previous work insinuates biocompatibility of HA-CNT composite,[1] the addition of bio-inert Al_2O_3 as reinforcement is expected to further enhance the fracture toughness and wear resistance of coatings without affecting its biocompatibility. Though the effect of Al_2O_3 and CNT reinforcements on the biocompatibility of HA composite is not the focus of the current work, it must be mentioned that research confirming biocompatibility of these composites is published elsewhere.[9] The two-fold importance of (i) enhancing toughness by Al_2O_3 (bio-inert) and rendering CNT re-bars (bio-active), while (ii) retaining biocompatibility (bioinertness of Al_2O_3 and apatite precipitation on CNTs)

How would you...

...describe the overall significance of this paper?

Reinforcement of hydroxyapatite (HA) with Al_2O_3 and carbon nanotubes (CNTs) have shown improvement in the hardness and elastic modulus by 65% and 50%, respectively, when compared to that of HA alone. In addition, wear volume reduction by more than 65 times is also observed in HA-Al_2O_3-CNT plasma sprayed coatings.

...describe this work to a materials science and engineering professional with no experience in your technical specialty?

Novel plasma spraying has been utilized to synthesize hydroxyapatite (HA) coatings reinforced with Al_2O_3 and carbon nanotubes (CNTs) on a real life Ti-6Al-4V body implant substrate. Undeterred biocompatibility with enhanced mechanical properties (modulus by 50%, hardness by 65%, and wear resistance by 68 times) has been observed in HA-Al_2O_3-CNT coatings in comparison to that of HA alone.

...describe this work to a layperson?

The rigorous body environment restricts the normal lifetime of body implants in the range of 10–15 years. An early age implant surgery requires repeated surgery operations after the usual lifetime of inserted implant is exhausted. Hence, newly developed HA-Al_2O_3-CNT biocoating will not only provide enhanced life, but will also provide a friendly surface for adhesion of newly growing bone (bone cells) for strong anchorage with the implant.

Available online at www.sciencedirect.com
ScienceDirect
Acta Materialia 56 (2008) 5984–5994
Acta MATERIALIA
www.elsevier.com/locate/actamat

Multiscale wear of plasma-sprayed carbon-nanotube-reinforced aluminum oxide nanocomposite coating

Kantesh Balani [a], Sandip P. Harimkar [b], Anup Keshri [a], Yao Chen [a], Narendra B. Dahotre [b], Arvind Agarwal [a,*]

[a] Mechanical and Materials Engineering, Florida International University, Miami, FL 33174, USA
[b] Materials Science and Engineering, University of Tennessee, Knoxville, TN 37996, USA

Received 24 April 2008; received in revised form 26 June 2008; accepted 5 August 2008
Available online 9 September 2008

Abstract

A multiple length scale wear study of plasma-sprayed Al_2O_3–carbon nanotube (CNT) nanocomposite coating is described. CNT content and dispersion have been shown to enhance the macro-wear resistance (pin-on-disk) by more than 49 times, and nano-wear (scratch) resistance up to 18 times. CNTs have been shown to reduce the wear of Al_2O_3 matrix by (i) increasing densification, (ii) CNT bridging and (iii) CNT lubrication. A strong dependence of wear volume loss on the microstructural features is described at different length scales, and the disparity of material loss observed in the macro- and nano-wear tests is explained. A wear model has been established to numerically quantify wear loss dependence in terms of bulk material properties and correlating these with wear parameters from nano-scratch testing.

Keywords: Plasma spraying; Al_2O_3–carbon nanotube (CNT) nanocomposite; Nano-scratch test; Multiscale-wear tribology

1. Introduction

Tribology involves the study of a complex phenomenon that depends on several variables: surface roughness, load application, local material interaction, lubrication condition and material properties of two mating surfaces. The functionality of an engineering component in sliding conditions is often decided by macro-wear, whereas the mechanism of material loss is decided at the micro- and nano-scales. Macro-wear involves multiple asperity contacts; in contrast, nano-wear interactions occur via single/few asperity contacts. Therefore, there exists a gap between the macro-wear and nano-wear owing to the different length scales [1–5]. There are very few studies that provide an insight into multi-scale wear and a description of the wear mechanisms [1–10]. Ingole et al. performed a wear test using a pin-on-disk tribometer on a boride coating on a tungsten substrate and analyzed the wear surface using atomic force microscopy (AFM) [2]. It was concluded that macro-wear occurred via mixed mode wear of boride coating that includes: (i) abrasion grooves at the micrometer length scale, and (ii) fracture of hard phase via cracking at the nanometer length scale [2]. Computational models for multi-scale material removal by progressive grinding and polishing have been proposed [7,9]. Seok et al. have described fundamental models of erosion and abrasion in chemical–mechanical polishing [9]. Three scaled statistical representations of abrasive particle, asperity and wafer were correlated in order to evaluate material loss with applied stress using computational modeling [9]. Bigerelle et al. developed a fractal model that utilized roughness and radius curvature for predicting progressive material loss upon grinding [7]. In spite of these isolated studies, a direct model and scaling mechanism connecting the different length scales is still unavailable. In addition, incorporation of secondary

* Corresponding author. Tel.: +1 305 348 1701; fax: +1 305 348 1932.
E-mail address: agarwala@fiu.edu (A. Agarwal).

1359-6454/$34.00 © 2008 Acta Materialia Inc. Published by Elsevier Ltd. All rights reserved.
doi:10.1016/j.actamat.2008.08.020

Available online at www.sciencedirect.com
ScienceDirect
Scripta Materialia 60 (2009) 1023–1026
Scripta MATERIALIA
www.elsevier.com/locate/scriptamat

Ionic conductivity of plasma-sprayed nanocrystalline yttria-stabilized zirconia electrolyte for solid oxide fuel cells

Y. Chen,[a] S. Omar,[b] A.K. Keshri,[a] K. Balani,[a,d] K. Babu,[c] J.C. Nino,[b] S. Seal[c] and A. Agarwal[a,*]

[a] *Plasma Forming Laboratory, Mechanical and Materials Engineering, Florida International University, Miami, FL 33174, USA*
[b] *Materials Science and Engineering, University of Florida, Gainesville, FL 32611, USA*
[c] *Advanced Materials Processing & Analysis Center (AMPAC) and Mechanical, Materials and Aerospace Engineering, University of Central Florida, Orlando, FL 32816, USA*
[d] *Materials and Metallurgical Engineering, Indian Institute of Technology, Kanpur, UP 208016, India*

Received 11 February 2009; accepted 22 February 2009
Available online 26 February 2009

Nanocrystalline 10 mol.% yttria-stabilized zirconia (YSZ) electrolyte was synthesized via the plasma spray technique. The ionic conductivity was measured using AC impedance spectroscopy within the temperature range 350–600 °C in air. The measured total ionic conductivity of plasma-sprayed YSZ electrolyte is ~2.3 times higher than that of sintered YSZ electrolyte at 600 °C in air. The improvement in ionic conductivity is ascribed to the nanocrystalline grain size and siliceous free grain boundary with grain-to-grain contact.

Keywords: Yttria-stabilized zirconia; Electrolyte; Plasma spray; Ionic conductivity

Solid oxide fuel cells (SOFCs) have been attracting attention due to their efficient conversion of electrochemical fuel to electricity with negligible pollution [1–3]. Yttria-stabilized zirconia (YSZ) with a cubic fluorite structure is considered to be the most reliable electrolyte because it exhibits thermal stability, good ionic conductivity at high-temperature (~1000 °C) and thermal expansion compatibility with electrode materials [2–3]. From the view of long-term durability and reliability, and cost efficiency, the current developmental target for SOFCs is to reduce the operating temperature into the intermediate temperature (IT) range (500–700 °C), which requires increased electrolyte ionic conductivity and enhanced gas/electrode reaction kinetics [4]. However, the relatively lower ionic conductivity of YSZ at intermediate temperatures limits its application as an electrolyte candidate for IT-SOFCs.

Nanocrystalline YSZ has a high number of atoms residing at grain boundaries and surfaces that increase the surface area of the active sites for reactions [5]. It is reported that nanocrystalline YSZ exhibits an increase of about 2–3 orders of the magnitude in electrical conductivity as compared to microcrystalline specimen [4]. Activation energy for microcrystalline YSZ is ~1.24–1.30 eV, whereas this reduces to ~0.93 eV for nanocrystalline YSZ [4]. Therefore, the development of nanocrystalline YSZ electrolyte is of considerable interest for IT-SOFCs. A few researchers have also reported a decrease in the electrical conductivity with decreasing grain size (0.2–20 μm) for zirconia and ceria-based electrolytes [5–10]. These contradictory observations further motivate our present study to understand the effect of grain size on electrical conductivity.

Plasma spray technique is a versatile process: it can deposit almost any material as coatings and bulk while retaining the benefits of rapid solidification, high deposition rate and cost efficiency [9]. Compared with conventional wet ceramic techniques [10] for SOFC electrolyte fabrication, plasma-sprayed materials usually exhibit porous and lamellar microstructures, subsequently leading to low open circuit voltage and cell efficiency. Hence, some post-deposition heat treatments such as high-temperature sintering and spark plasma sintering (SPS) are employed to improve the electrolyte density and alleviate the gas leakage issue [2]. Our research group has successfully synthesized nanocrystalline metal

* Corresponding author. Tel.: +1 305 348 1701; fax: +1 305 348 1932; e-mail: agarwala@fiu.edu

1359-6462/$ - see front matter © 2009 Acta Materialia Inc. Published by Elsevier Ltd. All rights reserved.
doi:10.1016/j.scriptamat.2009.02.036

VITA

ANUP KUMAR KESHRI

EDUCATION

Aug. 1998 – July 2002	Bachelor of Engineering (B.E.) in Metallurgical Engineering, Bihar Institute of Technology (now Birsa Institute of Technology, BIT), Sindri, Jharkhand, India (First Class with Honors)
Aug. 2002 – Aug. 2004	Masters of Science (M.S) in Metallurgical and Materials Engineering, Indian Institute of Technology (IIT) Madras, India. (First Class)
Sept. 2006 – Aug. 2010	Doctoral Candidate (Ph.D) in Materials Engineering, Department of Mechanical and Materials Engineering, Florida International University, Miami, Florida

PROFESSIONAL EXPERIENCE

Sept. 2006 – Aug. 2010	Research Assistant, Department of Mechanical and Materials Engineering, FIU
Sept. 2004 – Aug. 2006	Assistant Manager, R&D and Six Sigma Department, Ispat Industries Limited, Mumbai, India

ACADEMIC AWARDS AND HONOURS

1. Dissertation Year Fellowship: University Graduate School, Florida International University for 2009-2010
2. Arthur E. Focke leadership award by ASM Foundation for attending the leadership camp during Summer-2008 at University of Illinois, Urbana Champaign.
3. *Delegate of* "President's Council of Student Advisors (PCSA)"formed by The American Ceramic Society (ACerS)
4. Served as Chair of Material Advantage chapter in 2008-2009 at FIU, Miami, Florida, USA
5. First in Regional Technical presentation competition organized by Material Advantage at FIU, on 16th Nov. 2007

6. First in Student Technical Poster competition organized by Material Advantage at FIU, on 17th Nov. 2006.
7. Best Paper presentation award in "TRANSMAT EXPO-2004" International Conference held on Nov. 8th -10th in Mumbai, India

PUBLICATIONS AND PRESENTATIONS

1. Anup Kumar Keshri, Jun Huang, Virendra Singh, Wonbong Choi, Sudipta Seal and Arvind Agarwal, "Synthesis of Aluminum Oxide Coating with Carbon Nanotube Reinforcement Produced by Chemical Vapor Deposition for Improved Fracture and Wear Resistance", Carbon Vol. 48 (2010) 431-442

2. Anup Kumar Keshri, Jun Huang, Wonbong Choi, and Arvind Agarwal, "Intermediate Temperature Tribological Behavior of Carbon Nanotube Reinforced Plasma Sprayed Aluminum Oxide Coating", Surface and Coatings Technology Vol. 204 (2010) 1847-1855

3. Anup Kumar Keshri, Riken Patel, and Arvind Agarwal "Comprehensive Process Maps to Synthesize High Density Plasma Sprayed Aluminum Oxide Composite Coatings with Varying Carbon Nanotube Content", Surface and Coatings Technology (2010), in press.

4. Anup Kumar Keshri, Kantesh Balani, Srinivasa Rao Bakshi, Virendra Singh, Tapas Laha, Sudipta Seal and Arvind Agarwal, "Structural Transformation in Carbon Nanotubes During Thermal Spraying", Surface and Coatings Technology Vol. 203 (2009) 2193-2201 (Ranked 5th among TOP 25 articles in Surface and Coatings Technology journal for April-June 2009)

5. Anup Kumar Keshri, Srinivasa Rao Bakshi, Yao Chen, Tapas Laha, Xiaohua. Li, Cesar Levy and Arvind Agarwal, Nanomechanical Behavior of Plasma Sprayed PZT Coatings", Surface Engineering Vol. 25[4] (2009) 270-275

6. Debrupa Lahiri, Virendra Singh, Anup Kumar Keshri, Sudipta Seal and Arvind. Agarwal, "Carbon nanotube toughened hydroxyapatite by spark plasma sintering: microstructural evolution and multi-scale tribological properties", Carbon Vol. 48 (2010) 3103-3120

(Listed 6 out of 15 published papers, 1 more papers are under review in peer reviewed journals)